RATIOMETRIC NANOTHERMOMETRY BASED ON THE PHONON ASSISTED ANTI-STOKES LUMINESCENT MATERIALS

By

Chao Mi

Institute for Biomedical Materials & Devices

School of Mathematical and Physical Sciences, Faculty of Science

Supervisors:

Dr. Jiajia Zhou & Prof. Dayong Jin

This thesis is presented for the degree of Doctor of Philosophy

September 2019

Certificate of Original Authorship

I, Chao Mi declare that this thesis, submitted in fulfilment of the requirements for the award of Doctor of Philosophy, in the School of Mathematical and Physical Sciences, Faculty of Science, University of Technology Sydney.

This thesis is wholly my own work unless otherwise reference or acknowledged. In addition, I certify that all information sources and literatures used are indicated in the thesis.

This document has not been submitted for qualifications at any other academic institution.

This research is supported by an Australia Government Research Training Program.

Signature: Production Note:
Signature removed prior to publication.

Date: 22/02/2019

Acknowledgements

After 3 and half years' study at University of Technology Sydney (UTS), I have completed my PhD thesis with the help of others. Firstly, I would like to thank my supervisor Prof. Dayong Jin for the valuable opportunity of PhD scholarship in Australia. From the beginning of my study, Prof. Jin has paid much energy and time to my research plan development. He has insights to foresee the trend of related research area and provided great ideas and suggestions for my research. I could not imagine how to complete my research without his guidance. Moreover, supervised by Prof. Jin, I have improved my ability on how to conduct the research project logically.

Meanwhile, I also would like to express my heartfelt thanks to my supervisor Dr. Jiajia Zhou. Although Dr. Zhou has been my principle supervisor in the last year of my PhD study, she started to support my research since 2015 as my research project closely connected to her research area. Dr. Zhou helped me a lot with my experiment design, results discussion and we overcame the challenges in my research together. I thank her for devoting herself to the development of my work.

Greatly, thanks a lot to our group members and collaborators who contributed to my research. Thanks to Dr. Fan Wang for teaching me on the optical test systems. As my background is optical material synthesis, I learned a lot of new knowledge on the optical instrument build-up from him, and my research benefits a lot from this. Also, I would like to thank Dr. Shihui Wen, Dr. Jiayan Liao and Dr. Helen Xu for help with upconversion nanoparticles synthesis and morphology characterization, Dr. Gungun Lin for providing the microelectronic device used in my research, and Dr. Ziyuan Li in Australian National University for her assistance on my experiment.

Next, I would like to acknowledge all my colleagues who have given me help over the last several years. Thanks to the optics group including Zhiguang Zhou, Chaohao Chen, Yongtao Liu, Xuchen Shan and Baolei Liu. And my office mates, Hao He, Wei Ren, Ming Guan, Yinghui Chen, Jiayan Liao. Thank you for a lot of beneficial discussions and helps in both my study and life, and I appreciate your supports and friendship very much.

I give my deep appreciation to my family. I thank my parents for their moral support to my oversea PhD study, and my girlfriend for her thoughtfulness, understanding and sincere company.

Special thanks to our school manager Elizabeth Gurung Tamang, lab manager Katie McBean, and Ronald Shimmon for their technique support.

Finally, I would like to acknowledge the Australia Government and UTS for providing me with PhD scholarship and research opportunities.

Format of Thesis

This thesis has a conventional format with six chapters as illustrated by the flow chart below.

Chapter 1 is an introduction chapter based on a comprehensive literature review. The classifications, thermometric properties of nanothermometers, and the advantages of RE doped luminescent nanothermometers are discussed in details.

Chapter 2 provides detailed methods of the materials synthesis and sample characterizations used in the result chapters.

Chapter 3 investigates the thermal induced emission enhancement in RE doped anti-Stokes luminescent nanoparticles and proposes the surface-phonon-assistance behind this phenomenon, which provides the experimental foundation for the following chapters.

Chapter 4 describes the strategy to create ultra-sensitive nanothermemeters based on the phonon-assisted anti-Stokes emissions in RE doped nanoparticles.

Chapter 5 gives the nanothermometry demonstration results on two different applications to show the ability of the created nanothermometers.

Chapter 6 summarizes the main research results of this project and future research work based on the current progress described in this thesis.

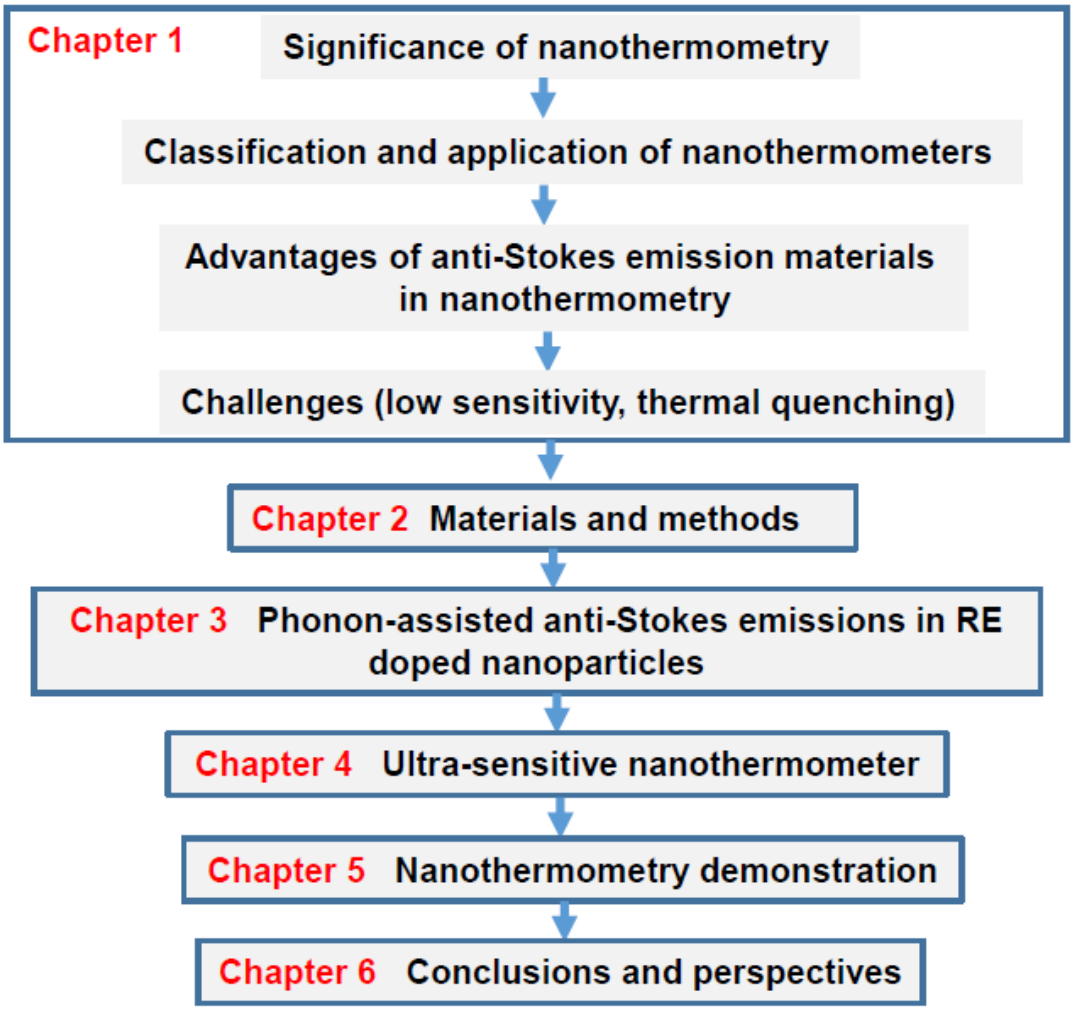

The flow chart outlines the thesis structure.

List of Publications

Research papers:

[1] Chao Mi, Jiajia Zhou*, Fan Wang and Dayong Jin, Anti-Stokes emission enhancement of near infrared nanothermometry probes, ***Nanoscale***, 2019, 11, 12547.

[2] Chao Mi, Jiajia Zhou*, Fan Wang, Gungun Lin and Dayong Jin, Ultra-sensitive ratiometric nanothermometer with large dynamic range and photostability, ***Submitted.***

[3] Jiajia Zhou*, Shihui Wen, Jiayan Liao, Christian Clarke, Sherif Abdulkader Tawfik, Wei Ren, Chao Mi, Fan Wang and Dayong Jin*, Activation of the surface dark-layer to enhance upconversion in a thermal field, ***Nature Photonics***, 2018, 12, 154-158.

[4] Yinghui Chen, Hien T. T. Duong, Shihui Wen, Chao Mi, Yingzhu Zhou, Olga Shimoni, Stella M. Valenzuela, and Dayong Jin*, Exonuclease III-assisted upconversion resonance energy transfer in a wash-free suspension DNA assay, ***Analytical Chemistry***, 2018, 90 (1), 663–668.

[5] Juan Xie, Xiaoji Xie, Chao Mi, Ziyu Gao, Yue Pan, Quli Fan, Haiquan Su, Dayong Jin*, Ling Huang*, and Wei Huang*, Controlled Synthesis, Evolution Mechanisms, and Luminescent Properties of ScFx:Ln (x = 2.76, 3) Nanocrystals, ***Chemistry of Materials***, 2017, 29 (22), 9758–9766.

[6] Deming Liu, Xiaoxue Xu*, Fan Wang, Jiajia Zhou, Chao Mi, Lixin Zhang, Yiqing Lu, Chenshuo Ma, Ewa Goldys, Jun Lin and Dayong Jin*, Emission stability and reversibility of upconversion nanocrystals, ***Journal of Materials Chemistry C***, 2016, 4, 9227-9234.

List of Acronyms (in alphabetic order)

3D	3 Dimensional
AC	Alternating Current
AFM	Atomic Force Microscope
AuNCs	Gold Nanoclusters
CCD	Charge-Coupled Device
CT	Computed Tomography
DC	Direct Current
DNA	Deoxyribonucleic Acid
EMCCD	Electron Multiplying Charge Coupled Device
ESA	Excited State Absorption
ETU	Energy Transfer Upconversion
FCCP	4-(trifluoromethoxy)phenylhydrazone
FTIR	Fourier Transform Infrared Spectroscopy
h-BN	Hexagonal Boron Nitrid
IR	Near Infrared
Mito-RTP	Ratiometric Fluorescent Molecular Probe
MR,	Magnetic Resonance
NIR	Near Infrared
OA	Oleic Acid
OA^-	Oleate Anions
OAH	Oleate Molecules
ODE	1-Octadecene
PET	Positron Emission Tomography

PMT	Photomultiplier Tube
QD	Quantum Dot
RE	Rear Earth
RNA	Ribonucleic Acid
SPA	Ionic Potassium 3-Sulfopropyl Acrylate
SPECT	Single-Photon Emission Computed Tomography
SThM	Scanning Thermal Microscopy
STM	Scanning Tunneling Microscope
TCSPC	Time-Correlated Single-Photon Counting
TEM	Transmission Electron Microscope

Abstract

Thermometers working at nanoscale provide new approaches of non-invasive temperature sensing with high spatial resolution to break the limitations in conventional methods. Over the past few decades, the developing of nanothermometry has been accelerated by the numerous challenging requests arising from the advanced areas like microelectronics, and nanomedicine. As nanothermometry can give the basic information on the temperature distribution of micrometric and nanostructured systems whose dynamic state is determined by temperature, the comprehensive studying on the performance of such small systems can be carried out in this way.

Based on the current literatures, the most studied nanothermometers can be grouped in two major categories: luminescent and non-luminescent nanothermometers. Luminescent thermometers is due to their temperature-dependent optical properties, which widely exist in luminescent nanomaterials including QDs, RE doped nanoparticles, artificial biomolecules, organic dyes, as well as hybrid polymeric nanomaterials and organic–inorganic hybrid materials. Non-luminescent thermometers contains the scanning thermal microscopy that combines the techniques of probe scanning microscope with nanoscale thermocouples or thermal resistance, while the temperature is determined by the electrical signal change of the nanoscale thermal sensors as scanning probes.

This thesis summarizes different kinds of luminescent nanothermometers and their unique thermometric properties including temperature induced spectra position shift, emission intensity change and luminescent lifetime change. Also, the development of probe scanning microscope is introduced in the first section. In the second section, on one hand, the advantages of RE doped anti-Stokes luminescent materials working as nanothermometers are described based on the literature review, and on the other hand the aim of this thesis is

established to solve the current problems in the developing of ultra-sensitive RE doped anti-Stokes luminescent nanothermometers. By developing the thermal induced emission enhancement in RE doped nanoparticles, the performance of luminescent nanothermometers at high temperature have been largely improved. Based on this investigation, a new generation of ratiometric nanothermometers is created with a high sensitivity. More significantly, the luminescence nanothermometry demonstration shows the high spatial resolution and high accuracy in the temperature sensing by the created RE doped anti-Stokes luminescent nanothermometers.

Key words: nanothermometry, anti-Stokes luminescence, phonon assistance, rear earth doped nanomaterials, upconversion,

Table of Contents

CHAPTER 1

Introduction

This PhD thesis focuses on the study of nanoscale thermometry and its applications, including discussions on the most widely used approaches. Among the different types of nanothermometers, trivalent rare earth (RE) ions doping nanocrystals have been widely developed, which benefit from unique anti-Stokes emissions. This introductory chapter makes a comprehensive generalisation on the state-of-the-art nanothermometry technologies, including the significance of nanothermometers in different applications, their classifications and thermometer performances, the advantages of RE doped anti-Stokes nanothermometers and the challenges in developing ultra-sensitive nanothermometers.

1.1 Nanothermometry

1.1.1 Significance of nanothermometry

Temperature is one of the most important physical variables that reflects the dynamics and functions of practically all natural and engineered systems. The technologies associated with the measuring of temperatures are called 'thermometry', which can be realised by a thermometer calibrated in one or more temperature scales. Traditional thermometers, such as liquid-in-tube thermometers, thermocouples, pyrometers and thermistors are generally used in medical, environics, physics, chemistry, and industrial manufacture. However, to meet the modern technological demands emerging in areas such as microelectronics[1-3], cell biology[4-14], microfluidics[15,16] and nanomedicine[17-24], conventional thermometers have lost their efficacy, as the temperature measurements in these applications require a spatial resolution down to the

micro- or even nanoscale, which conventional thermometers cannot provide[25]. Moreover, conventional thermometers lose their measurement accuracy as the intrinsic material properties change in nanoscale resolutions. For instance, when electronic thermometers based on temperature-dependent resistance are fabricated into nanoscale resolutions, some physical effects such as tunnel junctions and shot noise will become more significant[22,23]. Therefore, when at nanoscale resolution, the accuracy of the traditional thermometric properties becomes much worse.

To achieve high spatial resolution and high accuracy temperature measurements, nanothermometry has become a hot topic for the exploration of a new generation of nanoscale thermometers, and has become the tool for exploring new knowledge to better understand the numerous features of micro- and nanoscale electronic devices, integrated photonic devices, living organisms or cells and so on[24-34].

1.1.2 Classification of nanothermometers

Motivated by the increasing fundamental and practical applications, researchers have exploited several promising avenues for nanothermometry to understand specific micrometric and nanostructured systems. Apart from conversional thermometry, nanothermometry techniques all contain new features to break the limitation for high spatial temperature sensing, by either creating temperature-responsive nanoscale materials or devices with high sensitivity, or by utilising the advanced high-resolution detection method, such as the optical microscope and atomic force microscope (AFM). Consequently, based on these two most used strategies, the developed nanothermometers can be classified into three major categories:

(1) Luminescent nanothermometers;

(2) Scanning thermal microscopes;

(3) Nanoscale thermocouples and thermal resistance.

1.1.2.1 Luminescent nanothermometers

Among these three nanothermometry techniques, luminescent nanothermometers have attracted the most attention, and a broad group of luminescent nanomaterials have been created as thermometers, from inorganics such as semiconducting quantum dots (QD) [9,29,39,40], RE doped nanocrystals[41-47] and metal nanoclusters (NCs)[12,48], to organics such as polymers[49-51], organic dyes[52] and biomolecules[53]. Organic–inorganic hybrid structures have also been created[54,57], which benefit from their unique advantages over the other two techniques.

Photoluminescence is light emission from materials after excitation by photons, i.e. the radiative relaxation of electrons from electronic excited states to lower states. The inherent properties of the electronic excited states are temperature responsive; therefore, the same temperature-responsive emissions occur from the material[4,58-60]. Thus, it is feasible and significant to study the different types of luminescent materials with temperature-dependent properties towards highly sensitive luminescence nanothermometry. Meanwhile, optical microscopy has been advancing at a high speed over recent years[61-63], especially for biology imaging, due to its non-contact and non-invasive characteristics. With the same characteristics, luminescent nanothermometers can cooperate well with the existing and mature optical microscopy to provide a non-contact, non-invasive temperature sensing method. Compared with contact temperature sensing, where conductive heat transfer between the temperature sensor and the object exists, the non-contact and non-invasive temperature sensing method can avoid the thermal transfer that might influence the true temperature of the sample, especially regarding small systems.

Based on which luminescence parameter has been a temperature factor and used for temperature sensing, as shown in Figure 1.1, the luminescent nanothermometers can be classified into three sub-classes:

(1) Nanothermometers with emission peak shift;

(2) Nanothermometers with emission intensity or intensity ratio change;

(3) Nanothermometers with emission lifetime change.

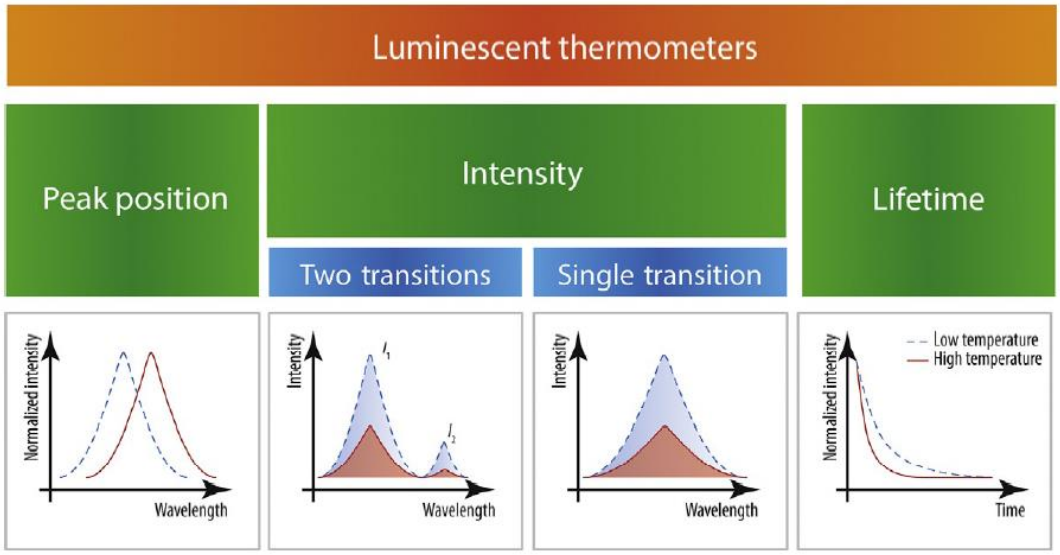

Figure 1.1 Classification of luminescent nanothermometers based on temperature-dependent emission peak position, emission intensity or intensity ratio, and emission lifetime change[59].

1.1.2.1.1 Spectral shift luminescent nanothermometer

Nanothermometers with emission peak shift depend on the peak wavelength of the single emission band for temperature sensing[64]. The peak wavelength represents the emission photon energy, which is approximate to the energy gap between the two electronic energy states in the radiative relaxation process. The energy gap is not only determined by the material structure, but is also influenced by some temperature-dependent parameters such as inter atomic density and refractive index; thus, the emission peak will shift, which is induced by temperature change.

Although this emission shift effect applies to many luminescent materials, in practice only the development of semiconductor QDs with emission peak shifts have been successful for high-sensitive nanothermometry.

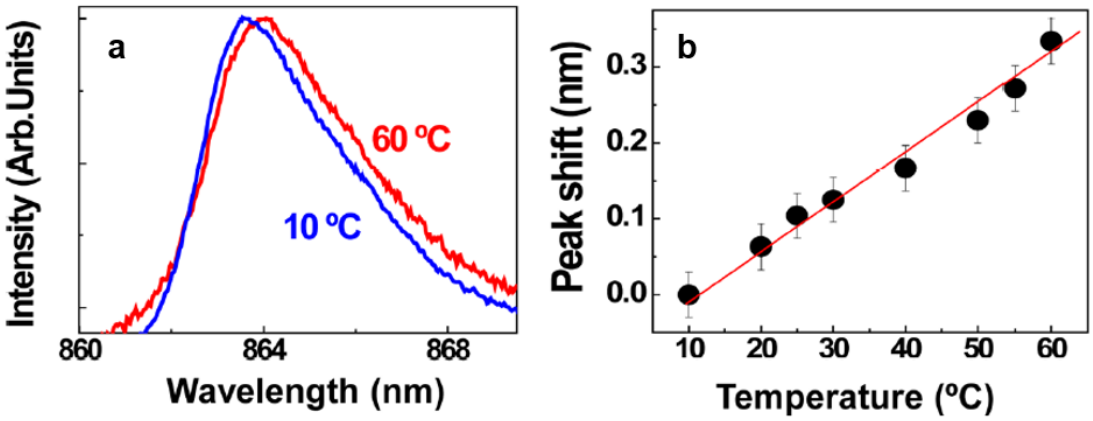

Figure 1.2 The temperature-dependent spectral shift property in Nd^{3+} ions[65]. (a) The red shift in the emission spectra of $LaF_3:Nd^{3+}$ nanoparticles from 10 ℃ to 60 ℃. (b) Temperature-dependent emission peak shift around 864 nm, from 10 ℃ to 60 ℃, the red shift is more than 0.3 nm. Dots and the solid line represent the data point and the best linear fit, respectively.

Figure 1.2 shows the temperature-dependent spectral shift in RE doped nanoparticles $LaF_3:Nd^{3+}$, which was reported by Rocha *et al.*[65] The spectra of Nd^{3+} with an emission peak around 864 nm, originating from the energy transfer $^4F_{3/2}\rightarrow{}^4I_{9/2}$, exhibits a novel red shift to a longer wavelength, and it is a linear relationship with temperature change. This type of spectral shifting in RE doped materials is caused by a temperature induced modification of the lattice environment surrounding the RE ions, i.e. the thermal induced strains around the Nd^{3+} environment caused by electron-phonon interaction. Although the $LaF_3:Nd^{3+}$ generates this emission peak shift at varying temperatures, with a speed of nearly 0.14 cm^{-1}/K, it is still too slow to measure the temperature accurately. Normally, RE doped materials with spectral shift only have a relative sensitivity of approximately 0.06 nm/K because the trivalent RE ions have

quite stable optical properties owing to the blocking of the fully filled 5s, 5p electronic orbitals, thus the emission peak position barely changes with temperature.

Compared with RE doped temperature induced peak shift nanothermometers, QDs are more promising candidates owing to their remarkable peak shift rate, which leads to higher sensitivity. Furthermore, QDs are insensitive to certain other environment changes such as pH change, which should always be considered for the intracellular nanothermometry. Taking advantages of these qualities, a lot of research has been undertaken on QDs nanothermometers.

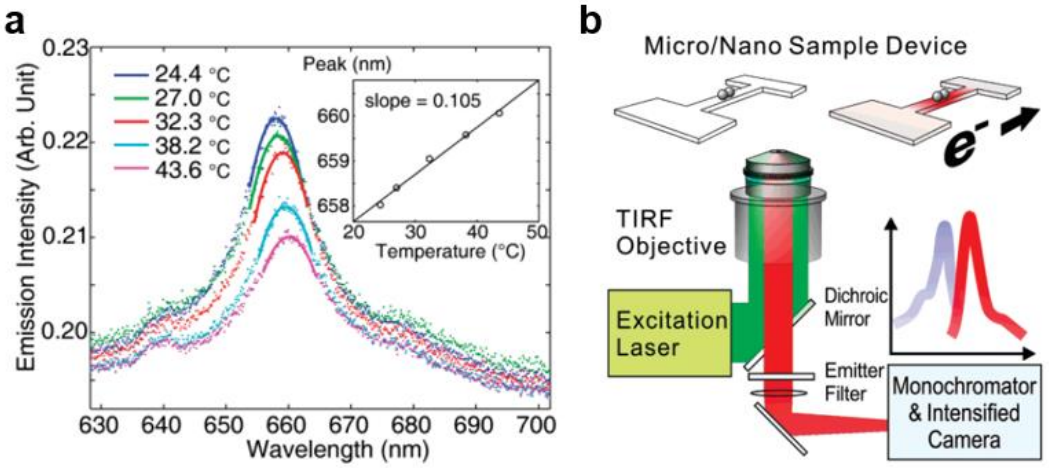

Figure 1.3 QDs with temperature induced peak shift for microdevice localised temperature sensing[66]. (a) The spectral shifts of CdSe QDs from 24.4 to 43.6 °C. (b) Strategy for non-contact temperature sensing on the microdevice using QDs and an optical microscope.

To the best of our knowledge, the first study of QD nanothermometers based on peak shift was reported by Li *et al.*[66] These authors observed that the CdSe QDs around 10 nm could produce a wavelength shift in the thermal field. As shown in Figure 1.3, from 24.4 to 43.6 °C, the emission peak of the CdSe QDs dramatically shifts from 658 nm to a longer wavelength 660 nm, with a shift rate of close to 0.1 nm/K. Using a photoluminescence spectrometer to collect the emission signal change and an optical microscope built together with a spectrometer to provide high spatial resolution imaging, these CdSe QDs of high sensitivity have been

successfully used for electrical microdevice localised temperature sensing. This demonstrates the application of QDs for temperature characterisation of microstructures. Besides, Jacque's group have used CdSe QDs for intracellular temperature sensing[67]. They combined the QD nanothermometers and the gold nanorods as nanoheaters to create a multifunction platform. By illuminating with an 808 nm laser, the nanoheaters inside HeLa cells will absorb the excitation photons and cause relevant intracellular heating, with this temperature increase simultaneously monitored by the QDs. The application demonstration results will be discussed in greater detail in the following section. This section focused on different materials and their unique temperature-responsive properties.

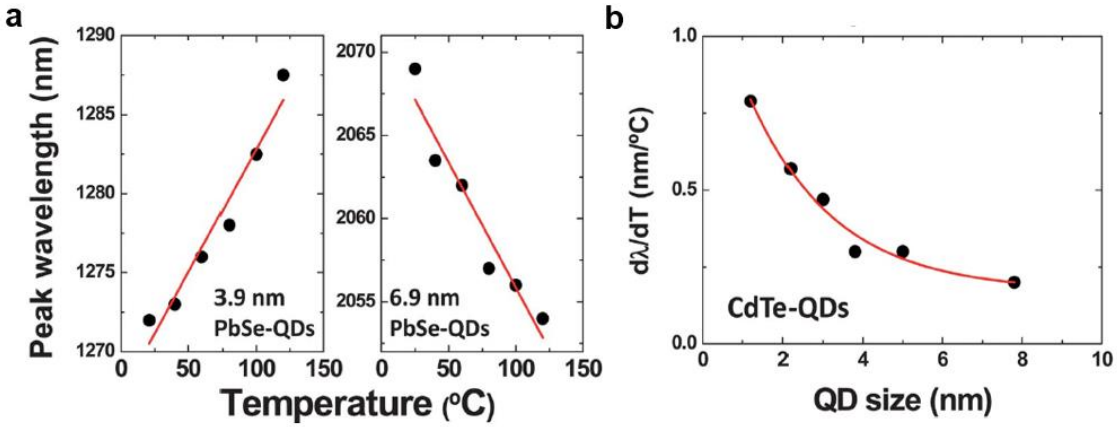

Figure 1.4 The influence of size on the temperature induced spectral shift in QDs[68,69]. (a) Temperature-dependent peak wavelength of 3.9 nm and 6.9 nm PbSe QDs. (b) Temperature coefficient of emission wavelength for cadmium telluride (CdTe) QDs of various size. The solid points represent the data point and the red lines are a guide to show the slope.

Several other studies have shown that the general thermal induced spectral shift effect occurs in other types of QDs including PbSe and CdTe[68,69], as shown in Figure 1.4. The mechanism behind this phenomenon is believed to be the temperature induced modification of the lattice and electron-lattice interaction in both RE doped materials and QDs, as discussed previously. However, in the case of QDs only, there has been limited research on the physics mechanisms

that are responsible for the spectral shift. Therefore, it is hard to predict this type of spectral shift to design the material for better nanothermometry. Generally speaking, the spectral shift in QDs is a common outcome of the electron-lattice interaction including electron-phonon coupling and the coefficient of both the bandgap energy and the quantum confinement energy.

Researchers have found that the thermal induced spectral shift in QDs could be totally different in the same type of QDs that have different sizes[68,69]. In Figure 1.4 (a), the PdSe QDs with sizes of approximately 3.9 nm and 6.9 nm show a spectral red shift and blue shift, respectively. From 24 to 124 ℃, the 3.9 nm sample generates an emission peak shift from 1272 to 1288 nm whereas the 6.9 nm sample generates an opposite wavelength shift from 2069 to 2054 nm. In another study by Maestro *et al*.[69] as shown in Figure 1.4 (b), they have studied the relationship between sample size and the spectral thermal coefficient for CdTe QDs, which indicates that the temperature spectral shift could be adjusted by sample size. The spectral thermal coefficient refers to how fast the spectral position changes with temperature and can be expressed as[68,70,71]:

$$\frac{\mathrm{d}\lambda}{\mathrm{d}T} \propto \frac{\mathrm{d}E_g^0}{\mathrm{d}T} + \frac{\mathrm{d}E_{conf}}{\mathrm{d}T} + \frac{\mathrm{d}J_{e-p}}{\mathrm{d}T}$$

where, λ and T represent the emission wavelength and the absolute temperature, respectively. Thus, the spectral thermal coefficient $\mathrm{d}\lambda/\mathrm{d}T$ is in direct proportion to three terms $\mathrm{d}E_g^0/\mathrm{d}T$, $\mathrm{d}E_{conf}/\mathrm{d}T$ and $\mathrm{d}J_{e-p}/\mathrm{d}T$. In these three terms, E_g^0, E_{conf} and J_{e-p} indicate the bandgap energy of QDs, the quantum confined energy and the electron-phonon coupling energy; therefore, the three terms in the formula account for the temperature coefficient of E_g^0, E_{conf} and J_{e-p}, respectively. In consideration of these interaction factors, the temperature induced spectral shift in specific QDs is quite complicated. However, because the size of the sample influences the intrinsic properties such as the geometrical properties and lattice environment, adjusting the size could be an effective way to optimise QDs for nanothermometry. For CdTe QDs, the

minimum size around 0.7 nm leads to a fastest spectral shift rate of 0.8 nm/K, which is sensitive enough for nanothermometry application.

In summary, nanomaterials with temperature-dependent spectral shift have advantages in nanothermometry. During measurements, the spectral intensity vibrations always exist in spectrometers, which leads to inaccuracy. The method of temperature-dependent spectral shift can avoid this intensity fluctuation as it is independent of the emission intensity, which is only dependent on the analysis of emission peak position shift during temperature change. Thus, compared to some other temperature sensing methods based on the evolution of intensities, this method could be used for temperature sensing without interference by the luminescence intensity fluctuations. However, as the temperature-dependent spectral shift rate of the studied materials was under 1 nm/K, for high temperature resolution test, this method requires commercial spectrometers with high spectra resolution equipped with proper gratings and detectors. Meanwhile, the studied QDs with thermal induced spectral shift all emit at the visible region outside the biology optical window; therefore, there are limitations for some applications such as deep bio-tissue temperature detection.

1.1.2.1.2 Single emission and ratiometric luminescent nanothermometer

Apart from monitoring the wavelength shift in the emission spectra to read the temperature, intensity changes in the spectra can also be used to deduce the temperature. This is because the luminescence intensity is influenced directly by thermal quenching. Under high temperatures, most of the luminescent materials experience thermal quenching, which leads to weak emissions as there is a faster multi-phonon non-radiative relaxation rate at higher temperatures. Only the minority of luminescent materials with specific emission bands benefit from an elevated temperature as the thermal intensified phonon assistance plays a role in more effective energy transfer. Despite the decreased or increased emissions induced by high temperatures,

both types of emission signal change can be used for temperature sensing.

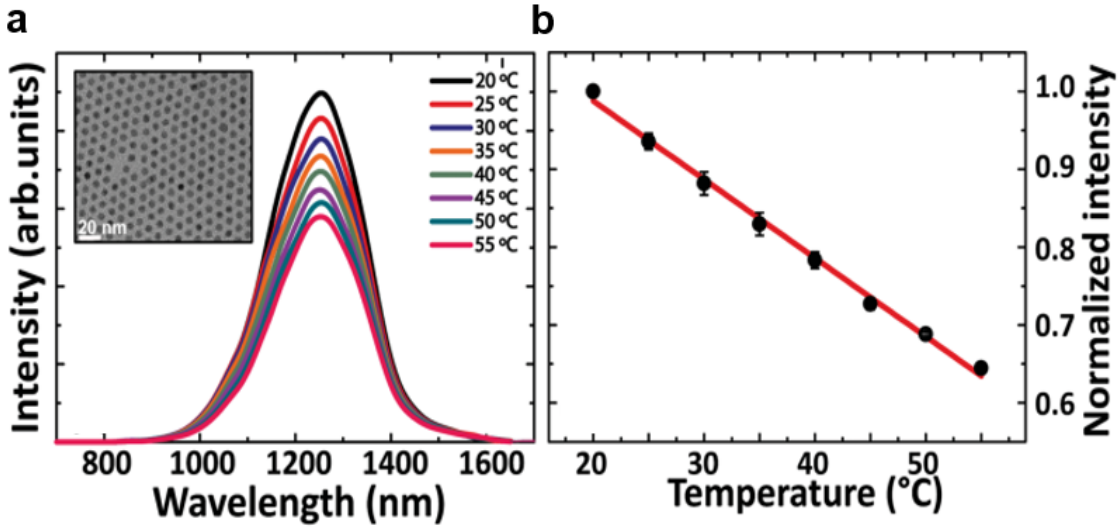

Figure 1.5 Thermal induced emission intensity evolution in core@shell@shell PbS@CdS@ZnS QDs[18]*. (a) Photoluminescence spectra of an aqueous dispersion of the QDs by gradually increasing temperature from 20 to 55 ℃. The insert transmission electron microscopy (TEM) image shows the size and morphology of the QDs. (b) Spectral emission intensity at 1270 nm from the QD sample, which performs as a function of the temperature, normalised at the intensity under 20 °C. The black dots and red line indicate the experimental data and the best linear fit, respectively.*

In 2016, Rosal *et al*. reported that the near infrared (NIR) emitting *PbS@CdS@ZnS* QDs with a core@shell@shell structure for nanothermometry assisted photothermal therapy[18]. As shown in Figure 1.5 (a), the 4 nm *PbS@CdS@ZnS* QDs synthesised by a seed-mediated one pot growth method have an NIR emission band around 1270 nm, which is located in the second biology optical window (1000–1350 nm). By increasing the temperature from 20 to 55 ℃, the emission intensity of 1270 nm decreases due to thermal quenching. Figure 1.5 (b) shows more clearly that the NIR emission is strongly dependent on the temperature, whereas the intensity changes linearly with temperature. With such a rapid rate of intensity change, the *PbS@CdS@ZnS* QD achieves a sensitivity as high as 1 %/K. From multiple tests of heating/cooling cycles, the intensity of *PbS@CdS@ZnS* QD does not show any obvious

difference, which confirms that the temperature dependence comes from thermal quenching rather than from thermal induced structural change.

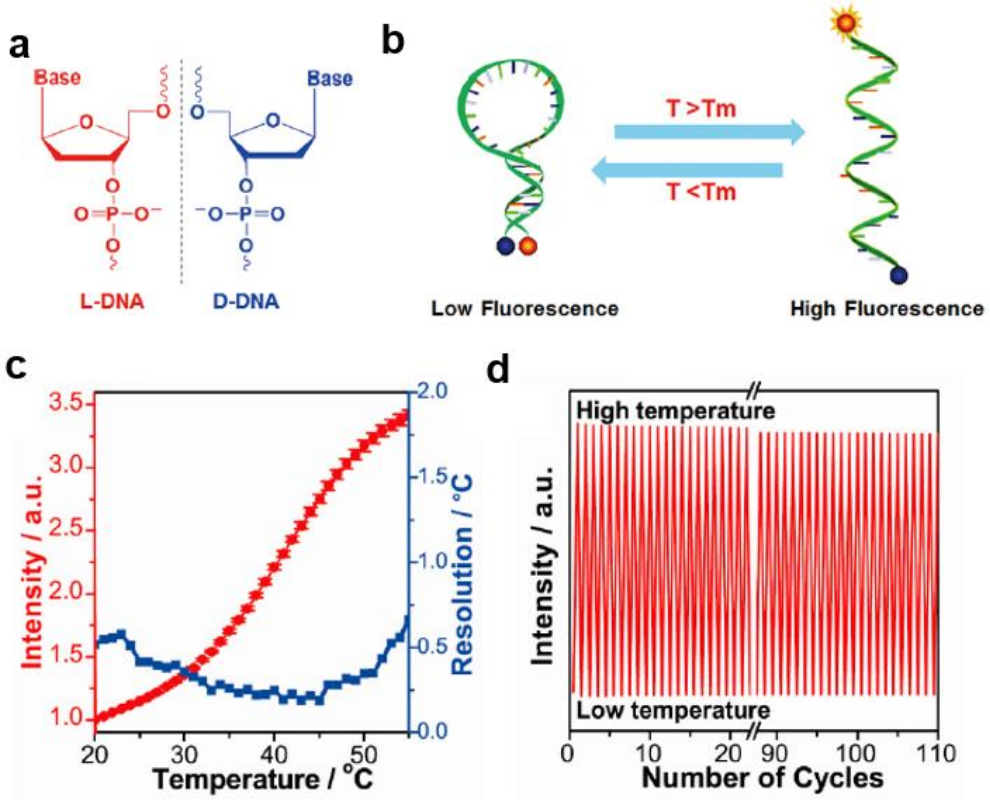

Figure 1.6 Design of a L-DNA molecular beacon working as a nanothermometer[53]*. (a) Structure of L-DNA. (b) Temperature properties of the L-DNA molecular beacon nanothermometer. (c) Thermal induced luminescence intensity evolution and temperature sensing resolution. (d) Reversibility of L-DNA molecular beacon in different tests of heating/cooling cycles.*

Unlike inorganics that need extra surface modification to achieve biocompatibility, some organics like biomolecules naturally have excellent compatibility for bio sensing applications, for example, artificial DNA molecular beacons. Ke *et al*. proposed a strategy on how to transform a L-DNA molecular beacon into a nanothermometer for intracellular temperature sensing[53]. In Figure 1.6 (a) and (b), the schematic diagrams explain the material composition of L-DNA, which contains two mains parts to work as an emitter and as a quencher. These emitters and quenchers are linked by a hairpin-structured DNA molecule, and the distance

between them is a function of temperature. When the environment is cool, the emitter will be quenched because of the closed hairpin, and oppositely it will have stronger emission under higher temperature as the distance is further from the quencher. Figure 1.6 (c) and (d) show the changes in the temperature-dependent emission intensity, which had a 3.4 times higher intensity from 20 to 55 ℃. Although organic substances are supposed to undergo structural changes more easily under high temperature than inorganic structures such as crystals, the multiple test of heating/cooling cycles showed that the L-DNA molecular beacon qualified as a nanothermometer in terms of stability and reusability for temperatures lower than 50 ℃

Luminescent nanothermometers triggered by single emission intensity change are critically disturbed by the instrument signal fluctuations and localised sample concentration difference. Although it is convenient to characterise single emission band change with temperature, this method is inappropriate for nanothermometry because it lacks the necessary calibration procedures for accurate temperature reading.

These disadvantages can be overcome by an additional emission band, which can serve as an internal standard for self-calibration[8,39,50,55,59,72-76]. More significantly, if the second emission band responds to temperature in an opposite trend to the first emission band, then the thermometric properties of the intensity ratio between these two emissions could provide a higher sensitivity than the one based only on a single emission. Utilising these strengths, ratiometric thermometry has become the most studied approach for nanoscale temperature sensing. Generally, by classifying whether the two emission bands come from thermal coupled energy states whose populations follow the Boltzmann distribution, the studied ratiometric nanothermometers can be separated into two types:

(1) Single emitter with emissions from thermal coupled energy states;

(2) Distinct dual emitters with respective emission band.

Ratiometric nanothermometers based on two emission bands that stem from a single emitter

offer a robust temperature measurement approach, as they can be calibrated for precise temperature measurements, or even without calibration they can be characterised by well-established equations for direct temperature calculation.

The most well-known ratiometric nanothermometers with single emitters are the RE doped materials that have abundant energy states including different pairs of thermal coupled states whose populations follow the Boltzmann distribution[26]. To be in a thermal coupled energy state, the upper and lower electronic energy levels must not be too far away from each other, or the population at the lower electronic energy level must not reach the upper energy levels by absorbing heat, so that thermalisation is no longer present. Empirically, the energy gap between thermal coupled energy states ranges from 200 to 2000 cm^{-1}, which guarantees that the two emission bands are spectrally separated for respective characterisation.

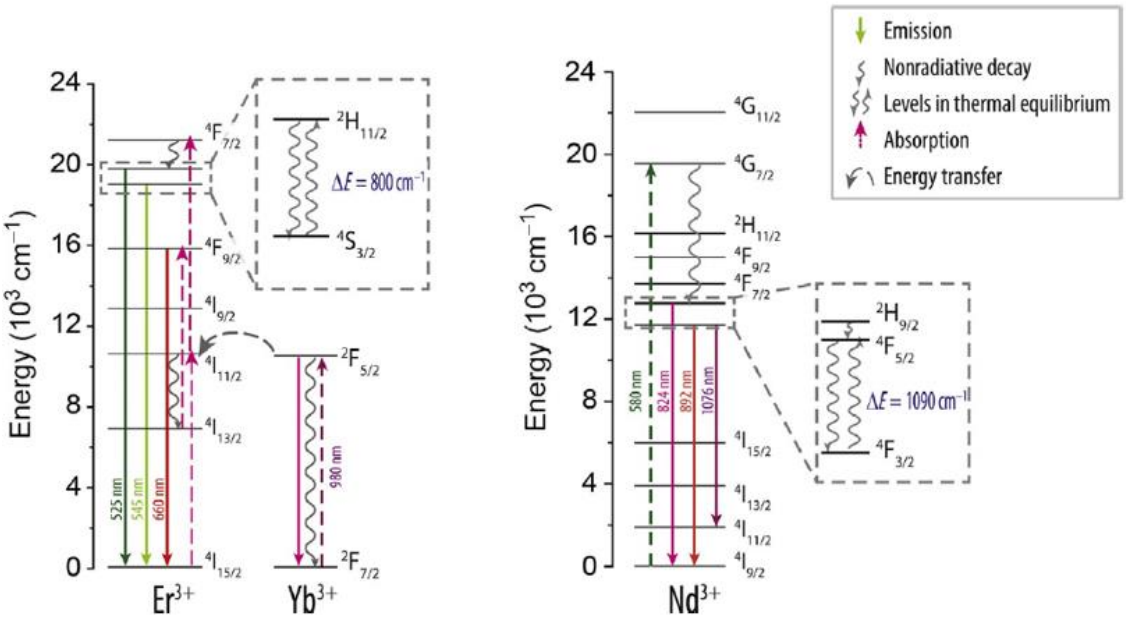

Figure 1.7 Diagram of energy states in Er^{3+}, $Yb^{3+}$and Nd^{3+} ions[59,80]. The thermal coupled energy states in $Er^{3+}$and Nd^{3+} for thermometry have been enlarged in the dashed-line block.

For example, the Er^{3+} and Nd^{3+} ions in Figure 1.7 are the most studied RE codoping system for ratiometric thermometers, with Yb^{3+} as the sensitiser and Er^{3+} as the emitter. The Yb^{3+}–Er^{3+}

codoping system is the most efficient upconversion luminescence system, and the $^2H_{11/2}$ and $^4S_{3/2}$ pair of thermal coupled energy states can generate strong green emissions for ratiometric thermometry[81-84]. In another example, Nd^{3+} has also been widely used for temperature sensing[85-91], not only in upconversion luminescent materials but also in downconversion materials. By doping into different host material such as oxides, fluorides and glass, it can produce multiple emission bands in NIR for temperature sensing, such as the two main emission bands from $^2H_{9/2}$, $^4F_{5/2}$ and $^4F_{3/2}$. Additionally, some other trivalent lanthanides such as Tm^{3+} and Ho^{3+} are also popular candidates for ratiometric thermometry[92-94]. Less studied cases including Eu^{3+}, Pr^{3+}, Dy^{3+} and Gd^{3+} have been proven to work well as temperature sensors[95-98].

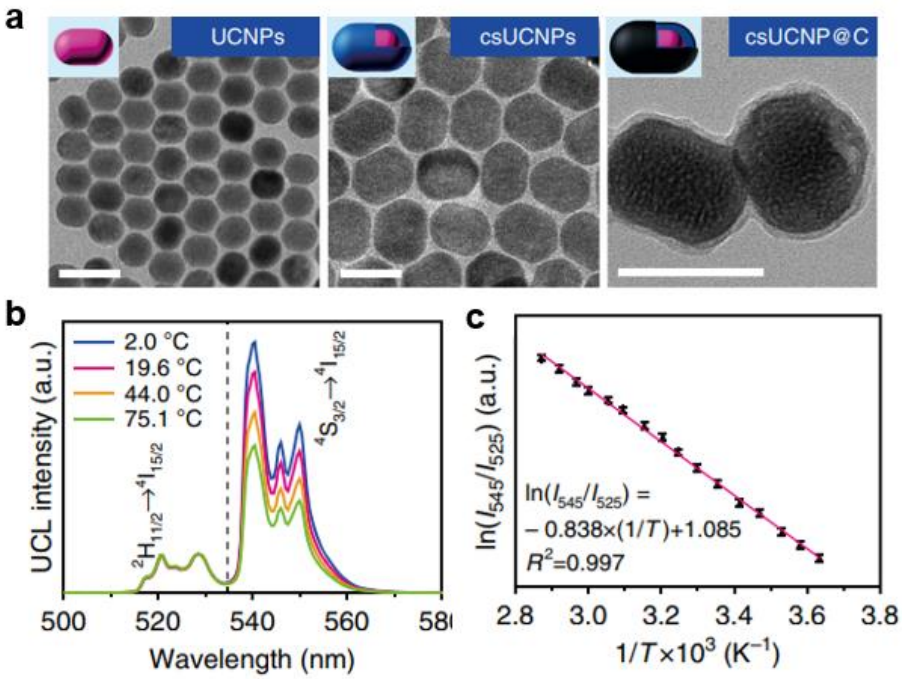

Figure 1.8 Nanothermometry for temperature-controlled photothermal therapy by Yb^{3+}–Er^{3+} codoping upconversion nanoparticles[99]. (a) TEM images show the size and morphology of $NaLuF_4:Yb^{3+}$, Er^{3+}(left), $NaLuF_4:Yb^{3+}$, Er^{3+}@$NaLuF_4$ (middle) and $NaLuF_4:Yb^{3+}$, Er^{3+}@$NaLuF_4$@C (right). Scale bar is 50 nm. (b) Temperature-dependent spectra of $NaLuF_4:Yb^{3+}$, Er^{3+}@$NaLuF_4$@C from 2 to 75 ℃. The intensities were normalised at 528.5 nm.

(c) Calibration curve of nanothermometer $NaLuF_4:Yb^{3+}$, Er^{3+}@$NaLuF_4$@C showing the temperature dependence of the intensity ratio (545 nm/525 nm) under excitation at 980 nm. Dots are experimental data and the dashed line is the best linear fit by the formula in the figure.

An example using Er^{3+} doping upconversion materials for temperature-controlled photothermal therapy was reported by Zhu *et al.*[99] As shown in Figure 1.8 (a), the authors synthesised a core@shell@shell structure $NaLuF_4:Yb^{3+}$, Er^{3+}@$NaLuF_4$@C nanocrystals for simultaneous temperature sensing and self-heating. Under 980 nm excitation, the core $NaLuF_4:Yb^{3+}$, Er^{3+} can absorb energy because of the large absorption cross-section of Yb^{3+} around 980 nm and the multi-photon energy transfer from Yb^{3+} to Er^{3+} makes upconversion luminescence from Er^{3+}. By coating with an inert shell, $NaLuF_4$, to block the emitting core as a temperature sensor and the outside carbon layer for self-heating, the hybrid nanoparticles could be used for temperature thermal ablation therapy with temperature feedback. Figure 1.8 (b) shows the upconversion spectra as a function of temperature, with the emission band with its centre at 545 nm having different behaviours to the 525 nm emission band. By normalising the intensity at 528.5 nm, the emission of 525 nm hardly changes, whereas the 545 nm emission band keeps decreasing with increasing temperature. The energy gap between the two emission energy states is approximately 800 cm^{-1}; therefore, it is feasible for the population transfer from $^4S_{3/2}$ to $^2H_{11/2}$ to achieve thermodynamic equilibrium according to the Boltzmann law. Figure 1.8 (c) shows the calibration curve between the emission intensity ratio of 525 nm to 545 nm and the inverse of the absolute temperature, which is well fitted by the linear formula. According to the literature, the ratio of the emission intensities arising from thermal coupled energy levels is described as a simplified model of the Boltzmann thermal equilibrium, and can be calculated by[59]:

$$R = \frac{I_2}{I_1} = \frac{N_2 A_2 \hbar\omega_2}{N_1 A_1 \hbar\omega_1} = \frac{A_2 \omega_2 g_2}{A_1 \omega_1 g_1} \exp(-\frac{\Delta E}{k_B T}) = B\exp(-\frac{\Delta E}{k_B T})$$

In the case of Er^{3+}, I_2 and I_1 are the 520 nm and 540 nm intensities from the transitions of $^2H_{11/2} \rightarrow {}^4I_{15/2}$ and $^4S_{3/2} \rightarrow {}^4I_{15/2}$, respectively. N_2 and N_1 are the populations at the $^2H_{11/2}$ and $^4S_{3/2}$ levels, and A_2 and A_1 are the total spontaneous-emission rates of the $^2H_{11/2}$ and $^4S_{3/2}$ levels transferred to the ground state, whereas g_2, g_1 and ω_2, ω_1 are the degeneracies and the angular frequencies of the $^2H_{11/2}$ and $^4S_{3/2}$ levels, respectively. ΔE and T represent the energy gap between the $^2H_{11/2}$ and $^4S_{3/2}$ levels and the absolute temperature, respectively. Thus, all the RE doped ratiometric thermometers can be calibrated, which is in contrast to some other kinds that are hard to calibrate, especially in nano size, and can only work as indicators of temperature change.

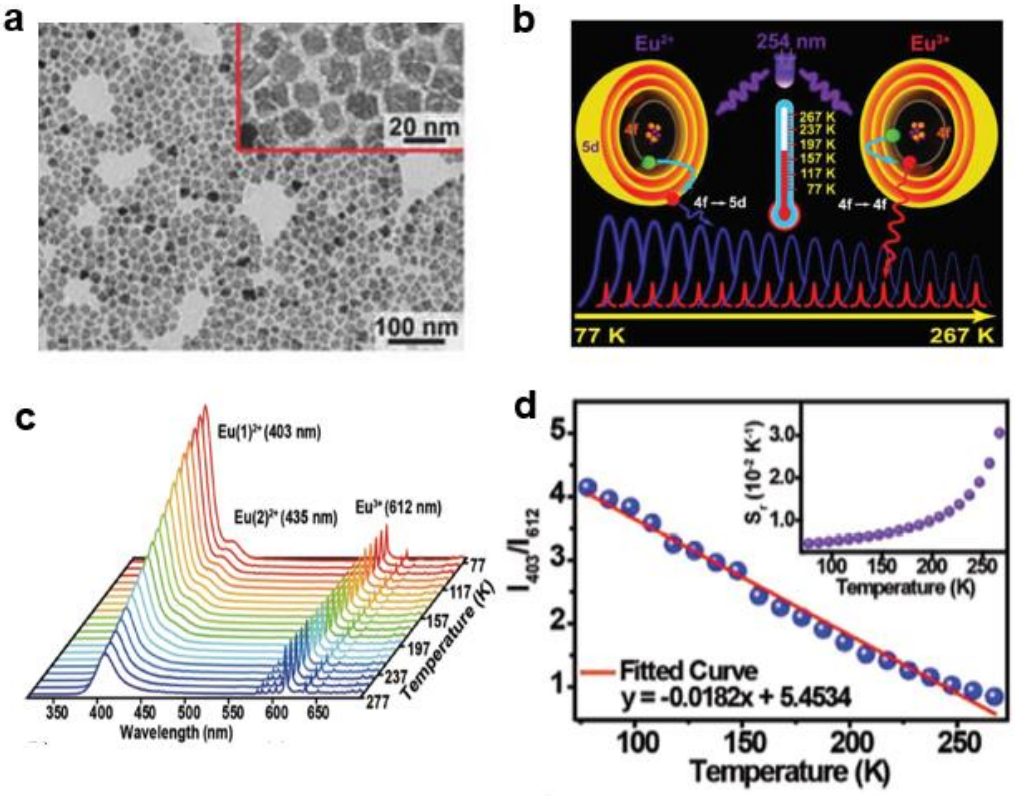

Figure 1.9 Dual-emitter Sc_2O_3: Eu^{2+}, Eu^{3+} nanoparticles for ratiometric nanothermometry[96].

(a) TEM image shows the size and morphology of Sc_2O_3: Eu^{2+}, Eu^{3+} nanoparticles. (b) Schematic diagram shows the thermometric principle of the nanothermometer. (c) Temperature-dependent spectra including emission bands from $Eu^{2+}$and Eu^{3+}ions from 77 to 267 K. (d) Calibration curve of nanothermometer Sc_2O_3: Eu^{2+}, Eu^{3+}; the insert shows sensitivity as a function of temperature. Dots are the experimental data and the red line is the linear fit by the formula in the figure.

Pan *et al*. reported one new ratiometric nanothermometer with Eu^{2+} and Eu^{3+} codoping[96], in which the emission band of Eu^{3+} was independent of temperature, whereas the second emission band was intensely influenced by temperature. Figure 1.9 indicates the Sc_2O_3: Eu^{2+}, Eu^{3+} nanoparticles with size around 20 nm, under 254 nm excitation, the emissions from the trivalent Eu^{3+} ion is hardly disturbed by the external environment because the f-f electron transition is shielded by the fully filled 5s and 5p electronic orbitals; therefore, the Eu^{3+} emission band can be used as an internal reference. By introducing the second emission band from Eu^{2+}, whose emissions originate from the f-d electron transition without the shelter of the 5s, 5p electronic orbitals, it will be easily influenced by environmental conditions such as the host lattice, temperature and so on[82,100-102]. Thus, we can see from the spectra the Eu^{2+} emissions with peak at 403 and at 435 nm emissions decrease quickly under high temperature, whereas the Eu^{3+} emission band at 612 nm barely changes. The calibration curve shows the linear relationship between the intensity ratio and the temperature, and the maximum relative sensitivity achieved 3.06 %/K at 267 K, which is much higher than previous results[84].

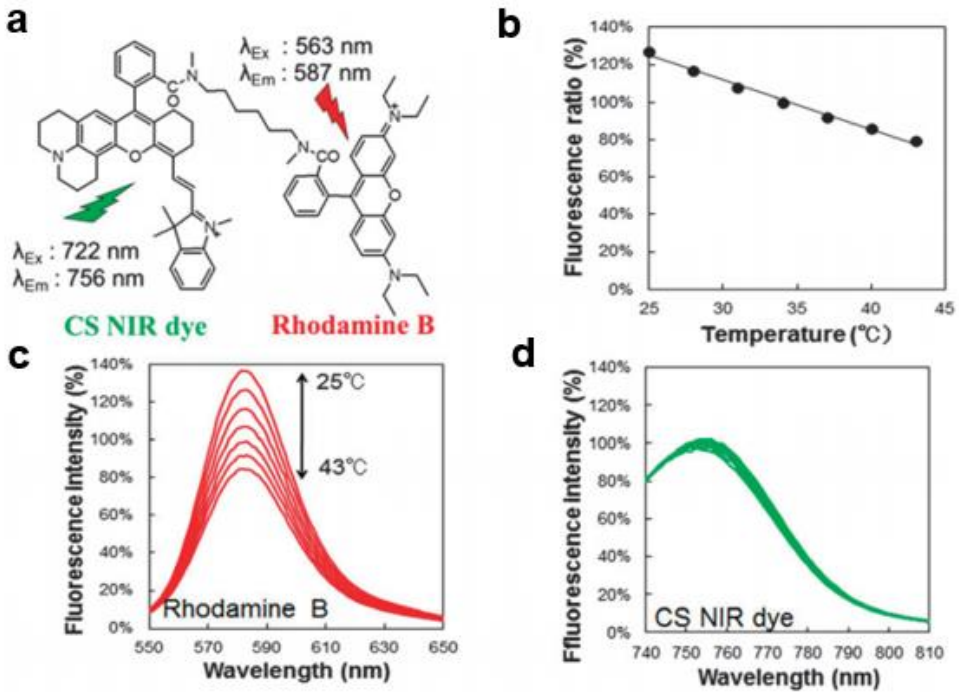

Figure 1.10 A ratiometric luminescent molecular probe (Mito-RTP) as the temperature sensor[8]. (a) The structure design of a dual-emitter Mito-RTP consisting of rhodamine B and CS NIR dye at two ends of the linker. (b) The intensity ratio of rhodamine B and CS NIR dye and temperature Luminescence spectra of (c) rhodamine B and (d) CS NIR dye at different temperatures.

For the purpose of temperature sensing in specific small organelle-like mitochondria, low molecular weight temperature probes are more applicable because their intracellular localisation is easy to control, which is still an issue in nanothermometers such as QDs, RE doped nanoparticles and polymer nanoparticles. Homma *et al*. designed a mitochondrial ratiometric thermosensor from a combination of two rhodamine dyes: rhodamine B and CS NIR dye[8], as shown in Figure 1.10 (a), which can specifically stain mitochondria in HeLa cells in less than 30 min. By using two lasers at 563 nm and 722 nm to pump the rhodamine B and CS NIR dye separately, each of the dyes produced an emission band at 587 nm and 756 nm. The intensity ratio of 587 nm to 756 nm declined linearly with temperature in Figure 1.10 (b) because the quantum efficiency of rhodamine B decays under high temperature in Figure 1.10

(c), owing to the rotational changes of the diethylamino groups on the xanthene ring. Simultaneously, the luminescence intensity from the CS NIR dye is quite stable even when the temperature increases from 25 to 43 ℃ (Figure 1.10 (d)), because the molecular rotation in the CS NIR dye is restricted.

By coupling these two emitters with a hexamethylenediamine linker to form a ratiometric luminescence nanothermometer, the accuracy to infer the temperature is improved compared to the single molecule luminescence nanothermometer, which cannot sense the tiny temperature changes in moving cells and organelles because the moving focus point leads to unsteady luminescence intensity for temperature measurements. Consequently, the ratiometric luminescence nanothermometry is a powerful method for measuring temperature changes at high spatial resolution because it can ignore the emission intensity changes caused by the inhomogeneous distribution of the thermometers or the equipment signal fluctuation.

1.1.2.1.3 Emission lifetime luminescent nanothermometer

Luminescence lifetime-dependent nanothermometry is another method for overcoming the above-mentioned shortness of the single emission intensity method. Moreover, it can also avoid the disturbance from background light scattering or reflection. However, this method lacks dynamic capabilities as it requires longer detection times than that of the luminescence lifetime of the material. In some situations, to obtain a high signal-to-noise ratio, accumulation of multiple tests is required. Another disadvantage is that lifetime luminescence detection always places higher demands on the component instrumentation than the simple spectra test used in the emission intensity-based method. The luminescence nanomaterials that have been proven to be lifetime-dependent nanothermometers can be classified into several different types[4], namely RE doped materials, QDs, metallic clusters, polymers and organic dyes.

Usually, once the luminescence decay curve has been recorded by a pulsed pumping source

with a fast-responsive detector, and the detected emission band belongs to one particular energy transfer, the thermometric information temperature can be deduced via the intrinsic lifetime of the emission energy states. In most cases, the luminescence intensity after the pulsed excitation starts to decrease in an exponential relationship with time, and lifetime τ can be described by[26]:

$$\tau = \frac{1}{W_r + W_{nr}(T)} = \frac{1}{\tau_0^{-1} + k\exp(-\frac{\Delta E}{k_B T})}$$

where, W_r and W_{nr} represent the radiative and non-radiative energy transfer rate, respectively; T is the absolute temperature; τ_0 is the radiative emission lifetime at 0 K; and ΔE, k and k_B indicate the energy gap between the two energy levels in the energy transfer, the pre-exponential factor and the Boltzmann constant, respectively.

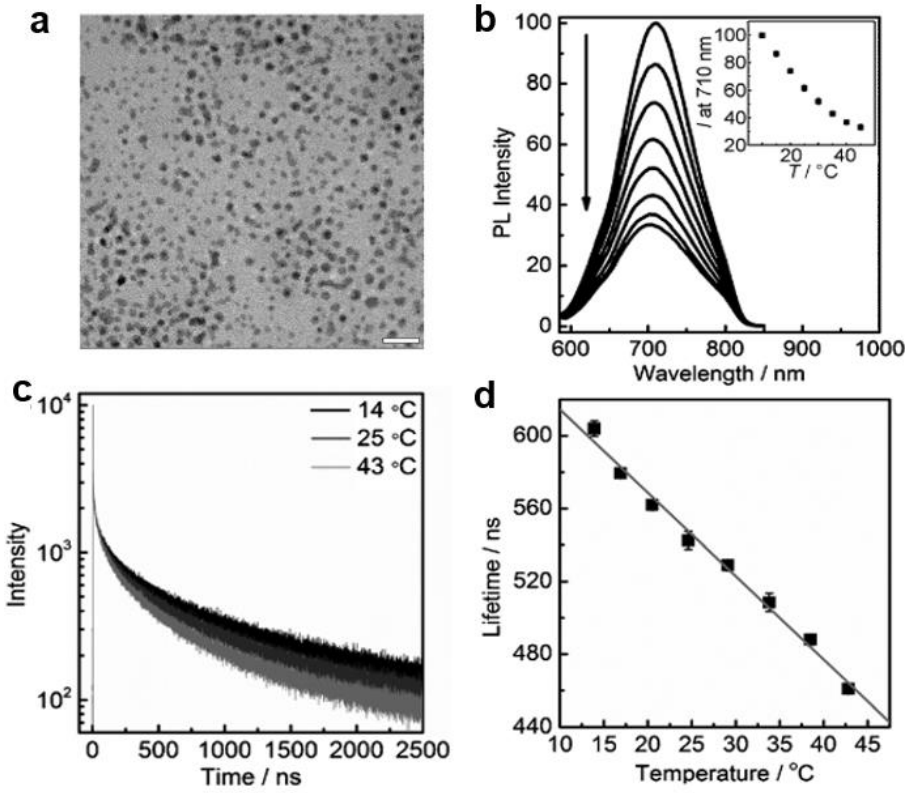

Figure 1.11 Fluorescent gold (Au) NCs for lifetime-dependent temperature sensor[12]. (a) TEM image shows the size and morphology of the AuNCs. The average diameter was approximately

1.6 nm. The scale bar is 10 nm. (b) Temperature- dependent emission spectra from 10 to 45 ℃. The insert shows the intensity at 710 nm versus temperature. (c) Emission decay curves at three different temperatures of 14, 25 and 43 ℃. (d) Luminescence lifetime of 710 nm emission as a function of temperature. The points and line indicate the experimental data and best linear fit, respectively.

Gold (Au) NCs have been developed for a series of practical applications, such as biosensors, imaging probes and for thermal therapy, because of their ultra-small size (<2 nm in diameter). By combining the temperature-responsive optical properties and time-correlated single-photon counting (TCSPC) technique, AuNCs can be developed into nanothermometers. One representative work on the lifetime-based AuNCs nanothermometer was reported by Shang *et al.*[12], as shown in Figure 1.11.The authors prepared the AuNCs using a facile synthesis method, the transmission electron microscopy (TEM) in Figure 1.11 (a) shows that the diameter of the sample was only approximately 1.6 nm, which is smaller than the reported RE doped nanoparticles and QDs. Under excitation of 580 nm, one broad emission band with its centre at 710 nm was observed from the emission spectra of the AuNCs in phosphate-buffered saline in Figure 1.11 (b). The emission intensity dropped quickly with increasing temperature from 10to 45 ℃, which proves the temperature-dependent properties of AuNCs. Further, by testing the sample on a confocal microscope equipped with pulsed diode lasers and TCSPC detection, the luminescence intensity evolution curves were recorded in Figure 1.11 (c). The shorter lifetime under higher temperatures confirmed the thermometric nature of the AuNCs. By fitting the intensity decay curve with an exponential formula, the lifetime was calculated (Figure 1.11 (d)), with the lifetime ranging in hundreds of nanoseconds, and the higher temperature decaying the lifetime linearly.

Moreover, the average lifetime of AuNCs is much longer than the lifetime of intracellular autofluorescence. Thus, AuNCs as cell temperature probes can work without the influence of

the autofluorescence background using the optical microscope equipped with TCSPC. However, a longer lifetime will lead to a slower detection process.

In 2012, Okabe *et al*. proposed a nanothermometry method for the first time for intracellular temperature mapping[103], using a novel fluorescent polymer with temperature-dependent lifetime. As shown in Figure 1.12 (a), this type of polymeric nanothermometer contains three main parts, which are responsible for the thermosensitive function, hydrophilic property and luminescent property.

The strategy for lifetime-based temperature sensing in Figure 1.12 (b) is based on the conventional method. When the temperature is low, the thermosensitive part poly-N-n-propylacrylamide is in an unfolded state with hydration of amide linkages, while the

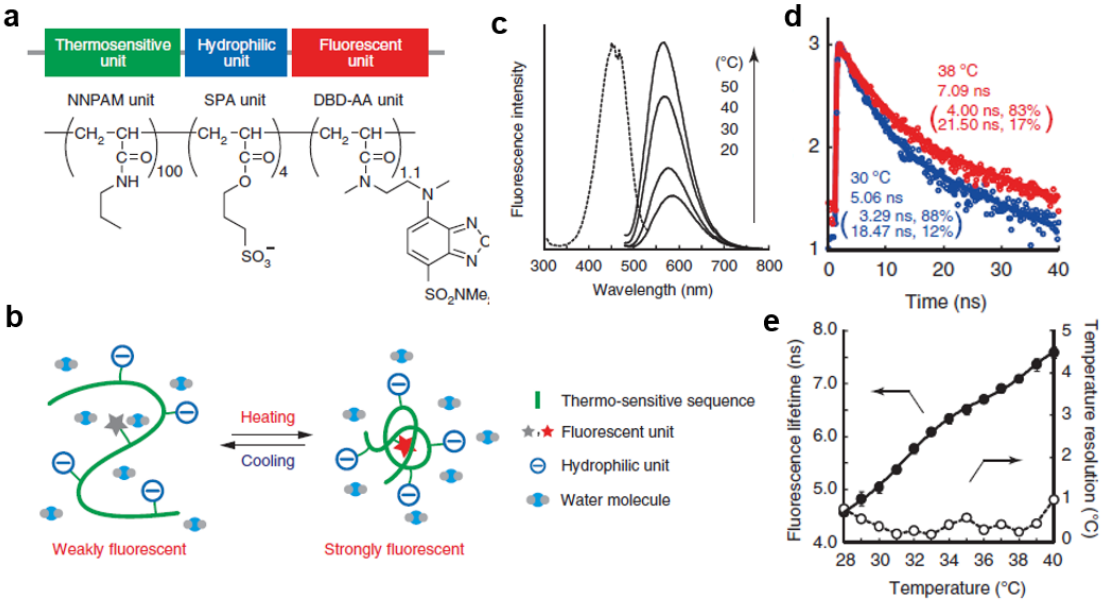

Figure 1.12 A polymeric nanothermometer for intracellular temperature sensing[103]. (a) The chemical structure of the polymer including three parts: the thermo responsive unit, the hydrophilic unit and the fluorescent unit. (b) The temperature sensing mechanism showing the state change of the polymer due to temperature change. (c) Excitation and emission spectra of the nanothermometer in a COSOS7 cell extract. The emission intensity is a function of temperature. (d) The fluorescence decay curves under different temperatures in a COSOS7 cell

extract. (e) The calibration curve shows the temperature-dependent lifetime, the temperature resolution is also shown.

luminescence from the part of N-{2-[(7-N,N-dimethylaminosulfonyl)-2,1,3-benzoxadiazol-4-yl](methyl)amino}ethyl-N-methylacrylamide (DBD-AA) unit will be quenched by the surrounding water molecules. When the temperature increases, the hydration of amide linkages is weakened and the polyNNPAM sequence shrinks due to the hydrophobic interaction among the NNPAM units, leading to a reduced amount of surrounding water molecules and stronger fluorescence from the emitting part, as shown in Figure 1.12 (c). Using a third unit, the ionic potassium 3-sulfopropyl acrylate sequence, makes the entire structure hydrophilic; therefore, the temperature probes can be used in the hydrophilic environment within a cell.

When recording the intensity changes under different temperatures, the intensity change may be caused by sample concentration change, so that using lifetime instead of intensity to infer temperature is more reliable, which is also independent of surrounding proteins and environmental viscosity. Figure 1.12 (d) and (e) show the emission lifetime as a function of temperature. The enhancement in the emission lifetime at high temperatures could be explained by the slower quenching process caused by water molecule release. From 28 to 40 ℃, the value of the emission lifetime increased from 4.5 to 7.5 ns, which resulted in a high temperature resolution under 1 ℃. Finally, this polymeric nanothermometer successfully performed intracellular localised temperature mapping for different organelles.

In summary, by retrospections on the published literature, we have given a detailed review on the three different types of luminescence nanothermometers based on spectral shift, luminescence intensity and lifetime change. The mechanisms of temperature dependence for all types of materials (e.g. QDs, RE doped materials, organic dyes, polymers, metallic nanoclusters, biomolecules) and how to apply them in nanothermometry have been explained.

It is not possible to include all the materials in one section, here we only focused on the most representative examples.

1.1.2.2 Scanning thermal microscopy with nanoscale thermocouple and thermal resistance

The scanning thermal microscopy (SThM) technique was invented 20 years ago and became popular for temperature mapping especially in the electronic industry[104]. The criteria for creating devices for nanoscale temperature sensing involves visualising the nanoscale objective and performing temperature measurements. Unlike luminescence nanothermometers, SThM does not rely on the optical properties of the material. It takes advantage of AFM or scanning tunnelling microscopy (STM) for microscopy imaging, by modifying the probe containing the nanoscale thermocouple or thermal resistance on the tip for temperature scanning[105,106].

The evolution of the SThM technique has undergone development from the STM-based method to the AFM-based method. In 1986, Williams *et al.* developed a non-contacting near-field thermocouple probe and combined it with STM to create a new approach for high-resolution temperature sensing[104]. The temperature changes within 1 K can be detected when the SThM is used for sample surface scanning. The method measures the temperature-dependent voltage, which generates from the thermocouple fabricated at the tip that is formed by two types of inner and outer conductors. The initial purpose was for a new high-resolution surface profiler development instead of for nanoscale temperature sensing.

Previous studies have reported on using STM with temperature-responsive probe for SThM[107], however, this method has a major weakness in that the target must have a conducting surface. Additionally, it is quite difficult to precisely control the distance between the target and the probe; therefore, the thermal transfer for accurate temperature sensing is a problem. Even small vibrations to the distance control lead to high error during high spatial resolution temperature

measurement; thus, a feedback control can improve the measurement accuracy, at the cost of a more complex facility.

Regarding these disadvantages using STM as a platform, AFM-based temperature measurement is a promising alternative method for SThM[108], in view of its easier operation and higher accuracy on distance control between the tip and the object. More importantly, AFM can be used for a broader range of materials, such as semiconductors that cannot be measured by STM. One study that used AFM-based SThM was undertaken by Sadat *et al.*[105], as shown in Figure 1.13. The method they proposed is conceptually simple. To

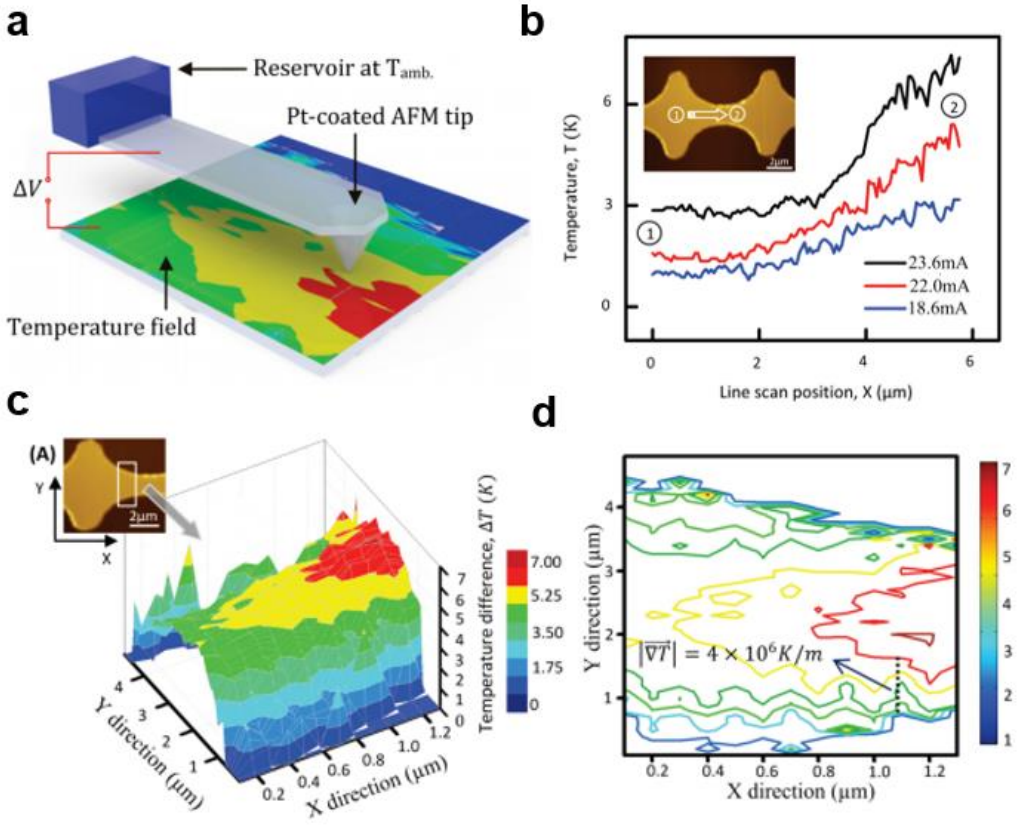

Figure 1.13 Point contact thermocouples used for SThM[105]. (a) Schematic diagram of the nanosized temperature scanning probe. A platinum -coated AFM probe was connected to a thermal reservoir. (b) The temperature distribution of the electronic device in the labelled direction under three different bottom electrode heating currents. (c) Three-dimensional

imaging of the temperature distribution on the selected device area. (d) Isotherm contour plot of the same area in (c).

fabricate the AFM probe for temperature sensing, they coated the silicon (Si) AFM cantilever with an ~5 nm titanium (Ti) adhesion layer and ~40 nm of platinum (Pt) on two sides of the probe, then they used AFM with the as-prepared probe for temperature detection on the target Au surface of the device. In Figure 1.13(a), by a soft mechanical point contact (~10 nN) with a diameter approximately 10 nm, the Pt-Au connection performed like a thermocouple and by measurement of the thermoelectric voltage in the Pt-Au thermocouple the temperature in the scanning point was determined. Figure 1.13(b) shows the temperature scanning results by AFM with a thermocouple tip, together with the labelled detection line. The temperature distributions show the Au device had different localised temperatures. By changing the current added on the device, the temperature also changed as high current-induced high temperature. In Figure 1.13(c) and (d), the topographical temperature mapping in a selected area of the device were experimentally obtained by two-dimensional scanning, each scanning point had a grid size of 100 nm. These results indicate that the AFM-based SThM technique with a modified temperature sensor tip allows localised temperature mapping on a microdevice with a temperature resolution of approximately 0.01 K and a spatial resolution of approximately 100 nm, which is very promising for use in nanothermometry.

The development of the SThM technique did not only depend on microscopes, but also relied on the optimisation of the scanning probes[109]. To date, many types of scanning probes have been exploited. Besides the most studied nanoscale thermocouples used as the sensing probe, a second type of probe is also widely used, which is by making a resistive wire into a sharp tip[110]. The temperature of the contact point between the sharp tip and the surface of the sample can be measured by the change in the electrical resistance, and both DC and AC modes of the resistive wire can be used. By using this resistive tip as a probe in STM or AFM, it can also

realise two-dimensional temperature scanning on the surface of the sample. A schematic diagram is shown in Figure 1.14.

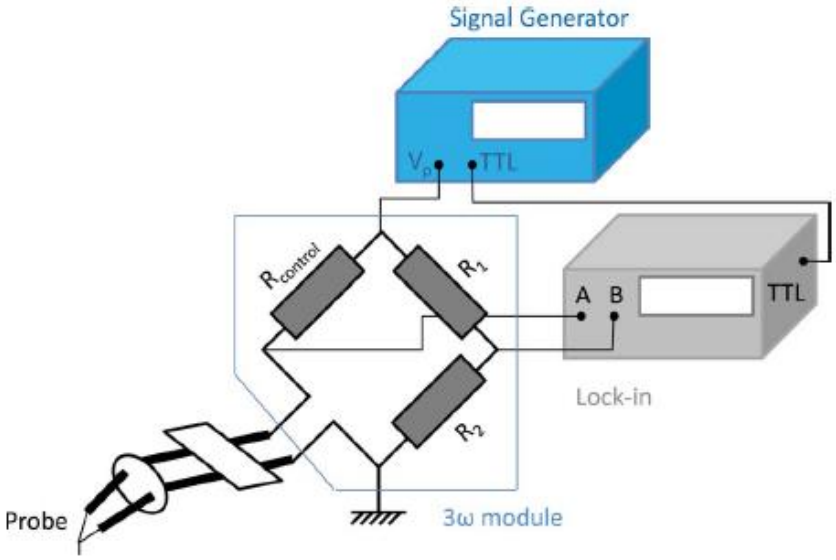

Figure 1.14 Schematic diagram of SThM using a resistive probe as the detection probe of AFM[111]. The temperature is measured by monitoring the AC current through the resistive probe.

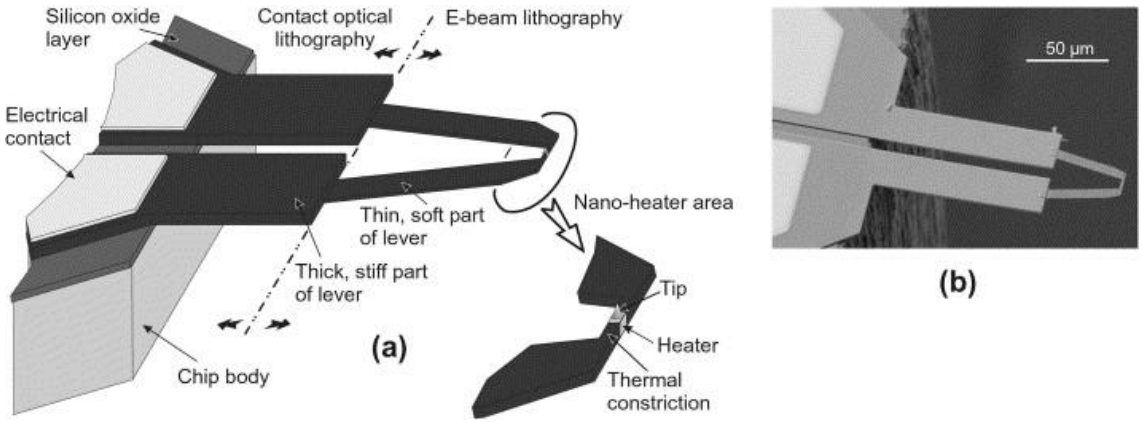

Figure 1.15 (a) Schematic diagram of the fabricated resistive probe for thermomechanical storage application. (b) Scanning electron microscope (SEM) image of the probe.[112]

In 2003, by utilising the advanced micro/nano electromechanical system fabrication technique, Drechsler *et al.* fabricated a silicon cantilever cooperated with AFM for data-storage application[112]. The structure of the AFM cantilever is shown in Figure 1.15. The authors choose silicon as the raw material of the cantilever because its electrical resistivity is strongly

dependent on the temperature, and its temperature can be obtained by recording the heater resistance.

The principle behind using the silicon cantilever for data storage is to use it as a heater to write on the polymer layer. On one hand, by adjusting the current to heat the cantilever to soften the polymer layer, the temperature can be controlled by monitoring the resistance change. On the other hand, the contact pressure on the polymer is also precisely controlled by AFM, which will make the tip sink into the polymer and then start to write on it.

Menges *et al*. modified this SThM for nanoscale temperature mapping in 2016[2,113]. They established the physical model for the calculation of temperature increase due to the Joule heating effect in electronic devices. By adding an AC voltage with enough small frequency on the interconnect of the device, it generates a temperature that increases steadily and a continuous modulation on the temperature with twice the frequency, the sample temperature T can be expressed as:

$$T = T_{rt} + \Delta T(1 + \sin(2\omega t))$$

where, T_{rt} indicates the room temperature and ΔT indicates the temperature change of the sample. ΔT will influence the heat transfer Q from sample to probe, which can be written as:

$$Q = Q_{DC} + Q_{AC} sin(2\omega t)$$

which is also related to the electrical power P in the probe, and the probe temperature T_{probe}:

$$T_{probe} = T_{DC} + T_{AC}\sin(2\omega t)$$

which is in direct proportion to the electrical resistance of the probe. Thus, by monitoring both the temperature-dependent DC and AC response of the probe, the measured temperature change of the sample can be written as:

$$\Delta T = T_{AC} - Q_{AC} \times R_{ps}$$

where, R_{ps} represents the probe-sample temperature-dependent electronic resistance, which can be expressed as:

$$R_{ps} = \frac{T_{DC} - T_{AC} - T_{rt}}{Q_{DC} - Q_{AC}}$$

Conventional methods of SThM for temperature mapping on sample surfaces have ignored that the temperature-dependent R_{ps} is position-related, which will lead to higher test errors in the temperature reading. In this new model, this issue has been resolved by recording position-dependent R_{ps}.

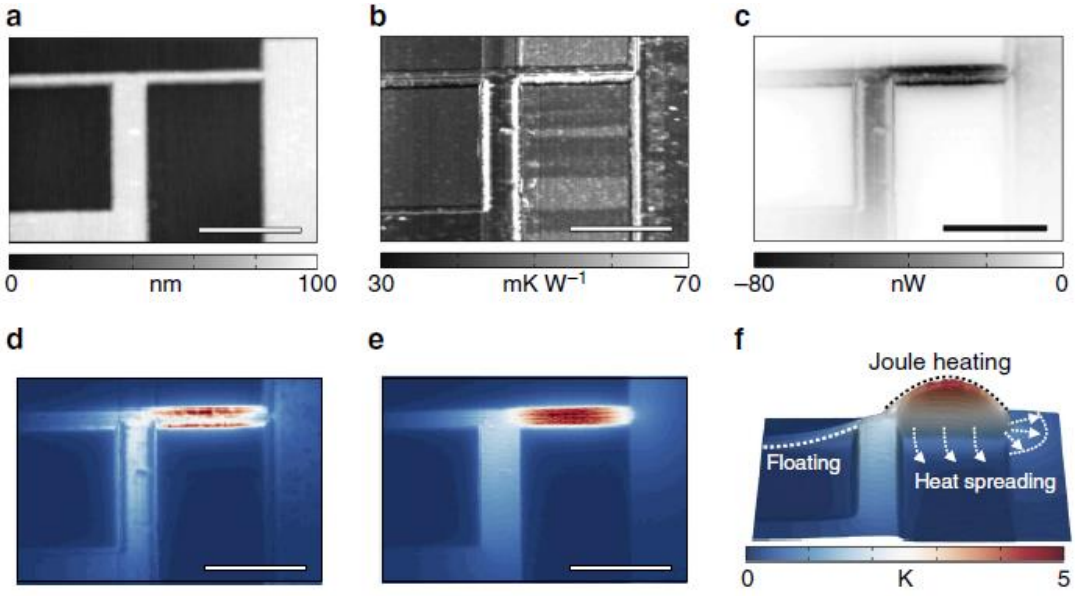

Figure 1.16 Temperature changes on the surface of Au interconnection[2]. (a) AFM image of the Au interconnection on silicon nitride. Scale bar is 1 μm. (b) The probe-sample thermal resistance R_{ps} in different positions on the Au interconnection. (c) The mapping of probe-sample thermal heat flux Q_{AC} on the device. (d) The temperature changes on the device obtained by the conventional method without consideration of position-dependent thermal resistance R_{ps}. (e) The true temperature changes on different areas of the surface using the position-dependent thermal resistance R_{ps}. and (f) The encoded temperature increase on the device to show the Joule heating including the heat transfer from the interconnection. The

colour bar applies to (d) and (e).

The temperature mapping results are shown in Figure 1.16. The AFM image shows the morphology and size of the gold interconnection fabricated by lithography technique (Figure 1.16 (a)). Figure 1.16 (b) shows the thermal resistance mapping results from scanning the device surface that is contacted to the silicon probe. The entire scanning process was conducted in a high vacuum environment to eliminate the influence caused by cross-ventilation and heat transfer to the air. The highly variable values caused by changes in position confirmed the position-dependent property of thermal resistance, which should be considered in SThM. Figure 1.16 (c) shows the topographic distribution of thermal heat flux between the sample and the probe during the same scanning process. Figure 1.16 (d) indicates the obvious systematic errors using the conventional method, which does not consider the position-dependent thermal resistance. This result is not reasonable because the interconnection part that is heated the most shows a lower temperature in the middle section than at the edges. This problem can be solved by taking the position-dependent property of thermal resistance into account, as shown in Figure 1.16 (e). Figure 1.16 (f) shows the encoded temperature map together with the height information, which shows more clearly the self-heating disturbance on the area with different thickness. The parabolic temperature profile is because of the Joule heating effect and the temperature decay to other linked parts of the device.

The nanometre spatial resolution and sub-degree temperature resolution makes the SThM technique suitable for the temperature characterisation of various types of materials. Technology changes and develops so fast that apart from the AFM- and STM-based platforms for SThM, a third approach has emerged, which was reported by Wagner *et al*. in 2018[108]. These authors successfully developed the Kelvin probe force microscopy for thermal scanning. This is a non-contact technique for local characterisation of samples with high spatial resolution, and makes up for the disadvantages in the other scanning probe methods, in which the contact

geometry in the probe-surface connection and the touch force control both affect the accuracy and make the operation convoluted. Although this nanothermometry method cannot be used for the testing of biological samples tests, it is specialised for metallic surface temperature detection, and has been widely used for surface thermal detection in electronic devices, which play an important role in the local self-heating effects, for instance, the spin-Peltier effect, the magnetocaloric effect and the thermoplasmonic effect.

1.1.3 Applications of nanothermometers

In the above-mentioned sections, we studied the intrinsic thermometric characterisations of luminescence nanomaterials and the development of the SThM technique based on probe scanning microscopes for nanothermometry. In this section, we focus on the demonstrated applications of nanothermometry from the literature. The use of the SThM technique is limited to sample surface analysis, which has already been described in detail in the previous sections; therefore, this section will cover the application of luminescent nanothermometers.

Luminescent nanothermometers have undergone fast growth since their emergence during the last century[64]. The diversity of luminescent nanothermometers guarantees a broad emergent interest of nanothermometry in different areas. By examining the research areas that will profit from the development of nanothermometry in terms of high feasibility, accuracy and sensitivity, the following three fundamental areas have future progress that is closely connected to nanothermometry:

(1) Biomedicine;

(2) Micro/nanoscale electronics;

(3) Integrated photonics.

1.1.3.1 Applications in biomedicine

Biomedicine requires the development of biosensors that have small size, high sensitivity, great targeting ability and biocompatibility. Among the many studied parameters in physiology, temperature is one of the most important factors affecting the physiological status of cell division speed, and the biological system consisting of tissues, cells and organelles[114,115]. For example, when body temperature is slightly higher than 37 ℃, the microscopic behaviour of biomolecules such as proteins will dramatically change because a denaturation process may occur to change their fundamental properties such as their structure[116]. Therefore, temperature is the signal that indicates that some type of physiological action is occurring, and studying the temperature distribution inside the biological system is an effective approach for understanding the dynamics and basic mechanisms behind complicated cell behaviours.

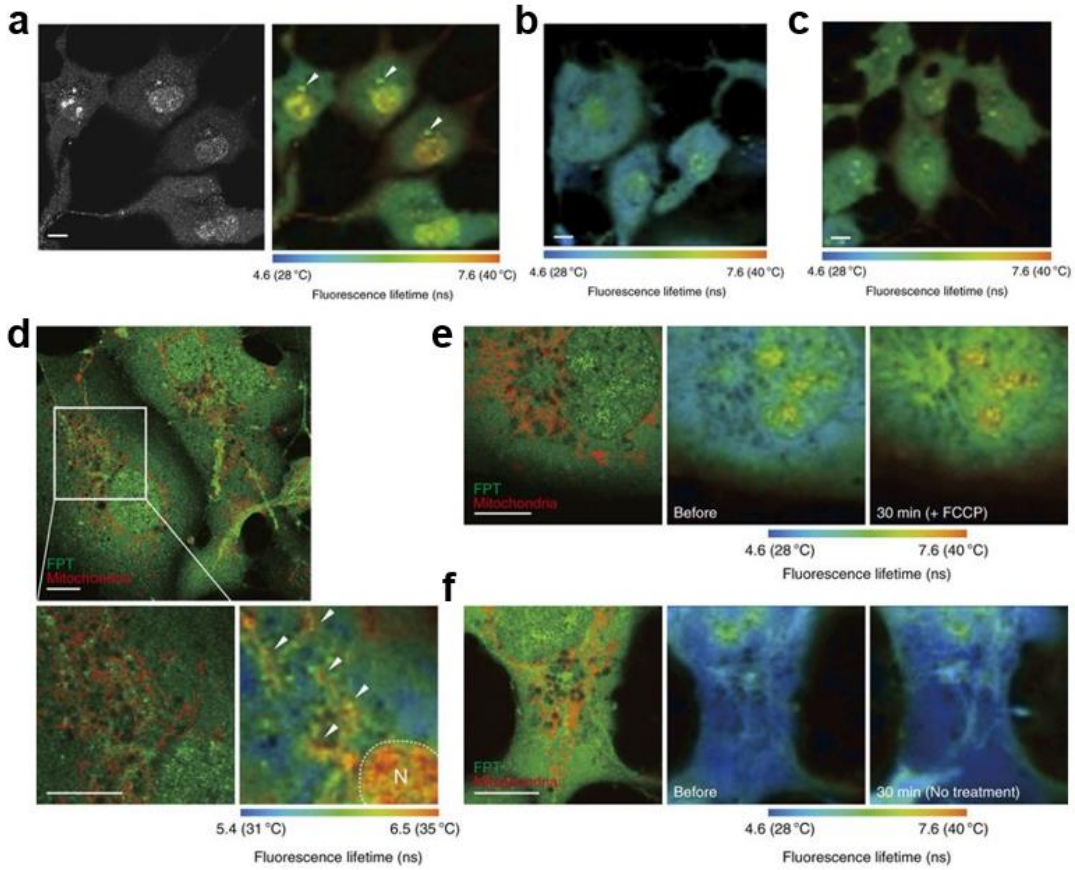

Figure 1.17 Temperature distribution and its dynamic change in single cells stained with the

temperature-responsive polymer[103]. (a) Confocal fluorescence image (left) and fluorescence lifetime image (right) of COS7 cells. (b) Fluorescence lifetime images of COS7 cells during the G1 phase. (c) Fluorescence lifetime images of COS7 cells during the S/G2 phase. (d) Confocal fluorescence images and fluorescence lifetime image of COS7 cells labelled by polymeric thermometer (green) and MitoTracker Deep Red FM (red; upper and left lower). Arrowheads show local thermogenesis. (e) Temperature increases around the mitochondria after the chemical stimulus. (f) Fluorescence lifetime remains stable without the chemical stimulus. The temperature of the medium was maintained at 30 °C. Scale bar is 10 μm.

In 2012, Okabe *et al*. reported on intracellular temperature mapping using a fluorescent polymer with a temperature-dependent lifetime[103], the temperature-responsive polymer has been shown previously in Figure 1.12. Here, in Figure 1.17, the attained intracellular temperature mapping results are shown. After staining the COS7 cells with the temperature-responsive polymer, an inhomogeneous temperature distribution inside the cell was obtained by analysing the luminescence lifetime values recorded with the TC-SPC module. Figure 1.17 (a) shows the higher temperature in the nucleus than that in the cytoplasm, which can be explained by the more frequent activities that occur in the nucleus, such as DNA replication, transcription and RNA processing. Figure 1.17 (b) and (c), further prove that this temperature difference is caused by the cell cycle state. When the cell is processed to the G1 phase, the nucleus is warmer by approximately 0.7 ℃ than the cytoplasm temperature. For cells in the S/G2 phase, the temperature difference is smaller. Additionally, a single spot near the nucleus (arrowheads in Figure 1.17 (d)) exhibits a higher temperature. This increased temperature in the centrosome might be caused by its multiple functions, such as mitosis and the organisation of microtubules.

Moreover, Okabe *et al.* also showed that the mitochondria in the cell will generate local thermogenesis. As show in Figure 1.17 (d), by labelling the mitochondria with MitoTracker

Deep Red FM, the area around mitochondria has a higher temperature similar to that of the nucleus. By an additional chemical stimulus, the thermal production of the mitochondria could be promoted. As shown in Figure 1.17 (e) and (f), by adding a reagent, 4-(trifluoromethoxy)phenylhydrazone (FCCP), the areas around the mitochondria had higher temperature results 30 min after the stimuli, which can be explained by the stopping of adenosine triphosphate synthesis inside the cell from the addition of FCCP.

These results indicate the significance of nanothermometers for understanding the relationships between the temperature and organelle functions. Beside this fundamental research on biology, temperature bio-probes also play a key role in several emerging medical therapeutics for the treatment of diseases[117-122]. One of the most convenient ways to check lesions appearing in living organisms is by monitoring the thermal singularities, e.g. tumours always have a higher temperature than the temperature of other healthy tissues because of the high activity occurring in tumours. It is assumed that when tumours grow into a specific size consisting of thousands of cancer cells, the thermal singularities in the tumours will be detectable. However, this method of sensing tumours by temperature sensors is not only dependent on the inhomogeneous temperature caused by the tumours themselves but is also decided by the sensitivity, biocompatibility and other basic properties of the sensor used. Developing nanothermometry into a mature method for cancer detection would have great advantage over the conventional medical imaging technology such as tomography, because the traditional methods are limited by the detectable tumour size required, which is up to several millimetres. More significantly, this new method would allow earlier medical treatment of tumours.

Photothermal therapy, with precise temperature control on specific targets, benefits greatly from luminescent nanothermometry[120,123,124]. By enhancing the local temperature of tumours externally up to a harmful level above 40 ℃, the tumours can be cured by thermal ablation. However, the localised temperature in tumours is hard to control as it requires high spatial

resolution temperature monitoring, and overheating or any accidental operation will lead to empyrosis in the surrounding healthy tissues. This concern can be resolved by real-time temperature monitoring on the tumour during the thermal ablation process, via labelling of the tumour by a nanothermometer that has targeting ability. Thus, overheating and other issues caused by inaccurate control can be avoided. This has been used in the platform design of photothermal therapy, and the developed platforms are equipped with the functions of both high-resolution temperature monitoring and photon induced self-heating.

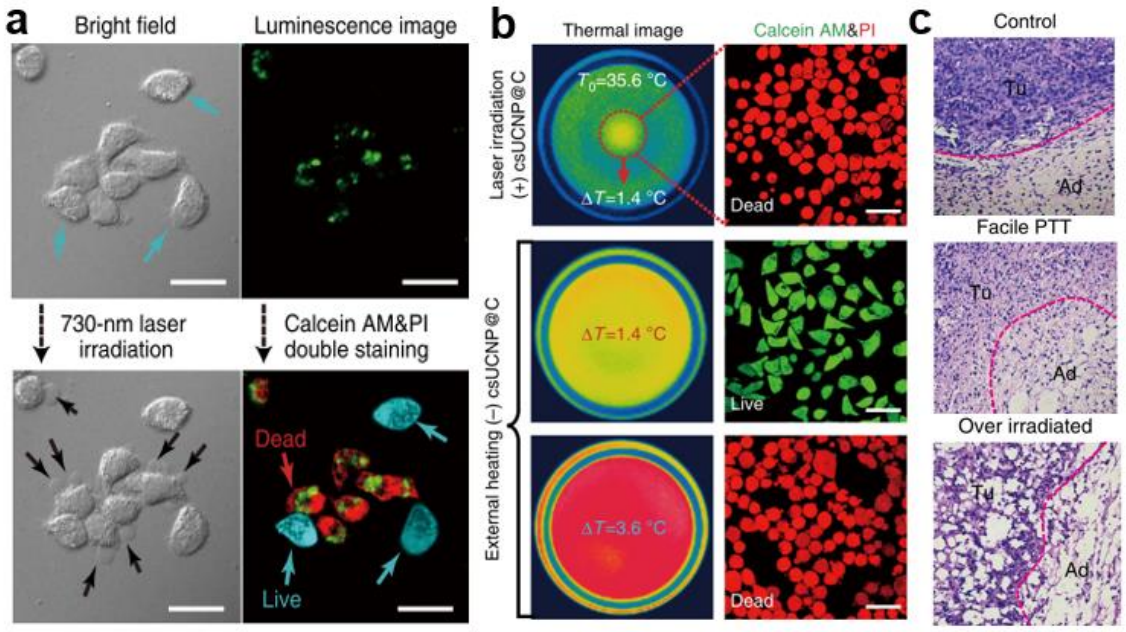

Figure 1.18 Accurate photothermal therapy using $NaLuF_4:Yb^{3+}$, Er^{3+}@$NaLuF_4$@C nanoparticles[99]*. (a) Photothermal therapy of HeLa cells. Cells with green emissions were stained with $NaLuF_4:Yb^{3+}$, Er^{3+}@$NaLuF_4$@C. After photothermal therapy by laser irradiation, dead cells labelled with black arrows showed cytoplasm leakage. Scale bar is 30 mm. (b) Comparison between external heating and photothermal therapy in HeLa cells. (c) Haematoxylin and eosin histologic section showing tumour and normal fat tissue.*

Zhu *et al*. reported on a photothermal therapy method that used a temperature feedback system to achieve precise control[99]. By coating the upconversion nanoparticles with an extra carbon

layer, they created a multifunctional $NaLuF_4:Yb^{3+}$, Er^{3+}@$NaLuF_4$@C platform for temperature reading and self-heating. Using dual laser excitation of 980 nm and 730 nm, the $NaLuF_4:Yb^{3+}$, $Er3^+$ core works as a temperature sensor and the carbon layer plays the role of a heating source by absorbing 730 nm irradiance. These authors studied the performance of photothermal therapy in cell levels, as shown in Figure 1.18 (a), and the HeLa cells stained by the nanothermometers showing strong green emission were mixed with the non-labelled cells. By application of a 0.3 W/cm^2 730 nm irradiance, the cells containing nanothermometers were killed owing to the thermal damage caused by the carbon layer, and the non-labelled cells were still alive, even though they were very close (few micrometres) to the labelled cells. Cytoplasm leakage was also found because of the damage of the membranes in the dead cells. The authors also compared the different effects between external heating and photothermal therapy. Figure 1.18 (b) shows after the application of 0.3 W/cm^2 730 nm irradiance, the nanothermometer-stained cells were dead by an apparent temperature increase of 1.4 ℃. Using external heating, the stained cells started to become damaged only when temperature increase was as high as 3.6 ℃, with the same fiducial temperature of 35.6 ℃. These results prove that the photothermal effect caused by $NaLuF_4:Yb^{3+}$, Er^{3+}@$NaLuF_4$@C works more effectively than that using an external heating source. The eigen temperature inside the cell should be higher than the apparent temperature, which was confirmed by inferring the eigen temperature through the nanothermometer. Furthermore, the authors investigated the feasibility of photothermal therapy *in vivo.* By studying the heat conduction behaviour under different irradiance powers systematically, the authors summarised a model of temperature-feedback photothermal therapy and applied it to *in vivo* treatment. After five days of treatment, the tumour in each mouse was eliminated successfully. Figure 1.18 (c) shows that the facile photothermal therapy can cause shrinkage and fragmented nuclei in the tumour with much less harm on the normal tissue. In another two contrast experiments, the inaccurate treatments both leads to incurable.

1.1.3.2 Applications in micro/nanoscale electronics

The Joule heating effect describes the temperature increase on the conductor when an electric current flows through the circuit. When the electronic linewidth is fabricated at micro/nanoscale size, this current-induced heating effect becomes more pronounced[125,126]. Thus, an imperfect production process will lead to defects in the circuit such as resistance variations, and it becomes a 'hot-spot' with higher Joule heating temperature, which may cause malfunctions or even component damage. The detection of such a hot-spot is crucial for the development of a qualified micro/nanoscale electronic device. Among the limited approaches for such a purpose, nanothermometry plays the pivotal role.

As discussed in the previous section, SThM is a feasible method to characterise the surface temperature distribution of electronics, with high spatial resolution and high sensitivity, and can provide much detailed temperature information on the scanning area. Apart from SThM, several luminescent nanothermometers have been developed for micro/nanoscale electronic temperature sensing. One work has been conducted by Brites *et al*.[127], who used a ratiometric nanothermometer layer to detect the temperature on a microdevice, the on-device experimental results are shown in Figure 1.19. These authors coated the microdevice with a layer of Eu^{3+}, Tb^{3+} codoping ratiometric nanothermometer and then, using an optical fibre to excite and collect the emissions simultaneously and calculate the intensity ratio with the calibration curve, the temperature of the device could be measured. The temperature mapping profiles showed a high spatial resolution around 35 μm that was achieved by this nanothermometry method, which was much better than the results measured with the IR camera (Figure 1.19 (c) and (d)).

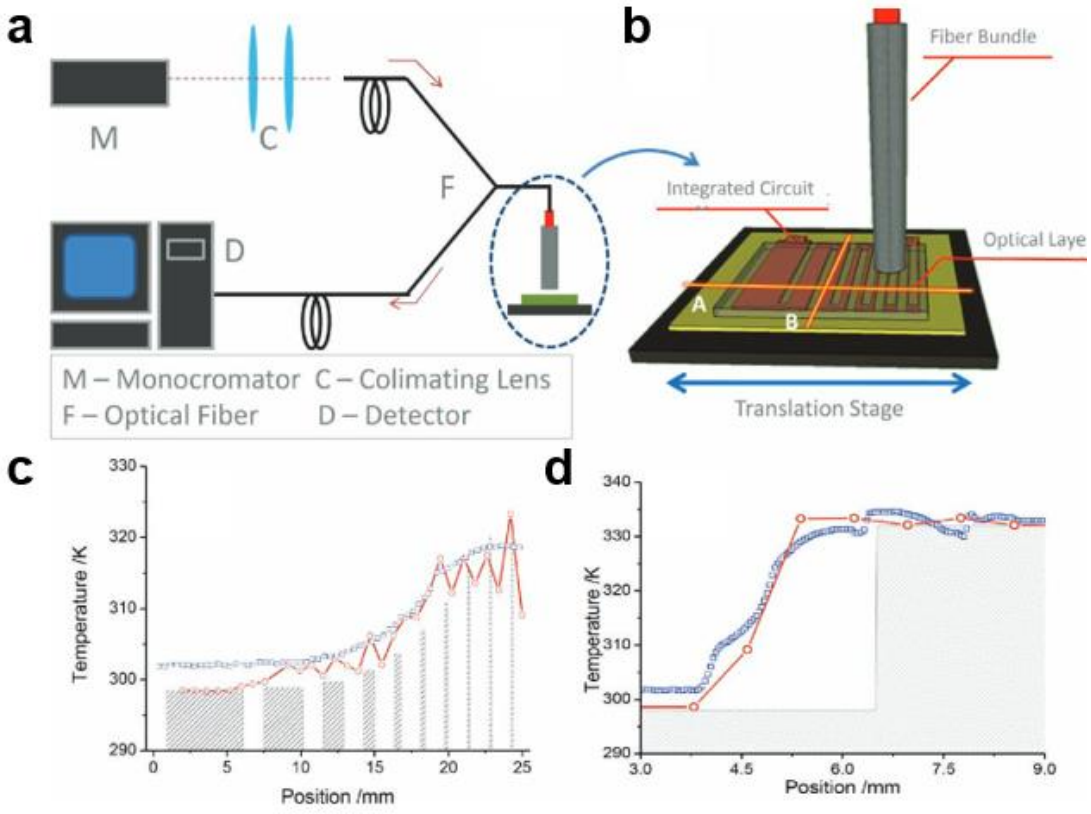

Figure 1.19 Localised temperature sensing on an integrated circuit[127]. (a), (b) Scheme diagram shows the temperature measurement on the device by covering with a layer of nanothermometers and signal collection with a controlled fibre. (c), (d) Detected temperature profiles by the luminescent nanothermometer (red circles) along the lines A and B compared with the measurements by an IR camera (blue squares).

1.1.3.3 Applications in integrated photonics

Integrated photonic devices are another area where temperature monitoring cannot be ignored because temperature affects many optical parameters that are widely used for light control and the operation of integrated photonic devices, such as the local refractive index, optical gain of the integrated laser, spectral properties of semiconductors and optical conversion efficiency of nonlinear converters[128,129]. For the integrated photonic devices that are based on these parameters control, temperature instability could lead to sub-micrometric variation in the

optical parameters, and it could strongly interfere with device performance or even cause irreversible failure. Similar to the case of micro/nano-electronics, by developing nanothermometry to check and exclude the temperature singularities that emerge in the integrated photonic devices is significant for guaranteeing the reliable quality of the device.

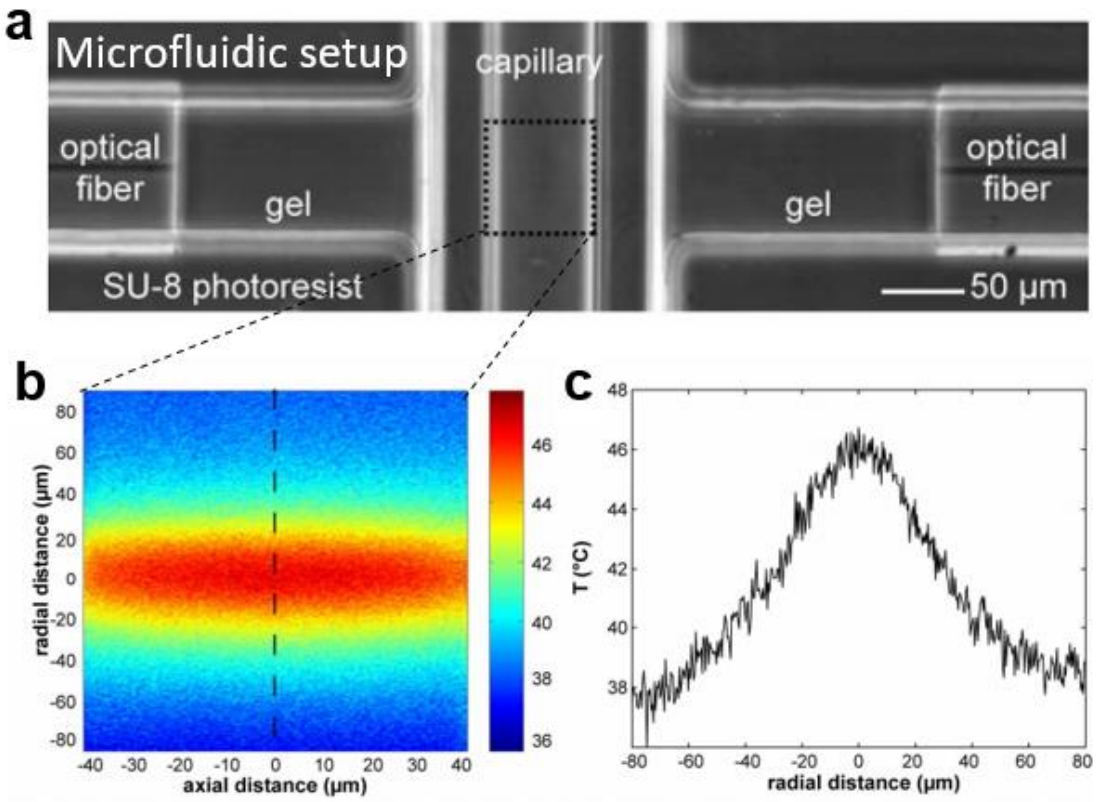

Figure 1.20 Ratiometric nanothermometry for temperature mapping on opto-fluidic[16]. (a) Microfluidic setup with a dual-beam laser from the optical fibre. The two opposing fibre laser beams passing through the index matching gel form an optical trap. (b) Two-dimensional temperature mapping on the select area in the setup. (c) Temperature distribution along the microfluidic channel labelled by the dashed line in (b). A slight asymmetry is caused. The output power of the two 1064 nm laser beams was 1 W.

One typical example is the application of nanothermometry for the temperature mapping of optofluidic devices in which optical forces are used to manipulate micron sized objects. Ebert *et al*. reported the application of the temperature-sensitive dye rhodamine B and the

temperature independent reference dye rhodamine 110 for ratiometric nanothermometry on optofluidics, as shown in Figure 1.20[16]. The optofluidic setup contained a capillary that was radiated by two fibre-coupled 1064 nm lasers on both sides (Figure 1.20 (a)). To measure the higher temperature induced by absorption at the laser radiation wavelength, an aqueous solution containing both rhodamine B and rhodamine 110 was injected into the capillary and the emission intensities were detected by a laser scanning confocal microscope at the chosen area of the capillary. Then, the temperature distribution was determined by the calibration curve based on the thermometric properties of the dyes. Figure 1.20 (b) shows the temperature mapping of the optofluidic device under two 1 W laser irradiations. The laser trap centre showed the highest temperature around 46 ℃, with a temperature increase of 25 °C compared to the room temperature at 21 °C (Figure 1.120(c)). These results are consistent with the theoretical simulations and confirm the reliability of this temperature sensing method.

1.1.4 Performances of nanothermometers

In this section, we will discuss the standards that are usually used to evaluate the performance of different nanothermometry methods. A universal nanothermometry method does not exist because different applications require different properties of nanothermometry. For example, for the intracellular temperature measurement, the first condition of the nanothermometer must be biocompatibility rather than high sensitivity, while the application in devices does not require this. Thus, the choice of nanothermometers in different situations should be considered on a case-by-case basis. To quantify the performance of distinct luminescence thermometers, the following parameters can be referenced:

(1) Relative sensitivity;

(2) Operating temperature range;

(3) Temperature resolution;

(4) Spatial resolution;

(5) Repeatability and reproducibility.

The first parameter, relative sensitivity S_r, indicates how fast the thermometric parameter Q changes with the absolute temperature T, and can be defined as[4,26,59]:

$$S_r = \frac{1}{Q}\left|\frac{\partial Q}{\partial T}\right|$$

The relative sensitivity represents the percentage change of Q under per degree of temperature change. The value always varies at different temperatures and the maximum relative sensitivity is widely used in the literature as a reference on how sensitive the material is. Besides, the absolute temperature sensitivity $\boldsymbol{S}$[130],

$$S = \frac{\partial Q}{\partial T}$$

cannot be compared among different nanothermometers, as it depends on the characteristics of the material such as the initial intensity or lifetimes, whereas the relative sensitivity is independent of the nature of the material and can be used for comparison.

The operating temperature range means the range that can be measured by a nanothermometry method, which usually depends on the chemical stability of the materials. Generally speaking, inorganics such as nanocrystals can be used at higher operating temperature, because of their excellent structure stability[131]. Specifically, polymer-based temperature sensors have narrow working ranges, which is restricted to their phase transition temperature region, normally 300–310 K, although a wider temperature range can be achieved by some improvement on synthesis such as the combination of two polymeric nanothermometers to cover different ranges, with polymeric temperature sensors still working below 373 K[132-140]. Additionally, the reported

methods usually target particular applications such as intracellular temperature sensing, in these situations, the study on nanothermometry is limited to the range of physiological temperatures instead of a broader temperature range.

The temperature resolution is the minimum temperature change that can be measured by the temperature sensing method, which depends on the relative sensitivity and the equipment performance. The temperature resolution δT regarding the thermal induced change of thermometric parameters Q can be expressed by the Taylor's series expansion as[59]:

$$\delta T = \frac{\partial T}{\partial Q}\delta Q + \frac{1}{2!}\frac{\partial^2 T}{\partial Q^2}(\delta Q)^2 + \cdots + \frac{1}{n!}\frac{\partial^n T}{\partial Q^n}(\delta Q)^n$$

where, δQ indicates the minimum changes of Q that can be detected by the equipment. The results of δT are dominated by the first term; therefore, the Taylor's series expansion can be written as:

$$\delta T = \frac{\partial T}{\partial Q}\delta Q = \frac{1}{S_r}\frac{\delta Q}{Q}$$

so that for one given thermometer with relative sensitivity S_r, the temperature resolution is decided by the experimental instrument. With a more sensitive instrument setup, the minimum detectable signal change δQ is lower, which leads to high temperature resolution. Generally, by using highly sensitive photomultiplier tubes or charge-coupled devices as the detector, the theoretical value of temperature resolution δT can be lower than 0.003 K.

The spatial resolution depends on the thermometer size, the temperature resolution and the temperature gradient of the test objective, which is defined as the minimum distance δd between two points whose temperature gap is higher than the temperature resolution δT, and can be written as[3]:

$$\delta d = \frac{\delta T}{\left|\vec{\nabla} T\right|_{max}}$$

where, $\left|\vec{\nabla} T\right|_{max}$ is the maximum temperature gradient in the test objective. The spatial resolution in nanothermometry can be improved either by a smaller temperature uncertainty with sensitive detectors or by a higher temperature gradient in the test objective. According to the literature, most nanothermometry methods can provide a spatial resolution down to the micron scale because of the ultra-small sensor size, high sensitivity and advanced instrument.

Repeatability and reproducibility greatly affect the test precision with regard to not only nanothermometers, but also to other types of sensors[141]. Repeatability means that with a certain quantity to be measured, several measurements using the same method can give the same results. It is almost impossible to achieve perfect repeatability in a real situation because errors in the test process cannot be avoid. Not all methods have great repeatability, such as organic dye-based nanothermometers have bad repeatability due to photobleaching, although these are competent for continuous and long-term measurements. Reproducibility refers to the variation in the same measurements caused by different batches of sensors, instrument modifications and changes to other conditions. To obtain better reproducibility of the experiments, the used sample should be prepared with a mature synthesis method to guarantee different batches have the same performance, meanwhile the measurement condition including the instrument should be maintained consistently. To study the repeatability and reproducibility of a given nanothermometry method, the most commonly used technique is to perform the multiple heating-cooling cycle measurement that lasts up to several hours. Table 1 summarises the different published nanothermometry methods based on the different sensing principles and the evaluation criteria as discussed.

Table 1 Summery of different thermometers displaying their best relative sensitivity, working temperature range, temperature resolution and repeatability.

Thermometer	Thermo metric signal	Maximum sensitivity (%/℃)	Temperature range/resolution (℃)	Repeatability	Year	Ref.
Organic fluorophores						
DyLight 549	EI	1.5	25–42	NA	2010	[139]
ER thermo yelllow	EI	3.9	32-37	Yes	2014	[142]
ER thermo yellow	EL	1.04	23-40	Yes	2016	[143]
Mito thermo yellow	EI	2.8	37-42	Yes	2015	[144]
Mito-RTP	EIR	2.65	25-43	Yes	2015	[8]
Polymers						
NIPAM-DBD nanogel	EI	NA	27-33/0.29-0.5	Yes	2009	[6]
NNPAM-DBD cationic copolymer	EL	NA	15-35/0.09-0.78	No	2013	[145]
NIPAM-DBD cationic copolymer	EL	NA	28-38/0.05-0.54	No	2015	[146]
Fe3O4@SiO2@ (pNIPAM-co-RhBITC) /Au	EI	4.84	26-41	Yes	2015	[147]
Quantum dots						
PbS/CdS/ZnS	EI	1	20-55	Yes	2016	[18]
CdSeS/ZnS@ polymer	EI	1.55	25-45/0.43	Yes	2015	[148]
QD655	EW	0.016	-20-12	Yes	2011	[9]
CdSe QDs	EW	0.016	30-60	Yes	2013	[149]

CdSe QDs	EW	0.015	30-60	Yes	2013	[150]
RE ions doping nanoparticles						
TTA-Nd	EIR	7.1	10-50/0.1	Yes	2018	[55]
Sc_2O_3: Eu^{2+}, Eu^{3+}	EIR	3.06	-200-4	Yes	2018	[96]
$NaYF_4$: Er^{3+}, Yb^{3+}	EIR	1.6	10-36	Yes	2016	[151]
Gd_2O_3:Yb^{3+}, Er^{3+}	EIR	0.2	22-727	NA	2009	[152]
ZnO:Er^{3+}	EI	0.6	0-200	NA	2007	[82]
LaF^3: Nd^{3+}	EIR	0.1	10-60	NA	2013	[65]
Eu-TTA@polymer	EI	2.2	20-60	Yes	2012	[11]
Other inorganics						
Au nanoclusters	EL	NA	15-45/0.3-0.5	Yes	2013	[12]
Cu nanoclusters	EI	NA	15-80	Yes	2015	[153]
nitrogen-vacancy centres in nanodiamond	Spin states	NA	-200-327	Yes	2015	[10]
Other organics						
L-MB	EI	NA	20-55/0.7	Yes	2012	[53]
GFP	EPA	0.4	20-60	Yes	2013	[154]
(EuDT/$Ir(ppy)_3$/ PS-MA)@PVA	EIR	4	25-46	Yes	2015	[153]

EI: emission intensity; EL: emission lifetime; EW: emission wavelength; EPA: emission polarisation anisotropy; NA: not available.

1.2 RE doped anti-Stokes materials in nanothermometry

1.2.1 Advantages of anti-Stokes luminescence

Anti-Stokes luminescence represents the radiative transitions that occur at energy levels higher than that of the absorbed excitation photons, and refers to the high energy photon emission generated by the absorption of low-energy photons. This unusual phenomenon has created many optical techniques, such as laser cooling[156,157], coherent anti-Stokes Raman spectroscopy[158,159], photon energy upconversion and optical thermometry[160-162]. In particular, nanoscopic-sized probes with anti-Stokes emission properties, such as the multi-photon upconversion nanoparticles, are highly attractive to many emerging applications in functional optical imaging and nanoscale sensing[163], as this process can efficiently remove the detection noise from excitation scatterings and fluorescence backgrounds that normally follows the easier Stokes process where the wavelength of the emissions is longer than that of the excitations. Moreover, anti-Stokes luminescence is usually induced by excitation within the biology optical window around NIR or IR (700–950 nm first biology optical window, 1000–1350 nm second biology optical window and 1500–1800 nm third biology optical window) [164-166], thus the excitation light has the maximum depth of penetration in biological tissues due to these living tissues scattering and absorbing less light at these wavelengths, and some of the anti-Stokes luminescence can generate in the biology optical window[93,167]. It is relatively easy to measure the anti-Stokes luminescence with short wavelengths such as visible light, and the NIR exciting sources are inexpensive.

1.2.2 RE doped anti-Stokes materials

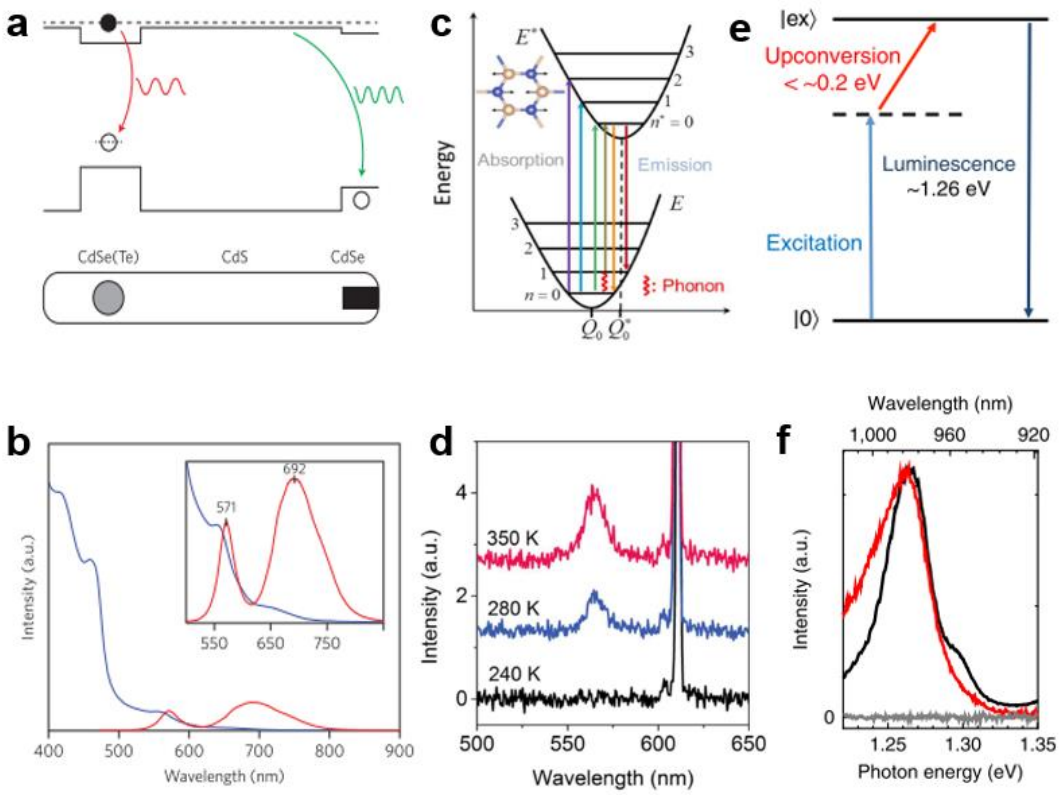

Figure 1.21 Anti-Stokes emissions and energy structures from CdSe(Te)/CdS/CdSe QDs[168], hexagonal boron nitride (h-BN)[169] and carbon dots[170]. (a, b) The green anti-Stokes emission generated from the bandgap structure of CdSe(Te)/CdS/CdSe with 680 nm pulse excitaion. (c, d) The anti-Stokes emission spectra of h-BN with excitation at 610 nm, which results from the phonon-assisted energy transitions as shown in the configurational coordinate. (e, f) The Stokes (black) and anti-Stokes (red) emission spectra from carbon dotsat 568 nm and 1100 nm excitation. The grey curve is a result from the carbon-free surfactant solution excited at 1100 nm for comparison.

In the search for efficient nanomaterials with large anti-Stokes shift, many inorganic nanomaterial systems have been investigated to produce linear anti-Stokes emissions, as shown in Figure 1.21, including the CdSe(Te)/CdS/CdSe QDs with an anti-Stokes shift of 110 nm from 680 nm to 570 nm[168], h-BN from 610 nm to 565 nm[169], carbon dots from 1100

nm to 984 nm[170], $CsPbBr_3$ perovskite nanocrystal from 532 nm to 518 nm[171] and CdS nanobelts from 532 nm to 496 nm[172]. These material systems commonly suffer from a lack of suitable excited states as the 'step-stones' to facilitate step-by-step energy transfer, and thereby their anti-Stokes emissions depend on the contingency of the defects or the bandgap restricted reconstruction.

Compared with these studied anti-Stokes emission materials, luminescent nanomaterial with trivalent RE elements doping can be an ideal candidate for anti-Stokes emissions, due to their abundant energy states, which work as a 'ladder' for energy transfer to higher levels, as shown in Figure 1.22.

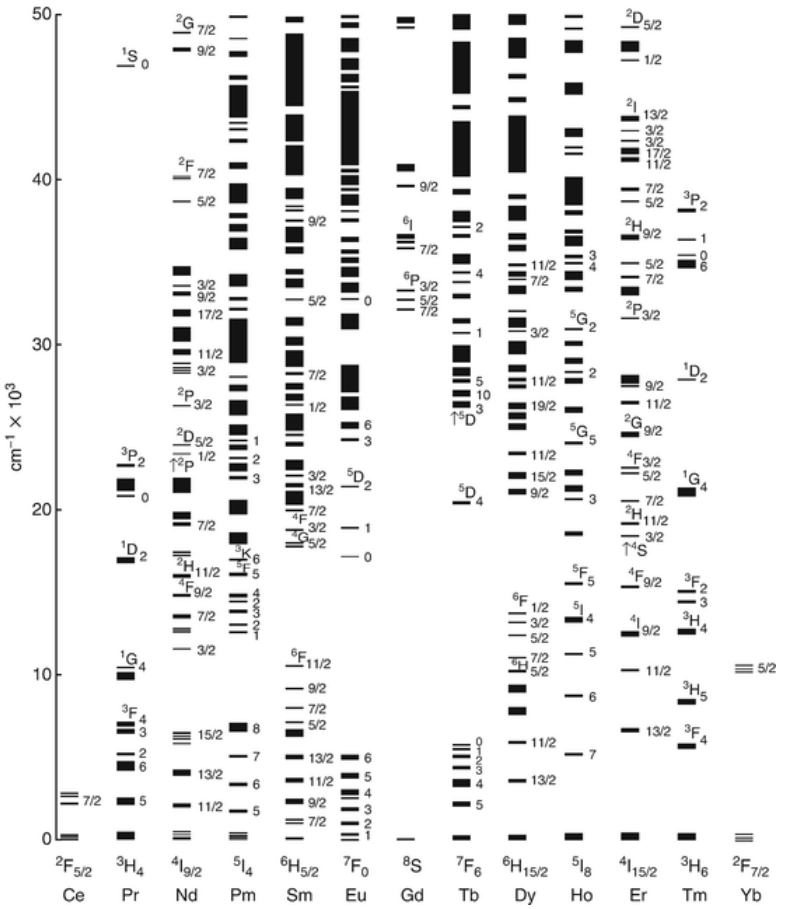

Figure 1.22 Dieke diagram showing the energy structures of the trivalent RE ions originating from their 4f electron configurations.

RE elements specifically include the 15 lanthanides, as well as scandium and yttrium. Many luminescence materials doped with RE activator ions generate sharp emission bands because of the special f-f electronic transitions. The 'atom-like' sharpness of the emission bands belong to the energy transitions occurring between the f orbitals, which are screened by the outer complete orbits 5s and 5p, thus the f-f radiative transitions are not very sensitive to the environment of the RE ions[173]. Multiple emission bands from different RE activators are located at different positions in the spectra, which originate from the high energy levels of their 4f configuration. Thus, trivalent RE elements have diverse optical properties.

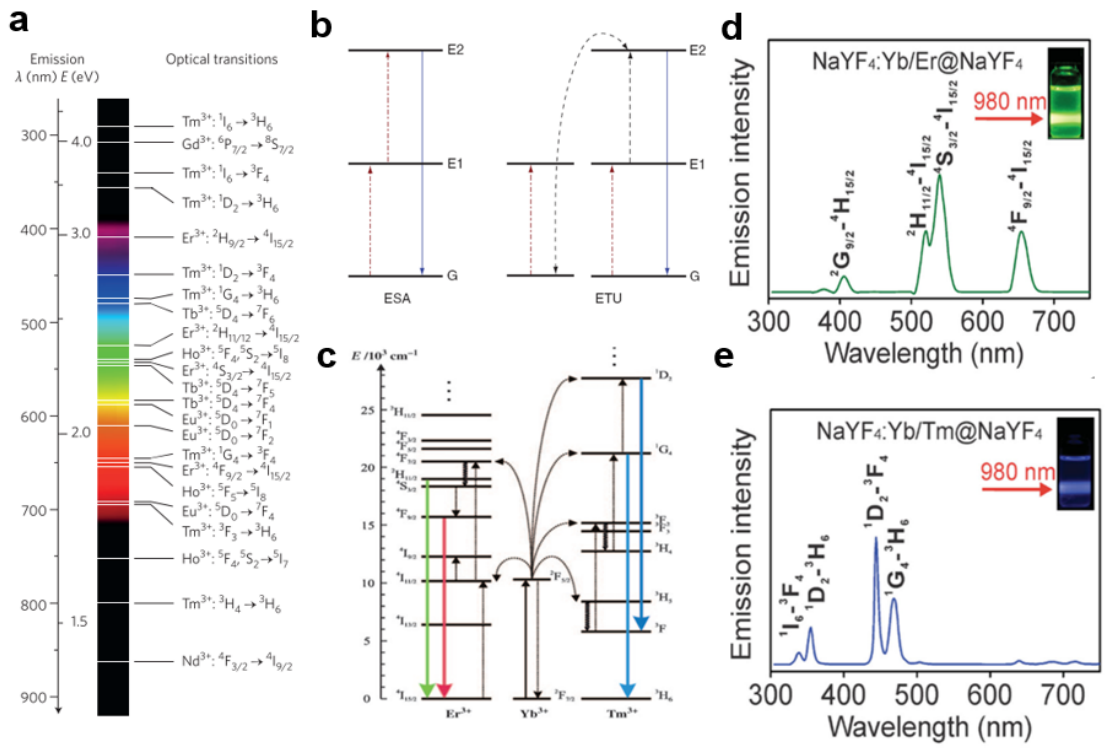

Figure 1.23 Upconversion luminescence and the energy transfers in trivalent RE ions[161,174]*. (a) Typical upconversion emissions from trivalent lanthanide series and the corresponding energy transitions. (b) The two most frequent upconversion modes: excited-state absorption and energy transfer upconversion. (c) The upconversion processes in* Yb^{3+}*-*Er^{3+} *and* Yb^{3+}*-*Tm^{3+} *codoping materials. (d)The upconversion spectra of* Er^{3+}*ions. (e) The upconversion spectra of* Tm^{3+}*ions. The excitation wavelength is 980 nm in (d) and (e).*

The anti-Stokes emission is also known as upconversion. Figure 1.23 (a) shows the numerous upconversion radiative transitions that cover the photoluminescence spectra from ultraviolet to NIR, which occur in the various trivalent RE ions[161]. To achieve the upconversion luminescence in trivalent RE, two main energy transfer modes are applied, as depicted in Figure 1.23 (b). Both excited-state absorption and energy transfer upconversion refer to an upconversion process that converts two or more photons into one higher-energy photon. More specifically, the highly used sensitiser Yb^{3+} can absorb excitation photons around 980 nm more efficiently due to its large absorption cross-section, thus by doping Yb^{3+} with another trivalent RE ion as the activator, such as Er^{3+} or Tm^{3+} in Figure 1.23 (c), the continuous energy transfer from Yb^{3+} to the activator can excite the population in the ground states to jump to high energy states, which is followed by radiative relaxation to the ground state. The results in Figure 1.23 (e) and (f) show the characteristic upconversion emission bands from Er^{3+} and Tm^{3+}, as a result of the energy transfer of $Yb^{3+}\rightarrow Er^{3+}$ and $Yb^{3+}\rightarrow Tm^{3+}$ [174], respectively.

With these built-in advantages, RE doped upconversion nanoparticles have been involved in the emerging applications in biology imaging[175,176], cancer therapy[177,178], information storage[179,180], anti-counterfeiting[181,182], laser technology[183,184] and so on. Here, some key applications of upconversion nanoparticles selected from those developed over the past decade are discussed and are shown in Figure 1.24.

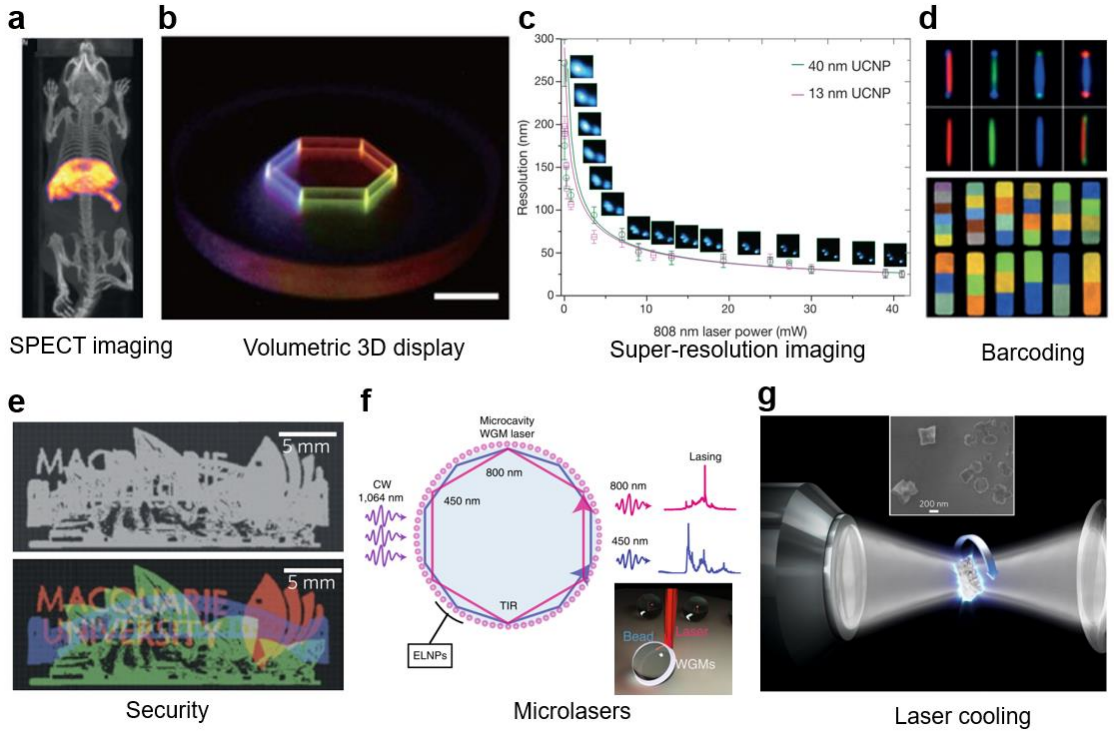

Figure 1.24 Selective applications using multifunctional RE doped upconversion nanoparticles. (a) In vivo Kunming mouse whole-body three-dimensional imaging through single-photon emission computed tomography (SPECT) after intravenous injection of $NaLuF_4$*:* Sm^{3+}*,* Yb^{3+} *and* Tm^{3+} *as contrast agents*[185]*. (b) Three-dimensional full-colour imaging in a transparent display matrix composed of* $NaYF_4$*:*Nd^{3+}*,* Yb^{3+}*@*$NaYF_4$*:*Yb^{3+}*,* Tm^{3+}*@*$NaYF_4$*@*$NaYF_4$*:*Yb^{3+}*,* Ho^{3+} *and* Ce^{3+}*@*$NaYF_4$ *core-shell nanoparticles under modulated pulse laser scanning*[186]*. (c) Super-resolution imaging by the amplified stimulated emission from* $NaYF_4$*:* Yb^{3+}*,* Tm^{3+}*nanoparticle under dual laser illumination*[62]*. (d) Single microrod doping with different RE ions in each section as barcoding through controllable synthesis*[180,182]*. (e) Security printing by the ink containing three sets of lifetime encoded* $NaYF_4$*:* Yb^{3+}*,* Tm^{3+} *nanoparticles*[187]*. The coded patterns (top) can be decoded (bottom) by a time-resolved laser scanning confocal microscope with a 980 nm laser. (f) Continuous-wave lasing generated from microbeads coated with* Tm^{3+} *doped nanoparticles, the microbeads work as a microcavity*[184]*. (g) Laser refrigeration in YLF:* Yb^{3+} *nanocrystals by anti-Stokes fluorescence induced with 1031 nm excitation*[157]*.*

RE doped upconversion nanoparticles can be applied as contrast agents from a series of biomedical imaging techniques such as magnetic resonance (MR), computed tomography (CT), single-photon emission computed tomography (SPECT) and positron emission tomography (PET)[185,188-190], because lanthanide ions have high attenuation and magnetic properties. Figure 1.24 (a) shows an example of SPECT with upconversion nanoparticles used as the contrast agent[185], because Sm generates the gamma photon with a long half-life. The exploitations of the new properties of anti-Stokes emissions have also led to some significant progress in optical display and imaging technology, such as three-dimensional display and super-resolution imaging. Figure 1.24 (b) shows the three-dimensional full-colour display using one type of pulse-duration sensitive upconversion nanoparticle[186], with the energy transfer well-adjusted by the excitation pulse duration. Thus, under different laser pulses and wavelengths, the synthesised core-shell nanoparticle emitted different colours. Jin and co-workers found the unique stimulated emissions from the $Yb^{3+} \rightarrow Tm^{3+}$ energy transfer under dual laser excitation, by harnessing these properties with super-resolution stimulated emission depletion microscopy, these authors realised an imaging resolution down to 28 nanometres[62], which is much higher than the general diffraction limit above 200 nm (Figure 1.24 (c)). The development of upconversion nanoparticles towards new information storage and anti-counterfeiting techniques is another hot topic, because the upconversion nanoparticles can be synthesised into specific sizes and shapes with excellent uniformity. Figure 1.24 (d) shows the fabricated RE doped nanorods as barcodes. These multi-section barcodes have different dopants in each section; therefore, they have diverse emission colours under the microscope, which can lead to large encoding capacities[180,182]. Figure 1.24 (e) shows security printing using three $NaYF_4$: Yb^{3+}, Tm^{3+} nanoparticles. Because their doping concentrations are different, the three samples had different emission lifetimes but the same blue emission, thus under laser excitation the three overlapped patterns printed by

corresponding upconversion nanoparticles could not be distinguished, the only way to decode the security printing was with a time-resolved laser scanning confocal microscope[187]. In 2018, Fernandez-Bravo *et al*. reported the continuous-wave upconverting lasing from Tm^{3+} doped upconversion nanoparticles at thresholds as low as 14 kW/cm^2, as shown in Figure 1.24 (f)[184], which proves that the RE doped upconversion nanoparticles are promising gain media for the production of anti-Stokes coherent radiation. Moreover, Rahman *et al.* demonstrated that laser cooling caused by anti-Stokes luminescence from YLF: Yb^{3+} crystals, then the temperature of YLF: Yb^{3+} can decrease from 300 K to 130 K[157], which was investigated by monitoring Brownian motion with optical forceps. Such refrigeration on the microscale opens new opportunities for studying the temperature effects of physiological processes.

1.2.3 Challenges in RE doped anti-Stokes nanothermometers

Except for the above applications, the scientific community is also interested in the development of RE doped anti-Stokes luminescent materials that are capable of high-resolution temperature sensing, including the integration of multi-functions in one structure for simultaneous heat generation and temperature sensing[191,192], which was discussed in Section 1.1. Having these advantages of deep tissue penetration and low background noise, anti-Stokes luminescent materials provide a promising approach for *in vivo* temperature sensing.

However, although some efficient upconversion luminescence combinations such as Yb^{3+}-Er^{3+}, Yb^{3+}-Ho^{3+} and Yb^{3+}-Tm^{3+} have been explored for ratiometric nanothermometry, the emission intensity is still not comparable with other luminescent materials such as QDs because of the energy loss during high energy level climbing in the anti-Stokes radiative process[193]. The smaller size of the nanoparticles will also lead to weaker emissions due to denser defects in the surface[194,195]. Additionally, temperature increase is always accompanied with reduced brightness as shown in Figure 1.25, which can be explained as thermal quenching[196-198]. Thus,

the lower signal-to-noise ratio of RE doped luminescent nanomaterials in high temperatures becomes a challenge in temperature sensing.

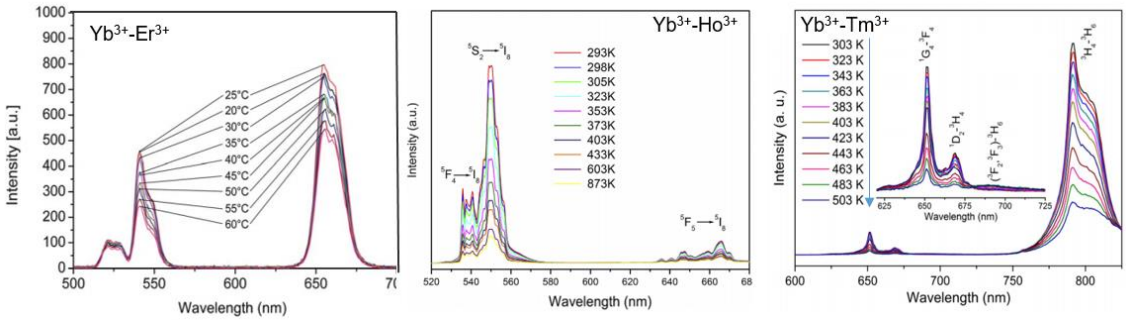

Figure 1.25 Thermal quenching of anti-Stokes emissions in Yb^{3+}-Er^{3+}, Yb^{3+}-$Ho^{3+}$and Yb^{3+}-Tm^{3+} codoping upconversion materials under 980 nm laser excitation[196-198].

To make RE doped luminescent nanothermometers a real possibility for high-sensitive and high-resolution measurements, further improvements in sensitivity must be achieved, aiming at the detection of slight temperature inhomogeneity. Most of the reported RE doped nanothermometers have a sensitivity lower than 2%/K based on the thermal coupled energy levels method introduced in section 1.1.1. Compared with other types of luminescent nanothermometers, RE doped nanothermometers have no obvious advantage in sensitivity[26], as shown in Figure 1.26. Although the thermometric signal can be calibrated by a simplified Boltzmann distribution model, the sensitivity of this thermometry method is limited by the stable properties of the thermal coupled levels. As previously mentioned, because of the 5s and 5p shelter of trivalent RE ions, the environment temperature change cannot cause much difference between the f-f optical transitions from the same RE ions. Thus, the emission ratio changes slowly and the sensitivity of RE doped materials with the same emitters are very similar although the host materials are different.

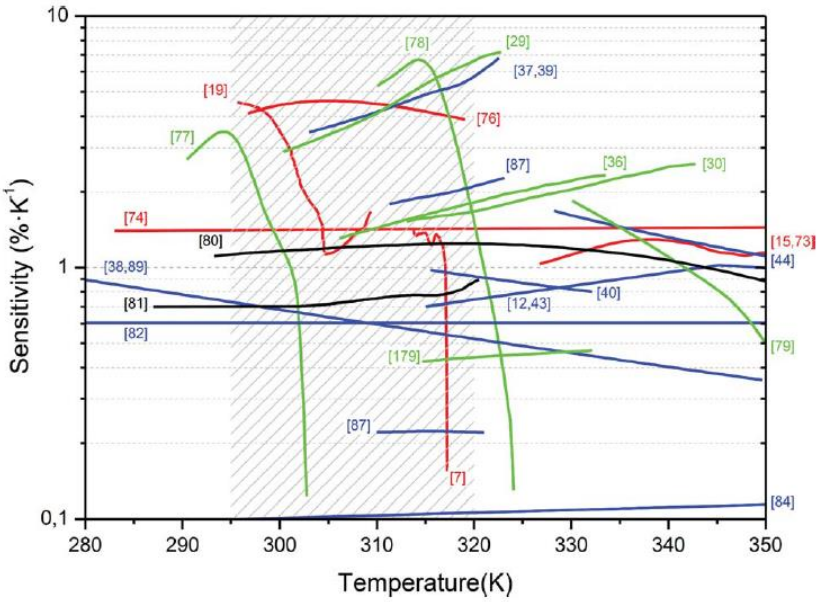

Figure 1.26 Relative sensitivity with temperature for a series of organic dye (red), polymer (green), QDs (black) and RE (blue)-based luminescent ratiometric thermometers.

Despite the considerable number of studies on RE doped nanothermometers over the past decade, comprehensive temperature characterisation on micro/nanoscale structures including electronics and living cells or tissues have still not been satisfactorily accomplished. As mentioned above, the major obstacles are the relatively low sensitivity and weak anti-Stokes emissions under the influence of thermal quenching. To conquer these challenges will have far-reaching effects on the design of next generation nanothermometers.

The first step should be towards the exploration of new optical properties that help remove the conventional thermometry method. RE doped nanocrystals offer valuable chances for strengthening their optical characters by the delicate design of their structure and controlled synthesis. The widely used core-shell structure is a good example, which can used for both more controllable energy migration from layer to layer and a combination of different RE emitters without cross-relaxation. The novel property itself has increased from the ultra-high surface-to-volume ratio in nanoparticles, in these nanomaterials surface plays a non-negligible role on the anti-Stokes radiation because the defects and organic ligands living in the surface

will also participate in the energy transfer process[212,213]. To clearly study the entire picture occurring on the surface will open great opportunities for refining the anti-Stokes emissions towards high efficiency.

Therefore, the main challenges in the RE doped anti-Stokes luminescence nanothermometers that researchers are facing are:

- To enhance anti-Stokes luminescence by fully understanding the energy transfer from ions to ions, or surface to ions/ions to surface more clearly, optimising emission efficiency with core-shell structure or multi-section rod structure is required to avoid energy loss in energy level mismatch or cross-relaxation, if necessary, surface modification can also be an effective way against surface quenching.
- To develop high-sensitive thermometers with a new method, the sensitivity limitation set by the use of thermal coupled energy levels must be changed by a new approach. This new method should include the advantages of the ratiometric method, more importantly, it should realise an intensity ratio with a fast response to temperature. One obvious possibility is finding one emission band that increases with temperature while the second emission band decreases with temperature. Thus, the high contrast ratiometric method can be realised by these two emissions. Due to the emissions with opposite thermal properties almost being non-existent in one type of trivalent RE ions, dual emitters would be a better choice.

1.3 Thesis aims and outline

In this thesis, the author will systematically introduce the research results on how to realise enhanced anti-Stokes emissions in a thermal field against thermal quenching, and the novel energy transfer process between the surface and lattice of the RE doped upconversion nanoparticles. For the first time, the mechanism behind the thermal enhanced anti-Stokes

emission has been clearly investigated. Further, after careful spatial design and controlled synthesis of two anti-Stokes emission bands in three different nanoscale structures, which include one thermal enhanced emission and one thermal quenched emission for high contrast, a new generation of nanothermometers with maximum relative sensitivity up to 10 %/K have been achieved. Moreover, the author has demonstrated the application of such sensitive nanothermometers for visualised temperature monitoring in a large area up to 1 cm^2, and also for the localised high spatial resolution temperature sensing on a microelectronic device with linewidth down to 10 μm. The explored thermal enhanced anti-Stokes properties provide a new strategy for the design of multifunctional RE doped materials and the new method used in this thesis suggests a large scope of nanothermometry applications.

1.4 References

1 Mecklenburg, M., Hubbard, W. A., White, E. R., Dhall R., Cronin, S. B., Aloni S., Regan, B. C. Nanoscale temperature mapping in operating microelectronic devices. *SCIENCE* **347**, 4 (2015).

2 Menges, F. *et al.* Temperature mapping of operating nanoscale devices by scanning probe thermometry. *Nat Commun* **7**, 10874 (2016).

3 Kim, K., W. J., Lee, W., Reddy P. Ultra-high vacuum scanning thermal microscopy for nanometer resolution quantitative thermometry. *ACS Nano* **6**, 10 (2012).

4 Bai, T., Gu, N. Micro/nanoscale thermometry for cellular thermal sensing. *Small* **12**, 4590-4610 (2016).

5 Chen, Q. *et al.* Protein modified upconversion nanoparticles for imaging-guided combined photothermal and photodynamic therapy. *Biomaterials* **35**, 2915-2923 (2014).

6 Gota, C., Okabe, K., Funatsu, T., Harada, Y., Uchiyama, S. Hydrophilic fluorescent nanogel thermometer for intracellular thermometry. *Journal of the American Chemical Society* **131**, 2 (2009).

7 Gao, L., Zhang, C., Li, C., Wang, L. V. Intracellular temperature mapping with fluorescence-assisted photoacoustic-thermometry. *Appl Phys Lett* **102**, 193705 (2013).

8 Homma, M., Takei, Y., Murata, A., Inoue, T., Takeoka, S. A ratiometric fluorescent molecular probe for visualization of mitochondrial temperature in living cells. *Chem Commun (Camb)* **51**, 6194-6197 (2015).

9 Yang, J. M., Yang H., Lin, L. Quantum dot nano thermometers reveal heterogeneous local thermogenesis in living cells. *ACS Nano* **5**, 5 (2011).

10 Kucsko, G. *et al.* Nanometre-scale thermometry in a living cell. *Nature* **500**, 54-58 (2013).

11 Oyama, K. *et al.* Walking nanothermometers: spatiotemporal temperature measurement of transported acidic organelles in single living cells. *Lab Chip* **12**, 1591-1593 (2012).

12 Shang, L., Stockmar, F., Azadfar, N., Nienhaus, G. U. Intracellular thermometry by using fluorescent gold nanoclusters. *Angew Chem Int Ed Engl* **52**, 11154-11157 (2013).

13 Zhou, L. *et al.* High-capacity upconversion wavelength and lifetime binary encoding for multiplexed biodetection. *Angew Chem Int Ed Engl* **57**, 12824-12829 (2018).

14 Lin, X. *et al.* Core-shell-shell upconversion nanoparticles with enhanced emission for wireless optogenetic inhibition. *Nano Lett* **18**, 948-956 (2018).

15 Samy, R., Glawdel, T., Ren, C. L. Method for microfluidic whole-chip temperature measurement using thin-film poly(dimethylsiloxane)/rhodamine B. *Anal Chem* **80**, 369-375 (2008).

16 Ebert, S., Travis, K., Lincoln, B., Guck, J. Fluorescence ratio thermometry in a microfluidic dual-beam laser trap. *OPTICS EXPRESS* **15**, 7 (2007).

17 Cheng, L. *et al.* Facile preparation of multifunctional upconversion nanoprobes for multimodal imaging and dual-targeted photothermal therapy. *Angew Chem Int Ed Engl* **50**, 7385-7390 (2011).

18 del Rosal, B. *et al.* Infrared-emitting QDs for thermal therapy with real-time subcutaneous temperature feedback. *Advanced Functional Materials* **26**, 6060-6068 (2016).

19 Dong, B. *et al.* Multifunctional $NaYF_4$: Yb^{3+},Er^{3+}@Ag core/shell nanocomposites: integration of upconversion imaging and photothermal therapy. *Journal of Materials Chemistry* **21**, 6193 (2011).

20 Huang, P. *et al.* Folic acid-conjugated silica-modified gold nanorods for X-ray/CT imaging-guided dual-mode radiation and photo-thermal therapy. *Biomaterials* **32**, 9796-9809 (2011).

21 Huang, Y. *et al.* Upconverting nanocomposites with combined photothermal and photodynamic effects. *Nanoscale* **10**, 791-799 (2018).

22 Liu, X. *et al.* CuS@mSiO2-PEG core-shell nanoparticles as a NIR light responsive drug delivery nanoplatform for efficient chemo-photothermal therapy. *Dalton Trans* **44**, 10343-10351 (2015).

23 O'Neal, D. P., Hirsch, L. R., Halas, N. J., Payne, J. D., West, J. L. Photo-thermal tumor ablation in mice using near infrared-absorbing nanoparticles. *Cancer Lett* **209**, 171-176 (2004).

24 Skripka, A. *et al.* Double rare-earth nanothermometer in aqueous media: opening the third optical transparency window to temperature sensing. *Nanoscale* **9**, 3079-3085 (2017).

25 Li, C., Dong, B., Li, S., Song, C. Er^{3+}–Yb^{3+} co-doped silicate glass for optical temperature sensor. *Chemical Physics Letters* **443**, 426-429 (2007).

26 Brites, C. D. *et al.* Thermometry at the nanoscale. *Nanoscale* **4**, 4799-4829 (2012).

27 Lee, J., Kotov, N. A. Thermometer design at the nanoscale. *Nano Today* **2**, 48-51 (2007).

28 Brites, C. D. S. *et al.* Thermometry at the nanoscale using lanthanide-containing organic–inorganic hybrid materials. *Journal of Luminescence* **133**, 230-232 (2013).

29 Hofer, P. P., Brask, J. B., Perarnau-Llobet, M., Brunner, N. Quantum Thermal Machine as a Thermometer. *Phys Rev Lett* **119**, 090603 (2017).

30 Plakhotnik, T., Doherty, M. W., Cole, J. H., Chapman, R., Manson, N. B. All-optical thermometry and thermal properties of the optically detected spin resonances of the NV(-) center in nanodiamond. *Nano Lett* **14**, 4989-4996 (2014).

31 Salmon, L. *et al.* A novel approach for fluorescent thermometry and thermal imaging purposes using spin crossover nanoparticles. *Journal of Materials Chemistry* **20**, 5499-5503 (2010).

32 Toyli, D. M., de las Casas, C. F., Christle, D. J., Dobrovitski, V. V., Awschalom, D. D. Fluorescence thermometry enhanced by the quantum coherence of single spins in diamond. *PNAS* **110**, 8417-8421 (2013).

33 Ximendes, E. C. *et al.* Unveiling in vivo subcutaneous thermal dynamics by infrared luminescent nanothermometers. *Nano Lett* **16**, 1695-1703 (2016).

34 Zhou, H., Sharma, M., Berezin, O., Zuckerman, D., Berezin, M. Y. Nanothermometry: from microscopy to thermal treatments. *Chemphyschem* **17**, 27-36 (2016).

35 Zhou, S. *et al.* Strategy for thermometry via Tm^{3+}-doped $NaYF_4$ core-shell nanoparticles. *Opt Lett* **39**, 6687-6690 (2014).

36 Zhou, S. *et al.* Optical thermometry based on upconversion luminescence in Yb^{3+}/Ho^{3+} co-doped $NaLuF_4$. *Journal of Alloys and Compounds* **588**, 654-657 (2014).

37 Zhou, Y., Yan, B. Lanthanides post-functionalized nanocrystalline metal-organic frameworks for tunable white-light emission and orthogonal multi-readout thermometry. *Nanoscale* **7**, 4063-4069 (2015).

38 Zhou, Y., Yan, B., Lei, F. Postsynthetic lanthanide functionalization of nanosized metal-organic frameworks for highly sensitive ratiometric luminescent thermometry. *Chem Commun (Camb)* **50**, 15235-15238 (2014).

39 Albers, A. E. *et al.* Dual-emitting quantum dot/quantum rod-based nanothermometers with enhanced response and sensitivity in live cells. *J Am Chem Soc* **134**, 9565-9568 (2012).

40 Correa, L. A., Mehboudi, M., Adesso, G., Sanpera, A. Individual quantum probes for optimal thermometry. *Phys Rev Lett* **114**, 220405 (2015).

41 Quintanilla, M., Zhang, Y., Liz-Marzán, L. M. Subtissue plasmonic heating monitored with CaF_2:Nd^{3+},Y^{3+} nanothermometers in the second biological window. *Chemistry of Materials* **30**, 2819-2828 (2018).

42 Shao, Q., Ouyang, L., Jin, L., Jiang, J. Multifunctional nanoheater based on $NaGdF_4$:Yb^{3+}, Er^{3+} upconversion nanoparticles. *Opt Express* **23**, 30057-30066 (2015).

43 Tikhomirov, V. K., Driesen, K., Rodriguez, V. D., Gredin, P., Mortier, M., Moshchalkov, V. V. Optical nanoheater based on the Yb^{3+}-Er^{3+} codoped nanoparticles. *OPTICS EXPRESS* **17**, 5 (2009).

44 Xu, W., Qi, H., Zheng, L., Zhang, Z., Cao, W. Multifunctional nanoparticles based on the Nd^{3+}/Yb^{3+} codoped $NaYF_4$. *Opt Lett* **40**, 5678-5681 (2015).

45 Yang, Y. *et al.* Optical thermometry based on the upconversion fluorescence from Yb^{3+}/Er^{3+} codoped La_2O_2S phosphor. *Ceramics International* **40**, 9875-9880 (2014).

46 Zhou, S., Li, C., Liu, Z., Li, S., Song, C. Thermal effect on up-conversion in Er^{3+}/Yb^{3+} co-doped silicate glass. *Optical Materials* **30**, 513-516 (2007).

47 Marciniak, L., Pilch, A., Arabasz, S., Jin, D., Bednarkiewicz, A. Heterogeneously Nd^{3+} doped single nanoparticles for NIR-induced heat conversion, luminescence, and thermometry. *Nanoscale* **9**, 8288-8297 (2017).

48 Carattino, A., Caldarola, M., Orrit, M. Gold nanoparticles as absolute nanothermometers. *Nano Lett* **18**, 874-880 (2018).

49 Augusto, V., Baleizão, C., Berberan-Santos, M. N., Farinha, J. P. S. Oxygen-proof fluorescence temperature sensing with pristine C_{70} encapsulated in polymernanoparticles. *J. Mater. Chem.* **20**, 1192-1197 (2010).

50 Cui, Y. *et al.* A ratiometric and colorimetric luminescent thermometer over a wide temperature range based on a lanthanide coordination polymer. *Chem Commun* **50**, 719-721 (2014).

51 Shiraishi, Y., Miyamoto, R., Hirai, T. A hemicyanine-conjugated copolymer as a highly sensitive fluorescent thermometer. *Langmuir* **24**, 7 (2008).

52 Shan, G., Weissleder, R., Hilderbrand, S. A. Upconverting organic dye doped core-shell nano-composites for dual-modality NIR imaging and photo-thermal therapy. *Theranostics* **3**, 267-274 (2013).

53 Ke, G. *et al.* L-DNA molecular beacon: a safe, stable, and accurate intracellular nano-thermometer for temperature sensing in living cells. *J Am Chem Soc* **134**, 18908-18911 (2012).

54 Cui, Y., Zhu, F., Chen, B., Qian, G. Metal-organic frameworks for luminescence thermometry. *Chem Commun* **51**, 7420-7431 (2015).

55 Xu, M. *et al.* Ratiometric nanothermometer in vivo based on triplet sensitized upconversion. *Nat Commun* **9**, 2698 (2018).

56 Li, L. *et al.* Visible-light excited luminescent thermometer based on single lanthanide organic frameworks. *Advanced Functional Materials* **26**, 8677-8684 (2016).

57 Lee, J., Govorov, A. O., Kotov, N. A. Nanoparticle assemblies with molecular springs: a nanoscale thermometer. *Angew Chem Int Ed Engl* **44**, 7439-7442 (2005).

58 del Rosal, B., Ximendes, E., Rocha, U., Jaque, D. In vivo luminescence nanothermometry: from materials to applications. *Advanced Optical Materials* **5**, 14 (2017).

59 Brites, C. D. S., Millán, A., Carlos, L. D. in *Handbook on the Physics and Chemistry of Rare Earths* Vol. 49, 89 (2016).

60 Zheng, W. *et al.* Near-infrared-triggered photon upconversion tuning in all-inorganic cesium lead halide perovskite quantum dots. *Nat Commun* **9**, 3462 (2018).

61 Chen, C. *et al.* Multi-photon near-infrared emission saturation nanoscopy using upconversion nanoparticles. *Nat Commun* **9**, 3290 (2018).

62 Liu, Y. *et al.* Amplified stimulated emission in upconversion nanoparticles for super-resolution nanoscopy. *Nature* **543**, 229-233 (2017).

63 Zhan, Q. *et al.* Achieving high-efficiency emission depletion nanoscopy by employing cross relaxation in upconversion nanoparticles. *Nat Commun* **8**, 1058 (2017).

64 Jaque, D., Vetrone, F. Luminescence nanothermometry. *Nanoscale* **4**, 4301-4326 (2012).

65 Rocha, U., *et al.* Subtissue Thermal sensing based on neodymium-doped LaF_3 nanoparticles. *ACS Nano* **7**, 12 (2013).

66 Li, S., Zhang, K., Yang J. M., Lin, L., Yang, H. Single quantum dots as local temperature markers. *Nano Letters* **7**, 4 (2007).

67 Maestro, L. M. *et al.* Fluorescent nanothermometers provide controlled plasmonic-mediated intracellular hyperthermia. *Nanomedicine (Lond)* **8**, 379-388 (2013).

68 Dai, Q. *et al.* Size-dependent temperature effects on PbSe nanocrystals. *Langmuir* **26**, 11435-11440 (2010).

69 Maestro, L. M. *et al.* CdSe quantum dots for two-photon fluorescence thermal imaging. *Nano Lett* **10**, 5109-5115 (2010).

70 Olkhovets, A., Hsu, R. C., Lipovskii, A., Wise, F. W. A. Size-dependent temperature variation of the energy gap in lead-salt quantum dots. *PHYSICAL REVIEW LETTERS* **81**, 4 (1998).

71 Narayanaswamy, A., Feiner, L. F., Meijerink, A., van der Zaag, P. J. The effect of temperature and dot size on the spectral properties of colloidal InP/ZnS core-shell quantum dots. *ACS Nano* **3**, 8 (2009).

72 Peng, H. S., Huang, S. H., Wolfbeis, O. S. Ratiometric fluorescent nanoparticles for sensing temperature. *Journal of Nanoparticle Research* **12**, 2729-2733 (2010).

73 Yang, J. *et al.* Ratiometric afterglow nanothermometer for simultaneous in situ bioimaging and local tissue temperature sensing. *Chemistry of Materials* **29**, 8119-8131 (2017).

74 Takei, Y., *et al*. A nanoparticle-based ratiometric and self-calibrated fluorescent thermometer for single living cells. *ACS Nano* **8**, 9 (2014).

75 Cadiau, A., Brites, C. D. S., Costa, P. M. F. J., Ferreira, R. A. S., Rocha, J., Carlos, L. D. Ratiometric nanothermometer based on an emissive Ln^{3+}-organic framework. *ACS Nano* **7**, 6 (2013).

76 Brites, C. D. *et al.* Ratiometric highly sensitive luminescent nanothermometers working in the room temperature range. Applications to heat propagation in nanofluids. *Nanoscale* **5**, 7572-7580 (2013).

77 Wang, C. *et al.* Tunable carbon-dot-based dual-emission fluorescent nanohybrids for ratiometric optical thermometry in living cells. *ACS Appl Mater Interfaces* **8**, 6621-6628 (2016).

78 McLaurin, E. J., Bradshaw, L. R., Gamelin, D. R. Dual-emitting nanoscale temperature sensors. *Chemistry of Materials* **25**, 1283-1292 (2013).

79 Cui, Y. *et al.* A luminescent mixed-lanthanide metal-organic framework thermometer. *J Am Chem Soc* **134**, 3979-3982 (2012).

80 Dieke, G. H. *Spectra and Energy Levels of Rare Earths in Crystal*. 401 (Interscience Publishers, 1968).

81 Wortmann, L., Suyari, S., Ube, T., Kamimura, M., Soga, K. Tuning the thermal sensitivity of β-$NaYF_4$: Yb^{3+}, Ho^{3+}, Er^{3+} nanothermometers for optimal temperature sensing in OTN-NIR (NIR II/III) biological window. *Journal of Luminescence* **198**, 236-242 (2018).

82 Wang, X., Kong, X., Yu, Y., Sun, Y., Zhang, H. Effect of annealing on upconversion luminescence of ZnO:Er^{3+} nanocrystals and high thermal sensitivity. *The Journal of Physical Chemistry C* **111**, 6 (2007).

83 Yu, W., Xu, W., Song, H., Zhang, S. Temperature-dependent upconversion luminescence and dynamics of $NaYF_4$:Yb^{3+}/Er^{3+} nanocrystals: influence of particle size and crystalline phase. *Dalton Trans* **43**, 6139-6147 (2014).

84 Zhou, S. *et al.* An abnormal fluorescence intensity ratio between two green emissions of Er3+ caused by heating effect of 980 nm excitation. *Journal of Rare Earths* **33**, 1031-1035 (2015).

85 Balabhadra, S. *et al.* Boosting the sensitivity of Nd^{3+}-based luminescent nanothermometers. *Nanoscale* **7**, 17261-17267 (2015).

86 Gao, G. *et al.* Wide-range non-contact fluorescence intensity ratio thermometer based on Yb^{3+}/Nd^{3+} co-doped La_2O_3 microcrystals operating from 290 to 1230 K. *Journal of Materials Chemistry C* **6**, 4163-4170 (2018).

87 Xu, W., Song, Q., Zheng, L., Zhang, Z., Cao, W. Optical temperature sensing based on the near-infrared emissions from Nd^{3+}/Yb^{3+} codoped $CaWO_4$. *Opt Lett* **39**, 4635-4638 (2014).

88 Yang, G. *et al.* A core/shell/satellite anticancer platform for 808 NIR light-driven multimodal imaging and combined chemo-/photothermal therapy. *Nanoscale* **7**, 13747-13758 (2015).

89 Kolesnikov, I. E. *et al.* New strategy for thermal sensitivity enhancement of Nd3+-based ratiometric luminescence thermometers. *Journal of Luminescence* **192**, 40-46 (2017).

90 Ximendes, E. C. *et al.* In vivo subcutaneous thermal video recording by supersensitive infrared nanothermometers. *Advanced Functional Materials* **27**, 1702249 (2017).

91 Marciniak, L., Prorok, K., Frances-Soriano, L., Perez-Prieto, J., Bednarkiewicz, A. A broadening temperature sensitivity range with a core-shell YbEr@YbNd double ratiometric optical nanothermometer. *Nanoscale* **8**, 5037-5042 (2016).

92 Li, D. D., Shao, Q. Y., Dong, Y., Fang, F., Jiang, J. Q. Ho^{3+}(or Tm^{3+})-activated upconversion nanomaterials: anomalous temperature dependence of upconversion luminescence and applications in multicolor temperature indicating and security. *Particle & Particle Systems Characterization* **32**, 728-733 (2015).

93 Dong, N., *et al*. NIR-to-NIR two-photon excited CaF_2: Tm^{3+},Yb^{3+} nanoparticles: multifunctional nanoprobes for highly penetrating fluorescence bio-imaging. *ACS Nano* **5**, 7 (2011).

94 Xing, L., Xu, Y., Wang, R., Xu, W., Zhang, Z. Highly sensitive optical thermometry based on upconversion emissions in Tm^{3+}/Yb^{3+} codoped $LiNbO_3$ single crystal. *Opt Lett* **39**, 454-457 (2014).

95 Cao, Z. *et al.* Temperature dependent luminescence of Dy^{3+} doped $BaYF_5$ nanoparticles for optical thermometry. *Current Applied Physics* **14**, 1067-1071 (2014).

96 Pan, Y. *et al.* Inherently Eu^{2+}/Eu^{3+} codoped Sc_2O_3 nanoparticles as high-performance nanothermometers. *Adv Mater* **30**, e1705256 (2018).

97 Tan, C., Wang, Q. Photophysical studies of novel lanthanide (Eu^{3+} and Tb^{3+}) luminescent hydrogels. *Inorganic Chemistry Communications* **14**, 515-518 (2011).

98 Gálico, D. A., Mazali, I. O., Sigoli, F. A. Nanothermometer based on intensity variation and emission lifetime of europium(III) benzoylacetonate complex. *Journal of Luminescence* **192**, 224-230 (2017).

99 Zhu, X. *et al.* Temperature-feedback upconversion nanocomposite for accurate photothermal therapy at facile temperature. *Nat Commun* **7**, 10437 (2016).

100 Dong, B. *et al.* Temperature sensing and in vivo imaging by molybdenum sensitized visible upconversion luminescence of rare-earth oxides. *Adv Mater* **24**, 1987-1993 (2012).

101 Kewell, A. K., Reed, G. T., Namavar, F. Integrated temperature sensor in Er-doped silicon. *Sensors and Actuators A* **65**, 5 (1998).

102 Xu, W., Zhang, Z., Cao, W. Excellent optical thermometry based on short-wavelength upconversion emissions in Er^{3+}/Yb^{3+} codoped $CaWO_4$. *OPTICS LETTERS* **37**, 3 (2012).

103 Okabe, K. *et al.* Intracellular temperature mapping with a fluorescent polymeric thermometer and fluorescence lifetime imaging microscopy. *Nat Commun* **3**, 705 (2012).

104 Williams, C. C., Wickramasinghe, H. K. Scanning Thermal Profiler. *Microelectronic Engineering* **5**, 5 (1986).

105 Sadat, S., Tan, A., Chua, Y. J., Reddy, P. Nanoscale thermometry using point contact thermocouples. *Nano Lett* **10**, 2613-2617 (2010).

106 Wagner, T., Menges, F., Riel, H., Gotsmann, B., Stemmer, A. Combined scanning probe electronic and thermal characterization of an indium arsenide nanowire. *Beilstein J Nanotechnol* **9**, 129-136 (2018).

107 Majumdar, A. Scanning thermal microscopy. *Annual Review of Materials Science* **29**, 81 (1999).

108 Majumdar, A., Carrejo, J. P., Lai, J. Thermal imaging using the atomic force microscope. *Applied Physics Letters* **62**, 2501-2503 (1993).

109 Yue, Y., Wang, X. Nanoscale thermal probing. *Nano Rev* **3**, 11586 (2012).

110 Sadat, S., Meyhofer, E., Reddy, P. High resolution resistive thermometry for micro/nanoscale measurements. *Rev Sci Instrum* **83**, 084902 (2012).

111 Lefèvre, S., Volz, S. 3ω-scanning thermal microscope. *Review of Scientific Instruments* **76** (2005).

112 Drechsler, U. *et al.* Cantilevers with nano-heaters for thermomechanical storage application. *Microelectronic Engineering* **67-68**, 397-404 (2003).

113 Menges, F., Riel, H., Stemmer, A., Dimitrakopoulos, C., Gotsmann, B. Thermal transport into graphene through nanoscopic contacts. *Phys Rev Lett* **111**, 205901 (2013).

114 Zohar, O., *et al*. Thermal imaging of receptor-activated heat production in single cells. *Biophysical Journal* **74**, 8 (1998).

115 Michaelson, J. S. *et al.* Gauging the impact of breast carcinoma screening in terms of tumor size and death rate. *Cancer* **98**, 2114-2124 (2003).

116 Somera, G. N. Proteins and temperature. *Annual Review of Physiology* **57**, 26 (1995).

117 El-Sayed, I. H., Huang, X., El-Sayed, M. A. Selective laser photo-thermal therapy of epithelial carcinoma using anti-EGFR antibody conjugated gold nanoparticles. *Cancer Lett* **239**, 129-135 (2006).

118 Tian, Q. *et al.* Sub-10 nm Fe_3O_4@$Cu_{2-x}S$ core-shell nanoparticles for dual-modal imaging and photothermal therapy. *J Am Chem Soc* **135**, 8571-8577 (2013).

119 Tian, Q. *et al.* Hydrophilic flower-like CuS superstructures as an efficient 980 nm laser-driven photothermal agent for ablation of cancer cells. *Adv Mater* **23**, 3542-3547 (2011).

120 Wang, Y. *et al.* Graphene oxide covalently grafted upconversion nanoparticles for combined NIR mediated imaging and photothermal/photodynamic cancer therapy. *Biomaterials* **34**, 7715-7724 (2013).

121 Xiao, Q. *et al.* A core/satellite multifunctional nanotheranostic for in vivo imaging and tumor eradication by radiation/photothermal synergistic therapy. *J Am Chem Soc* **135**, 13041-13048 (2013).

122 Xu, J. *et al.* Near-infrared-triggered photodynamic therapy with multitasking upconversion nanoparticles in combination with checkpoint blockade for immunotherapy of colorectal cancer. *ACS Nano* **11**, 4463-4474 (2017).

123 Cheng, L. *et al.* Multifunctional nanoparticles for upconversion luminescence/MR multimodal imaging and magnetically targeted photothermal therapy. *Biomaterials* **33**, 2215-2222 (2012).

124 Zhang, L., Li, Y., Jin, Z., Chan, K. M., Yu, J. C. Mesoporous carbon/CuS nanocomposites for pH-dependent drug delivery and near-infrared chemo-photothermal therapy. *RSC Advances* **5**, 93226-93233 (2015).

125 Shakouri, A. Nanoscale thermal transport and microrefrigerators on a chip. *Proceedings of the IEEE* **94**, 1613-1638 (2006).

126 Bar-Cohen, A., Wang, P. On-chip hot spot remediation with miniaturized thermoelectric coolers. *Microgravity Science and Technology* **21**, 351-359 (2009).

127 Brites, C. D. *et al.* A luminescent molecular thermometer for long-term absolute temperature measurements at the nanoscale. *Adv Mater* **22**, 4499-4504 (2010).

128 Nenna, G. *et al.* A study on thermal degradation of organic LEDs using IR imaging. *Macromolecular Symposia* **247**, 326-332 (2007).

129 Ashkin, A., Dziedzic, J. M., Yamane, T. Optical trapping and manipulation of single cells using infrared laser beams. *Nature* **330**, 3 (1987).

130 dos Santos, P. V., de Araujo, M. T., Gouveia-Neto, A. S., Medeiros Neto, J. A., Sombra, A. S. B. Optical temperature sensing using upconversion fluorescence emission in Er^{3+}/Yb^{3+}-codoped chalcogenide glass. *Applied Physics Letters* **73**, 578-580 (1998).

131 Debasu, M. L. *et al.* All-in-one optical heater-thermometer nanoplatform operative from 300 to 2000 k based on Er(3+) emission and blackbody radiation. *Adv Mater* **25**, 4868-4874 (2013).

132 Wan, X., Liu, S. Fluorescent water-soluble responsive polymers site-specifically labeled with FRET dyes possessing pH- and thermo-modulated multicolor fluorescence emissions as dual ratiometric probes. *Journal of Materials Chemistry* **21**, 10321 (2011).

133 McCabe, K. M., Lacherndo, E. J., Albino-Flores, I., Sheehan, E., Hernandez, M. LacI(Ts)-regulated expression as an in situ intracellular biomolecular thermometer. *Appl Environ Microbiol* **77**, 2863-2868 (2011).

134 Donner, J. S., Thompson, S. A., Kreuzer, M. P., Baffou, G., Quidant, R. Mapping intracellular temperature using green fluorescent protein. *Nano Lett* **12**, 2107-2111 (2012).

135 Herrera, A. P., Rodríguez, M., Torres-Lugo, M., Rinaldi, C. Multifunctional magnetite nanoparticles coated with fluorescent thermo-responsive polymeric shells. *Journal of Materials Chemistry* **18**, 855-858 (2008).

136 Chen, C. Y., Chen, C. T. A PNIPAM-based fluorescent nanothermometer with ratiometric readout. *Chem Commun* **47**, 994-996 (2011).

137 Wang, X. D. *et al.* Preparation of reversible colorimetric temperature nanosensors and their application in quantitative two-dimensional thermo-imaging. *Anal Chem* **83**, 2434-2437 (2011).

138 Ye, F. *et al.* Ratiometric temperature sensing with semiconducting polymer dots. *J Am Chem Soc* **133**, 8146-8149 (2011).

139 Huang, H., Delikanli, S., Zeng, H., Ferkey, D. M., Pralle, A. Remote control of ion channels and neurons through magnetic-field heating of nanoparticles. *Nat Nanotechnol* **5**, 602-606 (2010).

140 Gota, C., Uchiyama, S., Yoshihara, T., Tobita, S., Ohwada, T. Temperature-dependent fluorescence lifetime of a fluorescent polymeric thermometer, poly(N-isopropylacrylamide), labeled by polarity and hydrogen bonding sensitive 4-Sulfamoyl-7-aminobenzofurazan. *The Journal of Physical Chemistry B* **112**, 8 (2008).

141 Bland, J. M., Altman, D. G. Statistical methods for assessing agreement between two methods of clinical measurement. *Lancet* **1**, 4 (1986).

142 Arai, S., Lee, S. C., Zhai, D., Suzuki, M., Chang, Y. T. A molecular fluorescent probe for targeted visualization of temperature at the endoplasmic reticulum. *Sci Rep* **4**, 6701 (2014).

143 Itoh, H. *et al.* Direct organelle thermometry with fluorescence lifetime imaging microscopy in single myotubes. *Chem Commun* **52**, 4458-4461 (2016).

144 Arai, S. *et al.* Mitochondria-targeted fluorescent thermometer monitors intracellular temperature gradient. *Chem Commun* **51**, 8044-8047 (2015).

145 Tsuji, T., Yoshida, S., Yoshida, A., Uchiyama, S. Cationic fluorescent polymeric thermometers with the ability to enter yeast and mammalian cells for practical intracellular temperature measurements. *Anal Chem* **85**, 9815-9823 (2013).

146 Hayashi, T., Fukuda, N., Uchiyama, S., Inada, N. A cell-permeable fluorescent polymeric thermometer for intracellular temperature mapping in mammalian cell lines. *PLoS One* **10**, e0117677 (2015).

147 Wang, Z. *et al.* Preparation of a magnetofluorescent nano-thermometer and its targeted temperature sensing applications in living cells. *Talanta* **131**, 259-265 (2015).

148 Liu, H. *et al.* Intracellular temperature sensing: an ultra-bright luminescent nanothermometer with non-sensitivity to pH and ionic strength. *Sci Rep* **5**, 14879 (2015).

149 Haro-Gonzalez, P. *et al.* Quantum dot-based thermal spectroscopy and imaging of optically trapped microspheres and single cells. *Small* **9**, 2162-2170 (2013).

150 Maestro, L. M. *et al.* Heating efficiency of multi-walled carbon nanotubes in the first and second biological windows. *Nanoscale* **5**, 7882-7889 (2013).

151 Rodriguez-Sevilla, P. *et al.* Thermal scanning at the cellular level by an optically trapped upconverting fluorescent particle. *Adv Mater* **28**, 2421-2426 (2016).

152 Singh, S. K., Kumar, K. & Rai, S. B. Er^{3+}/Yb^{3+} codoped Gd_2O_3 nano-phosphor for optical thermometry. *Sensors and Actuators A: Physical* **149**, 16-20 (2009).

153 Wang, C., Ling, L., Yao, Y., Song, Q. One-step synthesis of fluorescent smart thermo-responsive copper clusters: A potential nanothermometer in living cells. *Nano Research* **8**, 1975-1986 (2015).

154 Donner, J. S., *et al*. Imaging of plasmonic heating in a living organism. *ACS Nano* **7**, 7 (2013).

155 Arai, S. *et al.* Micro-thermography in millimeter-scale animals by using orally-dosed fluorescent nanoparticle thermosensors. *Analyst* **140**, 7534-7539 (2015).

156 Ha, S. T., Shen, C., Zhang, J., Xiong, Q. Laser cooling of organic–inorganic lead halide perovskites. *Nature Photonics* **10**, 115-121 (2015).

157 Anishur Rahman, A. T. M., Barker, P. F. Laser refrigeration, alignment and rotation of levitated Yb^{3+}:YLF nanocrystals. *Nature Photonics* **11**, 634-638 (2017).

158 Dudovich, N., Oron, D., Silberberg, Y. Single-pulse coherently controlled nonlinear Raman spectroscopy and microscopy. *Nature* **418**, 3 (2002).

159 Zhang, Y. *et al.* Coherent anti-Stokes Raman scattering with single-molecule sensitivity using a plasmonic Fano resonance. *Nat Commun* **5**, 4424 (2014).

160 Shan, J., Uddi, M., Yao, N., Ju, Y. Anomalous raman scattering of colloidal Yb^{3+},Er^{3+} codoped $NaYF_4$ nanophosphors and dynamic probing of the upconversion luminescence. *Advanced Functional Materials* **20**, 3530-3537 (2010).

161 Zhou, B., Shi, B., Jin, D., Liu, X. Controlling upconversion nanocrystals for emerging applications. *Nat Nanotechnol* **10**, 924-936 (2015).

162 Brites, C. D. *et al.* Instantaneous ballistic velocity of suspended Brownian nanocrystals measured by upconversion nanothermometry. *Nat Nanotechnol* **11**, 851-856 (2016).

163 Liu, Q. *et al.* Single upconversion nanoparticle imaging at sub-10 W cm^{-2} irradiance. *Nature Photonics* **12**, 548-553 (2018).

164 Smith, A. M., Mancini, M. C., Nie, S. Bioimaging: second window for in vivo imaging. *Nat Nanotechnol* **4**, 710-711 (2009).

165 Marciniak, L., Bednarkiewicz, A., Kowalska, D., Strek, W. A new generation of highly sensitive luminescent thermometers operating in the optical window of biological tissues. *Journal of Materials Chemistry C* **4**, 5559-5563 (2016).

166 Marciniak, L. *et al.* Near infrared absorbing near infrared emitting highly-sensitive luminescent nanothermometer based on Nd^{3+} to Yb^{3+} energy transfer. *Phys Chem Chem Phys* **17**, 24315-24321 (2015).

167 Fan, Y., *et al*. Lifetime-engineered NIR-II nanoparticles unlock multiplexed in vivo imaging. *Nature Nanotechnology* **13**, 6 (2018).

168 Deutsch, Z., Neeman, L., Oron, D. Luminescence upconversion in colloidal double quantum dots. *Nat Nanotechnol* **8**, 649-653 (2013).

169 Wang, Q. *et al.* Photoluminescence upconversion by defects in hexagonal boron nitride. *Nano Lett* **18**, 6898-6905 (2018).

170 Akizuki, N., Aota, S., Mouri, S., Matsuda, K., Miyauchi, Y. Efficient near-infrared up-conversion photoluminescence in carbon nanotubes. *Nature Communications* **6:8920**, 6 (2015).

171 Roman, B. J., Sheldon, M. The role of mid-gap states in all-inorganic $CsPbBr_3$ nanoparticle one photon up-conversion. *Chem Commun* **54**, 6851-6854 (2018).

172 Morozov, Y. V., *et al*. Defect-mediated CdS nanobelt photoluminescence up-conversion. *Journal of Physical Chemistry C* **121**, 10 (2017).

173 Auzel, F. Upconversion and anti-Stokes processes with f and d Ions in solids. *Chemical Reviews* **104**, 36 (2004).

174 Heer, S., Kömpe, K., Güdel, H. U., Haase, M. Highly efficient multicolour upconversion emission in transparent colloids of lanthanide-doped $NaYF_4$ nanocrystals. *Advanced Materials* **16**, 2102-2105 (2004).

175 Wang, F. *et al.* Microscopic inspection and tracking of single upconversion nanoparticles in living cells. *Light: Science & Applications* **7**, 18007 (2018).

176 Chan, M. H. *et al.* Nanobubble-embedded inorganic 808 nm excited upconversion nanocomposites for tumor multiple imaging and treatment. *Chem Sci* **9**, 3141-3151 (2018).

177 Reddy, K. L. *et al.* Amine-functionalized, porous silica-coated $NaYF_4$:Yb/Er upconversion nanophosphors for efficient delivery of doxorubicin and curcumin. *Mater Sci Eng C Mater Biol Appl* **96**, 86-95 (2019).

178 Liu, Y., Meng, X., Bu, W. Upconversion-based photodynamic cancer therapy. *Coordination Chemistry Reviews* **379**, 82-98 (2019).

179 Lai, J., Zhang, Y., Pasquale, N., Lee, K. B. An upconversion nanoparticle with orthogonal emissions using dual NIR excitations for controlled two-way photoswitching. *Angew Chem Int Ed Engl* **53**, 14419-14423 (2014).

180 Lee, J. *et al.* Universal process-inert encoding architecture for polymer microparticles. *Nat Mater* **13**, 524-529 (2014).

181 You, M. *et al.* Three-dimensional quick response code based on inkjet printing of upconversion fluorescent nanoparticles for drug anti-counterfeiting. *Nanoscale* **8**, 10096-10104 (2016).

182 Zhang, Y. *et al.* Multicolor barcoding in a single upconversion crystal. *J Am Chem Soc* **136**, 4893-4896 (2014).

183 Chen, X. *et al.* Confining energy migration in upconversion nanoparticles towards deep ultraviolet lasing. *Nat Commun* **7**, 10304 (2016).

184 Fernandez-Bravo, A. *et al.* Continuous-wave upconverting nanoparticle microlasers. *Nat Nanotechnol* **13**, 572-577 (2018).

185 Yang, Y. *et al.* Hydrothermal synthesis of $NaLuF_4$: Sm,Yb,Tm nanoparticles and their application in dual-modality upconversion luminescence and SPECT bioimaging. *Biomaterials* **34**, 774-783 (2013).

186 Deng, R. *et al.* Temporal full-colour tuning through non-steady-state upconversion. *Nat Nanotechnol* **10**, 237-242 (2015).

187 Lu, Y. *et al.* Tunable lifetime multiplexing using luminescent nanocrystals. *Nature Photonics* **8**, 32-36 (2013).

188 He, M. *et al.* Dual phase-controlled synthesis of uniform lanthanide-doped $NaGdF_4$ upconversion nanocrystals via an OA/ionic liquid two-phase system for in vivo dual-modality imaging. *Advanced Functional Materials* **21**, 4470-4477 (2011).

189 Hou Y., *et al*. $NaGdF_4$ nanoparticle-based molecular probes for magnetic resonance imaging of intraperitoneal tumor xenografts in vivo. *ACS Nano* **7**, 9 (2013).

190 Johnson, N. J. J., Oakden, W., Stanisz, G. J., Scott Prosser, R., van Veggel, F. C. J. M. Size-tunable, ultrasmall $NaGdF_4$ nanoparticles: Insights into their T_1 MRI contrast enhancement. *Chemistry of Materials* **23**, 3714-3722 (2011).

191 Zhao, S. N. *et al.* Lanthanide ion codoped emitters for tailoring emission trajectory and temperature sensing. *Advanced Functional Materials* **25**, 1463-1469 (2015).

192 Fischer, L. H., Harms, G. S., Wolfbeis, O. S. Upconverting nanoparticles for nanoscale thermometry. *Angew Chem Int Ed Engl* **50**, 4546-4551 (2011).

193 Mi, C., Wu, J., Yang, Y., Han, B., Wei, J. Efficient upconversion luminescence from $Ba_5Gd_8Zn_4O_{21}$:Yb^{3+}, Er^{3+} based on a demonstrated cross-relaxation process. *Sci Rep* **6**, 22545 (2016).

194 Ye, S., Xiao, P., Liao, H., Li, S., Wang, D. Fast synthesis of sub-10 nm β-$NaYF_4$:Yb^{3+}, Er^{3+}@$NaYF_4$ core-shell upconversion nanocrystals mediated by oleate ligands. *Materials Research Bulletin* **103**, 279-284 (2018).

195 Lim, S. F., Ryu W. S., Austin, R. H. Particle size dependence of the dynamic photophysical properties of $NaYF_4$:Yb, Er nanocrystals. *Optics Express* **18**, 17 (2009).

196 Guo, Y., Wang, D., He, Y. Fabrication of highly porous Y_2O_3:Ho,Yb ceramic and its thermometric applications. *Journal of Alloys and Compounds* **741**, 1158-1162 (2018).

197 Cao, J., Zhang, J., Li, X. Upconversion luminescence of $Ba_3La(PO_4)_3$:Yb^{3+}-Er^{3+}/Tm^{3+} phosphors for optimal temperature sensing. *Appl Opt* **57**, 1345-1350 (2018).

198 Sedlmeier, A., Achatz, D. E., Fischer, L. H., Gorris, H. H., Wolfbeis, O. S. Photon upconverting nanoparticles for luminescent sensing of temperature. *Nanoscale* **4**, 7090-7096 (2012).

199 T. Barilero, T. L. S., C. Gosse, L. Jullien. Fluorescent Thermometers for dual-emission-wavelength measurements: molecular engineering and application to thermal imaging in a microsystem. *Analytical Chemistry* **81**, 3 (2009).

200 Nirmala Chandrasekharan, L. A. K. A dual fluorescence temperature sensor based on perylene/exciplex interconversion. *Journal of the American Chemical Society* **123**, 2 (2001).

201 Lupton, J. M. A molecular thermometer based on long-lived emission from platinum octaethyl porphyrin. *Applied Physics Letters* **81**, 2478-2480 (2002).

202 Jung, W., Kim, Y. W., Yim, D., Yoo, J. Y. Microscale surface thermometry using SU8/Rhodamine-B thin layer. *Sensors and Actuators A: Physical* **171**, 228-232 (2011).

203 Jorge, P., Martins, M. A., Trindade, T., Santos, J. L., Farahi, F. Optical fiber sensing using quantum dots. *Sensors* **7**, 46 (2007).

204 Vlaskin, V. A., Janssen, N., van Rijssel, J., Beaulac, R., Gamelin, D. R. Tunable dual emission in doped semiconductor nanocrystals. *Nano Lett* **10**, 3670-3674 (2010).

205 Peng, H. *et al.* Luminescent europium(III) nanoparticles for sensing and imaging of temperature in the physiological range. *Adv Mater* **22**, 716-719 (2010).

206 Fiorenzo Vetrone, R. N., *et al*. Temperature sensing using fluorescent nanothermometers. *ACS Nano* **4**, 5 (2010).

207 Saidi, E. *et al.* Scanning thermal imaging by near-field fluorescence spectroscopy. *Nanotechnology* **20**, 115703 (2009).

208 Pietsch, C., Vollrath, A., Hoogenboom, R., Schubert, U. S. A fluorescent thermometer based on a pyrene-labeled thermoresponsive polymer. *Sensors (Basel)* **10**, 7979-7990 (2010).

209 Borisov, S. M., Wolfbeis, O. S. Temperature-sensitive europium(III) probes and their use for simultaneous luminescent sensing of temperature and oxygen. *Analytical Chemistry* **78**, 8 (2006).

210 Tessier, G., Bardoux, M., Boué, C., Filloy, C., Fournier, D. Back side thermal imaging of integrated circuits at high spatial resolution. *Applied Physics Letters* **90**, 171112 (2007).

211 Baleizao, C. *et al.* An optical thermometer based on the delayed fluorescence of C_{70}. *Chemistry* **13**, 3643-3651 (2007).

212 Dong, B. *et al.* Size dependence of the upconverted luminescence of $NaYF_4$:Er,Yb microspheres for use in ratiometric thermometry. *Phys Chem Chem Phys* **16**, 20009-20012 (2014).

213 Li, D., Shao, Q., Dong, Y., Jiang, J. Anomalous temperature-dependent upconversion luminescence of small-sized $NaYF_4$:Yb^{3+}, Er^{3+} nanoparticles. *The Journal of Physical Chemistry C* **118**, 22807-22813 (2014).

CHAPTER 2

Materials and methods

In this chapter, the synthetic methods of the studied RE doped luminescent nanocrystals in this thesis and the characterisation methods used are introduced. The synthetic methods for different morphologies including core nanoparticle, core-shell nanoparticle and multi-section nanorod are included, and the characterisation methods including TEM, Fourier transform infrared (FTIR), photoluminescence spectroscopy, time-resolved photoluminescence lifetime determination and single nanoparticle microscopy imaging are described together with the commercial instruments and home-built optical systems used.

2.1 Chemicals and instruments for material synthesis

Table 2.1 The chemicals and reagents used for material synthesis.

Name	Specification	CAS number	Manufacturer
Yttrium(III) chloride hexahydrate ($YCl_3 \cdot 6H_2O$)	99.99% trace metals basis	10025-94-2	Sigma-Aldrich (Australia)
Ytterbium(III) chloride hexahydrate ($YbCl_3 \cdot 6H_2O$)	99.998% trace metals basis	10035-01-5	Sigma-Aldrich (Australia)
Thulium(III) chloride hexahydrate ($TmCl_3 \cdot 6H_2O$)	99.99% trace metals basis	1331-74-4	Sigma-Aldrich (Australia)
Erbium(III) chloride hexahydrate ($ErCl_3 \cdot 6H_2O$)	99.995% trace metals basis	10025-75-9	Sigma-Aldrich (Australia)
Neodymium(III) chloride hexahydrate ($NdCl_3 \cdot 6H_2O$)	99.995% trace metals basis	13477-89-9	Sigma-Aldrich (Australia)

Sodium hydroxide (NaOH)	Semiconductor grade, 99.99% trace metals basis	1310-73-2	Sigma-Aldrich (Australia)
Potassium hydroxide (KOH)	Semiconductor grade, 99.99% trace metals basis	1310-58-3	Sigma-Aldrich (Australia)
Ammonium fluoride (NH_4F)	≥99.99% trace metals basis	12125-01-8	Sigma-Aldrich (Australia)
Oleic Acid (OA)	Technical grade, 90%	112-80-1	Sigma-Aldrich (Australia)
1-Octadecene (ODE)	Technical grade, 90%	112-88-9	Sigma-Aldrich (Australia)
Ethanol	Undenatured, 100%, AR	64-17-5	Chem-Supply (Australia)
Methanol	≥99.9%, HPLC	67-56-1	Chem-Supply (Australia)
Cyclohexane	≥99.9%, HPLC	110-82-7	Chem-Supply (Australia)
Hydrochloric acid (HCl)	1.0 ± 0.005 mol/L (20 °C)	7647-01-0	Chem-Supply (Australia)

Table 2.2 The instruments with specifications used for material synthesis.

Instrument/Equipment	**Property**	**Manufacturer**
Magnetic stirrer	0-1800 rpm	Labquip (Australia)
Heating mantle	Range room temperature (25-30 ℃) to 400 ℃	Labquip (Australia)
Temperature controller	Range room temperature to 400 ℃	Labquip (Australia)

Three-neck round-bottom flask	50 mL, 100 mL	Synthware (China)
Flow control adapter	19/22	Synthware (China)
Teflon-coated, elliptical RE extra power stir bars	15 × 10 mm	Sigma-Aldrich (Australia)
Micropipettes	ranges: 10–100 µL , 100–1000 µL and 500–5000 µL	Eppendorf (Germany)
Centrifuge	Centrifuge 5424 Centrifuge 5804	Eppendorf (Germany)
Vortex mixer	LSE	Corning (Australia)
Ultrasonic cleaner	Commercial Benchtop Cleaners (FXP) 2.7 Litre	Unisonics (Australia)
Laboratory balance	SJF2104 (0.1 mg)	ProSciTech (Australia)

2.2 Synthesis of RE doped nanoparticles

2.2.1 General synthesis methods

To synthesise RE doped nanoparticles with high uniformity and dispersibility, three commonly used wet chemical methods are reported in the literature, namely hydrothermal, thermal decomposition and co-precipitation methods[1]. All these synthesis methods can produce high-quality nanoparticles with uniform size and morphology via accurate high temperature, reaction time and the control of other reaction conditions. Nonetheless, there are great differences among the processes involved in these three techniques.

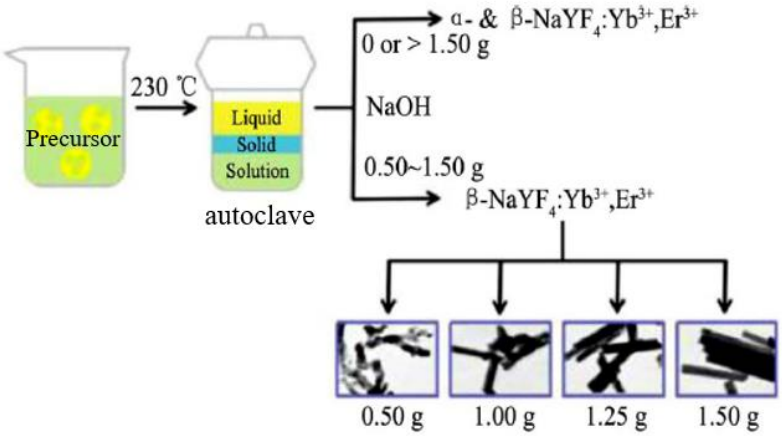

Figure 2.1 Schematic illustration of the hydrothermal synthesis of $NaYF_4:Yb^{3+}$, Er^{3+} nanocrystals[2].

Among the three wet chemical synthesis methods, hydrothermal synthesis is the most convenient method with few operation steps[2-4] (Figure 2.1). The solutions of reactants are placed in a Teflon bladder inside a stainless-steel autoclave where high temperature and high pressure are maintained for the growth of nanocrystals. The stainless-steel reactor can be kept in a high temperature autoclave without other operations before obtaining the sample by a precipitation reaction. Different materials with high crystallinity can be prepared using this method. However, the hydrothermal approach has some disadvantages. First, such a high-pressure reaction at hundreds of centigrade degrees may lead to potential hazard caused by the instability of the autoclave. Second, compared to the other two methods, the hydrothermal method is not promising for sample size control, as the reaction occurs in a sealed vessel where the exact pressure and temperature cannot be monitored. Thus, it is difficult to understand the process of crystal growth using this method, and thus make further modifications for improvement.

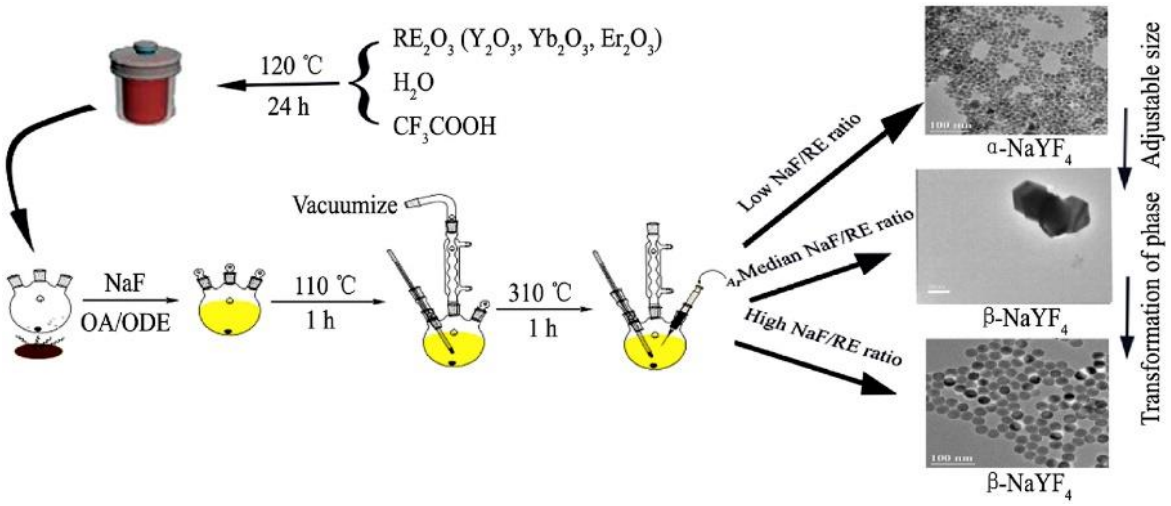

Figure 2.2 Schematic illustration of the thermal decomposition synthesis of $NaYF_4$:Yb^{3+}, Er^{3+} nanocrystals[5].

The thermal decomposition method is based on the decomposition of the organometallic precursors in an anaerobic inert environment with high temperature[5,6] (Figure 2.2). Different from the hydrothermal and co-precipitation methods, the most commonly used RE^{3+}-based precursors in this method are trifluoroacetate. The reaction solvent contains octadecene (ODE) as the high boiling-point organic solvent and oleic acid (OA) as the surfactant, which is similar to the co-precipitation method. The surfactant influences the size and shape of the nanocrystal growth. During the entire reaction, the temperature, heating rate and heating time of the reaction flask can be well controlled with a heating jacket. Thus, the nanocrystals with a desired size and shape can be obtained by the thermal decomposition synthesis method. However, the thermal decomposition synthesis of RE doped materials leads to toxic release because of the trifluoroacetate used. Varieties of toxic fluorinated and oxyfluorinated carbon species are formed from the thermal decomposition, which are not environmentally friendly. Additionally, the operations are more complicated than those of hydrothermal synthesis, including vacuuming as a pre-requisite for an oxygen-free environment.

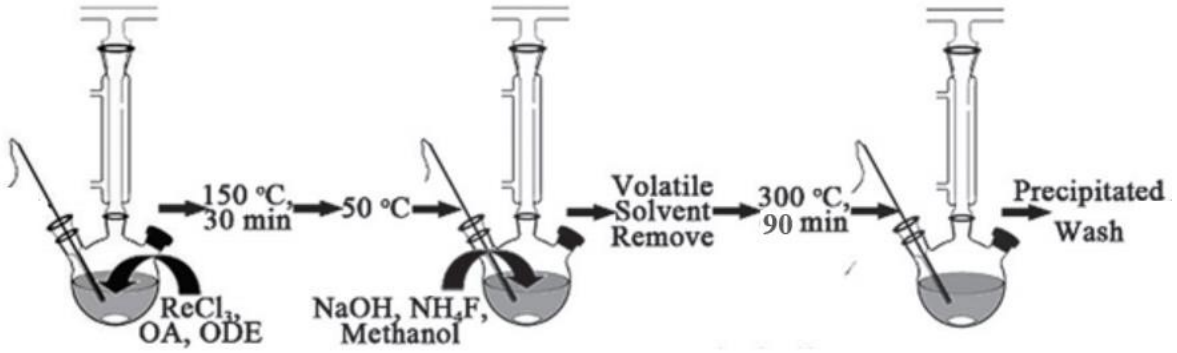

Figure 2.3 Schematic illustration of the co-precipitation synthesis of $NaREF_4$ nanocrystals.

The co-precipitation method is similar to the thermal decomposition method in that it requires an inert anaerobic environment and includes multiple temperature control steps, but it uses RE-based oleates, acetates, chlorides or nitrates instead of trifluoroacetate[7] (Figure 2.3). Thus, the release of toxic fluorinate species that originate from the decomposition of fluoride reactants are greatly reduced. Although different ions have different precipitation rates, this can be coordinated by the use of co-solvents, and the co-precipitation method can take advantage of aqueous or organic solvents. Generally, the reaction in the co-precipitation synthesis includes two main stages, the first stage is the nucleation of the RE doped nanoparticles, which starts at room temperature after the addition of a methanol solution containing Na^+ ions and F^- ions to the heated solution containing trivalent RE ions. When the lattice mismatch among different $NaREF_4$ crystals is negligible, various types of trivalent RE ions can grow into one lattice structure. The second stage starts at a higher temperature up to 300 ℃, where the crystal growth reaches a fast rate. When the temperature is lower than 300 ℃, such as 280 ℃, the NaREF4 nanocrystals will grow into a cubic phase (α phase) and will transfer to a hexagonal phase (β-phase) gradually after the temperature reaches ~300 ℃[4].

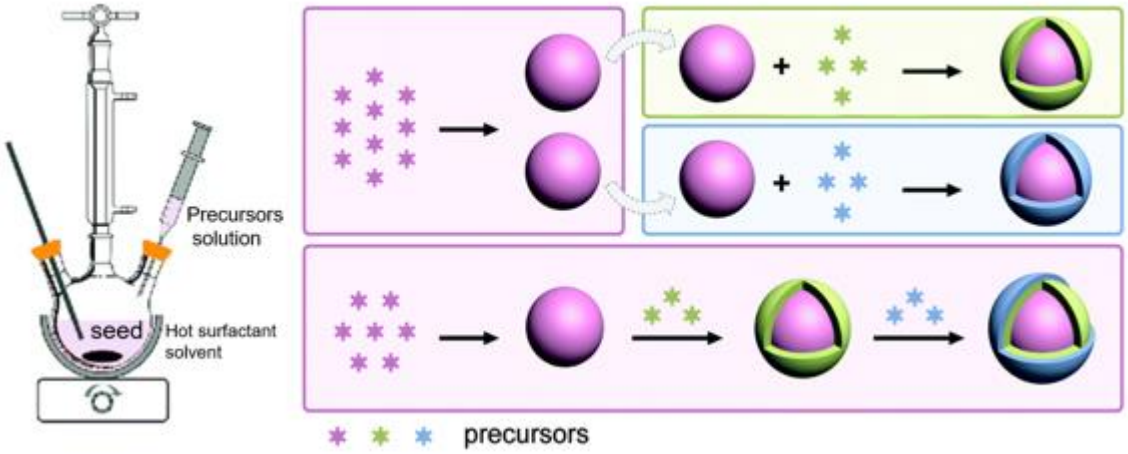

Figure 2.4 Schematic illustration of the epitaxial growth of $NaREF_4$ nanocrystals using the hot-injection process[9].

To control the shape and structure RE doped nanocrystals such as core-shell structure and multi-section nanorod, a second epitaxial growth of the pre-prepared samples is conducted using the hot-injection process[10-13], as shown in Figure 2.4. The general epitaxial growth process uses the prepared nanoparticles as the seed or core nanocrystals. Under a high temperature of approximately 300 ℃, the successive injection of shell precursors will lead to an additional shell on the surface of the core nanocrystal[9]. The injection of precursors starts at a high temperature with a precision-controlled speed, thus the hot-injection method can avoid the second homogeneous nucleation of precursors[14-16]. Based on the amount and size of the used core nanocrystal, the thickness of the shell coated by a specific dosage of precursors can be predicted with a simple volume ratio calculation[13]. Meanwhile, Figure 2.4 indicates multiple layers of the shell can be doped with different emitters or sensitisers. Providing the host materials $NaREF_4$ have no obvious lattice structure mismatch, the epitaxial growth of the additional shell on the core nanocrystal can be accomplished[17], as shown in Table 2.3.

Table 2.3 Summary of the lattice mismatch of the crystallographic parameters c for hexagonal phase $NaREF_4$ crystals. The crystallographic potential for high-quality epitaxial growth decreases from green to red[17].

	$NaLuF_4$	$NaYbF_4$	$NaTmF_4$	$NaErF_4$	**$NaYF_4$**	$NaDyF_4$	$NaPrF_4$	$NaTbF_4$	**$NaGdF_4$**	$NaEuF_4$	$NaSmF_4$	**$NaNdF_4$**	$NaCeF_4$	$NaLaF_4$
$NaLaF_4$	0.109	0.103	0.096	0.089	0.084	0.077	0.082	0.069	0.063	0.056	0.052	0.032	0.012	0.000
$NaCeF_4$	0.095	0.089	0.082	0.076	0.071	0.064	0.069	0.056	0.050	0.043	0.039	0.019	0.000	
$NaNdF_4$	0.075	0.069	0.062	0.056	**0.051**	0.044	0.049	0.037	**0.031**	0.024	0.020	0.000		
$NaSmF_4$	0.054	0.049	0.042	0.036	0.031	0.024	0.029	0.017	0.011	0.004	0.000			
$NaEuF_4$	0.050	0.044	0.037	0.032	0.027	0.020	0.025	0.013	0.007	0.000				
$NaGdF_4$	0.043	0.037	0.031	0.025	**0.020**	0.013	0.018	0.006	0.000					
$NaTbF_4$	0.037	0.031	0.025	0.019	0.014	0.007	0.012	0.000						
$NaPrF_4$	0.024	0.019	0.012	0.007	0.002	0.005	0.000							
$NaDyF_4$	0.029	0.024	0.017	0.011	0.007	0.000								
$NaYF_4$	0.022	0.017	0.010	0.005	0.000									
$NaErF_4$	0.018	0.012	0.006	0.000										
$NaTmF_4$	0.012	0.007	0.000											
$NaYbF_4$	0.005	0.000												
$NaLuF_4$	0.000													

0-0.03 | 0.031-0.05 | 0.051-0.11

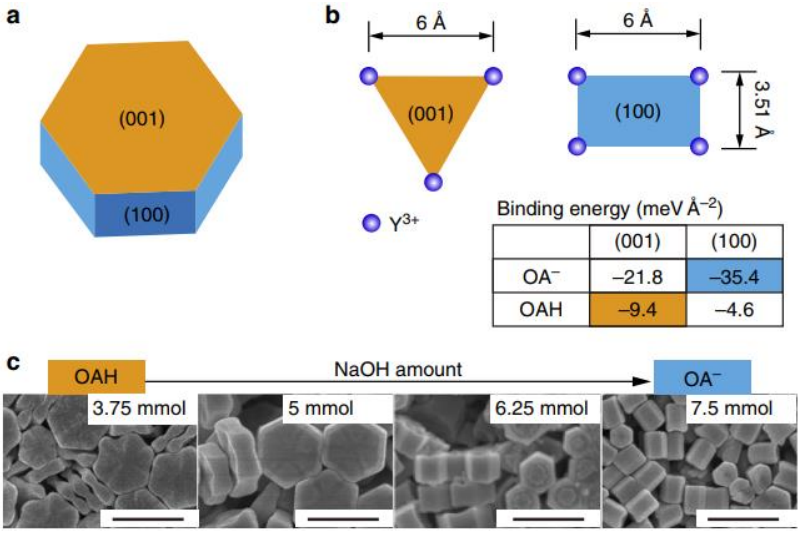

Figure 2.5 Surface anisotropy in β-$NaYF_4$ nanocrystals[17]. (a) The schematic shape of a β-$NaYF_4$ nanocrystal as the core that consists of the (001) facets and identical (100) and (010) facets. (b) The binding energies of OAH and OA^- on the (001) and (100) facets. (c) SEM results of different shaped β-$NaYF_4$ nanocrystals controlled by various amounts of NaOH in synthesis (scale bar is 500 nm).

Additionally, the direction of epitaxial growth on $NaREF_4$ nanocrystals can be fine-tuned by the concentration ratio of OA^- to OAH during the hot-injection synthesis. As proven by Liu *et al*., OA^- and OAH preferentially bind to RE^{3+} ions exposed on different facets of the hexagonal nanocrystal in Figure 2.5[17]. Due to the higher binding energy of OA^- on the (100) facet than that on the (001) facet, higher concentrations of OA^- can promote the epitaxial growth along a longitudinal direction to form a nanorod. However, the higher concentrations of OAH can lead to lateral growth for nanoplate synthesis as OAH has higher binding energy on the (001) facet. Thus, the ratio of OA^-/OAH plays an essential role in determining the epitaxial shell growth of $NaREF_4$ nanocrystals. By increasing the amount of NaOH or KOH used in the synthesis, the reactive solvents with a high ratio of OA^-/OAH will cause the one-dimensional length growth of $NaREF_4$ core nanocrystals to $NaREF_4$ nanorods, with almost no change in width.

In this thesis, the co-precipitation method was chosen for the synthesis of the uniform RE doped nanocrystals, and the hot-injection method was utilised for the epitaxial growth of the prepared $NaREF_4$ nanocrystals.

2.2.2 Synthesis protocols

2.2.2.1 Synthesis of RE doped $NaYF_4$ nanocrystals

In a typical co-precipitation synthesis experiment, taking $NaYF_4$: 20% Yb^{3+}, 6% Nd^{3+} as an example, 0.74 mmol $YCl_3 \cdot 6H_2O$, 0.2 mmol $YbCl_3 \cdot 6H_2O$ and 0.06 mmol $NdCl_3 \cdot 6H_2O$ with a molar ratio of 74:20:6 was added to a 50 mL flask containing 6 mL OA and 15 mL ODE. The mixture was heated to 180 ℃ for 30 min under argon and continuous stirring to obtain a clear solution and was then cooled to room temperature, followed by the addition of 5 mL methanol solution of NH_4F (4 mmol) and NaOH (2.5 mmol). After stirring for 30 min, the temperature was set at 100 ℃ and the solution was heated under argon for 30 min to remove the methanol, and then the solution was further heated to 300 ℃ for 90 min. Finally, the reaction solution

was cooled to room temperature, and the nanoparticles were precipitated by ethanol and washed with cyclohexane, ethanol and methanol three times to obtain the $NaYF_4$: 20% Yb^{3+}, 6% Nd^{3+} nanoparticles.

The studied $NaYF_4$: Yb^{3+}, Tm^{3+}, $NaYF_4$: Yb^{3+}, Er^{3+} and $NaYF_4$: Yb^{3+}, Nd^{3+}, Er^{3+} in the following chapters were all synthesised the same way.

2.2.2.2 Synthesis of ~10 nm RE doped $NaYF_4$: Yb^{3+}, Nd^{3+} nanocrystals

The family of ~10 nm $NaYF_4$: Yb^{3+}, Nd^{3+} nanocrystals with different doping concentrations was synthesised using a similar co-precipitation method. Similar to the above method, a mixture of $YCl_3 \cdot 6H_2O$, $YbCl_3 \cdot 6H_2O$ and $NdCl_3 \cdot 6H_2O$ with a suitable molar ratio, 6 mL OA and 15 mL ODE was heated to 180 ℃ under argon for 30 min and then cooled to room temperature. Then, 8 mL of methanol solution containing a higher dosage of 4 mmol NaOH was added to the mixture followed by 15 min of stirring. By heating the solution to 100 °C for 15 min, the methanol was removed under argon. Again, the mixture was cooled to room temperature and a 10 mL methanol solution of 4 mmol NH_4F was added to the mixture followed by 30 min stirring. Then, the temperature was set at 100 ℃ and the solution was heated for 30 min to remove the methanol. Next, the solution was heated to 300 ℃ for 40 min. Finally, the reaction solution was cooled to room temperature to obtain the ~10 nm nanocrystals after washing with cyclohexane, ethanol and methanol for three times

2.2.2.3 Epitaxial growth to form core-shell-shell nanocrystals

Epitaxial growth of the nanocrystals basing the hot-injection method first requires the preparation of the shell precursor solution.

In this experiment, $NaYF_4$ and $NaYF_4$: Yb^{3+}, Er^{3+} shell precursors were prepared. Taking the $NaYF_4$ shell precursor as an example, 1.0 mmol $YCl_3 \cdot 6H_2O$ was added to a 50 mL flask

containing 6 mL OA and 15 mL ODE. The mixture was heated to 160 ℃ under argon for 30 min to obtain a clear solution and then cooled to room temperature, followed by the addition of 5 mL methanol solution of NH_4F (4.0 mmol) and NaOH (2.5 mmol). After stirring for 30 min, the temperature was set at 100 ℃ and the solution was heated under argon for 30 min to remove methanol, and then the solution was further heated to 150 ℃ for another 30 min. Finally, the reaction solution was cooled to room temperature as the $NaYF_4$ shell precursors. Similarly, $NaYF_4$: Yb^{3+}, Er^{3+} shell precursors were prepared.

The epitaxial growth of $NaYF_4$: Yb^{3+}, Nd^{3+} nanocrystals to form $NaYF_4$: Yb^{3+}, Nd^{3+}@$NaYF_4$ or $NaYF_4$: Yb^{3+}, Nd^{3+}@$NaYF_4$@ $NaYF_4$: Yb^{3+}, Er^{3+} was realised by the hot-injection method. To determine the concentration of the nanoparticles in cyclohexane, 50 μl cyclohexane solution were dropped on a cover slide with a known weight. After drying by air, the weight of the nanoparticles can be measured by the balance and the concentration of the nanoparticles can be calculated. The amount ratio of the precursors to reagent is calculated by the basic spherical volume calculation for the core-shell structure growth. A total of 0.2 mmol $NaYF_4$: Yb^{3+}, Nd^{3+} core particles in cyclohexane were added to a 50 mL flask containing 4.5 mL OA and 11.5 mL ODE. The mixture was heated to 150 ℃ under argon for 20 min, and then the solution was further heated to 300 ℃ . Subsequently, 5 mL of $NaYF_4$ shell precursors in total were injected into the reaction mixture step-by-step with an injection rate of 0.2 mL every 2 min. After the injection of 5 mL of $NaYF_4$ shell precursors, the reaction solution was ripened at 300 °C for 5 min. Finally, the reaction solution was cooled to room temperature and $NaYF_4$: Yb^{3+}, Nd^{3+}@$NaYF_4$ nanocrystals were precipitated by ethanol and washed with cyclohexane, ethanol and methanol for three times. $NaYF_4$: Yb, Nd^{3+}@$NaYF_4$@ $NaYF_4$: Yb^{3+}, Er^{3+} nanocrystals were prepared by the same method using $NaYF_4$: Yb^{3+}, Nd^{3+}@$NaYF_4$ core particles and $NaYF_4$: Yb^{3+}, Er^{3+} shell precursors.

2.2.2.4 Longitudinal epitaxial growth to form multi-section nanorods

First, $NaYF_4$ and $NaYF_4$: Yb^{3+}, Er^{3+} shell precursors were prepared similarly by the method described above. Taking the $NaYF_4$ shell precursor as an example, 1.0 mmol $YCl_3 \cdot 6H_2O$ was added to a 50 mL flask containing 6 mL OA and 15 mL ODE. The mixture was heated to 160 ℃ under argon for 30 min to obtain a clear solution and then cooled to room temperature, followed by the addition of 5 mL methanol solution of NH_4F (4.0 mmol), NaOH (2.5 mmol) and KOH (2 mmol). After stirring for 30 min, the temperature was set at 100 ℃ and the solution was heated under argon for 30 min to remove the methanol, and then the solution was further heated to 150 ℃ for another 30 min. Finally, the reaction solution was cooled to room temperature as $NaYF_4$ shell precursors.

The longitudinal epitaxial growth of $NaYF_4$: Yb^{3+}, Nd^{3+} nanocrystals to form $NaYF_4$: Yb^{3+}, Nd^{3+}/ $NaYF_4$/ $NaYF_4$: Yb^{3+}, Er^{3+} multi-section nanorods was realised by the hot-injection method. A total of 0.2 mmol $NaYF_4$: Yb^{3+}, Nd^{3+} core particles in cyclohexane, 1.7 mmol NaOH and 1.4 mml KOH in 5 mL methanol were added to a 50 mL flask containing 4.5 mL OA and 11.5 mL ODE to reach a high ratio of OA^-/OAH. The mixture was heated to 150 °C under argon for 20 min, and then the solution was further heated to 300 °C. Subsequently, 3 mL of $NaYF_4$ shell precursors in total were injected into the reaction mixture step-by-step with an injection rate of 0.2 mL every 3 min. After the injection of 3 mL of $NaYF_4$ shell precursors, the reaction solution was ripened at 300 °C for 5 min, then followed by the injection of another 3 mL of $NaYF_4$: Yb^{3+}, Er^{3+} shell precursors with the same injection rate. Finally, the reaction solution was cooled to room temperature and the formed multi-section nanorods were precipitated by ethanol and washed four times with cyclohexane, ethanol and methanol.

2.2.2.5 Surface modification of nanocrystals

The oleate ligand on the surface of $NaYF_4$: Yb^{3+}, Tm^{3+} and $NaYF_4$: Yb^{3+}, Nd^{3+} nanocrystals was removed by a simple acid treatment process[18]. First, 4 mL methanol and 4 mL HCl (0.2 M) were added to the as-prepared OA-capped $NaYF_4$: Yb^{3+}, Nd^{3+} precipitate, then the solution was sonicated for 20 min and collected by centrifugation. For the ~10 nm $NaYF_4$: Yb^{3+}, Nd^{3+} nanocrystals, the solution was sonicated for 40 min to totally remove the oleate ligand. The precipitate was further washed three times with 4 mL ethanol and 4 mL deionised water to obtain the ligand-free nanoparticles.

To prepare of DNA-capped nanoparticles, typically, 50 μ l of 10 mg ml−1 nanoparticle suspension in cyclohexane was put into 400 μ l chloroform. 300 μ l of 5 μ M DNA water solution was added to the nanoparticle suspension. A gentle shake (600 rpm) followed, and after 2 hours the nanoparticles were transferred from chloroform to the water phase.

To prepare citrate-capped nanoparticles, typically, 50 μ l of 10 mg ml−1 nanoparticle suspension in cyclohexane was put into 400 μ l chloroform. 300 μ l as purchased SSC Buffer (20× concentrate, Sigma, SRE0068) was added to the nanoparticle suspension. A gentle shake (600 rpm) followed and, after 2 hours, the nanoparticles were transferred from chloroform to the water phase.

2.3 Characterisation methods and home-built optical instruments

2.3.1 Temperature-dependent spectra measurement

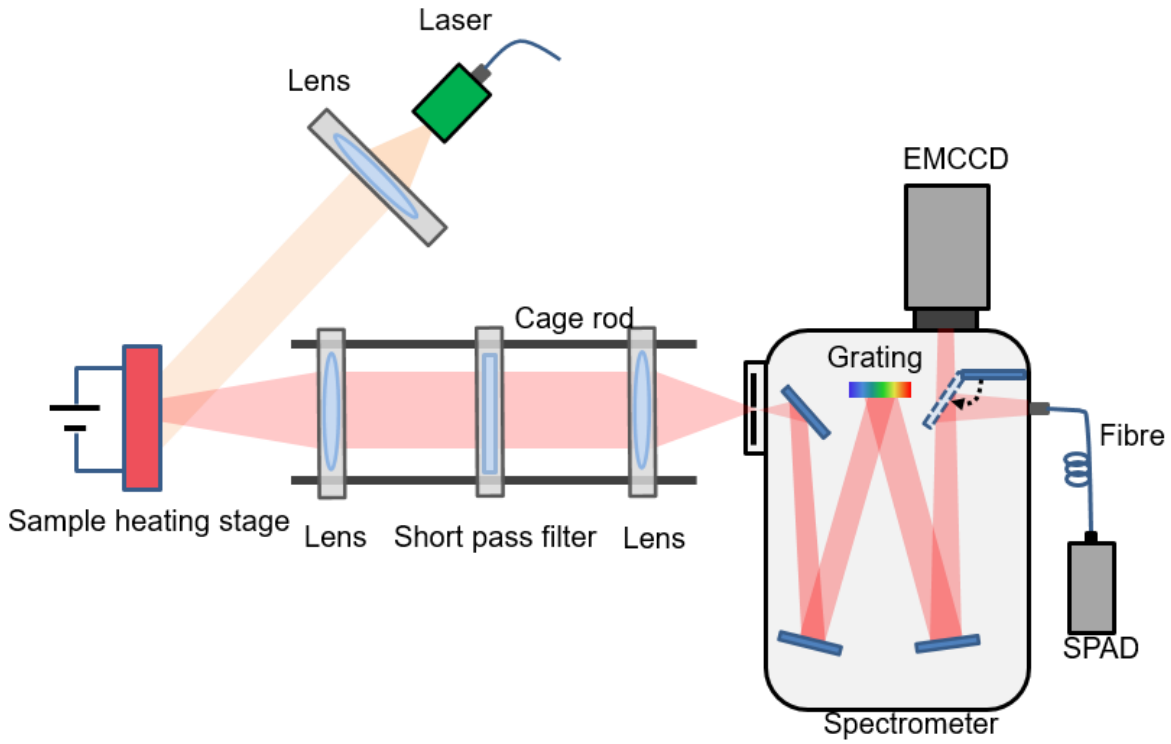

Figure 2.6 Schematic diagram of the home-built spectrometer with a 980 nm laser as the pumping source for temperature-dependent spectra, excitation power dependence and lifetime measurements.

For the optical property characterisation, a photoluminescence spectrometer was built based on a commercial monochromator, the schematic diagram is shown in Figure 2.6. The setup was equipped with a fibre-coupled 980 nm diode laser (BL976-PAG500, controller CLD1015, Thorlabs) with adjustable power up to 500 mW as the pumping source. The excitation power was confirmed by a laser power meter for the excitation power dependence study. To collect the anti-Stokes emission from the sample, a compact lightpath was built up with two convex lens and one short pass filter (FF01-842/SP-25, Semrock) to block the laser, which connected to a commercial spectrometer (Shamrock 193i, Andor) after alignment. With a diffraction grating (groove 150 line/mm, blaze wavelength 500 nm) inside the spectrometer to distinguish

the wavelength, the emission spectra were recorded by a EMCCD camera (iXon Ultra 888, Andor), and the lifetime of the chosen emission band was measured by a gate-mode single-photon avalanche diode (time resolution 22 ns, SPCM-AQRH, Excelitas) with fibre coupled to the second channel of the spectrometer, the pulse width of the laser is 2000 μs.

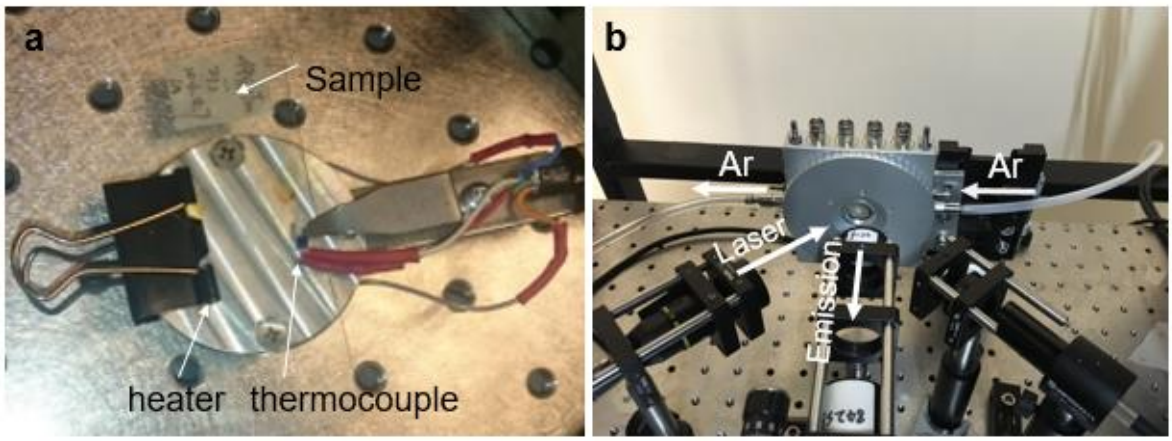

Figure 2.7 The two heating stages used for the temperature-dependent test of the sample in air (a) and in Ar (b).

The temperature-dependent measurements in air were performed using a home-built heating stage (thermocouple TH100PT, heater HT24S, controller TC200, Thorlabs). The temperature could be controlled from room temperature to 453 K with increments down to 0.1 K[19]. For the Ar atmosphere measurements, an additional enclosed heating stage (HFS600E-P, Linkam) was used to block the air, with a test measurement temperature up to 453 K. The two heating stages are shown in Figure 2.7.

Before the experiment, the sample stored in the cyclohexane solution was made into powder by natural air drying, then the sample powder was spread on the surface of the heating stage and covered by a glass cover slip, to prevent the powder from dropping from the stage surface during the measurement period.

2.3.2 Single nanoparticle imaging

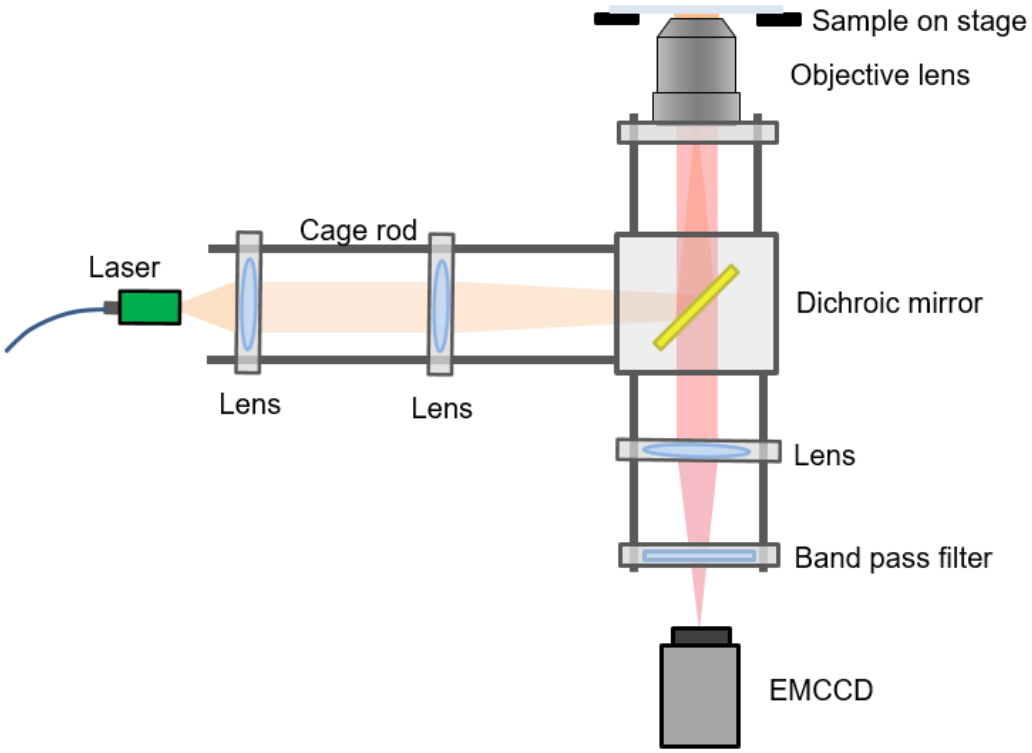

Figure 2.8 Schematic diagram of the home-built wide field microscope with a 980 nm laser as the pumping source for temperature-dependent single nanoparticle imaging and the on-device temperature mapping experiment.

A home-built wide field microscope was assembled for the temperature-dependent single nanoparticle imaging and localised temperature mapping of the micro magnetoresistive sensor. A simplified schematic diagram is shown in Figure 2.8. A fibre-coupled single mode 980 nm diode laser (BL976-PAG900, controller CLD1015, Thorlabs) with adjustable power up to 1 W was used as the pumping source. The laser was focused at the back aperture of the objective lens (Super Plan Fluor 60×/0.7 Nikon objective for single nanoparticle imaging, Plan 20×/0.4 Edmund objective for on-device experiment) to form a large spot size of laser with a diameter of approximately 30 μm or 100 μm at the object plane depending on whether a 60× or 20× objective lens, respectively, was used. The laser spot size was measured by a grid distortion target with 10 μm grid spacing (R1L3S3P, Thorlabs). The luminescence from the sample

passed through a short pass dichroic mirror (T875spxrxt, Chroma) and another short pass filter (FF01-842/SP-25, Semrock) or band pass filter was inserted in the lightpath to block the residual laser and protect the cameras. Additionally, a three-axis flexure stage (MAX311D, Thorlabs) was installed for sample position control.

For the temperature-dependent single nanoparticle imaging, the preparation of the dispersive nanoparticles on a glass slide is quite important[7]. Although the synthesised nanocrystals have excellent dispersibility for the TEM test, it is incomparable for optical microscopy imaging of individual nanoparticle because of the low optical resolution and weak luminescence from one nanoparticle. The nanoparticles must be uniformly dispersed on a glass slide surface with appropriate density, i.e. high concentration will lead to an overlapped image of several nanoparticles and low concentration makes it difficult to locate a promising sample area.

One commonly used method for the preparation of a uniformly dispersed nanoparticles glass slide is described here, and contained three steps. The first step was to wash the glass slide with ethanol and leave it to dry. Second, a cyclohexane solution of synthesised nanoparticles was diluted to an approximate concentration of 0.01 mg/mL empirically. Finally, 20 μL of diluted cyclohexane solution was dropped on a glass cover slip and, after drying, the cover slip was attached on a glass slide by glue with the sample inside.

After the sample preparation, the sample glass slide was attached to the home-built heating stage for temperature control and then the heating stage with the sample was fixed on the three-axis flexure sample stage for imaging area adjustment.

2.3.3 On-device localised temperature measurement

The author acknowledges Dr. Gungun Lin for providing the micro magnetoresistive sensor.

The magnetoresistive sensor was fabricated on a glass substrate of 50 mm × 50 mm in size. First, the geometry of the sensor (10 μm × 100 μm) was defined by patterning the glass

substrate with a photoresist using a maskless direct laser writer. Then, a magnetron sputtering technique was used to deposit $(Co/Cu)_{30}$ multilayer stacks on the patterned substrate, which were coupled at the second antiferromagnetic maximum, followed by lifting off the photoresist. The same lithography step was repeated to pattern the gold electrical contacts (Figure 2.9).

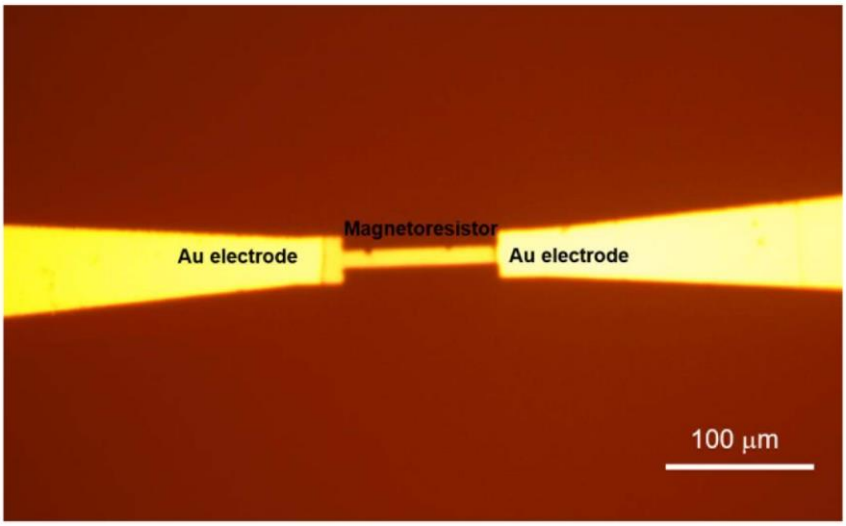

Figure 2.9 The micro magnetoresistive sensor used for on-device localised temperature sensing. The sensor in the middle is 10 μm×100 μm in size whereas the two ends connected to the Au electrodes are much larger.

The temperature measurement on the micro device was also conducted on the home-built wide field imaging microsope. First, the cyclohexane solution of synthesised nanoparticle was dropped on the micro device to form a thin layer of as-prepared nanothermometer, and the magnetoresistive device covered by the nanothermometer layer was powered by a source meter (2612B, Keithley). Then, the device was fixed on the three-axes sample stage for microscopy imaging. By increasing the electric current to 28 mA gradually, the power added on the sensor varied from 0 to 36 mW, which caused the temperature to change owing to the Joule effect. Finally, by taking images with two band pass filters (ET810/90m and ET655/40m, Chroma) the emission intensities of Nd^{3+} and Er^{3+} were recorded to obtain the corresponding temperature.

The calibration curve was measured in a similar way, the sample was spread on a glass slide attached to the heating stage, then the two emission intensities under different temperatures were captured by a EMCCD camera.

2.3.4 Sample morphology characterisation

The morphology of the formed materials was characterised via TEM imaging (Philips CM10 TEM with Olympus Sis Megaview G2 Digital Camera) with an operating voltage of 100 kV. The samples were prepared by placing a drop of a dilute suspension of nanocrystals onto copper grids.

The morphology of the annealed nanocrystal was characterised via scanning electron microscope (SEM) imaging (Supra 55VP, Zeiss) operated at 20.00 kV.

Fourier transform infrared (FTIR) spectra of the OA^--capped and OA^--free nanocrystals were measured on a FTIR spectrometer (Nicolet 6700, Thermo Scientific).

2.4 References

1 Li, X., Zhang, F., Zhao, D. Lab on upconversion nanoparticles: optical properties and applications engineering via designed nanostructure. *Chem Soc Rev* **44**, 1346-1378 (2015).

2 Li, S. *et al.* OH^- ions-controlled synthesis and upconversion luminescence properties of $NaYF_4:Yb^{3+},Er^{3+}$ nanocrystals via oleic acid-assisted hydrothermal process. *Journal of Rare Earths* **35**, 753-760 (2017).

3 Ma, Z. *et al.* Yb^{3+}/Er^{3+} co-doped Lu_2TeO_6 nanophosphors: Hydrothermal synthesis, upconversion luminescence and highly sensitive temperature sensing performance. *Journal of Alloys and Compounds* **772**, 525-531 (2019).

4 Liu, Q. *et al.* Multifunctional β-$NaGdF_4$: Ln^{3+} (Ln=Yb/Er/Eu) phosphors synthesized by l-arginine assisted hydrothermal method and their multicolor tunable luminescence. *Materials Research Bulletin* **110**, 141-148 (2019).

5 Liu, S. *et al.* Size, phase-controlled synthesis, the nucleation and growth mechanisms of NaYF4:Yb/Er nanocrystals. *Journal of Rare Earths* **36**, 1060-1066 (2018).

6 Wang, F., Deng, R., Liu, X. Preparation of core-shell $NaGdF_4$ nanoparticles doped with luminescent lanthanide ions to be used as upconversion-based probes. *Nat Protoc* **9**, 1634-1644 (2014).

7 Ma, C. *et al.* Optimal sensitizer concentration in single upconversion nanocrystals. *Nano Lett* **17**, 2858-2864 (2017).

8 Chen, G., *et al*. (α-$NaYbF_4:Tm^{3+}$)/CaF_2 core/shell nanoparticles with efficient near-infrared to near-infrared upconversion for high-contrast deep tissue bioimaging. *ACS Nano* **6**, 8 (2012).

9 Chen, X., Peng, D., Ju, Q., Wang, F. Photon upconversion in core-shell nanoparticles. *Chem Soc Rev* **44**, 1318-1330 (2015).

10 Yi, G. S., Chow, G. M. Water-soluble $NaYF_4$:Yb,Er(Tm)/$NaYF_4$/polymer core/shell/shell nanoparticles with significant enhancement of upconversion fluorescence. *Chemistry of Materials* **19**, 3 (2007).

11 Wang, F. *et al.* Tuning upconversion through energy migration in core-shell nanoparticles. *Nat Mater* **10**, 968-973 (2011).

12 Li, X. *et al.* Successive layer-by-layer strategy for multi-shell epitaxial growth: shell thickness and doping position dependence in upconverting optical properties. *Chemistry of Materials* **25**, 106-112 (2012).

13 Huang, P. *et al.* Lanthanide-doped $LiLuF_4$ upconversion nanoprobes for the detection of disease biomarkers. *Angew Chem Int Ed Engl* **53**, 1252-1257 (2014).

14 Qian, H., Zhang, Y. Synthesis of hexagonal-phase core-shell $NaYF_4$ nanocrystals with tunable upconversion fluorescence. *Langmuir* **24**, 3 (2008).

15 Mai, H., Zhang, Y., Sun, L., Yan, C. Highly efficient multicolor up-conversion emissions and their mechanisms of monodisperse $NaYF_4$:Yb,Er core and core/shell-structured nanocrystals. *The Journal of Physical Chemistry C* **111**, 9 (2007).

16 Johnson, N. J. J., van Veggel, F. C. J. M. Sodium lanthanide fluoride core-shell nanocrystals: A general perspective on epitaxial shell growth. *Nano Research* **6**, 547-561 (2013).

17 Liu, D. *et al.* Three-dimensional controlled growth of monodisperse sub-50 nm heterogeneous nanocrystals. *Nat Commun* **7**, 10254 (2016).

18 Han, S. *et al.* Multicolour synthesis in lanthanide-doped nanocrystals through cation exchange in water. *Nat Commun* **7**, 13059 (2016).

19 Zhou, J. *et al.* Activation of the surface dark-layer to enhance upconversion in a thermal field. *Nature Photonics* **12**, 154-158 (2018).

CHAPTER 3

Surface phonon assistance in RE doped anti-Stokes nanocrystals

In this result chapter, the main task was the development of thermally enhanced RE doped anti-Stokes emission materials. Thermal quenching at high temperatures always leads to a low luminescence efficiency in phosphors; therefore, in a broad sense, finding an approach to conquer this thermal quenching is necessary to improve the performance of luminescent nanothermometers. Thus, several research studies on RE doped anti-Stokes materials have been performed against thermal quenching. All these studies observed the phenomenon of luminescence enhancement under increasing temperature; however, the physical mechanisms behind this novel thermal induced emission enhancement is still controversial. With a logical experimental design, for the first time we have shown that thermal enhancement occurs in RE doped anti-Stokes materials and can be explained by the surface ligand assistance. By developing these types of thermal intensified luminescence materials, it builds up a basic foundation for the creation of high-sensitive nanothermometers with a large dynamic working range.

3.1 Introduction

During the energy transfer process of luminescent materials, radiative energy transfer is always accompanied with non-radiative decay, and the environment temperature will influence both. Commonly, thermal quenching appears in bulk materials that have a large size because the increased activity of phonons at high temperature will strengthen the non-radiative relaxation

instead of the radiative relaxation[1-3]. When the material size decreases to the nanoscale, the high surface-to-volume ratio determines the importance of the surface and it may influence the temperature-dependent properties. Therefore, studies on the nanocrystals instead of on large sized materials are helpful for further understanding of the function of surfaces and the seeking of new temperature-dependent properties for high temperature applications. Although thermal quenching still generally exists in luminescence nanomaterials, anomalous anti-Stokes emission enhancement at higher temperatures has already been observed in some specific nanomaterials like the 7 nm $NaYF_4:Yb^{3+}$, Er^{3+} [4-7].

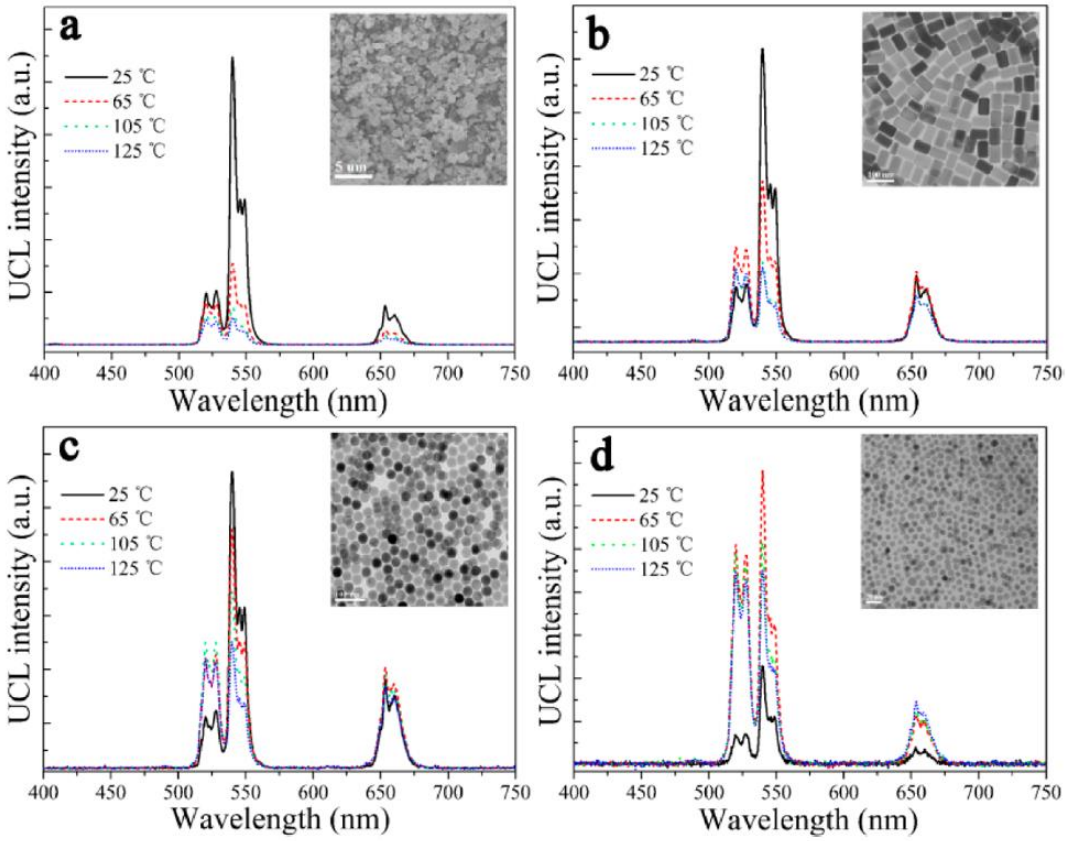

Figure 3.1 Temperature-dependent upconversion spectra of $NaYF_4:Yb^{3+}$, Er^{3+} with different sizes[4]. (a) Bulk material, (b) 66 × 48 nm, (c) 32 nm, (d) 7 nm. Insets are the TEM or SEM images.

Studying the temperature-dependent spectra of various sized materials is one feasible way to determine the reason behind the thermal enhancement emission. By the characterisation of a series of $NaYF_4:Yb^{3+}$, Er^{3+} materials from micron size to 7 nm, Shao and co-workers found the novel thermal enhancement upconversion luminescence in Figure 3.1[4], which shows a strong dependence on material size and only appears in $NaYF_4:Yb^{3+}$, Er^{3+} nanoparticles that are smaller than 32 nm. A 4.5-fold emission enhancement was achieved in 7 nm $NaYF_4:Yb^{3+}$, Er^{3+} nanoparticles when the temperature increased from room temperature to 65 °C. Meanwhile, the authors provided explanation that the high temperature could increase the phonon population of low-energy modes in the small nanoparticles; therefore, the phonon-assisted energy transfer processes would be more effective, which could be concluded as the weakened phonon confinement effect under high temperatures. In a similar study reported by the same group[5], the authors also found thermal enhancement in small sized $NaYF_4:Yb^{3+}$, Ho^{3+} and $NaYF_4:Yb^{3+}$, Tm^{3+} nanoparticles rather than in large nanowires with the same doping. Moreover, Song and co-workers have reported on the temperature-dependent properties of both β-$NaYF_4:Yb^{3+}$, Er^{3+} and α-$NaYF_4:Yb^{3+}$, Er^{3+} nanoparticles with different sizes[7], and they found β-$NaYF_4:Yb^{3+}$, Er^{3+} nanoparticles had similar trends, i.e. from 10 K to 100 K the emissions kept increasing, then started to decay from 100 K to 400 K. Whereas the ultra-small 6 nm α-$NaYF_4:Yb^{3+}$, Er^{3+} nanoparticles were quenched monotonously with higher temperature. The authors explained the two types of temperature dependence as being caused by the different lattice crystalline environments in these two phases of $NaYF_4:Yb^{3+}$, Er^{3+} nanoparticles.

In 2018, our group studied the 2000-fold enhancement achieved in blue emission of 9.7 nm $NaYF_4:Yb^{3+}$, Tm^{3+} nanoparticles from room temperature to 453 K[8]. The size dependence of the thermal enhancement was consistent with previous publications. More significantly, with surface modification of the $NaYF_4:Yb^{3+}$, Tm^{3+} nanoparticles and other experiments designed by reverse logic, we confirmed that the thermal enhancement was due to the unique surface

phonon assistance originating from the surface-capped OA molecules. More recently, Shao and co-workers published some new progress on the mechanism study of this phenomenon[9]. Again, the thermal induced luminescence enhancement appeared in Yb^{3+} doped $NaGdF_4$ upconversion nanoparticles with different emitters. However, the dramatic thermal induced enhancement disappeared when the experiments were conducted in an Ar atmosphere. With further measurements, the authors found that the emission enhancement benefitted from moisture release from the sample surface, as shown in Figure 3.2. The surface water molecules act as quenchers with high phonon energy vibration; therefore, under higher temperatures, the water molecules can be evaporated and the strong luminescence recovers again.

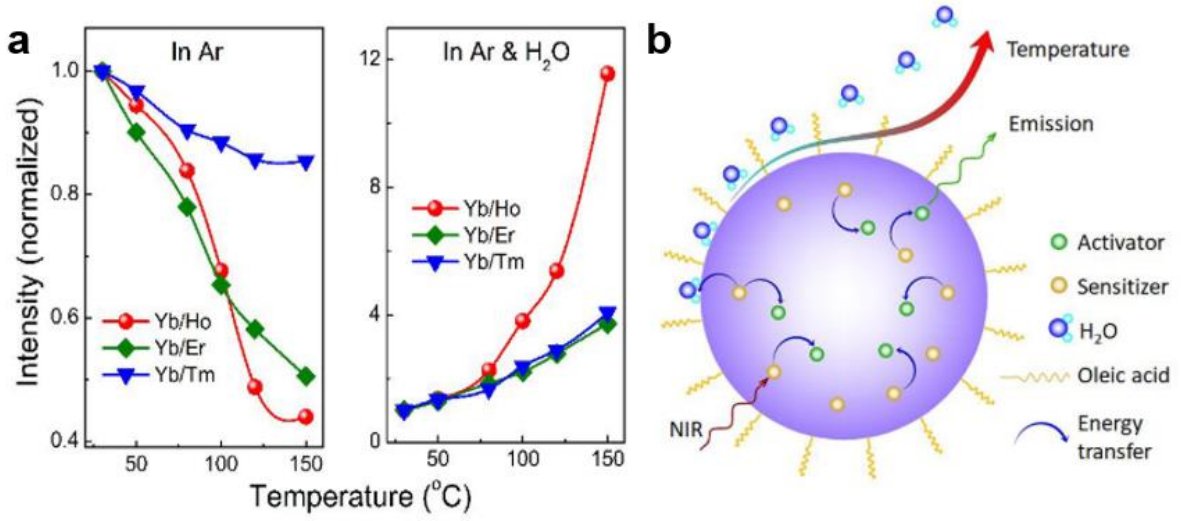

Figure 3.2 Emission enhancement because of thermal induced moisture release[9]. (a) Temperature-dependent upconversion intensities of Yb^{3+}-Ho^{3+}, Yb^{3+}-Er^{3+} and Yb^{3+}-Tm^{3+} codoped $NaGdF_4$ (~7 nm) nanopaticles in Ar and in Ar/H_2O atmosphere. (b) Schematic diagram of thermal induced moisture release from the surface of upconversion nanpoparticles.

At present, regarding the argument raised by the related literature, more targeted and deeper exploration towards the physical origins of the thermal induced emission increase is required. All possible mechanisms, including phonon confinement effect, lattice crystalline environment, surface ligand assistance and moisture release can contribute to a much stronger anti-Stokes

luminescence at higher temperatures[7,10], which can effectively overcome the problem of thermal quenching. However, only the principles behind the observed phenomenon have been studied clearly, with the new material properties being maximally optimised for practical applications.

In this chapter, the thermal enhancement in the upconversion emissions of $NaYF_4:Yb^{3+}$, Tm^{3+} and $NaYF_4:Yb^{3+}$, Nd^{3+} nanoparticles are discussed. From temperature-dependent spectra to single nanoparticle imaging, from air atmosphere to Ar atmosphere measurement, the particular anti-Stokes emission enhancement in a thermal field was studied from various aspects. Finally, the factors of the thermal induced enhancement were analysed comprehensively based on the experimental results.

3.2 Thermal enhancement upconversion in $NaYF_4$: Yb^{3+}, Tm^{3+} nanocrystals

3.2.1 Temperature-dependent upconversion emission in $NaYF_4$: Yb^{3+}, Tm^{3+} nanocrystals

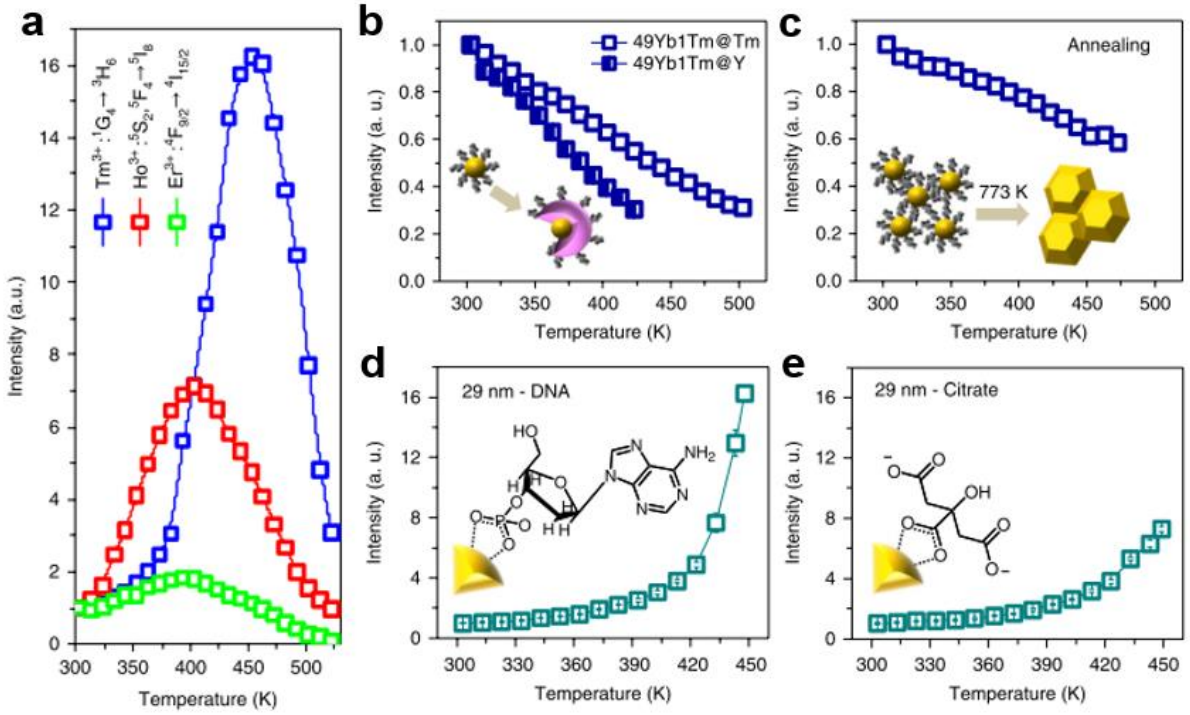

Figure 3.3 Surface modifications on RE doped nanocrystals to demonstrate surface phonon enhanced upconversion[8]. (a) Thermal induced upconversion enhancement in Yb^{3+}-Tm^{3+}, Yb^{3+}-Ho^{3+} and Yb^{3+}-Er^{3+} codoped $NaYF_4$ nanoparticles. By coating an inert shell (b) or using an additional annealing process (c) on the $NaYF_4$: Yb^{3+}, Tm^{3+} nanoparticles, the modified upconversion nanoparticles only show thermal quenching instead of thermal enhancement. With surface modification via ligand exchange, the synthesised $NaYF_4$: Yb^{3+}, Tm^{3+} with surface-capped DNA (d) and citrate (e) maintain upconversion enhancement at high temperatures.

In this section, I would like to acknowledge firstly all the other authors for their contributions on this project. Dr. Jiajia Zhou and Prof. Dayong Jin conceived the project and designed the experiments; Dr. Shihui Wen, Jiayan Liao, and Dr. Jiajia Zhou conducted synthesis; Christian Clarke and Jiajia Zhou performed the security ink printing and imaging; Dr. Sherif Abdulkader

Tawfik carried out simulation work; Dr. Wei Ren conducted the surface modification; Dr. Fan Wang and I built up the test systems.

By the co-precipitation method, we prepared Yb^{3+}-Tm^{3+}, Yb^{3+}-Ho^{3+} and Yb^{3+}-Er^{3+} codoped $NaYF_4$ nanoparticles with a size under 50 nm. By recording the spectra of the samples from room temperature to 523 K, we observed abnormal intensity change trends in three different doping samples, which first increased with temperature and then decreased, as shown in Figure 3.3 (a). The emission enhancements mainly occurred in the emission band of 475 nm emission from $^1G_4 \rightarrow {}^3H_6$ (Tm^{3+}), 545 nm emission from $^5S_2$, $^5F_4 \rightarrow {}^5I_8$ (Ho^{3+}) and 660 nm emission from $^4F_{9/2} \rightarrow {}^4I_{15/2}$. These anomalous emission enhancements show that there existed a new thermal effect during the upconversion energy transfer to resist thermal quenching.

To investigate where the enhancement orginates from, we further coated the 29 nm $NaYF_4$: Yb^{3+}, Tm^{3+} sample with an inert shell to form a core-shell structure. The emission enhancement under high temperatures vanished by thermal quenching (Figure 3.3 (b)). Based on these findings, we conjecture that the thermal enhancement is in connection with the sample surface, as the main difference between the core-only $NaYF_4$: Yb^{3+}, Tm^{3+} and the core-shell $NaYF_4$: Yb^{3+}, Tm^{3+}@Y nanoparticles was their surface. The surface of the core-shell $NaYF_4$: Yb^{3+}, Tm^{3+}@Y was separated from its active core by an inert shell whereas the surface of the core-only $NaYF_4$: Yb^{3+}, Tm^{3+} did not; therefore, the emission of core-shell $NaYF_4$: Yb^{3+}, Tm^{3+}@Y could not be influenced by the surface effect. To prove this hypothesis, an additional annealing process was conducted to modify the surface environment including removing the surface ligands, surface defects and other quenchers. As expected, the results indicated that the thermal quenching happened in the processed samples and the responsibility of the surface on the thermal enhancemnet in upconversion luminescence was confirmed (Figure 3.3 (c)).

To better understand how the surface influences the energy transfer in the RE doped materials, we used other sample design strategies, as shown in Figure 3.3 (d) and (e). With ligand exchange, the surface-capped OA molecules were replaced by DNA and citrate. After the surface ligand modification, the thermal induced upconversion enhancement still remained in the samples. Simultaneously, by FTIR and Raman spectrometry measurements, we confirmed the the surface ligand of the OAs contained multiple frequencies of vibrating states of phonons (Figure 3.4 (a)), including some low frequencies such as 471 cm^{-1}, 491 cm^{-1}, 559 cm^{-1} and 620 cm^{-1}, which should come from the [Yb···O] coordination, although there is limited knowledge reported from the literature. During the energy transfer process, the energy gap between Yb^{3+} -Tm^{3+}, Yb^{3+}-Ho^{3+} and Yb^{3+}-Er^{3+} was approximately 1400 cm^{-1}, 1000 cm^{-1} and 200 cm^{-1} (Figure 3.4 (b)). To compensate for these energy mismatches, phonon assistance made a great effort, especially in the energy transfer of Yb^{3+}→Tm^{3+}, Yb^{3+}→Ho^{3+} with a large energy gap, and the phonon acitivity was intensified by high temperature. The small energy gap between Yb^{3+}→Er^{3+} did not requie such intense phonon assistance, which was why the thermal induced enhancement in Yb^{3+}-Er^{3+} codoped materials was lower than the enhancement in Yb^{3+} -Tm^{3+} or Yb^{3+}-Ho^{3+} codoping nanoparticles. Thus, besides the phonon from the lattice vibration, the active phonon originating from the surface ligands under higher temperatures also played an essential role by giving suitable phonon energy assistance.

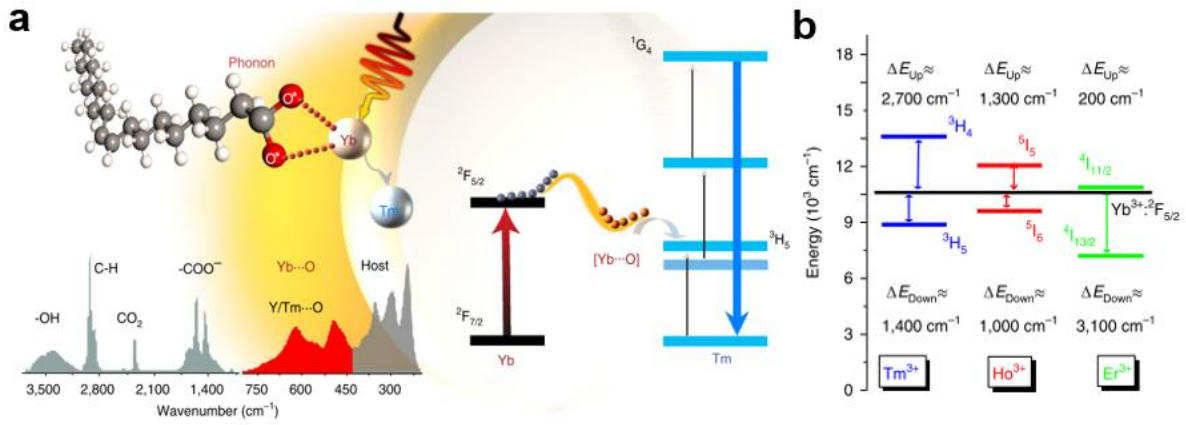

Figure 3.4 Efficient surface phonon assistance energy transfer in a thermal field[8]. (a) Schematic illustration of the surface phonon generated from surface ligand vibration for enhanced upconversion. (b) The energy mismatch between the sensitiser Yb^{3+} and the emitters Tm^{3+}, Ho^{3+}, Er^{3+} that must be filled by phonons for energy transfer.

Additionally, the results in Figure 3.3 (d) and (e) proved that as long as the [Yb/Y/Tm···O] coordination remained on the surface, the surface ligand could create a more effective energy transfer by phonon assistance at elevated temperatures.

3.2.2 Single nanoparticle imaging under different temperatures

Single nanoparticle characterisation can be used to locate the potential property that may be hidden in bulk materials[11]. For example, the spectrum of a single nanoparticle is quite different from the cluster, which has much sharper emission bands in a single nanoparticle, and the luminescence efficiency in a nanoparticle cluster is higher than that of the individual nanoparticles. This difference can be explained by the interactions, such as energy reabsorption, among nanoparticles that are sticking together[12,13]. To more directly prove the surface phonon enhanced upconversion process, the single nanoparticle characterisation was performed using the home-built wide field imaging microscope, as described in Chapter 2.

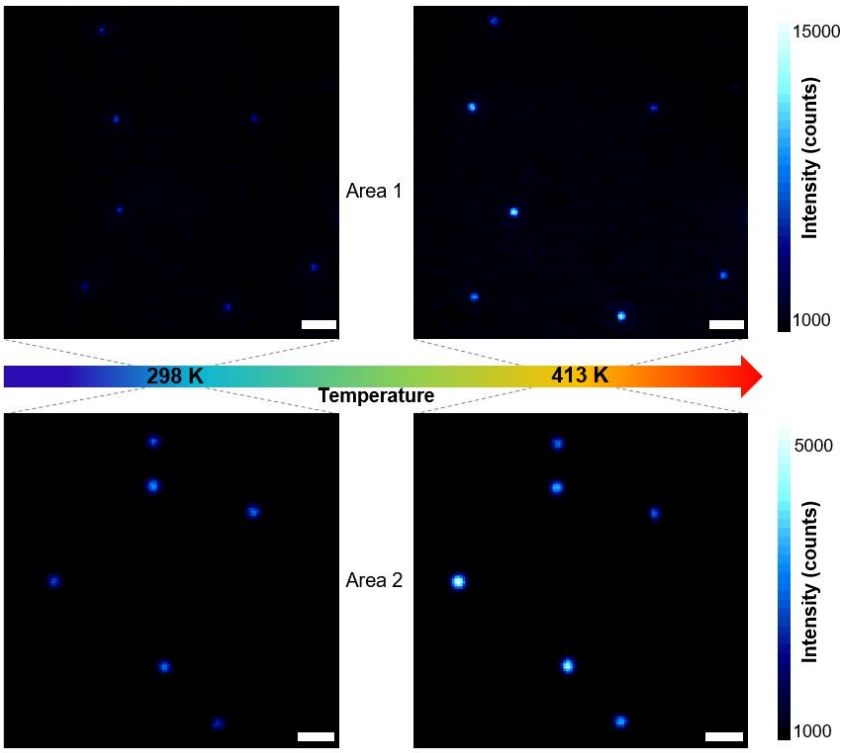

Figure 3.5 Single nanoparticle imaging under a wide field microscope in a thermal field. The emission intensity of each OA-capped $NaYF_4$: 49% Yb^{3+}, 1% Tm^{3+} single nanoparticle in the two selected areas shows thermal enhancement by a factor around 2 from 298 K to 413 K. All visible and NIR emissions from Tm^{3+} are included. The excitation power is approximately 10^4 W/cm^2, the scale bar is 2 µm.

In Figure 3.5, two sample regions of interest were illuminated by a 980 nm laser, and the luminescence from every OA-capped $NaYF_4$: 49% Yb^{3+}, 1% Tm^{3+} single nanoparticle was captured by an EMCCD camera. The temperarure of the nanoparticles was controlled by the heating stage from 298 K to 413 K to study the temperature-dependent emission from a single nanoparticle. From areas 1 and 2, the OA-capped $NaYF_4$: 49% Yb^{3+}, 1% Tm^{3+} nanoparticles clearly exhibited 2- to 3-fold emission enhancement, with a temperature increment of 115 K. The different emission intensity ranges between the two areas was caused by the camera setting changes.

The thermal enhancement in the nanoparticles was in agreement with the results of the bulk materials. Although the thermal enhancement times were lower than the enhancement times in the bulk materials, this discrepancy could be caused by the different emission bands in the two experiments. For the bulk materials test, the 475 nm emission band with maximun enhancement was considered separately as the other emission bands showed weaker enhancement, whereas in the OA-capped $NaYF_4$: 49% Yb^{3+}, 1% Tm^{3+} single nanoparticle test, all emission bands with peaks at 450, 475, 650, and 800 nm were included because the emission at 475 nm was too weak to perform the single nanoparticle imaging. A second reason could be the much higher excitation power density of the wide field microscope, which is around 10^4 W/cm^2 and is three orders higher than the power density of the spectra measurement. High excitation power can bring the luminescence close to intensity saturation; therefore, the thermal enhancement would not be as obvious.

Throughout the entire measurements, the monitored sample areas were kept at the same position under the wide field imaging microscope to ensure the same excitation condition at different temperatures, thus any intensity enhancement was caused by the different temperatures rather than changes in the excitation power. Additionally, the image rapidly went out of focus when the heating commenced; therefore, to guarantee the exact intensities in the captured images, image refocusing was adopted when the temperature became stable.

To prove the phonon assistance originated from the sample surface, we applied core-shell structure and annealing process to break the surface effect, and the results indicated that the bulk materials lost thermal enhancement, as shown in the last section. Similarly, to show the function of surface-phonon enhancement more directly, we also completed the OA-free $NaYF_4$: 49% Yb^{3+}, 1% Tm^{3+} single nanoparticle imaging with different temperatures. The capped OA molecules on the surface of $NaYF_4$: 49% Yb^{3+}, 1% Tm^{3+} were removed by a mature acid wash

method with ultrasound concussion[14]. Then, the single nanoparticles were characterised by the wide field microscope under the same conditions shown in Figure 3.5.

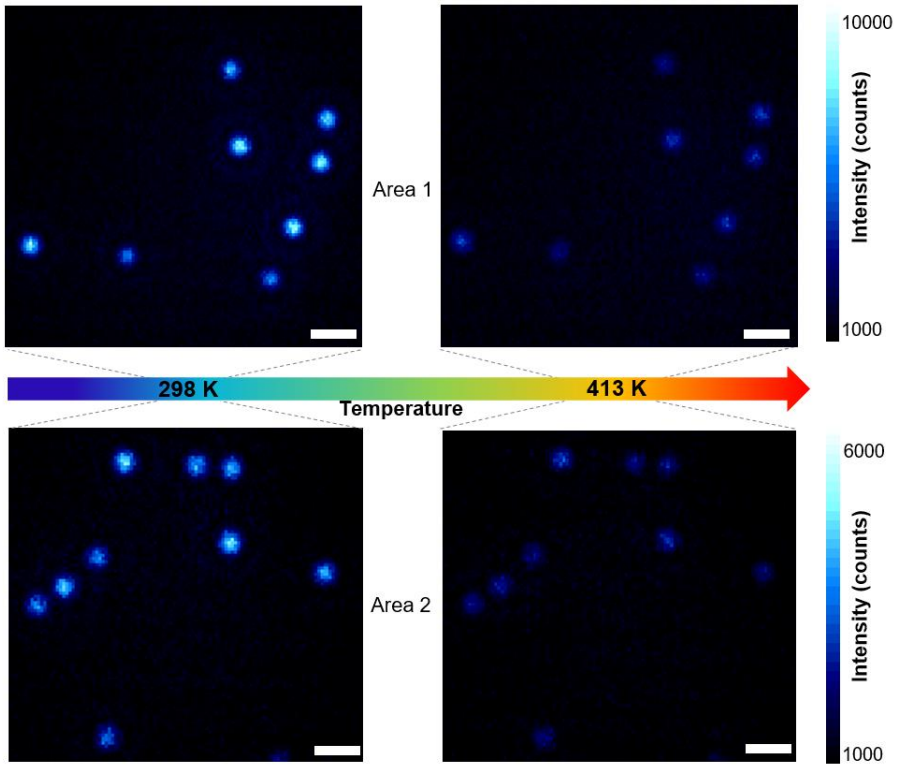

Figure 3.6 Single nanoparticle imaging of OA-free $NaYF_4$: 49% Yb^{3+}, 1% Tm^{3+} nanoparticles in the two selected areas, the deceased luminescence from 298 K to 413 K shows thermal quenching, which is different from the thermal induced enhancement in OA-capped samples. All visible and NIR emissions from Tm^{3+} are included. The excitation power is around 10^4 W/cm^2, the scale bar is 2 µm.

After removing the surface ligand, thermal quenching of surface-phonon assisted emission enhancement in single nanoparticles occurred, as shown in Figure 3.6. From 298 K to 413 K, the luminescence from all the OA-free $NaYF_4$: 49% Yb^{3+}, 1% Tm^{3+} single nanopaticles in the imaging areas was obviously quenched by over half, which was the opposite direction to the increased luminescence of OA-capped nanoparticles.

These results from the imaging of the single nanoparticles have confirmed the contribution of the surface ligand to the thermal induced phonon assistance. Under higer temperatures, the phonon generated from the coordination bond between the capped ligand and surface RE ions continually supported the energy transfer from sensitiser to emitter. Simultaneously, absorbed energy in the excited energy states could be quenched by non-radiative multi-phonon relaxation. Under high temperatures, this multi-phonon relaxation was more intense; however, with the same intensified surface phonon assistance in nanoparticle, thanks to the high surface to volume ratio, the thermal quenching of luminescence could be reversed.

3.2.3 Discussion

For the first time, we developed a new way to overcome thermal quenching in RE doped upconversion nanopaticles. In both temperature-dependent spectra measurement and single nanoparticle characterisation, the synthesised OA-capped nanoparticles codoped with Yb^{3+}-Tm^{3+}, Yb^{3+}-Ho^{3+} and Yb^{3+}-Er^{3+} produced stronger emissions at an elevated temperature, especially by synthesising sub-10 nm OA-capped $NaYF_4$: Yb^{3+},Tm^{3+} nanoparticles, an enhancement above 2000-fold was achieved from room temperature to 453 K[8]. The activation of thermal enhancement is due to the surface phonon assistance, i.e. with the interaction between the surface ligands and the RE ions that the ligands coordinate with, the surface phonon is generated for effective energy transfer.

This powerful surface phonon assistance was fully validated by a well-designed surface engineering experiment. Without the surface effect, including core-shell nanoparticles, annealed nanoparticles and acid-washed nanoparticles, all samples performed thermal quenched luminescence rather than thermal enhancement, which is consistent with the function of surface ligands. These new findings not only provide a new approch to develop high efficiency upconversion materials, but also new strategies for luminescence nanothermometers working at high temperatures.

3.3 Thermal enhancement upconversion in $NaYF_4$: Yb^{3+}, Nd^{3+} nanocrystals

3.3.1 Temperature-dependent spectra of $NaYF_4$: Yb^{3+}, Nd^{3+} nanocrystals

We also studied another upconversion system, the Yb^{3+}-Nd^{3+} codoping system. Unlike the two-photon or three-photon upconversion processes in Yb^{3+}-Tm^{3+}, Yb^{3+}-Ho^{3+} and Yb^{3+}-Er^{3+} codoped materials, the Yb^{3+}-Nd^{3+} codoping system only requires one lower-energy photon around 980 nm to produce one higher-energy photon around 800 nm via energy transfer of $Yb^{3+}\rightarrow Nd^{3+}$, with the assistance of phonons to fill the energy gap[16-18]. However, compared to the multi-photon upconversion process, a phonon-assisted linear anti-Stokes system such as Yb^{3+}-Nd^{3+} depends greatly on the limited phonon assistance. Thus, it is hard to achieve high efficiency. However, if the phonon assistance can be largely promoted, the phonon-assisted one-photon process is very likely to produce high-efficient anti-Stokes emissions, as the energy loss in one-photon transfer process can be less than the multi-photon upconversion with more energy transfer steps.

As illustrated in Figure 3.7, to promote the unusual anti-Stokes emission process and meet the energy gaps, the phonon, which represents an excited quantum state of vibration within the elastic structure of a material, plays an essential role. Conventional mechanisms to promote more anti-Stokes emissions include the excited-state absorption of phonons (Figure 3.7 (a)), Boltzmann distribution (Figure 3.7 (b)), and the phonon-assisted energy transfer process (Figure 3.7 (c)), which often occur inside the crystal hosts and require increased temperature to favour more phonon generation[19]. However, higher temperature often 'kills' the emission intensity, which is known as the thermal quenching effect. Therefore, solutions are often concerned with the exploration of more efficient host materials for generating heat-favourable phonons and the proper management of thermal quenching effect. It becomes more challenging when developing a nanoscopic anti-Stokes optical probe, as the increased

number of quenchers on the relatively large surface becomes more active in decreasing the brightness of the nanoparticle probes at increased temperature.

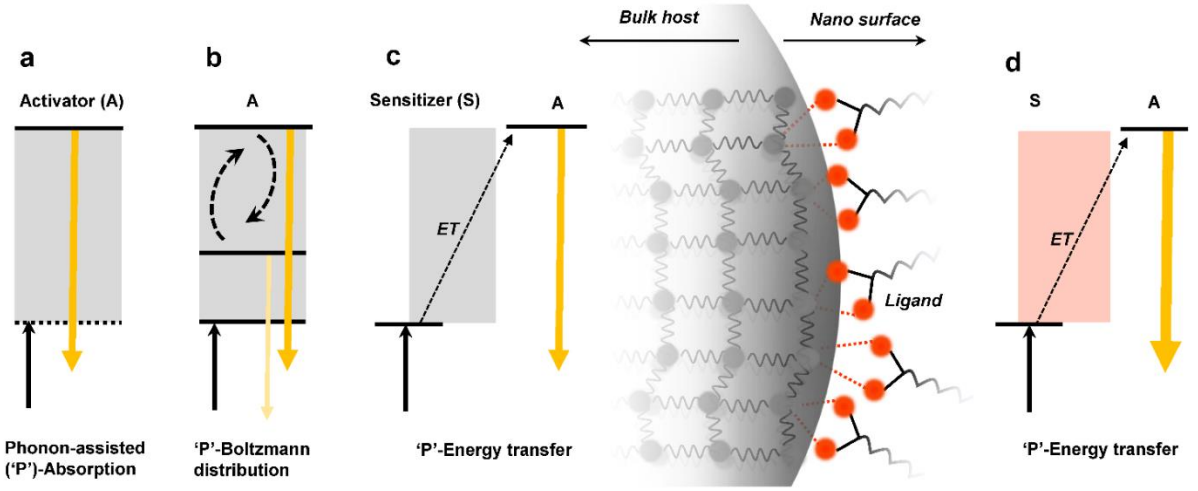

Figure 3.7 Phonon-assisted anti-Stokes emission enhancement. (a) Phonon-assisted ('P')-absorption represents the activation of an excited state from a real or imaginary intermediate excited (ground) state by additionally absorbing phonons. This mode enables a type of efficient optical cooler, namely Yb^{3+} doped crystals/glass, to decrease the temperature of the host system. (b) An emitter has two adjacent excited states, conforming Boltzmann distribution, which allows the phonons to be converted to the higher state with enhanced emission at elevated temperatures. This mechanism enables the design of ratiometric thermometry. (c) Phonon-assisted energy transfer process from the sensitiser ion to the activator ion. The classical energy transfer couple of Yb^{3+} and Nd^{3+} exhibits a configuration with a host phonon accessible energy gap, as most bonding by fluorides and oxides hold vibration energy of hundreds of wave numbers. (d) Apart from the bulk host generated phonons, the proposed surface assisted energy transfer process can significantly enhance the one-photon anti-Stokes emission in nanocrystals.

We have discovered the heat-favourable phonons that exist at the surface of several types of RE doped upconversion nanomaterials, as shown in Figure 3.7 (d). If this surface phonon assistance can also be applied to the Yb^{3+}-Nd^{3+} system, high-efficient linear anti-Stokes

emissions can be achieved. Although there are some reports on the Yb^{3+}- Nd^{3+} codoping anti-Stokes emission materials, most experiments have been limited in bulk host materials, such as Yb^{3+}-Nd^{3+} codoped $CaWO_4$[17], La_2O_3[16], by taking advantage of their maximum host phonon energies in the range of 800 cm^{-1} and 500 cm^{-1}, that can thermally enhance the anti-Stokes emissions of Nd^{3+} by nearly 200-fold at a high temperature up to 853 K from room temperature. However, for nanoparticles, previous studies have rarely examined $NaYF_4$: Yb^{3+}, Nd^{3+} nanocrystals with a thermal enhancement of 1.8-fold at 420 K[18].

Here, in a different way, we found dramatically enhanced linear anti-Stokes emissions from the RE doped luminescent $NaYF_4$:Yb^{3+}, Nd^{3+} nanocrystals system. This takes advantage of the phonons generated at the surface of nanomaterials to break through the limitation in producing the high-efficient linear anti-Stokes emissions.

The $NaYF_4$:Yb^{3+}, Nd^{3+} nanocrystals were synthesised by the co-precipitation method, and the prepared nanoparticles were capped by OA molecules on the surface. As shown in Figure 3.8, by testing the temperature spectra from 298 K to 433 K under 0.13 W/cm^2 980 nm laser excitation, we observed a 136-fold enhancement of the emission band around 800 nm in $NaYF_4$: 20% Yb^{3+}, 6% Nd^{3+} nanoparticles, which belongs to Nd^{3+}. The thermal enhancement can be attributed by two different approaches, one way is by lattice phonon assistance, which has also been shown in other studies, and the second way is the surface phonon assistance that comes from the bonding ligand on the sample surface. To prove the assumption, the sample was coated with a 5 nm thick inert shell by epitaxial growth to block the phonon energy transfer from the surface to the active core. After repeating the temperature-dependent spectra test from 298 K to 413 K, the core-shell structure $NaYF_4$: 20% Yb^{3+}, 6% Nd^{3+}@$NaYF_4$ nanoparticle showed much lower enhancement of around 14 times than that of the OA-capped core-only $NaYF_4$: 20% Yb^{3+}, 6% Nd^{3+} nanoparticles under 1 W/cm^2 980 nm laser excitation. By removing the surface ligand from the $NaYF_4$: 20% Yb^{3+}, 6% Nd^{3+}

nanoparticles by the annealing process at 773 K for 3 h, we collected evidence that the thermal enhancement decreased from 55 times to only 13 times after annealing, which confirmed the important role of surface molecule in phonon assistance.

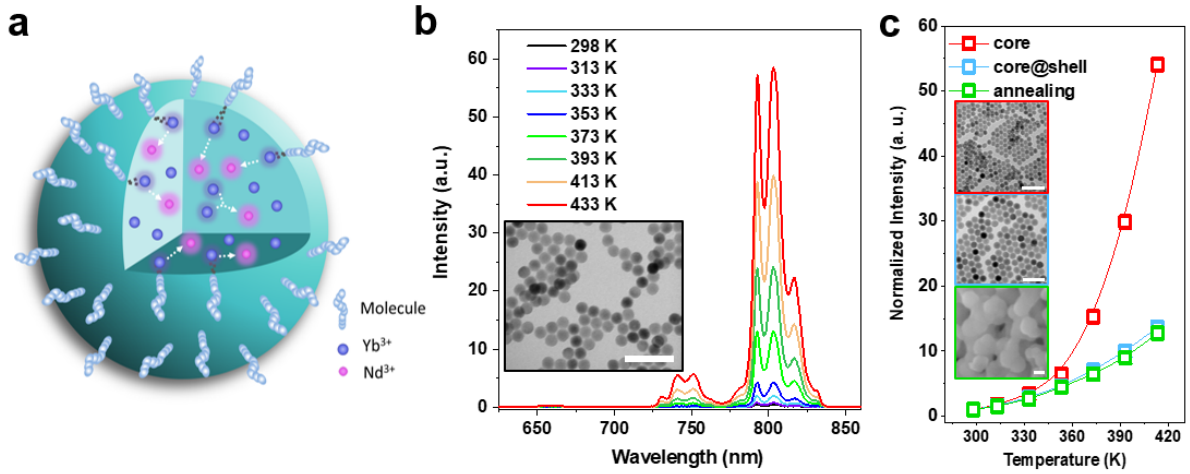

Figure 3.8 Phonon-enhanced one-photon anti-Stokes emission in Yb^{3+}, Nd^{3+} energy transfer system at elevated temperatures. (a) Schematic diagram showing the surface phonon assisted energy transfer from Yb^{3+} to Nd^{3+}. (b) Intensified anti-Stokes emission spectra of $NaYF_4$: 20% Yb^{3+}, 6% Nd^{3+} nanocrystals with temperature increasing, under the 980 nm continuous-wave laser excitation (0.13 W/cm^2). (c) The 803 nm emission enhancements of three different samples when the temperature increased from 298 K to 413 K. (980 nm CW excitation, 1 W/cm^2). Insets show the TEM and SEM images of the nanoparticle $NaYF_4$: 20% Yb^{3+}, 6% Nd^{3+} (24 nm), core-shell structure $NaYF_4$: 20% Yb^{3+}, 6% Nd^{3+}@ $NaYF_4$ (30 nm) and annealed $NaYF_4$: 20% Yb^{3+}, 6% Nd^{3+} samples. Scale bar: 100 nm.

To further optimise the enhancement in Yb^{3+}-Nd^{3+} codoping nanoparticles, we synthesised a family of ~10 nm nanoparticles with various Yb^{3+} and Nd^{3+} doping concentrations. The samples had similar size ranges from 9 nm to 11 nm, the almost identical sample size helped study the doping concentration dependence of the thermal enhancement, without the influence of size difference. The morphologies and size distributions of all the ~10 nm $NaYF_4$: Yb^{3+},

Nd^{3+} samples are shown in Figure 3.9. The doping concentration of Yb^{3+} changed from 20% to 60%, whereas the concentration of Nd^{3+} changed from 2% to 8%.

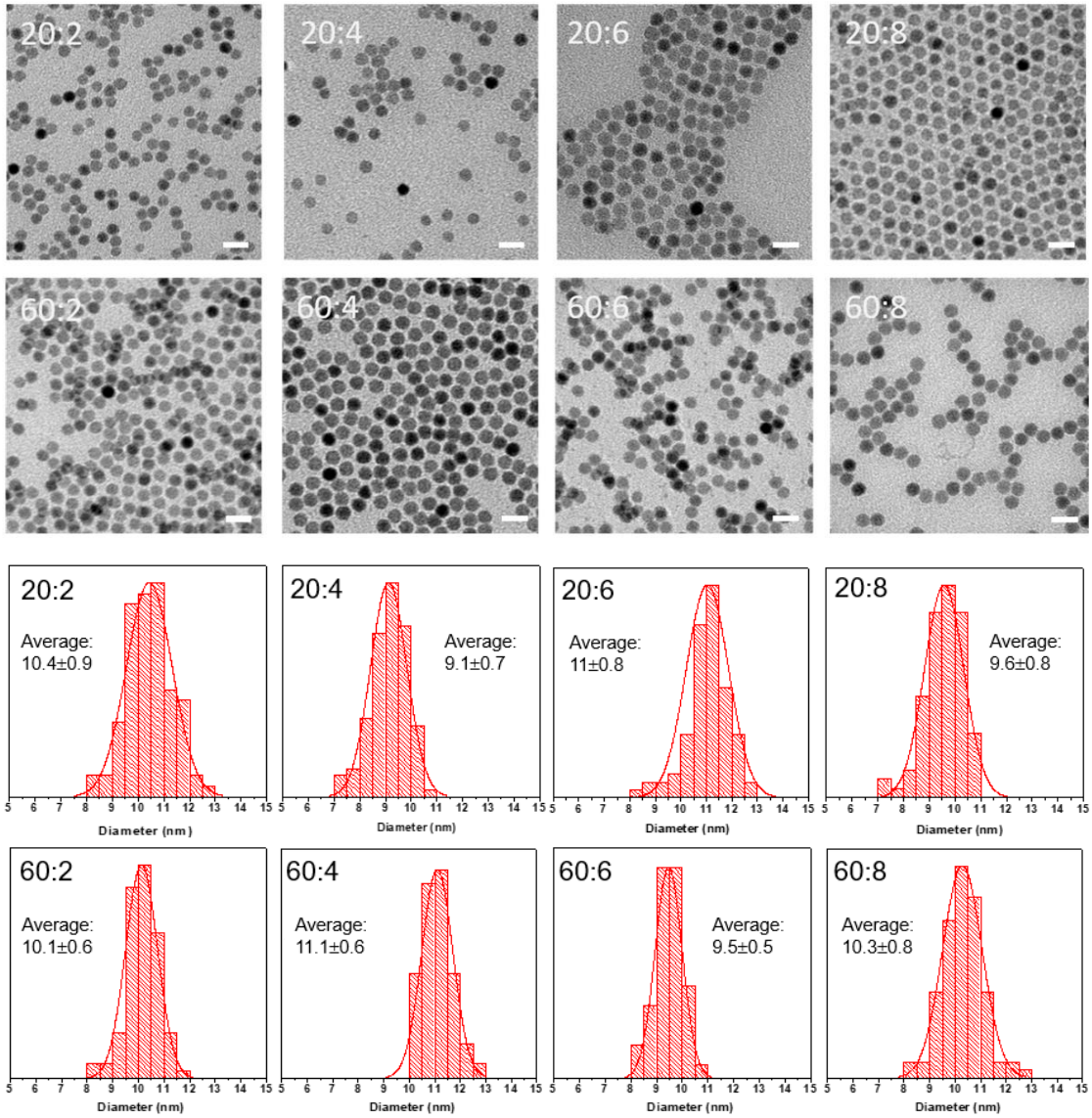

Figure 3.9 TEM images and size distributions of the ~10 nm $NaYF_4$: Yb^{3+}, Nd^{3+} samples. The doping concentration ratio of Yb^{3+}: Nd^{3+} (%) is labelled in each TEM image. Scale bar is 20 nm.

The temperature-dependent spectra of all ~10 nm samples were measured from 30 K to 453 K under the same experimental conditions. Remarkably, all these ~10 nm $NaYF_4$: Yb^{3+}, Nd^{3+} nanoparticles showed rapidly continuous emission enhancement during heating. By calculating the enhancement times of the emission peak at 803 nm, the ~10 nm nanoparticles showed quite

different results. As shown in Figure 3.10, all samples exhibited thermal enhancement over 200-fold for the 803 emission band; however, compared to the 20% Yb^{3+} doping samples, the other samples with higher Yb^{3+} concentration of 60% produced higher thermal induced emission increase of approximately 300-fold. All the samples had the same particle size; therefore, the only possibility to cause such different enhancement was because the different Yb^{3+} doping concentrations. As the surface phonon assistance stems from the ligand-RE ions coordination [Yb···O], higher Yb^{3+} doping concentration can lead to more ligands such as OA molecules combining on the surface of the ~10 nm nanoparticles. Thus, an increment of surface phonon assistance in the 60% Yb^{3+} doped $NaYF_4$: Yb^{3+}, Nd^{3+} nanoparticles contributed the extra emission enhancement in contrast to the 20% Yb^{3+} doped $NaYF_4$: Yb^{3+}, Nd^{3+} nanoparticles.

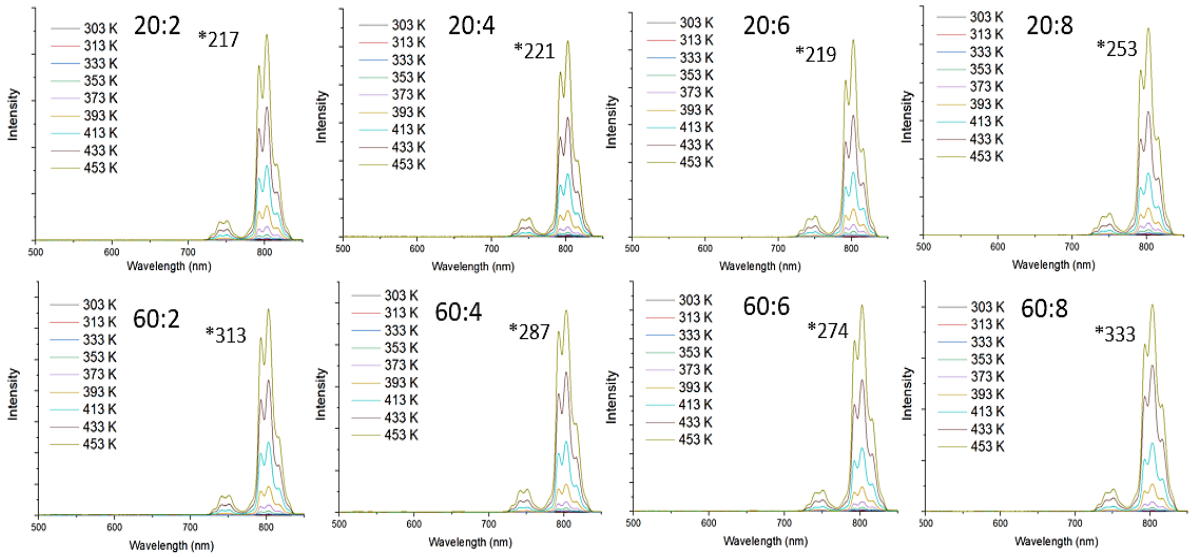

Figure 3.10 Temperature-dependent spectra of the ~10 nm $NaYF_4$: Yb^{3+}, Nd^{3+} samples with different doping concentration ratios of Yb^{3+}: Nd^{3+} (%). The enhancement times are shown for each sample. The temperature changed gradually from 303 K to 453 K. A 0.13 W/cm^2 980 nm laser excitation is applied in the experiment.

Additionally, the absolute luminescence intensity of the emission band around 803 nm for the ~10 nm sample family was also investigated at room temperature. The purpose was to determine whether the thermal enhancement in the $NaYF_4$: Yb^{3+}, Nd^{3+} nanoparticles depended on their absolute luminescence intensity. To measure the absolute luminescence intensity, each of the eight ~10 nm $NaYF_4$: Yb^{3+}, Nd^{3+} sample powders were placed in a specimen cell with the same volume. The emission spectra were recorded using the same measurement conditions at room temperature. The measurements were repeated three times for each sample, thus the average emission intensities of all samples were comparable, as shown in Figure 3.11. After analysing the absolute luminescence intensity together with the corresponding thermal enhancement, the quantitative assessment indicated that the enhancement factor had no obvious correlation with the absolute intensity of the nanocrystals.

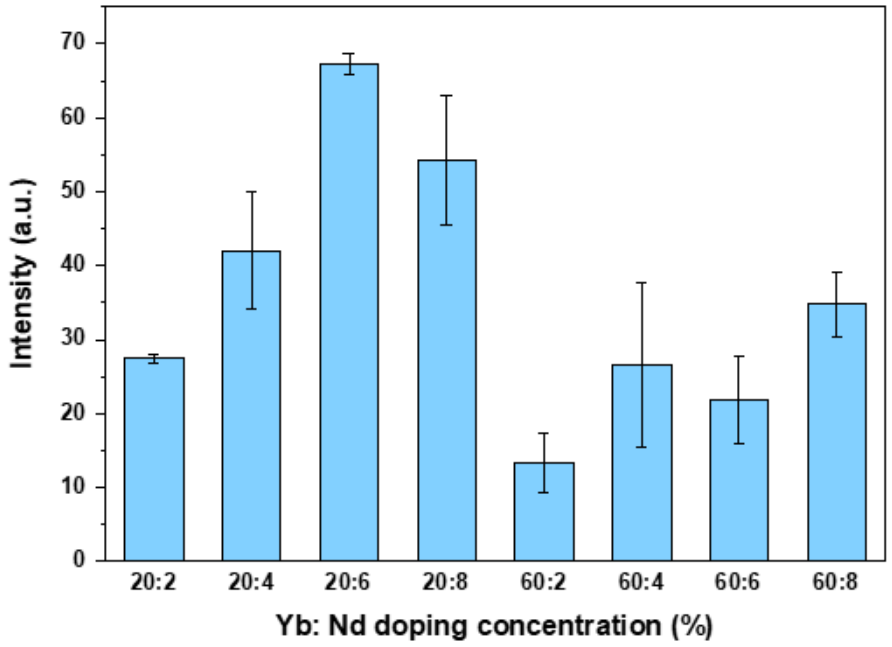

Figure 3.11 Comparison of 803 nm emission intensity of the ~10 nm $NaYF_4$: Yb^{3+}, Nd^{3+} samples at room temperature. The emission intensities of the ~10 nm samples are comparable, although the doping concentrations are different.

3.3.2 Pumping power-dependent property at different temperatures

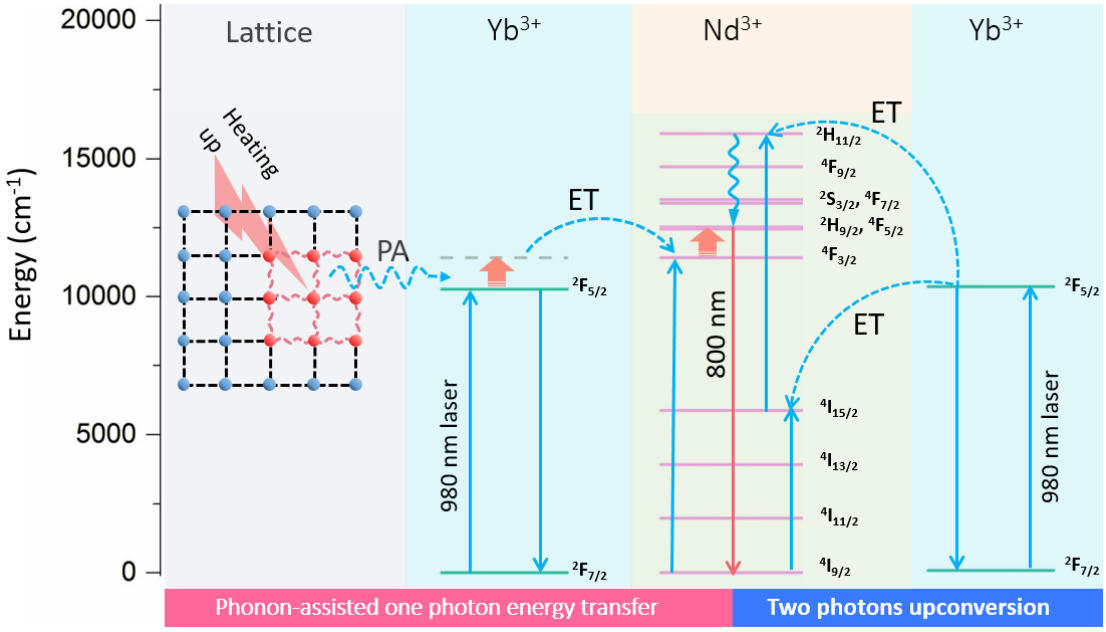

Figure 3.12 Energy level structure diagram of Yb^{3+} and Nd^{3+} including two different energy transfer routes for the 800 nm emission band.

To analyse the energy transfer routes in the Yb^{3+}-Nd^{3+} system that lead to the thermal-field enhanced emissions, the energy level structure diagram of Yb^{3+} and Nd^{3+} is shown in Figure 3.12, with the 800 nm emission band belonging to the radiative energy transfer $^2H_{9/2}$, $^4F_{5/2}\rightarrow{}^4I_{9/2}$ in Nd^{3+} ions. Two potential energy transfer ways were responsible for the 800 nm emission band, one way was by one-photon energy transfer from Yb^{3+} to Nd^{3+}. To repair the two energy gaps of 1200 cm^{-2} between $^2F_{5/2}$-$^4F_{3/2}$ and 1100 cm^{-2} between $^4F_{3/2}$-$^2H_{9/2}$, $^4F_{5/2}$, phonon assistance was the key mechanism as it absorbed phonon energy from the lattice vibration and surface ligand. Under higher temperatures, phonon assistance can be more active to help with energy transfer. The second way was a two-photon cooperative upconversion process, by absorbing two photons from Yb^{3+} successively, the excited energy state $^2H_{11/2}$ could be populated, and followed by a non-radiative relaxation the radiative energy transfer $^2H_{9/2}$, $^4F_{5/2}\rightarrow{}^4I_{9/2}$ could be realised.

Experiments on the excitation power dependence have been widely applied to study the multi-phonon energy transfer process in anti-Stokes luminescence, as the slope of the double-log power-dependent curve indicates how many photons are involved to produce the anti-Stokes luminescence. This can be explained by the relational expression[20]:

$$I_{up} \propto P^{n}_{pump}$$

where, the upconversion emission intensity I_{up} is proportional to the *n*th power of the pump power P_{pump}, and *n* is the number of photons that are used to populate the exited emission energy state.

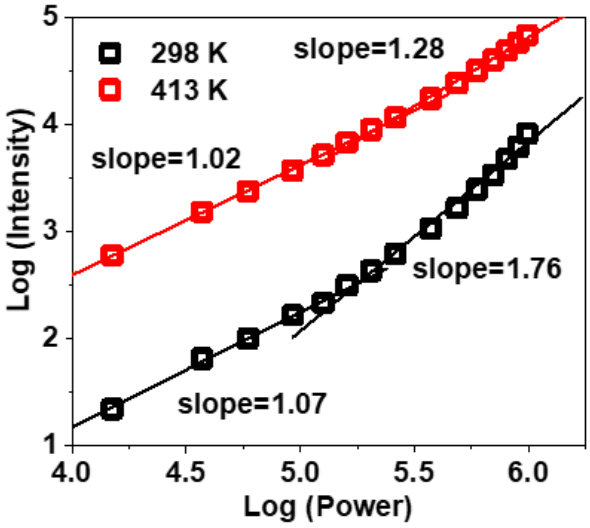

Figure 3.13 Double-log intensity-power slopes of 803 nm emission from $NaYF_4$: Yb^{3+}, Nd^{3+} with 980 nm laser excitation power density increasing at 298 K and 413 K.

To confirm that the phonon-assisted one-photon energy transfer plays a dominant role rather than the two-photon upconversion in the Yb^{3+}-Nd^{3+} codoping system, double-log power-dependent curves were measured in Figure 3.13, by gradually increasing the laser excitation power from ~10^4 W/cm^2 to ~10^6 W/cm^2 and recording the emission intensities under every corresponding laser power. The black curve shows the power dependence of the 800 nm emission intensity under 298 K. When the excitation power density was relatively low, the

slope of the black curve was approximately 1.07. Only after the excitation power increased as high as ~10^5 W/cm^2 did the slope increase to 1.76, which indicates that the one-photon energy transfer was the main way for the 800 nm emission, although the two-photon could become stronger at extremely high excitation powers due to more excited Yb^{3+} ions. The results under 413 K were similar to the room temperature results in the low excitation power region; however, they became quite different under high excitation power with the slope being approximately 1.28, which was much lower than it was at room temperature (1.76). These results show that high temperature can make the one-photon energy transfer more efficient, thus, under 413 K the Yb^{3+}-Nd^{3+} codoping system prefers the one-photon energy transfer over the two-photon process.

Based on the energy level structure diagram and the excitation power-dependent study on the Yb^{3+}-Nd^{3+} codoping system, the linear anti-Stokes emission produced from phonon-assisted one-photon energy transfer of Yb^{3+}→Nd^{3+} was clearly confirmed. The strong phonon assistance, from both the lattice environment and surface molecule, realised the increased anti-Stokes emission from Nd^{3+}, even when the temperature was hundreds of degrees higher. These results suggest that $NaYF_4$: Yb^{3+}, Nd^{3+} nanoparticles with efficient anti-Stokes emissions via thermal enhanced one-photon energy transfer can be used for temperature sensing and other applications.

3.3.3 Lifetime evolution with temperature

Besides intensity, lifetime is another parameter of light that reveals the optical property[21,22]. The luminescence lifetime shows the decay process of the population for the emission energy states, which contains the dynamic information on the radiative relaxation after excitation. Studying the luminescence lifetime can help understand the energy transfer dynamics, such as the sequence order of the energy transfer steps[23]. Meanwhile, unlike the emission intensity, the emission lifetime can change in a different way with changing parameters including doping

concentrations, sample size and temperature[21,23]. For example, generally speaking, emission intensity increases with the doping concentration of the sensitiser ions Yb^{3+} when it is lower than 30%, and the intensity is very likely to drop with higher Yb^{3+} concentrations because of the concentration quenching, which is widely found in phosphors. Concentration quenching is caused by the frequent cross-relaxation in high doping materials. Unlike the intensity, the emission lifetime from emitters is inversely proportional to the sensitiser concentration, because after excitation, the population in the higher-energy states of emitters can decay to the unoccupied lower-energy states in the sensitiser, which have been called back energy transfer[24]. With high concentrations of sensitisers surrounding the emitters, the vacant energy states in the sensitisers can be plentiful after excitation; therefore, the transfer rate of the back energy can be so fast that the lifetime is short[19,24]. Thus, lifetime measurements can provide a different angle for investigating the properties of the materials. Moreover, as mentioned in Chapter 1, luminescence nanomaterial with a temperature-dependent lifetime is one of the promising approaches for reliable temperature sensing, and thus it is necessary to study how the lifetime changes with temperature in the Yb^{3+}-Nd^{3+} codoping system.

To check whether the phonon-assisted anti-Stokes emissions in $NaYF_4$: Yb^{3+}, Nd^{3+} have a temperature-sensitive lifetime, similar to their intensity, the luminescence decay process of ~800 nm emission band from 23 nm $NaYF_4$: 20% Yb^{3+}, 6% Nd^{3+} and 42 nm $NaYF_4$: 60% Yb^{3+}, 6% Nd^{3+} nanoparticles were recorded by a gate-mode single-photon detector under pulsed laser excitation. The lifetime was obtained by a simple single-exponential fitting on the luminescence decay curve.

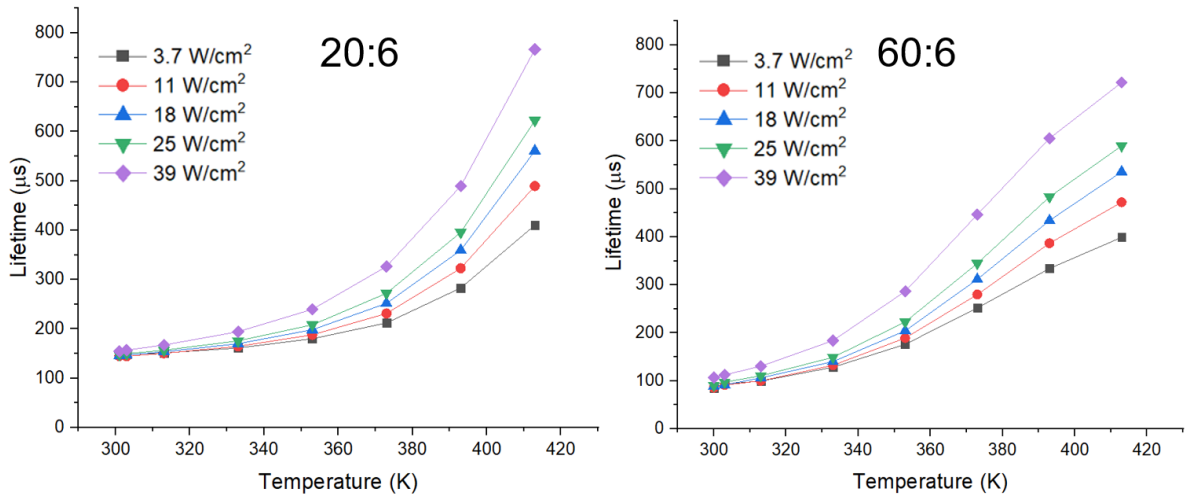

Figure 3.14 Lifetime evolution with temperature in 23 nm $NaYF_4$: 20% Yb^{3+}, 6% Nd^{3+} and 42 nm $NaYF_4$: 60% Yb^{3+}, 6% Nd^{3+} nanoparticles under 2000 μs pulse-width laser excitation with different powers.

As shown in Figure 3.14, the results of both samples showed that lifetime increased dramatically with an increased temperature. From room temperature to 413 K, the lifetime of ~800 nm emission of $NaYF_4$: 20% Yb^{3+}, 6% Nd^{3+} extended from approximately150 μs to near 800 μs, and the lifetime from $NaYF_4$: 60% Yb^{3+}, 6% Nd^{3+} nanoparticles grew from approximately 100 μs to 700 μs, which is highly sensitive to temperature change. The enhanced lifetime can be explained by the Boltzmann distribution between the energy levels of $^4F_{3/2}$ and $^2H_{9/2}$, $^4F_{5/2}$ in Nd^{3+}. Under high temperatures, the lower-energy state $^4F_{3/2}$ works as a reservoir to provide populations to the higher-energy state $^2H_{9/2}$, $^4F_{5/2}$ by absorbing heat, as they are thermal coupled. This type of repopulation can prolong the energy decay from the emission energy state $^2H_{9/2}$, $^4F_{5/2}$ and can lead to a longer lifetime under high temperatures. Simultaneously, thermal induced phonon assistance can take advantage of the remaining excited Yb^{3+} ions for energy transfer to Nd^{3+} even after excitation, thus the transfer of back energy can be balanced out.

Moreover, it seems that high excitation power can improve the temperature sensitivity based on the lifetime, which is the opposite to temperature-dependent intensity. We assumed this was because the emission intensity became saturated more easily than did the lifetime under high excitation power, thus the near-saturated intensity changed slowly with temperature while the lifetime did not.

3.4 Quantitative analysis of thermal enhancement factors by Ar atmospheric measurement

3.4.1 Hysteresis effect in heating-cooling cycle test

Apart from the demonstrated host lattice and surface ligand phonon assistance, there are some other reported effects that can lead to emission enhancement under high temperatures. Therefore, it is significant to investigate whether other possible factors contribute to thermal enhancement, and the proportion of each of these enhancement factors.

Bednarkiewicz *et al*. found that the annealing effect via a long-time NIR laser excitation induced a dramatic luminescence enhancement in ultra-small $NaYF_4$ nanoparticles[25], which was caused by the structural change of the nanoparticles, and this type of luminescence enhancement is irreversible. If the thermal induced luminescence enhancement in $NaYF_4$: Yb^{3+}, Nd^{3+} is also caused by the annealing effect, the luminescence will not recover to the initial intensity after the temperature decreases again. With this principle, we conducted a heating-cooling cycle test on the ~10 nm $NaYF_4$: Yb^{3+}, Nd^{3+} nanoparticles to confirm whether the annealing effect exists in the heating process.

This heating-cooling cycle experiment was completed in air, with an additional cooling process, the emission spectra were recorded first from room temperature to 453 K, and then the spectra were tested again from 453 K to room temperature at the same points. All the spectra were recorded until the temperature was stable. The results of the emission intensity at 803 nm for all the ~10 nm $NaYF_4$: Yb^{3+}, Nd^{3+} nanoparticles with different doping concentrations are shown on Figure 3.15. This figure shows clearly that the thermal induced emission enhancement in these samples was near reversible at room temperature, which negated the existence of the annealing effect during the temperature change. This also proved that the

sample structure did not change under high temperatures up to 453 K, showing to the excellent structure stability of the synthesised $NaYF_4$: Yb^{3+}, Nd^{3+} nanoparticles.

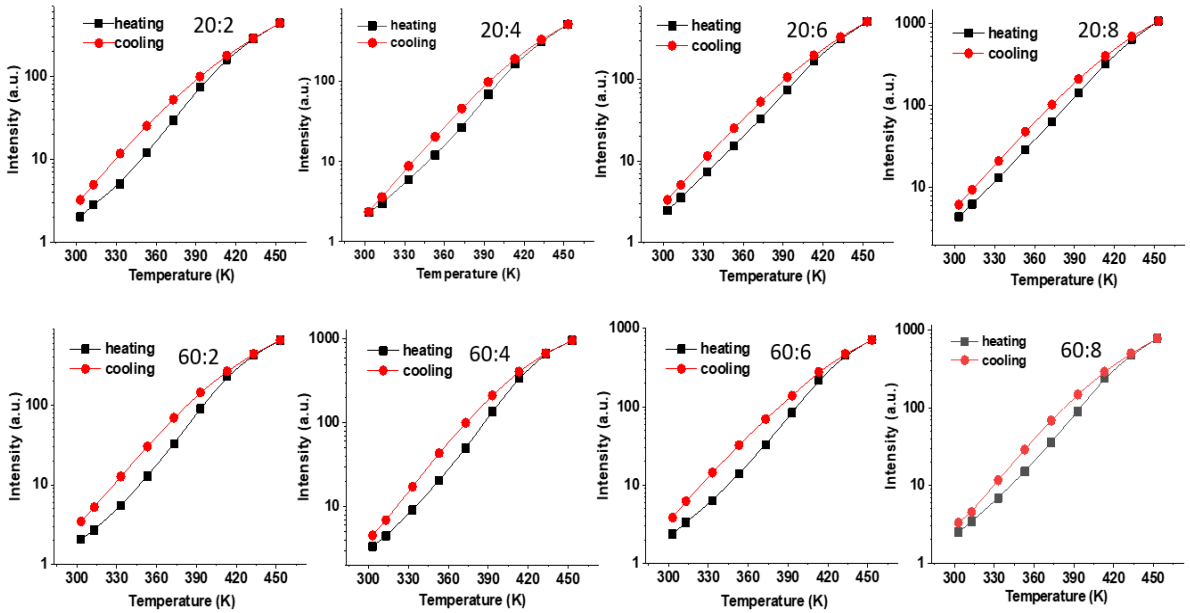

Figure 3.15 Heating-cooling cycle test on the ~10 nm $NaYF_4$: Yb^{3+}, Nd^{3+} sample family, the results show near reversible emission intensities of 803 nm at 303 K, and hysteresis effect during the temperature cycle. The doping concentration of Yb^{3+}: Nd^{3+}(%) for each sample is given in the figure.

However, overall, the intensity curve during the cooling process was higher than the curve during the heating process, which shows a hysteresis effect. To explain this strange phenomenon, we refer to the reported moisture release effect as mentioned in the Introduction of this chapter.

The relatively large surface of nanoparticles has been commonly known as parasitic sites for quenchers; therefore, it is possible that the emission enhancement was also a result of the activation of the quenched sites, similar to the surface water molecule release during the heating process[9]. After moisture release from the sample surface at high temperatures, the water molecules in the air can be absorbed on the nanopaticle again when the temperature decreases;

however, the reabsorbtion process takes time to complete. Thus, when the $NaYF_4$: Yb^{3+}, Nd^{3+} nanoparticles cool down from 453 K, where the moisture release happens quickly, the reduced amount of surface moisture as quenchers can lead to a higher emission intensity than the emission during the heating process. After the temperature decreases to room temperature, the absorption of moisture on the surface is nearly recovered.

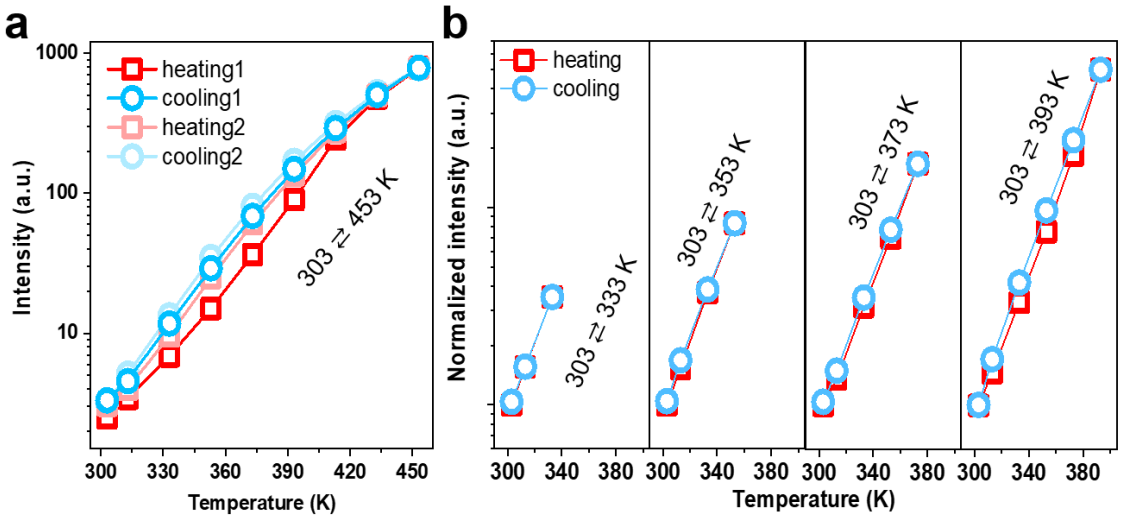

Figure 3.16 Demonstration of the moisture release effect. (a) Dual-cycle heating-cooling test of the 10 nm $NaYF_4$: 60% Yb^{3+}, 8% Nd^{3+} nanocrystals showing the release of hysteresis effect during heating-cooling. (b) Heating-cooling cycle tests of the 10 nm $NaYF_4$: 60% Yb^{3+}, 8% Nd^{3+} nanocrystals with temperatures stopped at different levels before cooling.

To further investigate the moisture release effect during the thermal enhancement of $NaYF_4$: Yb^{3+}, Nd^{3+} nanoparticles, we designed two different experiments, as shown in Figure 3.16. First, the hysteresis effect in 10 nm $NaYF_4$: Yb^{3+}, Nd^{3+} nanoparticles was further checked by a dual-cycle heating-cooling test. The results revealed the irreversible hysteresis behaviour for the first cycle, implying a strong moisture removal process by the elevated temperature to 453 K (Figure 3.16 (a)). With an immediate second heating-cooling cycle, the hysteresis behaviour was weakened with a slower quencher release. Thus, the intensity curves were more overlapped during the second cycle than during the first cycle. Moreover, by recording the hysteresis effect

with different maximum temperatures, we found that the hysteresis effect depended on the maximum heating point applied to the sample (Figure 3.16 (b)). These results indicate a possible adsorption and desorption process of the moisture in the air.

3.4.2 Thermal enhanced luminescence in Ar atmosphere

Thus far, three different thermal induced luminescence enhancement factors, namely host phonon assistance, surface phonon assistance and moisture release, have been studied in the anti-Stokes $NaYF_4$: Yb^{3+}, Nd^{3+} nanoparticles. To further prove that the phonon assistance (from the host and the surface) plays an essential role in the Yb^{3+}-Nd^{3+} energy transfer and anti-Stokes emission enhancement, not the simple moisture recovery, a quantitative analysis on the three thermal induced luminescence enhancement factors is urgently required.

For this purpose, a sample measurement in Ar atmosphere was used to prevent the reabsorption of moisture from the air, then by comparing the emission intensity before and after the moisture release, the contribution of moisture release on the emission enhancement was clarified. For the quantitative analysis of the host phonon assistance and surface phonon assistance during the thermal enhancement, two contrastive samples were measured in the Ar atmosphere, which were OA-capped $NaYF_4$: Yb^{3+}, Nd^{3+} nanoparticles and OA-free $NaYF_4$: Yb^{3+}, Nd^{3+} nanoparticles. After totally removing the moisture with high temperature heating, the thermal enhancement in OA-free $NaYF_4$: Yb^{3+}, Nd^{3+} samples only came from the host phonon assistance, whereas the OA-capped $NaYF_4$: Yb^{3+}, Nd^{3+} nanoparticles were supposed to show higher thermal enhancement because of the surface phonon assistance from the OA molecules. Thus, the extra emission enhancement in the OA-capped $NaYF_4$: Yb^{3+}, Nd^{3+} nanoparticles compared with the OA-free samples came from surface phonon assistance.

With this logical research plan, we established the Ar atmosphere spectra test system as described in Chapter 2 and prepared the OA-free $NaYF_4$: Yb^{3+}, Nd^{3+} nanoparticles by an acid

treatment on the same OA-capped samples. FTIR spectroscopy was conducted to ensure that the OA ligand had been washed off, as shown in Figure 3.17. The lack of CH_2 stretching and COOH stretching indicated that the surface OA molecule was removed from the OA-free 25 nm and 10 nm nanoparticles[14].

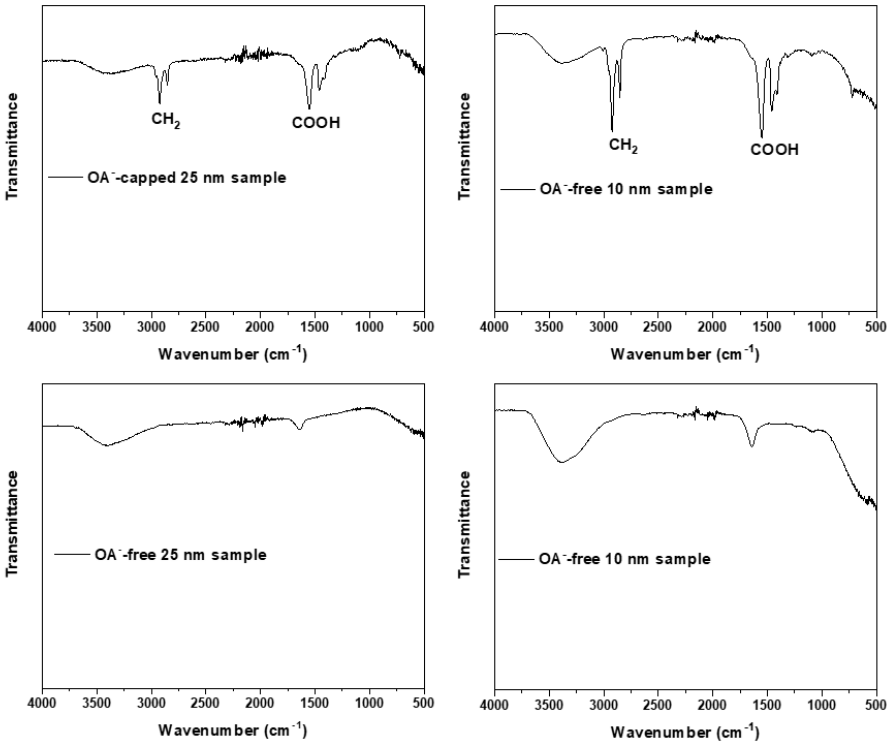

Figure 3.17 FTIR results of the as-prepared OA-capped and OA-free samples. After acid treatment, both CH_2 stretching and COOH stretching disappeared; therefore, surface OA was removed from the 25 nm $NaYF_4$: 20% Yb^{3+}, 6% Nd^{3+} and 10 nm $NaYF_4$: 20% Yb^{3+}, 6% Nd^{3+} nanoparticles.

Before testing the samples in Ar atmosphere, we first compared the thermal performance of OA-capped and OA-free $NaYF_4$: Yb^{3+}, Nd^{3+} in air to confirm the essential role of surface ligands. Sample performance in air provides us with much more reference for future application development than in Ar atmosphere. As shown in Figure 3.18, both 25 nm and 10 nm $NaYF_4$: 20% Yb^{3+}, 6% Nd^{3+} samples that were OA-capped realised much higher emission enhancement

before the removal of OA; therefore, the OA-capped samples were more suitable for working as nanothermometers or as efficient anti-Stokes emission agents.

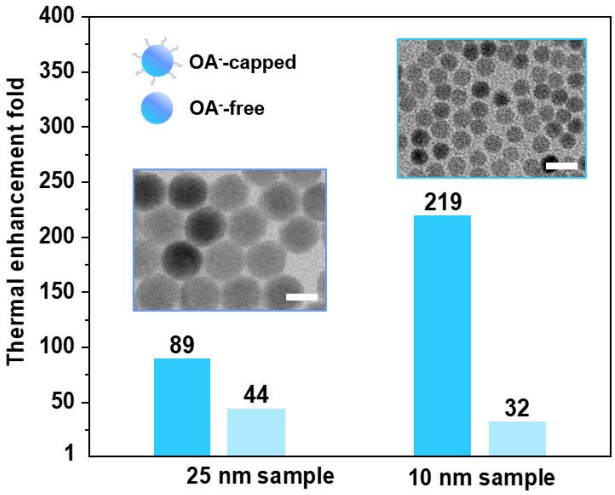

Figure 3.18 Intensity enhancement comparisons between OA-capped and OA⁻-removed samples in air. The two sets of samples are 25 nm $NaYF_4$: 20% Yb^{3+}, 6% Nd^{3+} and 10 nm $NaYF_4$: 20% Yb^{3+}, 6% Nd^{3+} nanocrystals. Temperature changes from 303 K to 453 K.

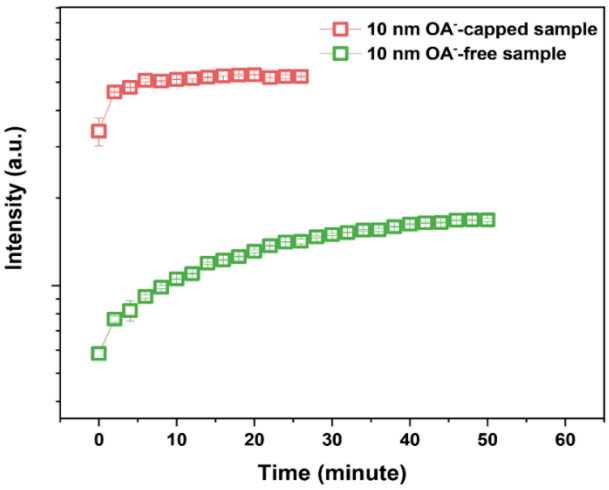

Figure 3.19 Moisture release process at 453 K. Time was recorded from the moment when the setting temperature arrives at 453 K.

The measurements of the OA-capped and OA-free samples were then repeated in a moisture-free environment by Ar gas circulation. The moisture-free condition was evaluated by

maintaining the samples at 453 K until achieving stable emission intensities, this moisture release process can last for over 30 min depending on the sample, as shown in Figure 3.19. The gradual intensity increase was attributed by moisture release, and the intensity became stable when the moisture was totally removed in the enclosed sample holder.

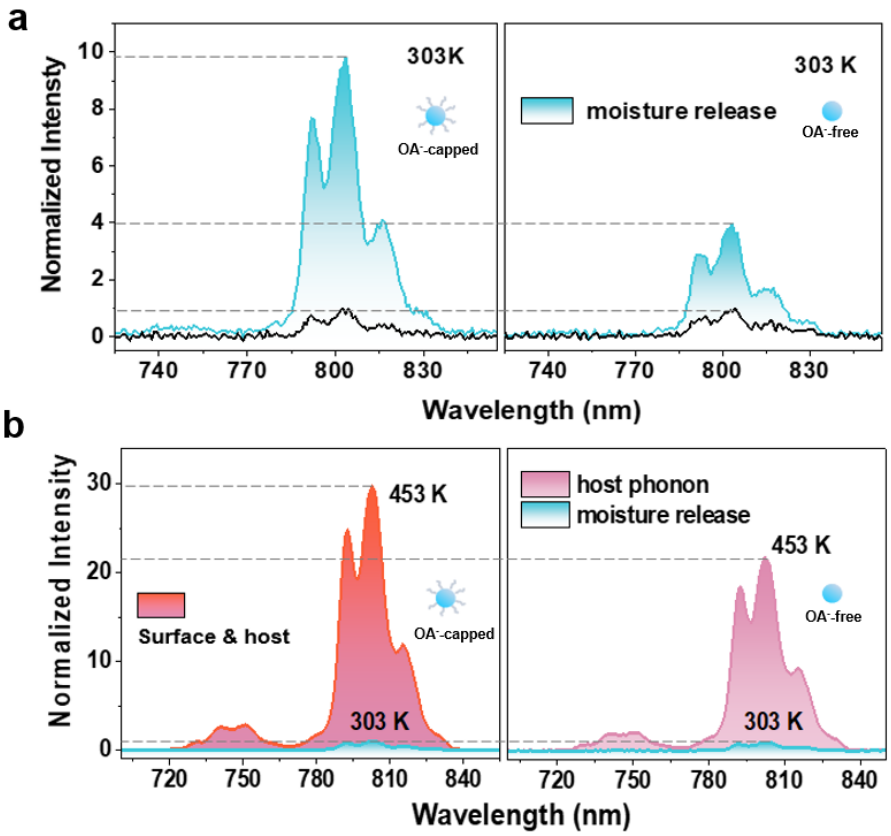

Figure 3.20 Phonon assistance and moisture release when enhancing the anti-Stokes emissions of 10 nm OA-capped and OA-free $NaYF_4$: 20% Yb^{3+}, 6% Nd^{3+} nanoparticles. (a) At room temperature, emission spectra were recorded before (black profiles) and after (cyan profiles) moisture release. (b) The emission spectra at 303 K (cyan profiles) and 453 K (orange and magenta profiles) after moisture release.

Subsequently, the emission spectra before and after moisture release was obtained after the temperature was decreased to 303 K. As shown in Figure 3.20 (a), the increased 800 nm emission band at 303 K from both OA-capped and OA-free samples indicates moisture release.

With the thermal treatment, the quenched emissions were recovered. More significantly, as shown in Figure 3.20 (b), after removing the interference from moisture, we found that the thermal enhancement of OA-capped samples was stronger than that of OA-free samples, as predicted. Thus, the thermal enhancement in the OA-free samples was contributed by only host phonon assistance. As surface treatment did not influence the host environment of the sample, the OA-capped sample should have had equal host phonon assistance with the OA-free sample and the additional surface phonon assistance. By dividing the thermal enhanced emission component caused by the host phonon assistance, the extra emission enhancement in the OA-capped sample originated from the surface phonon assistance.

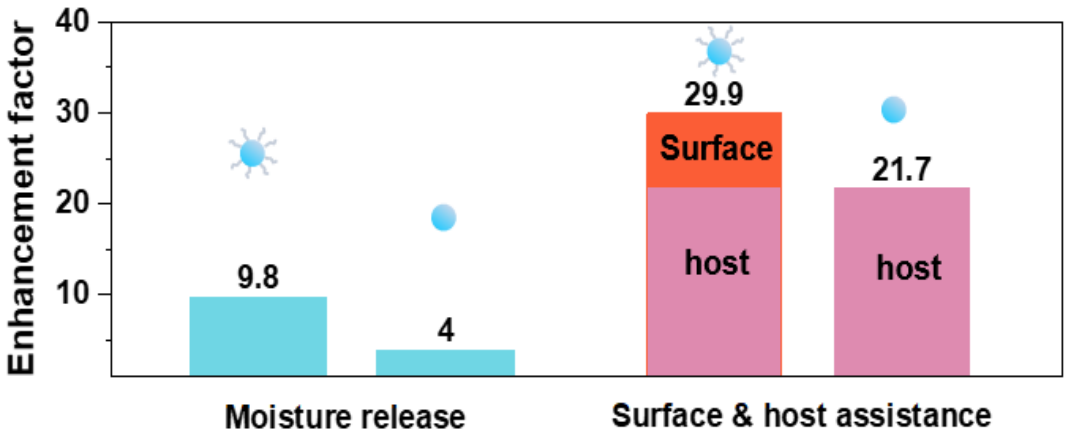

Figure 3.21 Quantitative analysis to reveal the roles of host phonon assistance, surface phonon assistance and moisture release in 10 nm OA-capped and OA-free $NaYF_4$: 20% Yb^{3+}, 6% Nd^{3+} nanoparticles.

Finally, in Figure 3.21, we calculated the enhancement factors of moisture release, which corresponded to enhancements of 9.8- and 4-fold for the OA-capped and OA-free samples, respectively, and the host phonon assistance had a higher contribution (21.7-fold). The surface phonon assistance of OA ligand contributed to the thermal enhancement from a factor of 21.7

to 29.9 (Figure 3.21), which confirmed the importance of the surface mode during the enhancement.

3.5 Conclusion

In summary, we successfully demonstrated that surface phonon assistance by surface ligands occurs in OA-capped $NaYF_4$: Yb^{3+}, Tm^{3+} and $NaYF_4$: Yb^{3+}, Nd^{3+} anti-Stokes nanoparticles. Unlike other structure optimisations that require further modifications of the materials, the surface phonon assistance can be pronounced in the directly synthesised RE doped nanoparticles using the co-precipitation method, which gives a convenience method for achieving high anti-Stokes luminescence and for overcoming the thermal quenching in a thermal field. Compared with the multi-photon upconversion in the Yb^{3+}-Tm^{3+} codoped systems, Yb^{3+}-Nd^{3+} codoping showed a stronger host phonon assistance during the one-photon energy transfer in both OA-capped and OA-free nanoparticles, so that even without the function of surface phonon assistance, the OA-free $NaYF_4$: Yb^{3+}, Nd^{3+} nanoparticles still can fight against the thermal quenching with robust enhanced luminescence, whereas it does not work on OA-free $NaYF_4$: Yb^{3+}, Tm^{3+} nanoparticles.

The fast-growing intensities and lifetimes of the luminescence with temperature indicates the direction for next generation nanothermometers. By reversing the thermal quenching to thermal enhancement, the next generation nanothermometers can provide much better performance for high temperature detection, and the high sensitivity that benefits from the rapid response makes the target measurements more accurate.

3.6 References

1 Guo, Y., Wang, D., He, Y. Fabrication of highly porous Y_2O_3:Ho,Yb ceramic and its thermometric applications. *Journal of Alloys and Compounds* **741**, 1158-1162 (2018).

2 Cao, J., Zhang, J., Li, X. Upconversion luminescence of $Ba_3La(PO_4)_3$:Yb^{3+}-Er^{3+}/Tm^{3+} phosphors for optimal temperature sensing. *Appl Opt* **57**, 1345-1350 (2018).

3 Sedlmeier, A., Achatz, D. E., Fischer, L. H., Gorris, H. H., Wolfbeis, O. S. Photon upconverting nanoparticles for luminescent sensing of temperature. *Nanoscale* **4**, 7090-7096 (2012).

4 Li, D., Shao, Q., Dong, Y., Jiang, J. Anomalous Temperature-dependent upconversion luminescence of small-sized $NaYF_4$:Yb^{3+}, Er^{3+} nanoparticles. *The Journal of Physical Chemistry C* **118**, 22807-22813 (2014).

5 Li, D. D., Shao, Q. Y., Dong, Y., Fang, F., Jiang, J. Q. Ho^{3+}(or Tm^{3+})-activated upconversion nanomaterials: anomalous temperature dependence of upconversion luminescence and applications in multicolor temperature indicating and security. *Particle & Particle Systems Characterization* **32**, 728-733 (2015).

6 Shao, Q., Ouyang, L., Jin, L., Jiang, J. Multifunctional nanoheater based on $NaGdF_4$:Yb^{3+}, Er^{3+} upconversion nanoparticles. *Opt Express* **23**, 30057-30066 (2015).

7 Yu, W., Xu, W., Song, H., Zhang, S. Temperature-dependent upconversion luminescence and dynamics of $NaYF_4$:Yb^{3+}/Er^{3+} nanocrystals: influence of particle size and crystalline phase. *Dalton Trans* **43**, 6139-6147 (2014).

8 Zhou, J. *et al.* Activation of the surface dark-layer to enhance upconversion in a thermal field. *Nature Photonics* **12**, 154-158 (2018).

9 Hu, Y., Shao, Q., Zhang, P., Dong, Y., Fang, F., Jiang, J. Mechanistic investigations on the dramatic thermally induced luminescence enhancement in upconversion nanocrystals. *The Journal of Physical Chemistry C* **122**, 26142-26152 (2018).

10 Zhou, S., Li, C., Liu, Z., Li, S., Song, C. Thermal effect on up-conversion in Er^{3+}/Yb^{3+} co-doped silicate glass. *Optical Materials* **30**, 513-516 (2007).

11 Ma, C. *et al.* Optimal sensitizer concentration in single upconversion nanocrystals. *Nano Lett* **17**, 2858-2864 (2017).

12 Nadort, A. *et al.* Quantitative imaging of single upconversion nanoparticles in biological tissue. *PLoS One* **8**, e63292 (2013).

13 Rodriguez-Sevilla, P. *et al.* Assessing single upconverting nanoparticle luminescence by optical tweezers. *Nano Lett* **15**, 5068-5074 (2015).

14 Han, S. *et al.* Multicolour synthesis in lanthanide-doped nanocrystals through cation exchange in water. *Nat Commun* **7**, 13059 (2016).

15 Brites, C. D. *et al.* Thermometry at the nanoscale. *Nanoscale* **4**, 4799-4829 (2012).

16 Gao, G. *et al.* Wide-range non-contact fluorescence intensity ratio thermometer based on Yb^{3+}/Nd^{3+} co-doped La_2O_3 microcrystals operating from 290 to 1230 K. *Journal of Materials Chemistry C* **6**, 4163-4170 (2018).

17 Xu, W., Song, Q., Zheng, L., Zhang, Z., Cao, W. Optical temperature sensing based on the near-infrared emissions from Nd^{3+}/Yb^{3+} codoped $CaWO_4$. *Opt Lett* **39**, 4635-4638 (2014).

18 Xu, W., Qi, H., Zheng, L., Zhang, Z. & Cao, W. Multifunctional nanoparticles based on the Nd^{3+}/Yb^{3+} codoped $NaYF_4$. *Opt Lett* **40**, 5678-5681 (2015).

19 Brites, C. D. S., Millán, A., Carlos, L. D. in *Handbook on the Physics and Chemistry of Rare Earths* Vol. 49, 89 (2016).

20 Pollnau, M., Gamelin, D. R., Lüthi, S. R., Güdel, H. U., Hehlen, M. P. Power dependence of upconversion luminescence in lanthanide and transition-metal-ion systems. *PHYSICAL REVIEW B* **61**, 10 (2000).

21 Lu, Y. *et al.* Tunable lifetime multiplexing using luminescent nanocrystals. *Nature Photonics* **8**, 32-36 (2013).

22 Zhou, L. *et al.* High-capacity upconversion wavelength and lifetime binary encoding for multiplexed biodetection. *Angew Chem Int Ed Engl* **57**, 12824-12829 (2018).

23 Deng, R. *et al.* Temporal full-colour tuning through non-steady-state upconversion. *Nat Nanotechnol* **10**, 237-242 (2015).

24 Mi, C., Wu, J., Yang, Y., Han, B., Wei, J. Efficient upconversion luminescence from $Ba_5Gd_8Zn_4O_{21}:Yb^{3+}$, Er^{3+} based on a demonstrated cross-relaxation process. *Sci Rep* **6**, 22545 (2016).

25 Bednarkiewicz, A. *et al.* Giant enhancement of upconversion in ultra-small $Er^{3+}/Yb^{3+}:NaYF_4$ nanoparticles via laser annealing. *Nanotechnology* **23**, 145705 (2012).

CHAPTER 4

Ultra-sensitive nanothermometer design by surface phonon assistance

In this results chapter, a new method to fabricate ultra-sensitive ratiometric nanothermometers is proposed based on the surface and host phonon assistance in $NaYF_4$: Yb^{3+}, Nd^{3+} anti-Stokes nanoparticles. To take advantage of the reliable ratiometric nanothermometry approach, we combined the thermal quenching and the thermal enhancement in one nanothermometer using a second emitter Er^{3+}. With the formed high intensity contrast, we observed a high relative sensitivity up to 7.6%/K in the tri-doped $NaYF_4$: Yb^{3+}, Nd^{3+}, Er^{3+} nanoparticles. By further optimisation via different sample structure design and doping concentrations, we finally promoted the temperature sensitivity to around 10%/K by a sandwich multi-section nanorod structure, which is the most sensitive RE doped nanothermometer reported thus far. These results indicate the feasibility of the new method to create high-sensitive luminescence nanothermometers for high spatial resolution temperature sensing applications.

4.1 Introduction

As discussed in Chapter 1, nanothermometry provides a potent tool to monitor the temperature change within biosystems and micromechanical systems to understand their functions. At present, the goal for this field is to challenge the level of sensitivity and dynamic range, with photostability and repeatability. RE doped anti-Stokes emission nanocrystals have the advantages of structure stability, non-photobleaching behaviour and low background luminescence noise, and show great potential in luminescent nanothermometry. The

conversional method uses the florescence intensity ratio between two thermal coupled energy states, whose electronic state populations obey the Boltzmann thermal equilibrium, thus the temperature can be calculated by the intensity ratio[1-4]. Nonetheless, because these energy states are close to each other to be thermally coupled, they usually have similar temperature dependences that are influenced by thermal quenching, leading to a slow change of emission intensity ratio with temperature. Generally, RE doped nanocrystals have wide operation ranges of hundreds of degrees, but maximum sensitivity only around 1%/K, and the average sensitivity in a wide working range is even lower[5].

By confirming the phonon-enhanced upconversion in the Yb^{3+}, Nd^{3+} system, we realised that this new thermal property could be applied to develop a new generation of nanothermometers. In consideration of the superiorities of the introduced ratiometric nanothermometers, we preferred to create a dual-emitter nanothermometer for the intensity ratio change rather than the defective single emission intensity dependent nanothermometer. More importantly, besides the thermal enhanced ~800 nm emission band from Nd^{3+}, the other emission band from a second emitter should have thermal properties in high contrast to the Nd^{3+} emission, thus aiming to achieve a high temperature-sensitive intensity ratio[6-8]. Thus, an emission band with thermal quenching behaviour is the ideal candidate, even though it will quench at high temperatures, choosing an efficient emitter will make up for this deficiency.

Here, we used Er^{3+} as the second activator for the quenching segment based on its thermal quenching behaviour and efficient energy transfer of $Yb^{3+}\rightarrow Nd^{3+}$. Their well-matched excited states allowed for efficient energy transfer from Yb^{3+} to Er^{3+} without the requirement of phonon assistance, which is irrelevant to the thermal enhancing process. This design also allowed traditional temperature sensing by measuring the Boltzmann distribution of thermal coupled levels in the Er^{3+} ion. With a nanoscale structure design and doping engineering, emissions from Nd^{3+} and Er^{3+} in the nanothermometer showed opposite evolution trends to that of

temperature change, leading to the rapid change of emission intensity ratio for ultra-high sensitivity.

4.2 Nanothermometer structure optimisation

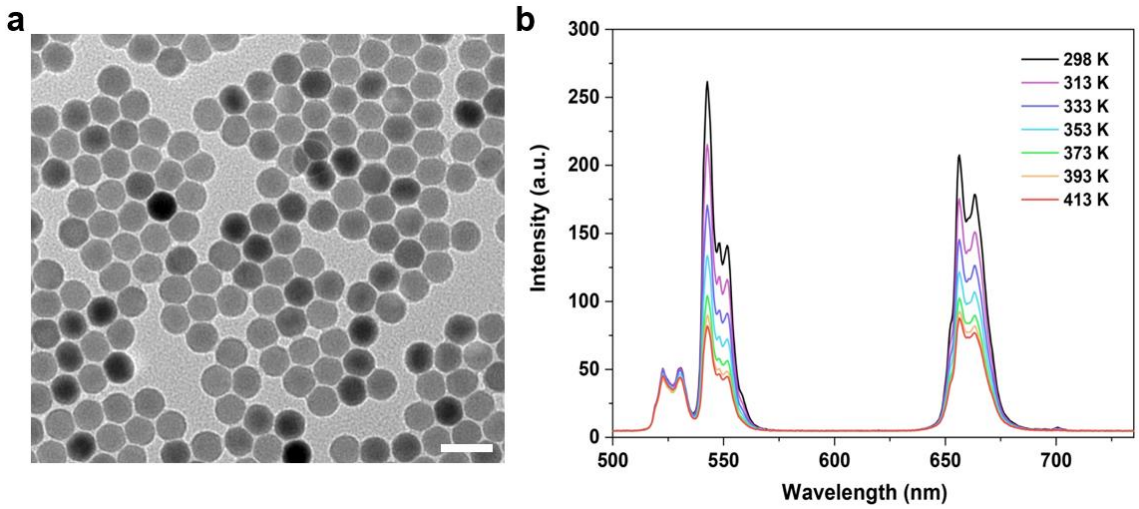

Figure 4.1 Thermal quenching in the upconversion emission of 29 nm $NaYF_4$: 20% Yb^{3+}, 2% Er^{3+} at elevated temperature. (a) TEM images show the size and morphology of $NaYF_4$: 20% Yb^{3+}, 2% Er^{3+} nanoparticles. Scale bar is 50 μm. (b) From 298 K to 413 K, the multi-phonon relaxation became stronger, which resulted in decreased emission intensities. The sample was excited by 1 W/cm^2 980 nm laser.

Before doped Er^{3+} ions into the $NaYF_4$: Yb^{3+}, Nd^{3+} nanoparticles, we confirmed their thermal quenching property, as shown in Figure 4.1. By increasing the temperature from 298 K to 413 K, we observed that luminescence decayed by more than half at two emission peaks around 550 nm and 660 nm, which resulted from the thermal quenching[9]. Only the small emission band around 525 nm barely changed with temperature because of the Boltzmann distribution that high temperature will induce repopulation in the ~525 nm excited state coming from the ~550 nm emission excited state. Therefore, choosing the ~660 nm emission band of Er^{3+} to cooperate with the ~800 nm emission band in Nd^{3+} is promising for high-sensitive ratiometric temperature sensing. Additionally, both the ~660 nm and ~800 nm emission bands belong to

the biology optical window that has deep tissue penetration for bioluminescence imaging applications.

4.2.1 Yb^{3+}-Nd^{3+}-Er^{3+} tri-doping structure

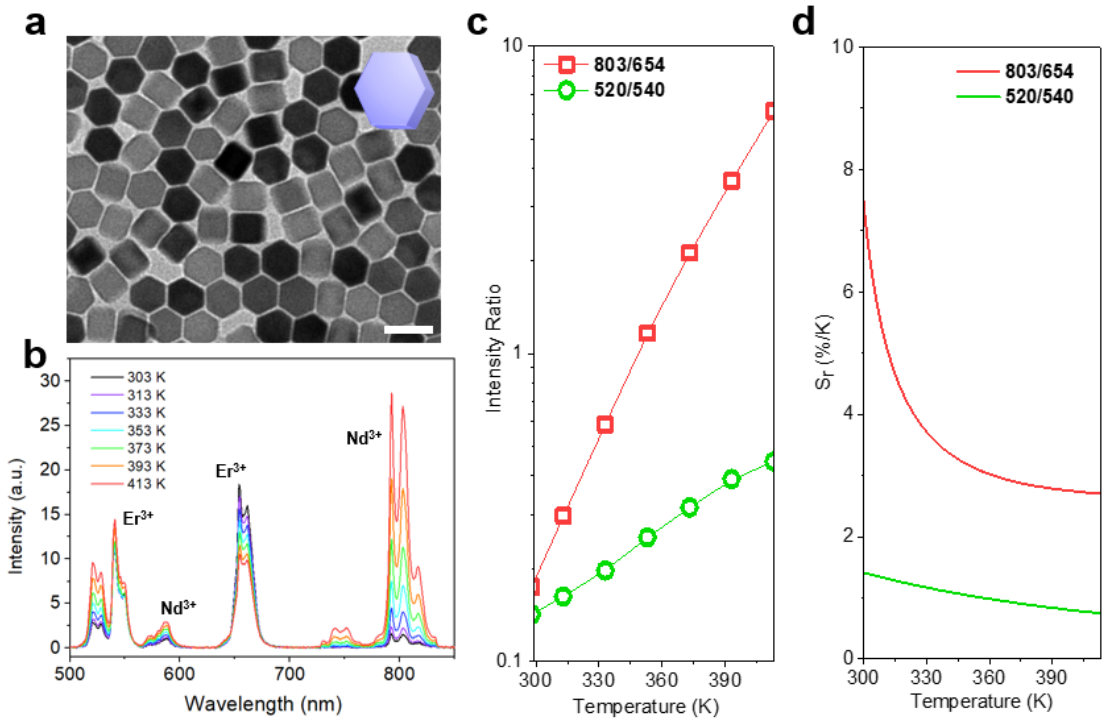

Figure 4.2 Tri-doping $NaYF_4$: 20% Yb^{3+}, 6% Nd^{3+}, 0.5% Er^{3+} nanoparticles for temperature sensing at elevated temperatures. (a) TEM images show the size and morphology of $NaYF_4$: 20% Yb^{3+}, 6% Nd^{3+}, 0.5% Er^{3+} nanoparticles. Scale bar is 40 nm. (b) The spectra of both Nd^{3+} and Er^{3+} emissions from 303 K to 413 K. (c) The luminescence intensity ratio of ~803 nm emission to 654 nm emission as a function of temperature, with the ~520 nm emission to 540 nm emission ratio from thermal coupled levels of Er^{3+} shown as a contrast. (d) The calculated relative sensitivities for two intensity ratios indicate the much better performance of the Nd^{3+}-Er^{3+} dual-emitter nanothermometer. The sample was excited by 1 W/cm^2 980 nm laser.

The first structure we studied was the tri-doping $NaYF_4$: 20% Yb^{3+}, 6% Nd^{3+}, 0.5% Er^{3+} nanoparticles. By a simple co-precipitation synthesis, the prepared tri-doping structure did not require further epitaxial growth by the hot-injection method. As shown in Figure 4.2 (a), the

$NaYF_4$: 20% Yb^{3+}, 6% Nd^{3+}, 0.5% Er^{3+} nanoparticles were approximately 36 nm and were very uniform. By testing the temperature-dependent spectra from 303 K to 413 K in Figure 4.2 (b), the sample showed multiple emission bands not only from Nd^{3+} around 580 nm, 750 nm and 800 nm, but also from Er^{3+} around 525 nm, 540 nm and 654 nm, which confirmed that both emitters were successfully doped in the nanoparticles. Moreover, as expected, although the Nd^{3+} ions and Er^{3+} shared the same lattice environment in the host material $NaYF_4$, they produced distinctly different optical properties under the elevated temperature, i.e. the ~654 nm emission from Er^{3+} decreased quickly and the ~800 nm emission from Nd^{3+} kept increasing, similar to when they were studied separately. Further, the intensity ratio of 803 nm to 654 nm emission peaks was calculated in Figure 4.2 (c). At room temperature, the intensity ratio was approximately 0.2, with this value increasing exponentially to near 7 when the temperature reached 413 K. For comparison purposes, the intensity ratio of 520 nm to 540 nm emission from the thermal coupled energy levels in Er^{3+} was also investigated, which changed more slowly to temperature than that of the Nd^{3+}-Er^{3+} intensity ratio. Therefore, the feasibility of this method to form a high contrast intensity change was proven.

Undoubtedly, the relative sensitivity of the dual-emitter $NaYF_4$: 20% Yb^{3+}, 6% Nd^{3+}, 0.5% Er^{3+} nanothermometer achieved a high level above 7.5%/K around room temperature and remained higher than 2%/K over a wide temperature range, as indicated in Figure 4.2 (d). However, the relative sensitivity based on the thermal coupled energy level in Er^{3+} was lower than 2%/K, which was similar to the reported data. With the improved temperature sensing performance, the $NaYF_4$: 20% Yb^{3+}, 6% Nd^{3+}, 0.5% Er^{3+} nanothermometer has great potential to undertake highly accurate detection measurements.

By a simple tri-doping structure, we have improved the nanothermometry sensitivity by several times compared to the conventional method. Nevertheless, we recognise that optimisation is still necessary, and the tri-doping structure is not the most suitable structure as it has one fatal

weakness. The two emitters are distributed close to each other in the lattice; therefore, the energy transfer in the $NaYF_4$: Yb^{3+}, Nd^{3+}, Er^{3+} cannot be simply explained by Yb^{3+}→Nd^{3+} and Yb^{3+}→Er^{3+}, i.e. there still exists a third energy transfer system between Nd^{3+} and Er^{3+}, which can be called cross-relaxation. The cross-relaxation is uncontrollable in a tri-doping structure and it may lead to energy loss in the interlaced energy transfer systems and unbalance the emission intensities among different emitters[10,11]. When we attempted to optimise the Er^{3+} doping concentration from 0.5% to 1%, we found that the emission of Nd^{3+} disappeared in the $NaYF_4$: 20% Yb^{3+}, 6% Nd^{3+}, 1% Er^{3+} sample, which can be explained by a cross-relaxation process between Nd^{3+} and Er^{3+}, as shown in Figure 4.3. The higher concentration and excited states of Nd^{3+} compared to Er^{3+} benefited the possible cross-relaxation from $^4F_{3/2}$ in Nd^{3+} to $^4I_{11/2}$ in Er^{3+}. Thus, the uncontrollable cross-relaxation relationship limits the optimisation on a tri-doped $NaYF_4$: Yb^{3+}, Nd^{3+}, Er^{3+} structure.

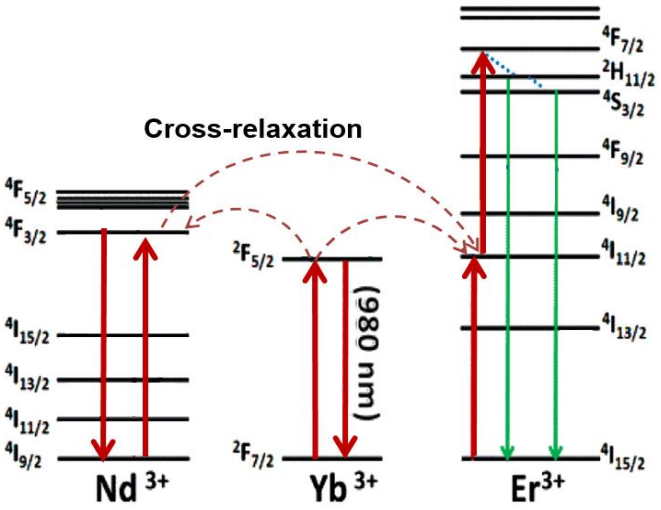

Figure 4.3 The possible cross-relaxation process between the dual emitters in a tri-doped $NaYF_4$: Yb^{3+}, Nd^{3+}, Er^{3+} sample under 980 nm laser excitation.

4.2.2 Core-shell-shell structure

In consideration of the drawback in the tri-doping $NaYF_4$: Yb^{3+}, Nd^{3+}, Er^{3+} nanothermometer, we focused on the new core-shell structure design. As mentioned, core-shell structures have

been widely applied in the study of RE doped upconversion nanoparticles. By doping different types of RE ions in each separate layer, the energy transfer direction can be controlled[12-14]. Thus, our first plan was to prepare $NaYF_4$: Yb^{3+}, Er^{3+} nanoparticles as a core sample, then epitaxially grow an inert shell of pure $NaYF_4$ and an active shell of $NaYF_4$: Yb^{3+}, Nd^{3+}. Thus, the energy transfer between the Er^{3+} and Nd^{3+} was blocked by the inert shell. Moreover, the active shell of $NaYF_4$: Yb^{3+}, Nd^{3+} with a large surface should have produced surface phonon assistance for thermal enhanced emission.

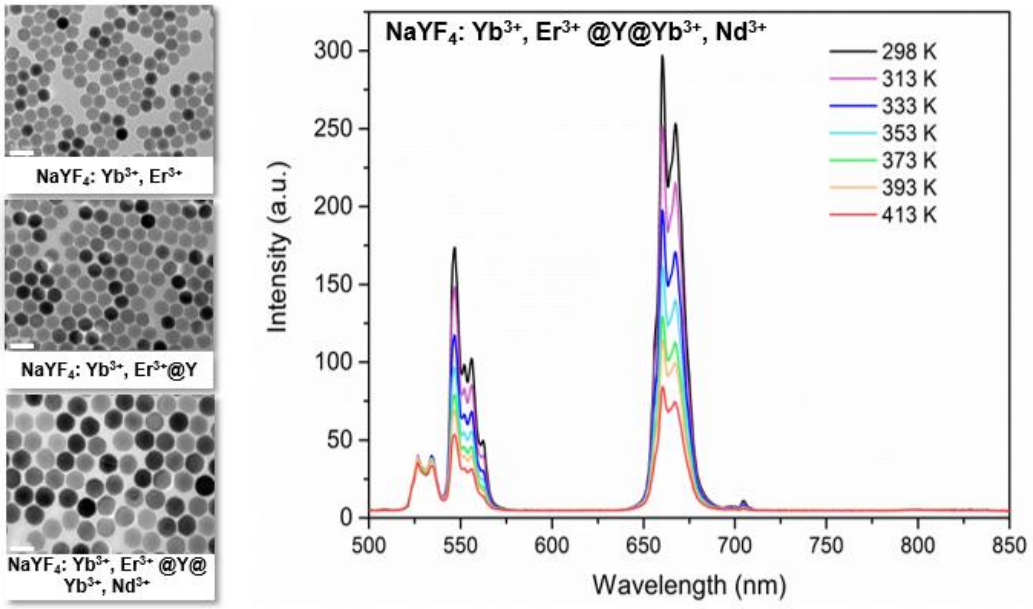

Figure 4.4 Temperature-dependent spectra from core-shell-shell structure $NaYF_4$: 20% Yb^{3+}, 0.5% Er^{3+} @Y@20% Yb^{3+}, 6% Nd^{3+} nanoparticles, TEM results of the core $NaYF_4$: Yb^{3+}, Er^{3+} (22 nm), core-shell $NaYF_4$: Yb^{3+}, Er^{3+}(31 nm) @Y and $NaYF_4$: Yb^{3+}, Er^{3+} @Y@Yb^{3+}, Nd^{3+}(40 nm) are also presented. Scale bar is 50 nm. The sample was excited by 1 W/cm^2 980 nm laser.

However, the experimental result showed that this core-shell-shell structure was not feasible. As shown in Figure 4.4, the size of each component of the core-shell-shell structure $NaYF_4$: Yb^{3+}, Er^{3+} @Y@Yb^{3+}, Nd^{3+} nanoparticles was checked by TEM images and showed that the layer of $NaYF_4$: Yb^{3+}, Nd^{3+} was approximately 5 nm thick, which should be enough volume

for strong emissions. However, from the temperature-dependent spectra measurement, the emission bands of Nd^{3+} totally vanished, even under a high sensitivity setting for low light detection. By increasing the temperature to 413 K, the emission from Er^{3+} showed strong thermal quenching, whereas the ~800 nm emission band was still not observed.

The vanishing of emission bands from Nd^{3+} can be explained by the surface quenching, which was caused by surface defects in the nanomaterials[15]. By epitaxial growth of the $NaYF_4$: Yb^{3+}, Nd^{3+} layer on the surface of the core nanoparticle, there must be denser distribution of lattice defects in the outside shell than that in the inside core area. Additionally, the energy mismatch of Yb^{3+} and Nd^{3+} made the energy transfer in $NaYF_4$: Yb^{3+}, Nd^{3+} layer harder. In another experiment, the layer thickness of $NaYF_4$: Yb^{3+}, Nd^{3+} increased to 9 nm; however, the emission around 800 nm was still undetectable.

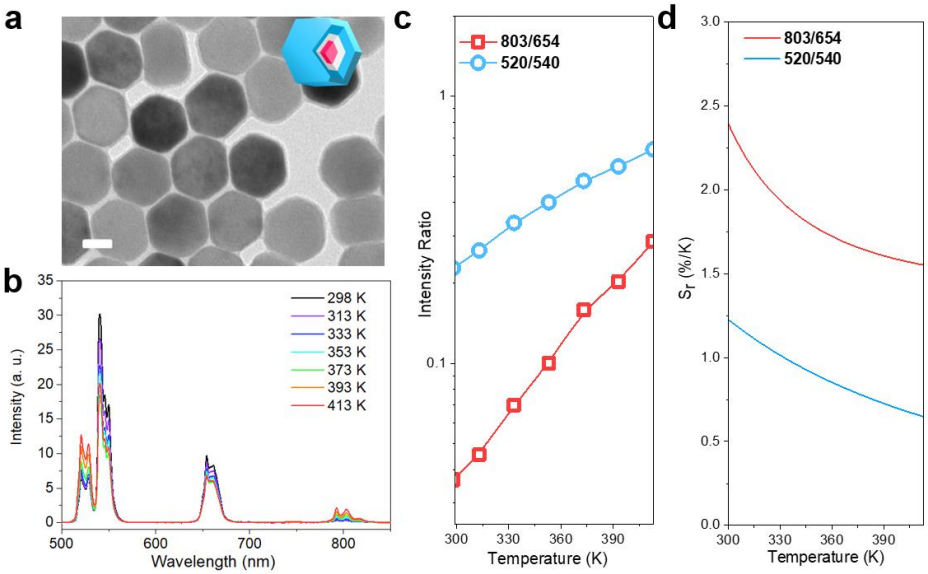

Figure 4.5 Core-shell-shell structure of $NaYF_4$: 20% Yb^{3+}, 6% Nd^{3+} @Y@20% Yb^{3+}, 0.5% Er^{3+} nanoparticles for temperature sensing. (a) TEM image of the prepared core-shell-shell structure sample. Scale bar is 20 nm. (b) Temperature-dependent emission spectra. (c) Intensity ratios of 803 nm to 654 nm emission and 520 nm to 540 nm emission. (d) The

corresponding relative sensitivity of intensity ratios to temperature. The sample was excited by 1 W/cm^2 980 nm laser.

In view of the failed experiment, we moved to the core-shell structure of $NaYF_4$: Yb^{3+}, Nd^{3+} @Y@Yb^{3+}, Er^{3+}. After changing the position of the Yb^{3+}-Nd^{3+} codoping part from the surface to the core, we repeated the experiment. The 44 nm core-shell-shell structure $NaYF_4$: 20% Yb^{3+}, 6% Nd^{3+} @Y@20% Yb^{3+}, 0.5% Er^{3+} nanoparticles in Figure 4.5 (a) were synthesised using a 24 nm $NaYF_4$: 20% Yb^{3+}, 6% Nd^{3+} core, and both the inert and active layers were coated by hot-injection with a thickness of approximately 5 nm. Under the same test conditions, the laser induced emission spectra from 298 K to 413 K showed the emission bands from both the emitters. Similar to the tri-doped sample, the 800 nm emission bands were in direct proportion to temperature; however, the increase rate was much lower than the tri-doped sample, which only showed emission enhancement of approximately 6-fold. These results can be explained by the sample structure, in which the inner core of $NaYF_4$: 20% Yb^{3+}, 6% Nd^{3+} lost the surface phonon assistance for fast thermal enhancement owing to blockage by the coated shell. Although the 800 nm 650 nm emissions still responded to temperature in opposite directions, the intensity ratio of the Nd^{3+} to Er^{3+} emission and the corresponding sensitivity in Figure 4.5 (c) and (d) are not as promising as the results from the tri-doped sample. However, the 803 nm to 654 nm emission ratio still had better performance for temperature sensing than that of the thermal coupled emission band ratio 520/540 from Er^{3+}.

In this section, we investigated the Nd^{3+}-Er^{3+} in dual-emitter core-shell structure for nanothermometry, even though the core-shell-shell structure $NaYF_4$: Yb^{3+}, Er^{3+} @Y@Yb^{3+}, Nd^{3+} nanoparticles were the best structure for thermal enhanced ~800 nm emission with surface phonon assistance and the thermal quenched ~654 nm emission without surface phonon assistance. The experimental results proved that the assumption was invalid as the ~800 nm emission from the external layer of Nd^{3+} could not fight against the surface quenching. With a

second structure by doping Nd^{3+} in the core, the situation improved but was still not ideal for high sensitivity. Based on the above analysis, the core-shell structure was not suitable for the high-sensitive surface phonon assisted nanothermometer design.

4.2.3 Sandwich structure nanorod

The hot-injection method can also be used to synthesise the multi-section nanorod structure with one longitudinal epitaxial growth, as introduced in Chapter 2. Based on this method, a sandwich structure nanorod was designed. In this structure, each section of the nanorod had an exposed surface, thus the surface phonon assistance still worked for the ~800 nm emission band thermal enhancement even when the $Yb^{3+}$and Nd^{3+} were codoped in the core. Moreover, the volume for each different doping section was well controlled because the width of the multi-section nanorod was barely changed during the epitaxial growth[16]. Thus, the luminescence intensities from both emitters of Nd^{3+} and Er^{3+} in different sections could be regulated to avoid the wide gaps between the two emissions.

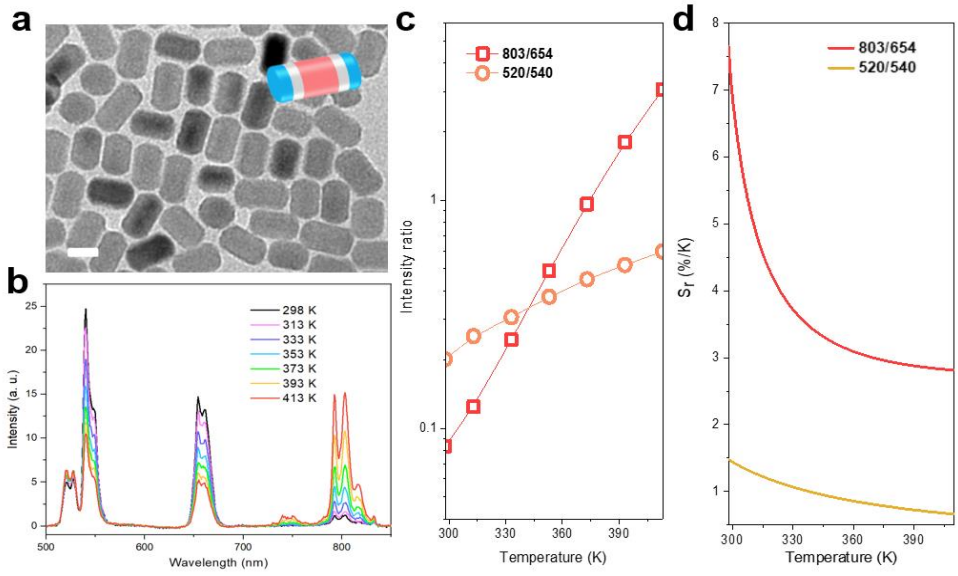

Figure 4.6 The sandwich structure nanorods $NaYF_4$: 20% Yb^{3+}, 6% Nd^{3+}/Y/20% Yb^{3+}, 0.5% Er^{3+} for temperature sensing. (a) TEM image of the prepared sandwich structure nanorods sample. Scale bar is 20 nm. (b) Temperature-dependent emission spectra. (c) Intensity ratios

of 803 nm to 654 nm emission and 520 nm to 540 nm emission. (d) The corresponding relative sensitivity of intensity ratios to temperature. The sample was excited by 1 W/cm^2 980 nm laser.

In Figure 4.6 (a), after the hot-injection process, the synthesised 36 nm multi-section nanorods $NaYF_4$: 20% Yb^{3+}, 6% Nd^{3+}/Y/20% Yb^{3+}, 0.5% Er^{3+} grew from 22 to 36 nm longitudinally, whereas the width was maintained at approximately 22 nm, which was similar to the core. In the temperature-dependent spectra test, all the emission bands showed the desirable change trend with temperature. Which was similar to the results of the tri-doped nanoparticles. Similarly, the intensity ratio and the relative sensitivity were analysed based on the two groups of emission bands around 654 nm and 800nm and the emission around 520 nm and 540 nm. As predicted, the sensitivity based on the two green emissions of 520 nm and 540 nm stayed low under 2%, irrespective of how the sample structure changed. The sensitivity for the ratio of 803 nm to 654 nm achieved a maximum value at 7.7%/K, which was slightly higher than the value of the tri-doped nanothermometer. Although the sensitivity decreased at higher temperatures, it was always higher than 2.5%/K in the wide working range, and the sensitivity obtained by the conventional method based on the thermal coupled levels was nowhere near to the new method.

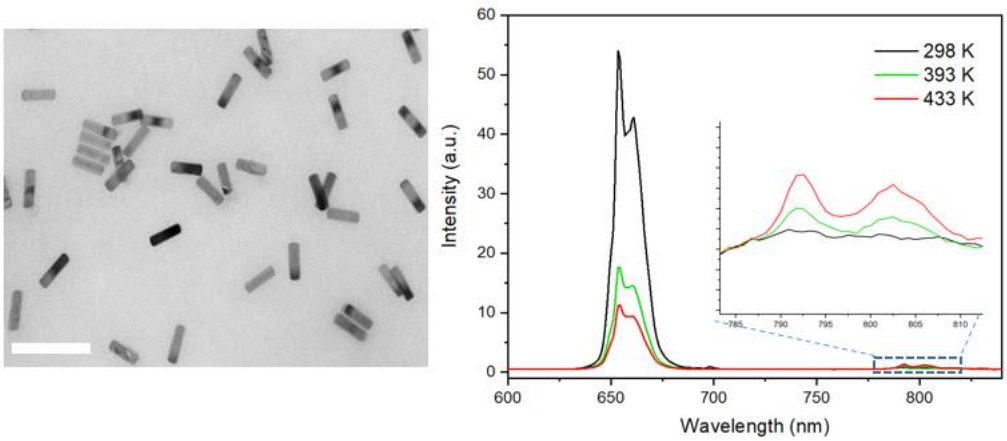

Figure 4.7 Temperature-dependent spectra of the sandwich structure nanorods $NaYF_4$: 20% Yb^{3+}, 2% Er^{3+}/Y/20% Yb^{3+}, 1% Nd^{3+} for temperature sensing. TEM image shows the prepared

sandwich structure nanorods around 86 nm in length and 27 nm in width. Scale bar is 200 nm. The sample was excited by 1 W/cm^2 980 nm laser.

Moreover, we synthesised another structure of nanorods with Er^{3+} doping in the middle section and Nd^{3+} doping at the two ends in Figure 4.7. The aim was to have a greater exposed surface on the Nd^{3+} doped section for surface phonon assistance. The TEM image showed the synthesised nanorods $NaYF_4$: 20% Yb^{3+}, 2% Er^{3+}/Y/20% Yb^{3+}, 1% Nd^{3+} having a length of ~86 nm, while each section of the $NaYF_4$: 20% Yb^{3+}, 1% Nd^{3+} at the two ends was estimated to be 26 nm. Even with such large volumes of $NaYF_4$: 20% Yb^{3+}, 1% Nd^{3+}, the emission from Nd^{3+} was still weak, as shown in the enlarged area of the emission spectra. By increasing the temperature from room temperature to 433 K, the thermal enhancement in the ~800 emission band was only approximately 4-fold. The weak emission and the low thermal enhancement from Nd^{3+} indicated that the surface quenching must be too strong to be defeated in this $NaYF_4$: Yb^{3+}, Er^{3+}/Y/Yb^{3+}, Nd^{3+} multi-section nanorod structure, which was a similar result to that obtained for the core-shell structure $NaYF_4$: Yb^{3+}, Er^{3+}@Y@Yb^{3+}, Nd^{3+} by doping Nd^{3+} via epitaxial growth of the $NaYF_4$: Yb^{3+}, Er^{3+} core.

4.2.4 Discussion

Based on all the investigated sample structures including the tri-doping structure, core-shell structure and multi-section nanorod structure, we preliminarily confirmed the performance of the Nd^{3+}-Er^{3+} dual-emitter nanothermometers. Owing to the strong surface quenching for luminescence of the Yb^{3+}-Nd^{3+} system, we could not synthesise the Nd^{3+} layer on to the sample with epitaxial growth. Simultaneously, to guarantee the surface phonon assistance for the ~800 emission band, the Nd^{3+} doping part of the sample must have an exposed surface to realise the energy transfer from the surface ligand.

Therefore, the tri-doping nanoparticles and the sandwich structure nanorods with Nd^{3+} doping in the middle section were the eligible candidates. Both structures showed great potential for nanothermometry by their high sensitivities over a wide temperature range. However, in consideration of the strong cross-relaxation in tri-doping nanoparticles, the doping concentration optimisation for higher temperature sensing sensitivity was difficult to undertake. In contrast, the sandwich structure nanorods had better flexibility for different doping concentrations in each section because the energy transfer was controllable.

4.3 Optimisation of the sandwich structure nanorods

4.3.1 Doping concentration optimisation

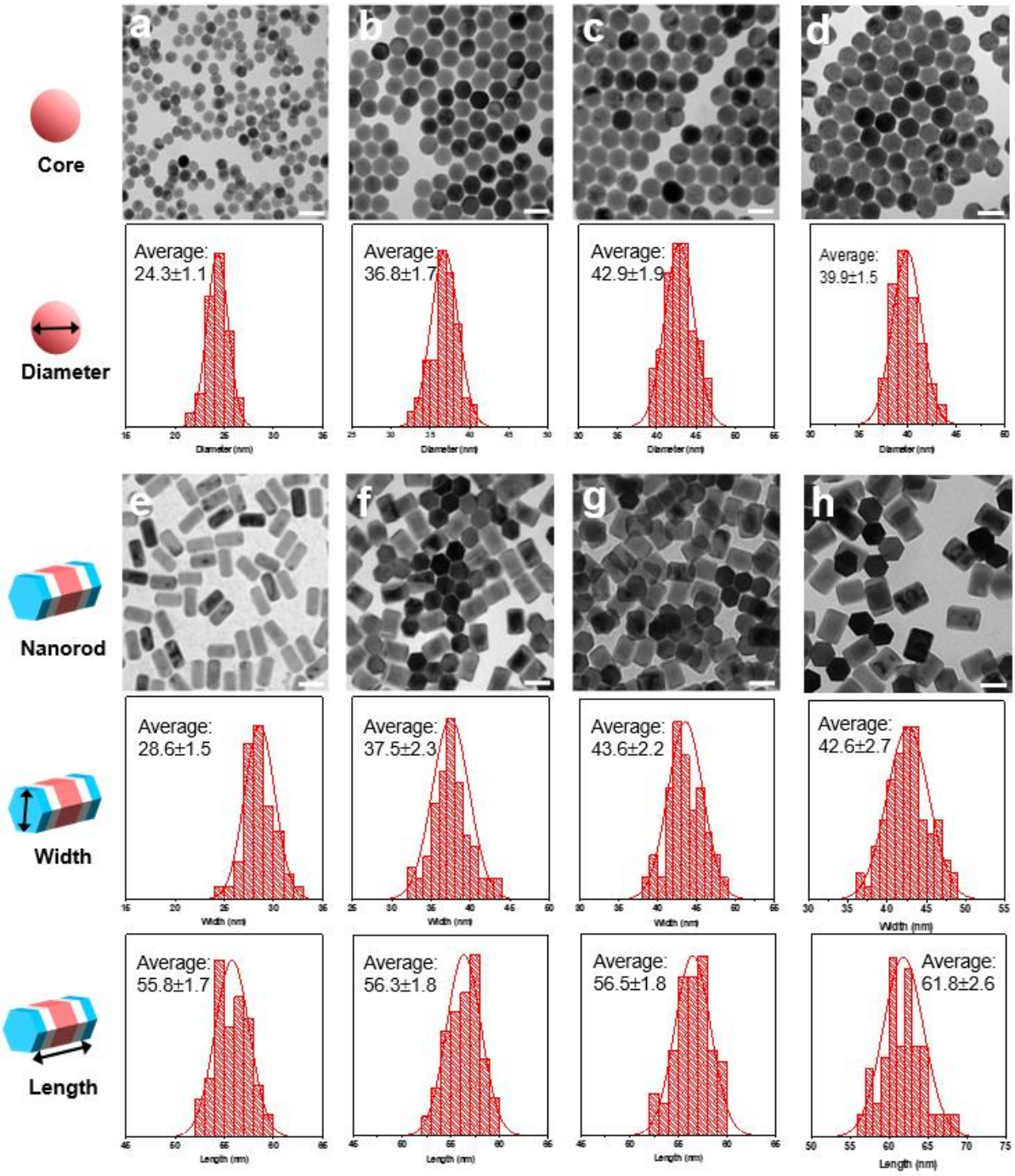

Figure 4.8 TEM images and size distributions of the core nanoparticles $NaYF_4$: Yb^{3+}, Nd^{3+} and sandwich structure nanorods $NaYF_4$: Yb^{3+}, Nd^{3+}/Y/ Yb^{3+}, Er^{3+} with different doping concentration. (a) $NaYF_4$: 60% Yb^{3+}, 4% Nd^{3+} (b) $NaYF_4$: 60% Yb^{3+}, 6% Nd^{3+} (c) $NaYF_4$: 60%

Yb^{3+}, 6% Nd^{3+} (d) $NaYF_4$: 60% Yb^{3+}, 4% Nd^{3+} (e) $NaYF_4$: 60% Yb^{3+}, 4% Nd^{3+}/Y/ 40% Yb^{3+}, 4% Er^{3+} (f) $NaYF_4$: 60% Yb^{3+}, 6% Nd^{3+}/Y/ 20% Yb^{3+}, 2% Er^{3+} (g) $NaYF_4$: 60% Yb^{3+}, 6% Nd^{3+}/Y/ 40% Yb^{3+}, 4% Er^{3+} (h) $NaYF_4$: 60% Yb^{3+}, 4% Nd^{3+}/Y/ 20% Yb^{3+}, 2% Er^{3+}. Scale bar is 50 nm.

A general strategy for enhancing upconversion luminescence in RE doped materials is doping concentration optimisation, including both the doped sensitiser ions and the emitter ions. Here, this strategy was used to achieve the highest sensitivity in sandwich structure nanorods $NaYF_4$: Yb^{3+}, Nd^{3+}/Y/ Yb^{3+}, Er^{3+} for temperature sensing. Figure 4.8 shows the synthesised $NaYF_4$: Yb^{3+}, Nd^{3+} nanoparticles as the core, and the sandwich structure nanorods with epitaxial growth of $NaYF_4$: Yb^{3+}, Er^{3+} at the two ends, which all had the same structure as that of the studied sandwich structure nanorods in Figure 4.6 but different doping concentrations. The TEM images confirmed that the core nanoparticles and the nanorods had uniform sizes and morphologies. The size distributions for each sample were also given as a reference. All the Yb^{3+}-Nd^{3+} codoped samples had a 60% Yb^{3+} doping concentration in accordance with the previous results of higher ~800 nm emission thermal enhancement in 60% Yb^{3+} doped nanoparticles than that of the 20% Yb^{3+} doped nanoparticles. For the Yb^{3+}-Er^{3+} codoping section, two doping concentrations of Yb-Er^{3+}, including the ratio of 20%:2% and 40%:4% of Yb^{3+}:Er^{3+}, were used to find the most suitable thermal quenching for high sensitivity.

After the epitaxial growth of the $NaYF_4$ section and $NaYF_4$: Yb^{3+}, Er^{3+} section successively, the width of the synthesised nanorod was still similar to the diameter of the corresponding core nanoparticles, whereas the length of the nanorod was much longer than the size of the core. Therefore, the successful shape-controllable synthesis of the nanorod made the core sample only grow along the longitudinal direction as expected. Although most of the nanorods grew with ~2 nm in width compared to the core, the coated layer was not sufficient to block the phonon assistance from the lateral surface to the Yb^{3+}-Nd^{3+} doped core. Additionally, as all the

nanorods in Figure 4.8 (e) are in a flat position, the sample width is represented by the diagonal line in the cross-section, which should be larger than the true width as illustrated.

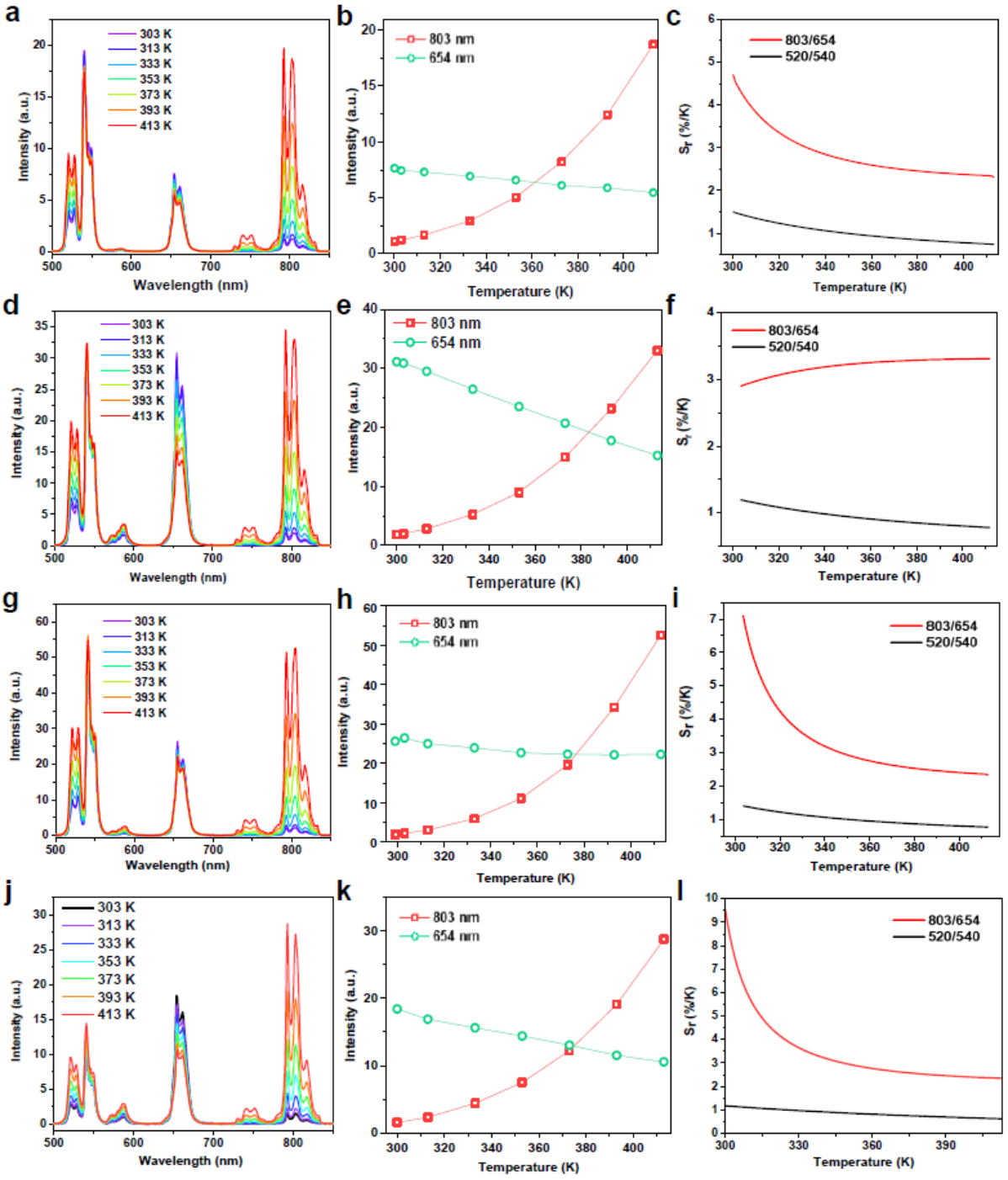

Figure 4.9 Optimisation of the sandwich structure nanorods working as nanothermometers. The results show the temperature-dependent spectra, emission intensity changes and relative sensitivities of $NaYF_4$: 60% Yb^{3+}, 4% Nd^{3+}/$NaYF_4$/$NaYF_4$: 40% Yb^{3+}, 4% Er^{3+} (a, b, c), $NaYF_4$:

60% Yb^{3+}, 6% Nd^{3+}/$NaYF_4$/$NaYF_4$: 20% Yb^{3+}, 2% Er^{3+} (d, e, f), $NaYF_4$: 60% Yb^{3+}, 6% Nd^{3+}/$NaYF_4$/$NaYF_4$: 40% Yb^{3+}, 4% Er^{3+}(g, h, i), and $NaYF_4$: 60% Yb^{3+}, 4% Nd^{3+}/Y/ 20% Yb^{3+}, 2% Er^{3+}(j, k, l).

Then, the temperature-dependent spectra was measured for the family of synthesised sandwich structure nanorods to show their thermometric properties. As shown in Figure 4.9 (a), (d), (g) and (j), all the emission spectra consisted of multiple emission bands from 500 nm to 820 nm, which arose from both Nd^{3+} and Er^{3+}. By increasing the temperature from 303 K to 413 K, the emission bands of Nd^{3+} around 750 nm and 800 nm increased quickly, whereas the emission from Er^{3+} around 654 nm showed thermal quenching. The two green emission bands had a more complicated trend with temperature because of the Boltzmann distribution. The intensity-to-temperature curves in Figure 4.9 (b), (e), (h) and (k) show more clearly that the ~800 nm emission bands all had exponential growth that was in line with experimental expectations. However, although the 654 nm emission bands all decayed at high temperature, the decreasing tendency from the sample of 40% Yb^{3+}, 4% Er^{3+} doped nanorods shown in Figure 4.9 (b) and (h) was much weaker than that of the 20% Yb^{3+}, 2% Er^{3+} doped nanorods in Figure 4.9 (e) and (k). Thus, the doping concentrations of 20% for Yb^{3+} and 2% for Er^{3+} in the Yb^{3+}-Er^{3+} codoped section is the optimised formula.

To further distinguish which one was the best nanothermometer among the four samples, relative sensitivities were calculated in Figure 4.9 (c), (f), (i) and (l) based on the 654 nm emission and 803 nm emission intensity changes. The results showed that the highest sensitivity belonged to $NaYF_4$: 60% Yb^{3+}, 4% Nd^{3+}/Y/ 20% Yb^{3+}, 2% Er^{3+} in Figure 4.9 (l), which achieved a value as high as 9.6%/K around room temperature and over a wide temperature range the sensitivity was greater than 2%/K. To the best of our knowledge, this is the highest sensitivity ever found for RE doped nanothermometers[2]. Meanwhile, the $NaYF_4$: 60% Yb^{3+}, 6% Nd^{3+}/$NaYF_4$/$NaYF_4$: 20% Yb^{3+}, 2% Er^{3+} in Figure 4.9 (f) showed the best

sensitivity over 3%/K when the temperature was higher than 340 K and the other nanothermometers had a sensitivity above 3%/K in that range. Additionally, the sensitivities based on the two green emissions of Er^{3+} are shown. Due to the stable optical property of trivalent RE ions, the thermometric property of the Er^{3+} ion did not show obvious differences in the four samples, and the sensitivity was always lower than 2%/K; therefore, it is hardly going to make any improvement for the thermometry based on the thermal coupled energy levels method.

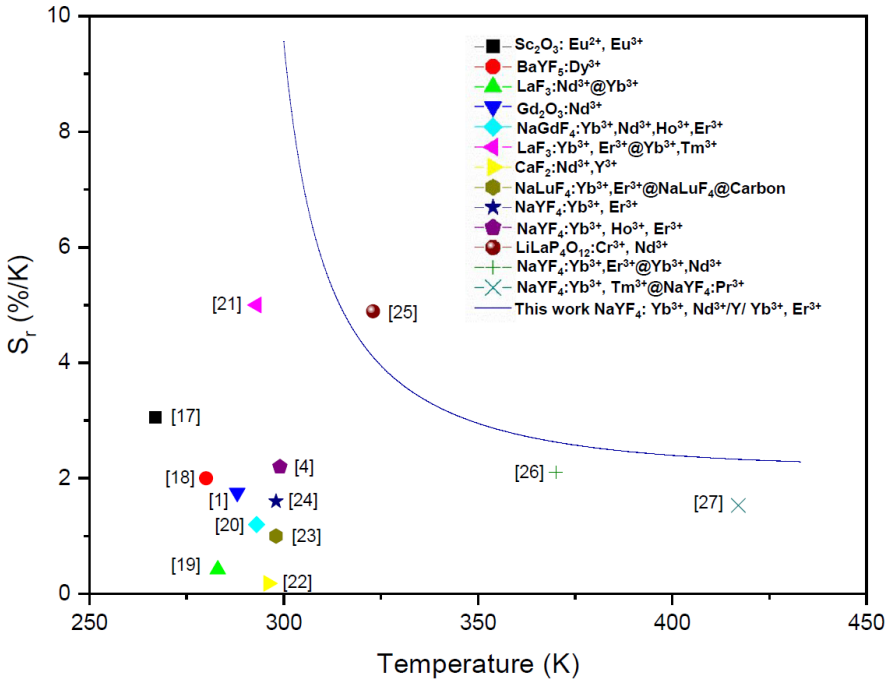

Figure 4.10 Relative sensitivity for the reported RE doped luminescent nanothermometers with different structures. The data points indicate the maximum relative sensitivities at the corresponding temperature and the data curve shows the relative sensitivity of the $NaYF_4$: 60% Yb^{3+}, 4% Nd^{3+}/Y/ 20% Yb^{3+}, 2% Er^{3+} nanothermometer created in this thesis over a wide temperature range.

Figure 4.10 summarises the maximum relative sensitivity among various kinds of RE doped luminescent nanothermometers. Most of the reported sensors had their best performances at low temperatures, ranging from 250 K to 300 K, which was similar to our results. More

significantly, the synthesised new generation nanothermometer in this thesis provided prominent advantages over a wide temperature range from room temperature to over 400 K. The comparison of the relative sensitivity among these reported nanothermometers showed the validity and advancement of the new thermometry strategy proposed in this thesis.

4.3.2 Excitation power dependence of the sandwich structure nanorods

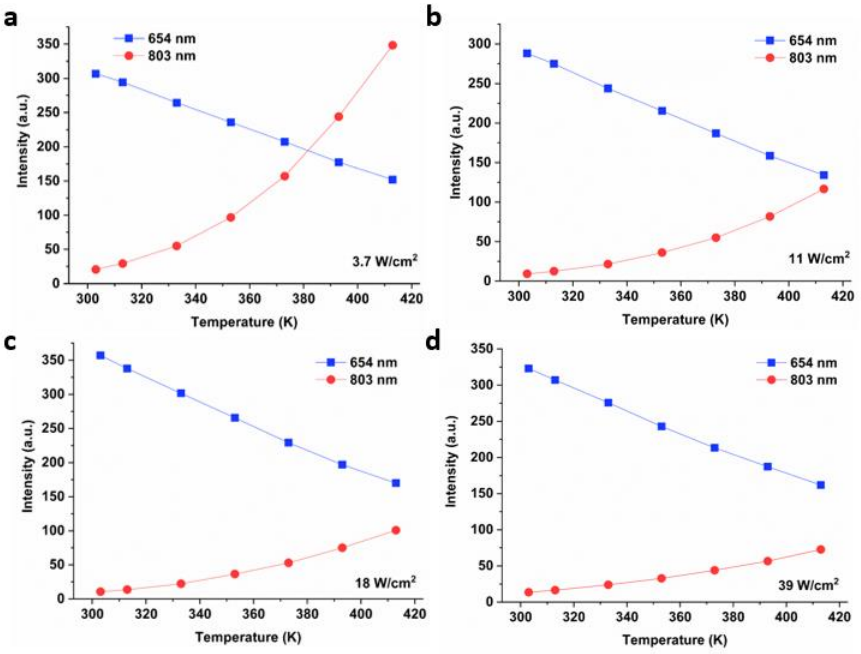

Figure 4.11 The temperature-dependent intensities of 654 nm and 803 nm from $NaYF_4$: 60% Yb^{3+}, 4% Nd^{3+}/Y/20% Yb^{3+}, 2% Er^{3+} under 980 nm excitation with power density of 3.7 W/cm^2 (a), 11 W/cm^2 (b), 18 W/cm^2 (c) and 39 W/cm^2 (d).

In Chapter 3, we found that the surface phonon assisted thermal enhancement closely connected to the excitation power, as the enhancement times were lower in the single nanoparticle imaging under a high excitation power. Thus, we measured the power dependence of the prepared $NaYF_4$: 60% Yb^{3+}, 4% Nd^{3+}/Y/20% Yb^{3+}, 2% Er^{3+} nanothermometer from 303 K to 413 K. As shown in Figure 4.11, four different excitation power densities, 3.7 W/cm^2, 11 W/cm^2, 18 W/cm^2 and 39 W/cm^2, were used for the luminescence-to-temperature curve measurement. The trends of 654 nm emission and 803 nm emission with temperature are

described separately. The thermal quenching of the red emission intensity from Er^{3+} did not change with the excitation power, whereas the thermal enhancement in the 803 nm emission from Nd^{3+} became calm and steady under high excitation power, which was similar with previous results. The contrast between the two emission change trends decreased with the high excitation power, because the sensitivity based on the intensity ratio would also be lower. Fortunately, the opposite thermal responses from the 654 nm and 803 nm emissions could still provide an available sensitivity under the 39 W/cm^2 excitation power.

With the power-dependent study of the nanothermometer, we confirmed the capacity of the prepared new generation nanothermometer under different excitation conditions, especially for the applications that can be realised under low excitation power where the nanothermometer can provide an ultra-sensitive response to temperature change. There are other situations that require high excitation power, which are necessary to induce strong luminescence from a small quantity of luminescent nanothermometer, for example, thermal sensing under microscopy. Sensitivity degradation would appear in these situations but it still qualified for the temperature detection because the intensity ratio of 654 nm and 803 nm emission bands are always highly dependent on the temperature.

4.4 Conclusion

In this chapter, we have successfully applied the investigated surface phonon assistance in anti-Stokes emission of $NaYF_4$: Yb^{3+}, Nd^{3+} for ultra-sensitive temperature sensor design. By combining the thermal enhanced emission via phonon assistance and the thermal quenched emission band, we created a dual-emitter nanothermometer $NaYF_4$: Yb^{3+}, Nd^{3+}, Er^{3+}, and its high sensitivity was verified not only by the qualification of the nanoscale thermometer $NaYF_4$: Yb^{3+}, Nd^{3+}, Er^{3+}, but also by the effectiveness of the novel method. Further, with experiments on different sample structure, we found the most suitable structure of multi-section nanorod that had advantages over the other designs.

After the optimisation on structure and doping concentration, the created nanothermometer $NaYF_4$: Yb^{3+}, Nd^{3+}/Y/ Yb^{3+}, Er^{3+} achieved a maximum sensitivity up to 9.6%/K, such a high sensitivity gives new perspective to nanoscale thermometry. Moreover, from the study on power dependence, the ability of the new generation nanothermometer was confirmed for different excitation situations. Besides the nanocrystal synthesised in the present thesis, with this new method, higher potential RE doped materials could be created for high-sensitive temperature sensing, as phonon assistance and thermal quenching both exist in radiative processes from different RE ions.

4.5 References

1 Balabhadra, S. *et al.* Boosting the sensitivity of Nd^{3+}-based luminescent nanothermometers. *Nanoscale* **7**, 17261-17267 (2015).

2 Brites, C. D. *et al.* Thermometry at the nanoscale. *Nanoscale* **4**, 4799-4829 (2012).

3 Fiorenzo Vetrone, R. N., *et al*. Temperature sensing using fluorescent nanothermometers. *ACS Nano* **4**, 5 (2010).

4 Wortmann, L., Suyari, S., Ube, T., Kamimura, M., Soga, K. Tuning the thermal sensitivity of β-$NaYF_4$: Yb^{3+}, Ho^{3+}, Er^{3+} nanothermometers for optimal temperature sensing in OTN-NIR (NIR II/III) biological window. *Journal of Luminescence* **198**, 236-242 (2018).

5 Brites, C. D. S., Millán, A., Carlos, L. D. in *Handbook on the Physics and Chemistry of Rare Earths* Vol. 49, 89 (2016).

6 Gao, L., Zhang, C., Li, C., Wang, L. V. Intracellular temperature mapping with fluorescence-assisted photoacoustic-thermometry. *Appl Phys Lett* **102**, 193705 (2013).

7 Cadiau, A., Brites, C. D. S., Costa, P. M. F. J., Ferreira, R. A. S., Rocha, J., Carlos, L. D. Ratiometric nanothermometer based on an emissive Ln^{3+}-organic framework. *ACS Nano* **7**, 6 (2013).

8 Albers, A. E. *et al.* Dual-emitting quantum dot/quantum rod-based nanothermometers with enhanced response and sensitivity in live cells. *J Am Chem Soc* **134**, 9565-9568 (2012).

9 Sedlmeier, A., Achatz, D. E., Fischer, L. H., Gorris, H. H., Wolfbeis, O. S. Photon upconverting nanoparticles for luminescent sensing of temperature. *Nanoscale* **4**, 7090-7096 (2012).

10 Xu R., Wang, M., Tian, Y., Hu, L., Zhang, J. 2.05 μm emission properties and energy transfer mechanism of germanate glass doped with Ho^{3+}, Tm^{3+}, and Er^{3+}. *Journal of Applied Physics* **109**, 053503 (2011).

11 Tang, J. F. *et al.* Power driven tunable white upconversion luminescence from Lu_2TeO_6 tri-doped with Yb^{3+}, Tm^{3+} and Ho^{3+}. *CrystEngComm* **17**, 9048-9054 (2015).

12 Deng, R. *et al.* Temporal full-colour tuning through non-steady-state upconversion. *Nat Nanotechnol* **10**, 237-242 (2015).

13 Yang, G. *et al.* A core/shell/satellite anticancer platform for 808 NIR light-driven multimodal imaging and combined chemo-/photothermal therapy. *Nanoscale* **7**, 13747-13758 (2015).

14 Chen, X., Peng, D., Ju, Q. & Wang, F. Photon upconversion in core-shell nanoparticles. *Chem Soc Rev* **44**, 1318-1330 (2015).

15 Liu, Q. *et al.* Single upconversion nanoparticle imaging at sub-10 W cm^{-2} irradiance. *Nature Photonics* **12**, 548-553 (2018).

16 Liu, D. *et al.* Three-dimensional controlled growth of monodisperse sub-50 nm heterogeneous nanocrystals. *Nat Commun* **7**, 10254 (2016).

17 Pan, Y. *et al.* Inherently Eu^{2+}/Eu^{3+} codoped Sc_2O_3 nanoparticles as high-performance nanothermometers. *Adv Mater* **30**, e1705256 (2018).

18 Cao, Z. *et al.* Temperature dependent luminescence of Dy^{3+} doped $BaYF_5$ nanoparticles for optical thermometry. *Current Applied Physics* **14**, 1067-1071 (2014).

19 Ximendes, E. C. *et al.* Unveiling in vivo subcutaneous thermal dynamics by infrared luminescent nanothermometers. *Nano Lett* **16**, 1695-1703 (2016).

20 Skripka, A. *et al.* Double rare-earth nanothermometer in aqueous media: opening the third optical transparency window to temperature sensing. *Nanoscale* **9**, 3079-3085 (2017).

21 Ximendes, E. C. *et al.* In vivo subcutaneous thermal video recording by supersensitive infrared nanothermometers. *Advanced Functional Materials* **27**, 1702249 (2017).

22 Quintanilla, M., Zhang, Y., Liz-Marzán, L. M. Subtissue plasmonic heating monitored with $CaF_2:Nd^{3+},Y^{3+}$ nanothermometers in the second biological window. *Chemistry of Materials* **30**, 2819-2828 (2018).

23 Zhu, X. *et al.* Temperature-feedback upconversion nanocomposite for accurate photothermal therapy at facile temperature. *Nat Commun* **7**, 10437 (2016).

24 Rodriguez-Sevilla, P. *et al.* Thermal scanning at the cellular level by an optically trapped upconverting fluorescent particle. *Adv Mater* **28**, 2421-2426 (2016).

25 Marciniak, L., Bednarkiewicz, A., Kowalska, D., Strek, W. A new generation of highly sensitive luminescent thermometers operating in the optical window of biological tissues. *Journal of Materials Chemistry C* **4**, 5559-5563 (2016).

26 Marciniak, L., Prorok, K., Frances-Soriano, L., Perez-Prieto, J., Bednarkiewicz, A. A broadening temperature sensitivity range with a core-shell YbEr@YbNd double ratiometric optical nanothermometer. *Nanoscale* **8**, 5037-5042 (2016).

27 Zhou, S. *et al.* Strategy for thermometry via Tm^{3+}-doped $NaYF_4$ core-shell nanoparticles. *Opt Lett* **39**, 6687-6690 (2014).

CHAPTER 5

Temperature sensing demonstration on large area imaging and microelectronic device

In this chapter, we focused on the practical applications using the created ultra-sensitive luminescent nanothermometers, including a combination using the optical imaging approach. By building up the specific optical test systems, we first conducted large area imaging with the luminescent nanothermometers. By changing the temperature of the sample layer, the temperature-responsive emission multicolour changes fast, which indicates the function of the prepared nanothermometer as anti-counterfeit material. Moreover, we obtained the exact sample temperature by additional spectra monitoring at the same time. Next, we challenged the localised temperature sensing on a 100 × 10 μm^2 microelectronic device under a wide field microscope. Successfully, with a calibration curve, the luminescent nanothermometer on the device achieved a high spatial resolution temperature reading on three different positions of the device. To prove the repeatability and traceability of the new generation nanothermometer, we tested the sample for multiple heating-cooling cycles and the results showed the excellent performance of the ratiometric nanothermometer. These results showed the wide range of possible applications based on the nanothermometers created in this thesis.

5.1 Introduction

RE doped materials with anti-Stokes emissions gain exceptional properties including large anti-Stokes shifts, sharp emission spectra and long excited-state lifetimes, which has led to a diversity of applications. One of the applications is temperature sensing via the unique thermal

properties of the RE doped materials. However, an innovative approach is urgently required to overcome the low sensitivity limitation associated with the conventional method. Based on these facts, we proposed a method to fabricate RE doped materials into nanothermometers in the last chapter by taking advantage of thermal enhanced anti-Stokes emissions. Equipping with a sensitivity up to 9.6%/K, the synthesised nanothermometers that are smaller than 100 nm can be an excellent choice for high spatial resolution temperature sensing.

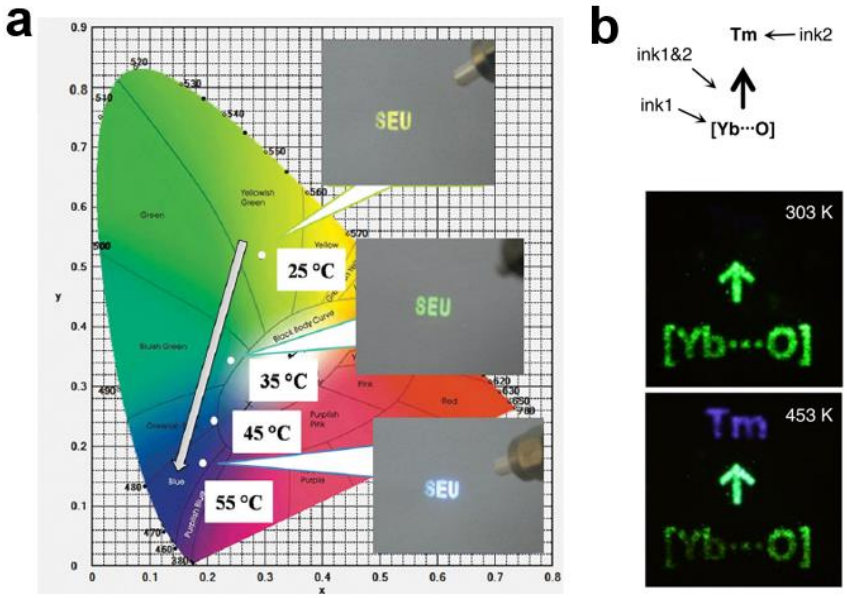

Figure 5.1 Temperature-responsive anti-counterfeiting security inks by RE doped nanomaterials[1,2]. (a) The chromaticity coordinate shifts and colour changes of composite nanopowders of $NaYF_4:Yb^{3+}$, Ho^{3+} nanowires and $NaGdF_4:Yb^{3+}$, Tm^{3+} nanoparticles. (b) The patterns printed by $NaYF_4:Yb^{3+}$, Tm^{3+} (ink1) and $NaYF_4:Yb^{3+}$, Tm^{3+} (ink2) show obvious emission intensity changes under different temperature.

Moreover, RE doped anti-Stokes emission materials are widely used to define security features in many potential applications such as currency, identity cards and bank accounts, owing to their NIR-to-visible luminescence[1-4]. The reversible temperature-responsive colour change of these RE doped anti-Stokes emission materials are favourable for real-time recognition but are difficult to copy, showing great promise for developing more secure anti-counterfeiting

patterns. A shortcoming for these composite nanomaterials is that a heating process is required to achieve the multicolour shifting. As shown in Figure 5.1, two reported results show the ability of the RE doped anti-Stokes emission materials working as temperature-responsive anti-counterfeiting security agents[1,2]. Both examples utilised the thermal enhanced blue emission in the Yb^{3+}-Tm^{3+} codoping upconversion system, thus when temperature is high the emission colour turns to blueness, whereas the green emission from Ho^{3+} or Er^{3+} has faded away.

To demonstrate other significant applications of the prepared nanothermometer such as localised temperature sensing on a microelectronic device or in a single cell, the experiments will be more complicated. To visualise such a small region of interest, optical microscope is a necessary tool to image the target. Other questions, such as the temperature control of the sample on a microscope and the integration of the nanothermometer with the test objective, should be solved in advance of the temperature measurement. In consideration of these requirements, the high spatial resolution temperature measurement is not only the synthesis of nanothermometers, but also interdisciplinary research realised by different types of technologies. In view of this, we completed the large area temperature measurement and on-device temperature sensing using a purpose-designed optical system.

5.2 Large area temperature sensing

5.2.1 Method

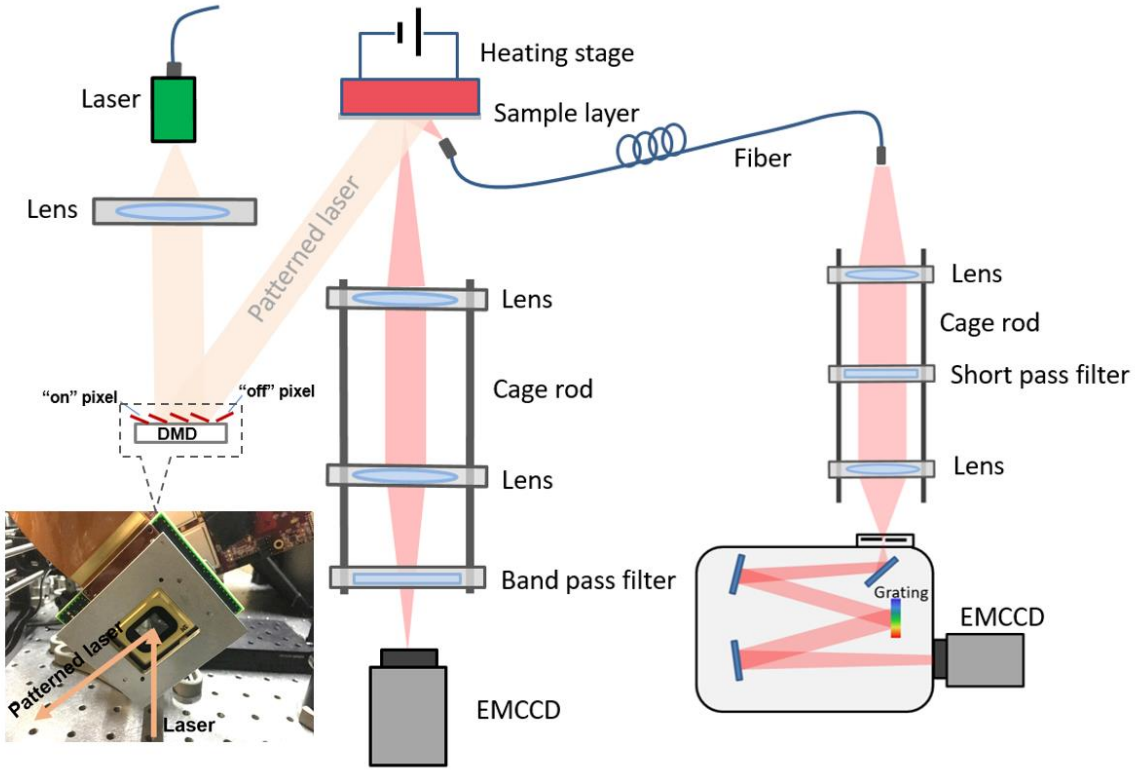

Figure 5.2 Schematic diagram of the home-built optical system for the large area temperature sensing and imaging experiments.

To provide an example of the large area temperature measurement by the tri-doping $NaYF_4$: Yb^{3+}, Nd^{3+}, Er^{3+} nanothermometer, a specific optical system was built to simultaneously control temperature, monitor real-time spectra and record images, as shown in Figure 5.2. This purpose-designed optical system is equipped with a digital micro-mirror device (DMD, DLP Discovery D4100 kit, Texas Instruments) for patterned laser excitation. This DMD chip can form binary images at two grayscale levels, 0 and 255, with a resolution of 1024 × 768 pixels. Each pixel is one micro-mirror with a size of 10.8 × 10.8 μm^2 that can be modulated to orientation states corresponding to the "on" or "off" state; therefore, the laser reflected by the modulated DMD contained the same illumination pattern on the chip[5].

The nanopowder of the tri-doping $NaYF_4$: Yb^{3+}, Nd^{3+}, Er^{3+} nanothermometer was made into a thin sample film fixed by two glass slides and then attached on the heating stage. With the patterned laser illumination on the nanothermometer layer, the same luminescence image from the sample film was captured by the EMCCD camera, and two imaging channels were realised by two single band pass filters around 655 nm and 810 nm. Meanwhile, the emission spectra were measured by a fibre-coupled luminescence spectrometer, with the multi-mode optical fibre having a core diameter of 400 μm, which was enough for signal collection. Finally, the temperature of the sample was controlled by the heating stage from room temperature to 413 K in this experiment.

5.2.2 Temperature-dependent imaging and sensing results

The results of the large area temperature measurements are shown in Figure 5.3 (a), the image formed by the ~800 nm emission band from Nd^{3+} gradually became much brighter with higher temperature, whereas with a red band pass filter, the image containing the ~650 nm emission from Er^{3+} faded away because of thermal quenching. The imaging results are in accord with the luminescence spectra at each set temperature in Figure 5.3 (b). By calculation of the peak intensity ratio from spectra, the value changed from 0.2037, 0.5931 and 2.1071 to 6.1565 under 303 K, 333 K, 373 K and 413 K, respectively. By interpolation of these ratio values in the calibration curve in Figure 5.3 (c), the corresponding temperatures measured by the $NaYF_4$: Yb^{3+}, Nd^{3+}, Er^{3+} nanothermometer were 301.65 K, 333.19 K, 372.69 K and 412.97 K, which were very close to the set temperature values.

These results provide an example of how to combine the optical characterisation method with luminescent nanothermometry and offer new insights into the possible application of the nanothermometers for both accurate temperature sensing and temperature-response anti-counterfeiting. Moreover, as the 650 nm and 800 nm emissions both fall in the biological

transmission window, Nd^{3+}- Er^{3+} codoped thermometers are an ideal candidate especially for biological temperature detection.

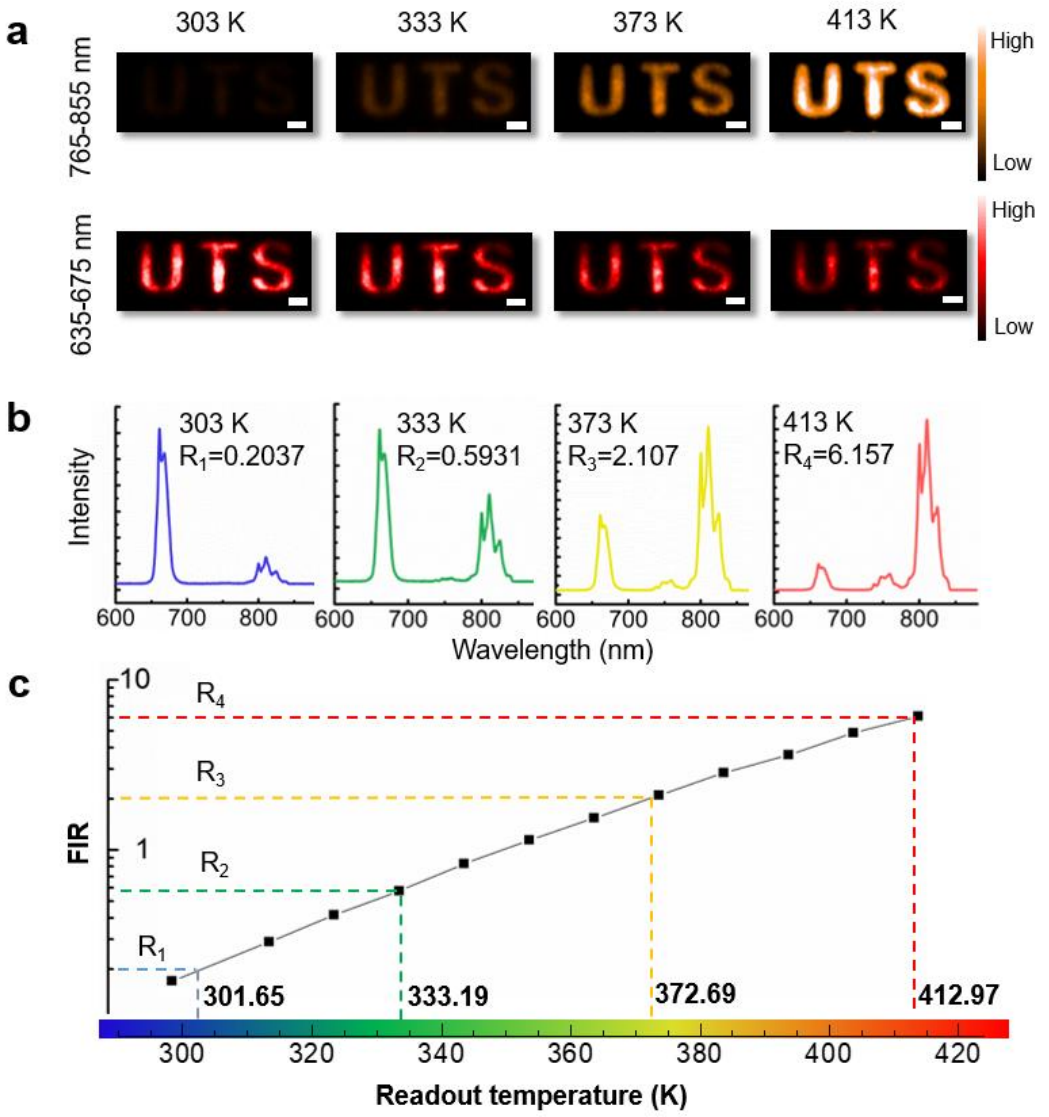

Figure 5.3 (a) Dual-channel imaging of ratiometric luminescence responses of the homogeneous tri-doped $NaYF_4$: 20% Yb^{3+}, 6% Nd^{3+}, 0.5% Er^{3+} nanocrystals were recorded under a 980 nm patterned laser excitation (power density of 1.5 W/cm^2), when the temperature increased from 303 K to 413 K. To show the contrast, pseudocolour-coded images were obtained using an EMCCD camera through a 765–855 nm bandpass filter and a 635–675 nm bandpass filter. Scale bar is 1 mm. (b) Corresponding spectra of the patterns in (a). (c) Temperature readouts by the intensity ratio values with a calibration curve.

5.3 Localised temperature sensing on microdevice

5.3.1 Method

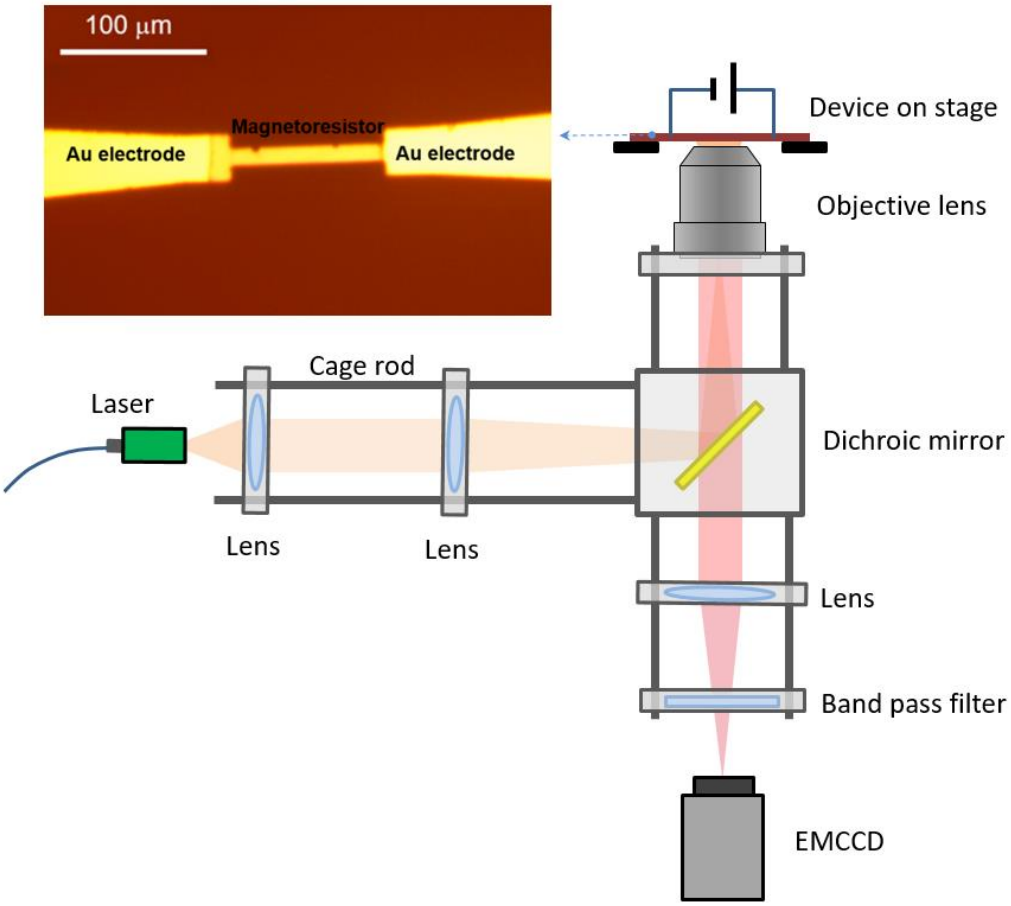

Figure 5.4 Schematic diagram of the home-built wide field microscope for the on-device temperature mapping experiment. The image shows the micro magnetoresistive sensor used for on-device localised temperature sensing. The sensor in the middle is 10 μm × 100 μm in size, whereas the two ends connected Au electrodes have a much larger size.

The high spatial resolution temperature measurement on the microelectronic device was also conducted on the home-built wide field imaging microsope for the single nanoparticle imaging (Figure 5.4), as described in Chapter 2. First, the cyclohexane solution of synthesised multi-section nanorod $NaYF_4$: 60% Yb^{3+}, 4% Nd^{3+}/Y/ 20% Yb^{3+}, 2% Er^{3+} was dropped on the micro device to form a thin layer of as-prepared nanothermometer, and the magnetoresistive device covered by nanothermometer layer was powered by a source meter (2612B, Keithley). Then,

the device was fixed on the three-axes sample stage for microscopy imaging. By increasing the electric current to 28 mA gradually, the power added on the sensor varied from 0 to 36 mW and the resistance value of the device was maintained at around 52 Ω, which caused a temperature change due to the Joule effect. Finally, by taking images with two band pass filters (ET810/90m and ET655/40m, Chroma), the emission intensities of Nd^{3+} and Er^{3+} were recorded to obtain the corresponding temperature. The calibration curve was measured in a similar way, the sample was spread on a glass slide attached on the heating stage, then the two emission intensities under different temperatures were captured by an EMCCD camera.

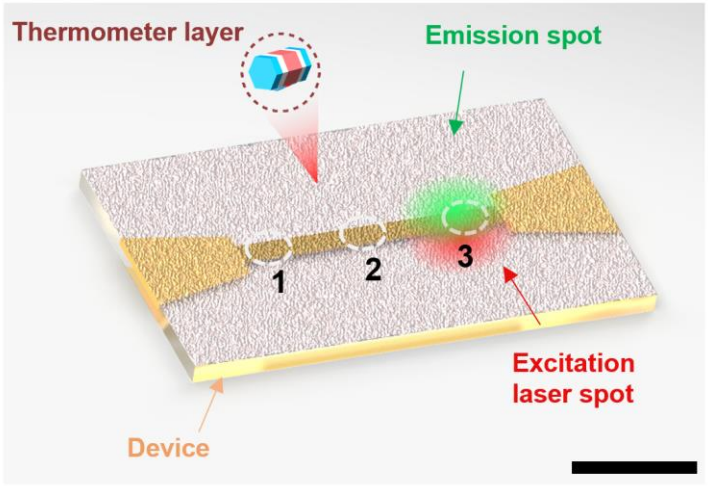

Figure 5.5 Illustration of real-time sensing of the localised (three circled areas) temperature changes on a microelectronic device coated with nanothermometry probes (excitation power density of 70 W/cm^2). Scale bar is 50 µm.

To demonstrate the temperature mapping ability of the prepared nanothermometer on the ultra-small device, we chose three different positions on the magnetoresistive sensor with one at each of the ends and the third in the middle as shown in Figure 5.5. Moreover, in consideration of the studied excitation power-dependent properties of the nanothermometer, the three measured positions should be excited by the same laser power with the calibration curve to guarantee consistency of the data. Thus, during the measurement, the position of the device

was precisely controlled to ensure the three chosen areas on the sensor had the same illumination by the Gaussian laser beam. The spot diameter was about 100 μm. Then, the average intensity of all the pixels in each region of interest was calculated for the intensity ratio. Finally, by a simple interpolation method, the exact temperature on the three positions of the electronic sensor was determined from the calibration curve.

5.3.2 Results of the localised temperature sensing on the microdevice

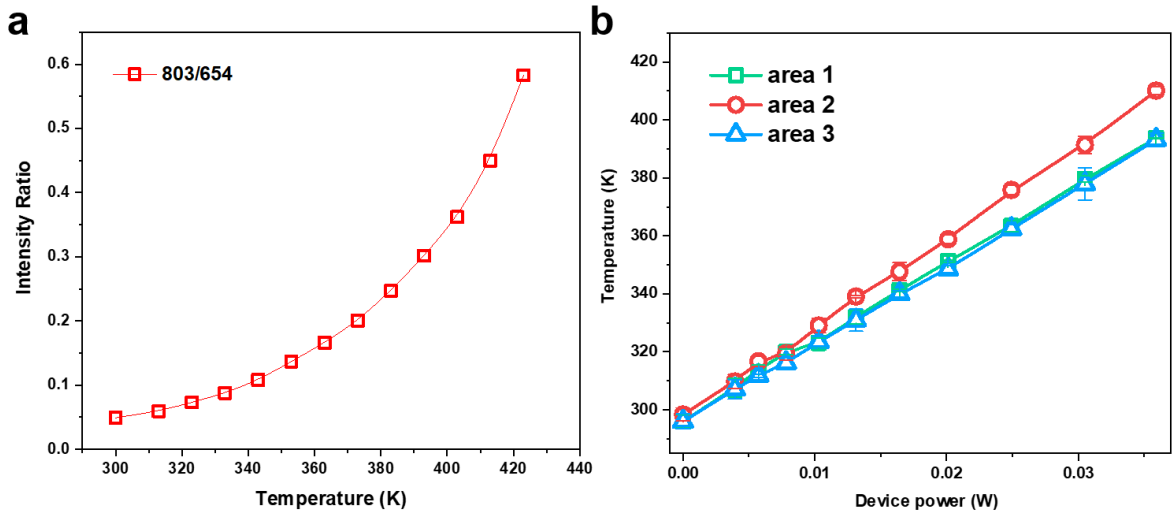

Figure 5.6 The on-device temperature mapping with the calibration process. (a) Calibration curve of the nanothermometer $NaYF_4$: 60% Yb^{3+}, 4% Nd^{3+}/Y/ 20% Yb^{3+}, 2% Er^{3+}. We increased the temperature using a heating stage. (b) Measured temperatures from the three different areas when the device power consumption increased from 0 to 0.036 W. The emission intensity ratios were recorded under the excitation power of ~70 W/cm^2 for both measurements.

Figure 5.6 (a) shows the calibration curve achieved by the microscopic imaging of the nanothermometer on the glass slide under ~70 W/cm^2 980 nm excitation power, a heating stage was used for sample temperature adjustment. As before, the intensity ratio of the 803 nm emission of Nd^{3+} to the 654 nm emission of Er^{3+} increased exponentially with the temperature. For the on-device temperature measurement, the same excitation power was used for the illumination of the nanothermometer layer on the microelectronic device. Under different

device power, the images of the ~654 nm and ~800 nm emission from the three regions of the nanothermometer layer were recorded in sequence. To reduce the influence of signal fluctuation of the camera, every image of the nanothermometer luminescence was repeated three times to obtain the average temperature value and the error bar.

As shown in Figure 5.6 (b), when the microelectronic device was powered off, the results indicated by the nanothermometer were around room temperature in the three areas. To cause the temperature change, the electricity of the device was increased slowly, and the measured temperature for all the areas increased linearly with the electric power of the device. Moreover, when the power was high enough, a difference in localised temperature changes emerged between area 2 and areas 1/3. This temperature difference became more and more obvious with high device power and finally the temperature from area 2 was 16 K higher than that from areas 1 and 3 under the supply power of 0.036 W, which suggests the worse thermal conductivity in the middle section of the device than the other two section near to the Au electrodes. The temperature mapping result on the strip-type electrical resistance is quite similar to the reported results in Figure 1.16 (f), which also indicated higher Joule heat in the middle than at the two ends of the resistance.

5.4 Investigation on traceability and repeatability

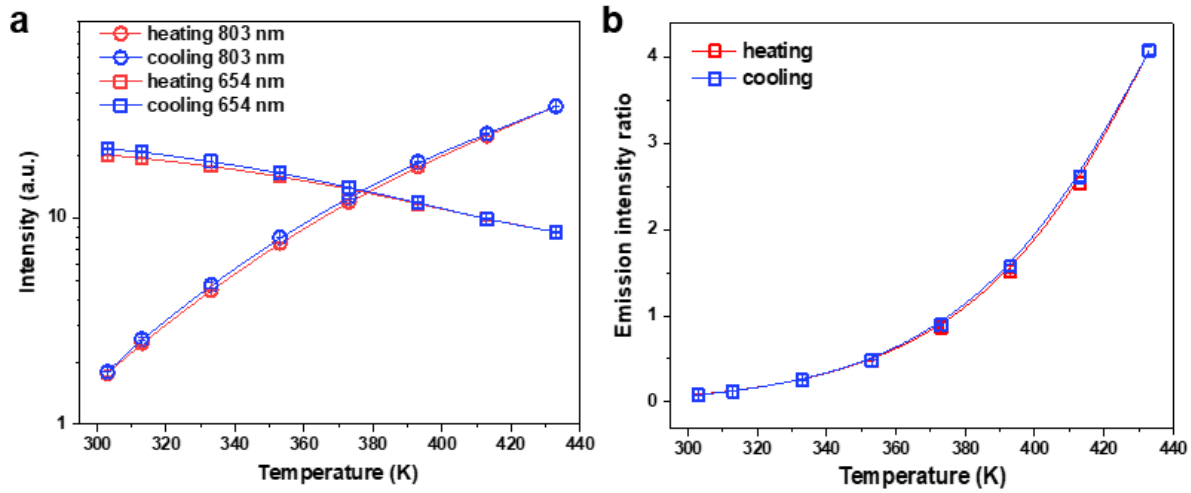

Figure 5.7 Traceability of the nanothermometer during heating and cooling. The sample is excited by 0.13 W/cm^2 980 nm laser.

To confirm that the dependable nanothermometer can provide repeated usage in the temperature sensing applications, we investigated the traceability and repeatability of the new generation nanothermometer. The traceability means that no matter whether the test target is heating up or cooling down, the ratiometric nanothermometer will always provide the correct result with one calibration curve[6-10]. As shown in Figure 5.7 (a), in a heating-cooling cycle, both emission bands around 654 nm and 803 nm from $NaYF_4$: 60% Yb^{3+}, 4% Nd^{3+}/Y/ 20% Yb^{3+}, 2% Er^{3+} showed the hysteresis effect, which was similar to the results shown in Chapter 3. The hysteresis effect is caused by the moisture release from the nanothermometer surface at high temperature, then when the temperature is cooling down both emission bands show higher intensities due to less quenching on the surface. Because the performance of the two emissions was inconsistent during the heating and cooling process, this hysteresis effect led to bad traceability in the single emission band dependent temperature sensing based on either the 654 nm or 803 nm emission; therefore, the single emission-based nanothermometer could not ensure a correct result during the actual temperature test. Fortunately, by creating a

ratiometric nanothermometry, the emission intensity ratio of 803 nm to 654 nm showed a negligible hysteresis effect during the heating-cooling cycle test in Figure 5.7 (b). This is because the hysteresis effect in the 654 nm and 803 nm emission was very similar during the heating-cooling process, thus the intensity ratio of the two emissions relieved the influence by the hysteresis effect. Therefore, because of the advantages of the ratiometric nanothermometer, the created nanothermometer could also achieve excellent traceability whenever the temperature was increasing or decreasing.

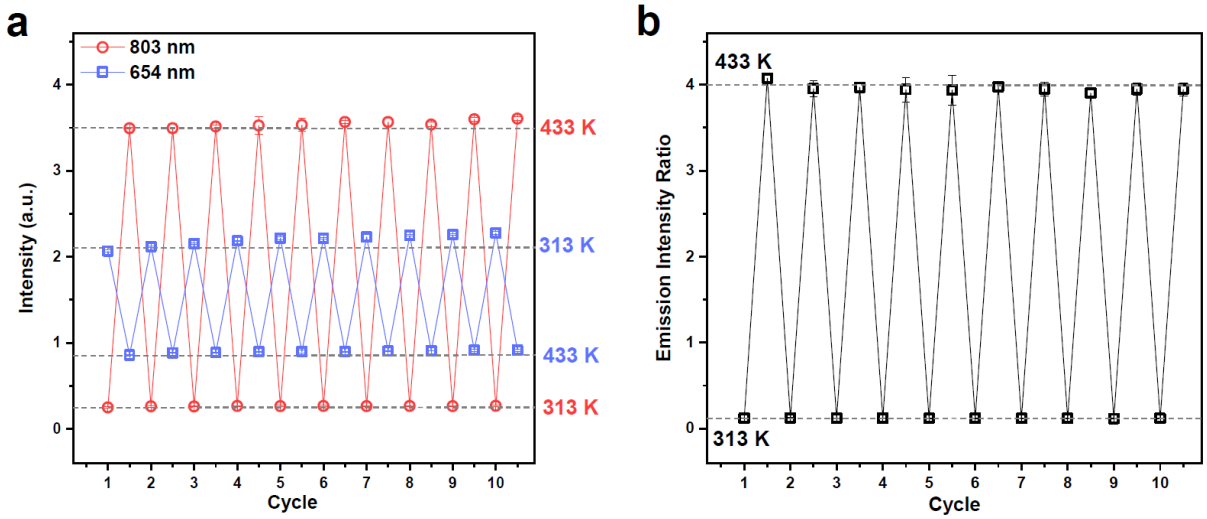

Figure 5.8 Repeatability of the nanothermometer in 10 heating-cooling cycles. The spectra intensities of 803 nm and 654 nm were recorded from 313 K to 433 K at each cycle (a), the stable emission intensity ratios at 313 K and 433 K during 10 cycle tests show a good repeatability of the nanothermometer (b). The sample was excited by 0.13 W/cm^2 980 nm laser.

Repeatability, as discussed in Chapter 1, indicates that the thermometer can always give the same result during multiple tests that have a certain quantity to be measured. Repeatability requires the luminescent nanothermometer to have a stable physicochemical property, because the applications that require repetitive tests will involve long-term measurements. During the entire process, the luminescent nanothermometer should maintain a steady emission signal and the material structure will not be influenced by frequent temperature changes. As shown in

Figure 5.8, the 10 heating-cooling cycles test between 313 K and 433 K indicated the robust qualities of the nanothermometer $NaYF_4$: 60% Yb^{3+}, 4% Nd^{3+}/Y/ 20% Yb^{3+}, 2% Er^{3+}, which can be explained by the stable crystal structure of the RE doped inorganic nanoparticles. The entire process took up to 5 h and the luminescent nanothermometer did not show any photobleaching in the measurement. By heating up to 433 K for 10 times, the two emission bands did not show any obvious intensity change, only a small increase caused by the moisture release, as shown in Figure 5.8 (a). More significantly, the emission intensity ratio used for temperature sensing barely changed with the multi-round heating-cooling process. The outstanding repeatability demonstrated again the superiority of the ratiometric nanothermometers.

With the study on the traceability and repeatability of the proposed nanothermometer in this thesis, we have clearly shown that it has great potential for application in temperature sensing in more complicated situation rather than the two demonstrated applications in this chapter.

5.5 Conclusion

In this chapter, we focused on the application demonstration of the ultra-sensitive nanothermometer designed in this thesis. By making use of two purpose-built optical test systems, we performed a basic temperature sensing experiment in a large thermal area. The temperature results obtained by the nanothermometer perfectly matched with the set temperatures by the heating stage, which proved the sensing ability of the nanothermometer. With an EMCCD camera monitoring the temperature-dependent luminescence image, we observed the obvious intensity change of the nanothermometer. Such a quick visual response provides another possible method for anti-counterfeiting technology. Moreover, we further applied the sandwich structure nanothermometers for localised temperature diagnosis of microelectronic devices. By gradually increasing the device power, the three testing areas exhibited different temperature increase rates, i.e. the two sections at the ends had lower temperatures than the section in the middle, which can be explained by the inferior heat conduction in the middle of the device. These results confirmed the high spatial resolution nanothermometry using the ultra-sensitive nanothermometer. Additionally, the traceability and repeatability of the temperature sensor was investigated during the heating-cooling cycle test. The hysteresis effects in the emission band were eliminated in the emission intensity ratio, which revealed the advantage of the ratiometric nanothermometer. With its excellent traceability and repeatability, the nanothermometer can be used for long-term temperature measurement, irrespective of how the temperature changes.

5.6 References

1 Li, D. D., Shao, Q. Y., Dong, Y., Fang, F., Jiang, J. Q. Ho^{3+}(or Tm^{3+})-activated upconversion nanomaterials: Anomalous temperature dependence of upconversion luminescence and applications in multicolor temperature indicating and security. *Particle & Particle Systems Characterization* **32**, 728-733 (2015).

2 Zhou, J. *et al.* Activation of the surface dark-layer to enhance upconversion in a thermal field. *Nature Photonics* **12**, 154-158 (2018).

3 Kim, W. J., Nyk, M., Prasad, P. N. Color-coded multilayer photopatterned microstructures using lanthanide (III) ion co-doped $NaYF_4$ nanoparticles with upconversion luminescence for possible applications in security. *Nanotechnology* **20**, 185301 (2009).

4 Zhao, J. *et al.* Single-nanocrystal sensitivity achieved by enhanced upconversion luminescence. *Nat Nanotechnol* **8**, 729-734 (2013).

5 Dan, D. *et al.* DMD-based LED-illumination super-resolution and optical sectioning microscopy. *Sci Rep* **3**, 1116 (2013).

6 del Rosal, B., Ximendes, E., Rocha, U., Jaque, D. In vivo luminescence nanothermometry: from materials to applications. *Advanced Optical Materials* **5**, 14 (2017).

7 Jaque, D., Vetrone, F. Luminescence nanothermometry. *Nanoscale* **4**, 4301-4326 (2012).

8 Zhou, H., Sharma, M., Berezin, O., Zuckerman, D., Berezin, M. Y. Nanothermometry: From microscopy to thermal treatments. *Chemphyschem* **17**, 27-36 (2016).

9 Brites, C. D. *et al.* Thermometry at the nanoscale. *Nanoscale* **4**, 4799-4829 (2012).

10 Brites, C. D. S., Millán, A., Carlos, L. D. in *Handbook on the Physics and Chemistry of Rare Earths* Vol. 49, 89 (2016).

CHAPTER 6

Conclusion and perspective

6.1 Conclusion

In this thesis, surface phonon assistance for thermal induced emission enhancement in RE doped anti-Stokes luminescent materials was discussed for the first time. Under high temperature, both the Yb^{3+}-Tm^{3+} and Yb^{3+}-Nd^{3+} codoping nanocrystals showed much stronger anti-Stokes emissions owing to the unique surface and host phonon assistance in the energy transfer process[1]. Moreover, quantitative analysis on the contribution of different emission enhancing factors was conducted via the temperature-dependent spectra measurement in Ar atmosphere. After removing the moisture from the surface of the sample, the emission intensity of the moisture-free Yb^{3+}-Nd^{3+} codoping nanocrystals were recovered to a higher value, whereas the main contribution on the thermal induced emission enhancement was made from the surface and host phonon assistance. The surface ligands and lattice vibration were proven to play a dominant role in the thermal enhancement of the RE doped anti-Stokes materials.

By combining phonon assistance with thermal quenching to form a ratiometric nanothermometer in the sandwich structure nanorod $NaYF_4$: Yb^{3+}, Nd^{3+}/Y/Yb^{3+}, Er^{3+}, the author successfully created the next generation ultra high-sensitive nanothermometer, and a relative sensitivity up to 9.6%/K makes it the most sensitive nanothermometer. With the application demonstration under two different conditions, the temperature sensing ability with high accuracy and spatial resolution suggested a wide range of potential applications based on the fabricated nanothermometer in this thesis.

The successful outcomes reported in this thesis are listed below in more detail:

(1) The author achieved obvious thermal induced emission enhancement in OA-capped $NaYF_4$: Yb^{3+}, Tm^{3+} and $NaYF_4$: Yb^{3+}, Nd^{3+} anti-Stokes luminescence nanoparticles under high temperature. With a series of verified experiments, for the first time the author proved the unique surface phonon assistance in the RE doped nanoparticles with ligand capped on the surface.

(2) The thermal enhancement found in the RE doped nanoparticles provides a new strategy to overcome the widely existed thermal quenching effect in the luminescent materials.

(3) By applying the investigated surface phonon assistance to the ultra-sensitive nanothermometer design, an Yb^{3+}-Nd^{3+}-Er^{3+} tri-doped ratiometric nanothermometer with a temperature-responsive intensity ratio of 803 nm to 654 nm emission from Nd^{3+} and Er^{3+}, respectively, was successfully created. After optimisation on structure and doping concentration, the created multi-section nanorod structure $NaYF_4$: Yb^{3+}, Nd^{3+}/Y/ Yb^{3+}, Er^{3+} achieved a maximum sensitivity up to 9.6%/K. Such a high sensitivity provides new perspective on nanoscale thermometry.

(4) The temperature sensing results in a large area proved the accurate sensing ability of the created nanothermometer, and the visual thermal-responsive real-time imaging based on the luminescent nanothermometer provided another possible method for anti-counterfeiting technology.

(5) Moreover, the localised temperature measurement on three different areas of a microelectronic device confirmed the high spatial resolution ability of the ultra-sensitive nanothermometer with a size smaller than 100 nm.

(6) From the studies on power dependence, traceability and repeatability, the author confirmed the capability of the next generation nanothermometer to deal with long-term temperature measurement and other complex situations.

6.2 Perspective

Thermal quenching is a problem that must be solved for efficient luminescent materials[2,3], although the surface phonon assistance reported in this thesis can fight against the thermal quenching and contribute to stronger luminescence at high temperature. This unique thermal enhancement effect currently only shows extraordinary influence in Yb^{3+}-Tm^{3+} and Yb^{3+}-Nd^{3+} codoped anti-Stokes nanomaterials, which benefit from the heat-favourite phonons generated from the surface-capped ligand. Theoretically, this surface phonon assistance can be extended to other RE doped luminescence materials as long as the energy mismatch during the energy transfer is not great, then the ligand capped nanocrystals can produce additional phonon energy at a thermal field to fill up the energy gap and make the energy transfer more efficient. Thus, developing the surface phonon assistance to a widely applicable approach for other types of luminescent materials will be the future potential focus.

Meanwhile, apart from the ratiometric nanothermometer created in this thesis, the author also found the temperature-responsive lifetime of the ~800 nm emission in $NaYF_4$:Yb^{3+}, Nd^{3+} as described in Chapter 3. From room temperature to 413 K, the emission lifetime increased greater than 5 times. These results hint at the possibility to create new types of temperature sensors in view of the advantages of the lifetime-based nanothermometers[4]. Moreover, the intrinsic lifetime of the luminescent material can be optimised by different doping concentrations, material sizes and structures based on the reported methods[5,6].

Finally, the results from the present study have shown the excellent performance of the created ratiometric nanothermometer for applications in microelectronic devices. Future studies will

be aimed at applications in intracellular temperature sensing. Although the researchers have achieved significant progress on the intracellular temperature mapping[4,7,8], there are still some issues that must be solved. Due to the complex environments in biological systems, the study on nanothermometer should be more comprehensive as some factors can influence the accuracy a lot, such as the environmental humidity and the *in-vivo* excitation power. To get the correct readout in such case, the calibration experiment is quite important, and the key is to keep the same test conditions in the calibration experiment with the *in-vivo* temperature measurement by simulating the biological microenvironment, using the same excitation power and so on. Thus, the *in-vivo* temperature readout by the nanothermometer can be well calibrated. To fully understand the basic activities in the cellular and tissues, new methods on the intracellular temperature mapping must be explored. Furthermore, the created ratiometric nanothermometer based on 654 nm and 800 nm emission has the advantage of deep tissue penetration as both emission wavelengths are in the biology optical window, which has created favourable conditions for future applications in intracellular temperature sensing.

6.3 References

1 Zhou, J. *et al.* Activation of the surface dark-layer to enhance upconversion in a thermal field. *Nature Photonics* **12**, 154-158 (2018).

2 Chen, Z. *et al.* Facile synthesis of self-activated oxyfluorotungstate phosphor with high QE and its thermal quenching. *Journal of Alloys and Compounds* **770**, 559-563 (2019).

3 Kim, Y. H. *et al.* A zero-thermal-quenching phosphor. *Nat Mater* **16**, 543-550 (2017).

4 Okabe, K. *et al.* Intracellular temperature mapping with a fluorescent polymeric thermometer and fluorescence lifetime imaging microscopy. *Nat Commun* **3**, 705 (2012).

5 Lu, Y. *et al.* Tunable lifetime multiplexing using luminescent nanocrystals. *Nature Photonics* **8**, 32-36 (2013).

6 Jaque, D., Vetrone, F. Luminescence nanothermometry. *Nanoscale* **4**, 4301-4326 (2012).

7 Arai, S. *et al.* Mitochondria-targeted fluorescent thermometer monitors intracellular temperature gradient. *Chem Commun (Camb)* **51**, 8044-8047 (2015).

8 Donner, J. S., Thompson, S. A., Kreuzer, M. P., Baffou, G., Quidant, R. Mapping intracellular temperature using green fluorescent protein. *Nano Lett* **12**, 2107-2111 (2012).